

Gamma-Blind Fast Neutron Detection for Spent Nuclear Fuel Characterization

Présentée le 17 mars 2023

Faculté des sciences de base
Laboratoire de physique des réacteurs et de comportement des systèmes
Programme doctoral en énergie

pour l'obtention du grade de Docteur ès Sciences

par

Alexander WOLFERTZ

Acceptée sur proposition du jury

Prof. C. Ludwig, président du jury
Prof. A. Pautz, Dr R. E. Adams, directeurs de thèse
Dr V. Dangendorf, rapporteur
Prof. O. Pooth, rapporteur
Prof. A. Manera, rapporteuse

Humanity is a species of knowledge.

Acknowledgements

I would like to thank Prof. Andreas Pautz for providing the opportunity to do my doctoral studies with him at EPFL.

I am deeply thankful towards Robert Adams and Grégory Perret for the supervision of the thesis and their continuous support throughout my entire doctoral studies. I would also like to thank my (former) colleagues at FNL Benoit Soubelet and Heiko Kromer for taking me under their wings at the start of my time at PSI. I would also like to thank Michael Prasser who sparked my interest into the field of nuclear energy and who was always willing to share from his seemingly inexhaustible pool of new ideas.

I would further like to thank the Bachelor and Master students Marianna Papadionysiou, Enrico del Re, Caroline Seyffert, Lorenz Becker-Sander, Vincent De Buys Roessingh, and Nicolas König who contributed to the project via their semester, bachelor and master theses (I would like to mention here that Nicolas König specifically not only dedicated his bachelor and semester theses to the project but also continued to contribute afterwards by staying on as an assistant researcher).

I would like to thank several people who made the construction of the detector possible. Jean-Baptiste Mosset and Alexey Stoykov explained their detector design, which is the basis for the detectors presented in this thesis, in great details to help me get started with my own development. The help of Florian Barchetti was crucial for the manufacturing process as he not only gave me good recommendations for the assembly process but also agreed to polish all my detectors. I would also like to thank Urs Greuter for his help with the electronics design, manufacturing, and testing. For their involvement in the design of new electronics, I would also like to thank Michael Müller and Elmar Schmid. I would also like to thank Viktor Boutellier and Patrick Suter for their input on the design for the new collimator and sample positioning system at the AHL. I would also like to thank Rico Niccolini for his input on the mechanical design and the machining of several of the detector pieces.

I would further like to thank the scientists and groups who allowed me to use their facilities for my measurements and supported me during these measurements. First and foremost, I would like to thank the PSI hot laboratory for the measurement opportunity they provided and specifically Viktor Boutellier and Holger Wiese for their support during the measurements as well as the preparation of them. I would also like to thank the Laboratory for Reactor Physics and System Behavior (LRS) at EPFL for the opportunity to use the LOTUS facility and specially Vincent Lamirand and Pavel Frajtag for their support in planning and executing the measurements there. I would like to thank Udo Strauch for his help with the calibration of the

Acknowledgements

^{252}Cf source at the PSI Eichstelle.

I would like to thank swissnuclear for providing the funding and PSI for providing the research infrastructure for me to work on my thesis.

I would like to thank the members of the PhD and Postdoc association at PSI and of the PSI Employee Committee for the fruitful work together on the non-scientific aspects of work and leisure at PSI.

I want to thank my good friends Leonie Echsle, Christian Frei, Nils Kern, Timo Tietje, and Silke Seyock, as well as my friends at Gladius et Codex for all the fun we had together during the times I was not working on my thesis. They also were a great source of company during lockdown periods when, even though limited to remote interactions, they made me feel like almost having more social contacts than before.

Last but not least I want to thank my mother, father, and brother, who have been supporting me immensely my entire life, including my PhD. Without their extraordinary support, I would likely not even have made it to the start of my PhD studies.

Abstract

In this thesis, the development and testing of a system for measuring the axial distribution of fast neutron emission of spent nuclear fuel rods is presented. Emphasis is placed on the novel fast neutron detector used which can reliably work in extremely high gamma fields.

The detector has a sensitive volume made of a silver-activated zinc sulfide (ZnS:Ag) scintillator powder mixed with a transparent epoxy, with wavelength-shifting fibers (WLSFs) embedded in this mixture. Neutron detection happens via elastic scattering with hydrogen in the optical epoxy. The resulting recoil protons activate the ZnS:Ag and its scintillation light is partly collected by the WLSFs. Silicon photomultipliers are used to read out the bursts of scintillation light reaching the end of the fibers and a digital filter algorithm based on single photon counting is employed to recognize neutron events from clusters of captured optical photons. The thesis contains the description of the extensive characterization measurements that were performed for the detector. The main prototype had a length of 3 cm and a sensitive volume of 3 cm³. It contained 196 WLSFs embedded at a pitch of 0.7 mm read out by four SiPMs. The testing was mainly focused on its performance in environments with a strong gamma background since this is the type of environment of the targeted spent fuel characterization. In a first step, the parameters of the filter algorithm were chosen with neutron detection efficiency and gamma rejection properties in mind. The detector achieved an intrinsic neutron detection efficiency (counts per neutron hitting the front face of the detector sensitive volume) of ~1% for neutrons emitted by a ²⁵²Cf source. At the same time, the detector efficiently rejected gamma rays (less than 0.01 s⁻¹ counts) from a ⁶⁰Co source at an estimated average gamma flux density of ~5 · 10⁶ cm⁻²s⁻¹ over its sensitive volume. The damage due to gamma radiation was characterized as well. After prolonged irradiation of the sensitive volume at a high gamma flux (1.8 · 10¹³ cm⁻² accumulated gamma fluence from ⁶⁰Co), a significant reduction of ~40% in neutron detection efficiency was observed.

The overall detector characterization was extended to environments with less strong gamma backgrounds. This is intended as the groundwork for future developments applying this promising detector concept to applications in other fields than spent fuel characterization (for example fast neutron imaging or monitoring). With the relaxed requirements on gamma rejection, it was possible to tune the filter parameters and reach an intrinsic detection efficiency above 11%. Yet another set of parameters for the filter algorithm led to the detector being able to measure the arrival time of neutrons with an accuracy of ~60 ns.

The thesis further reports on a spent fuel measurement campaign where the detector, together with some existing infrastructure designed for gamma emission measurements, was

Abstract

used to measure the neutron emission of four known mixed oxide fuel (MOX) and uranium oxide (UO_2) fuel samples. The fuel samples had a wide range of burn-ups and relatively long cooling times of ~ 25 y. The measured total neutron emission of the samples agrees well with previous measurements of the same samples that used a different technique. The measured total neutron emission of the samples relative to each other agrees within two standard deviations with the previous measurements while the absolute neutron emission agrees within 2.5 standard deviations. For one of the samples an axial scan was performed and it was possible to reconstruct the neutron emission with a resolution of 2.5 cm.

Finally, the thesis contains information about the ongoing development of a new version of the spent fuel measurement system and an overall outlook of the work. A significant part of the development has already been done. The new system is planned to feature, among other things, a better collimation of neutrons to improve resolution, a bigger and more gamma-blind detector for faster measurements, and the ability to measure spent fuel with shorter cooling times.

Zusammenfassung

Diese Doktorarbeit beschreibt die Entwicklung und Erprobung eines Messsystems für die axiale Verteilung von Emittlern von schnellen Neutronen in abgebrannten nuklearen Brennelementen. Der Fokus liegt dabei auf dem verwendeten neuartigen Detektor für schnelle Neutronen welcher in der Lage ist selbst in starken Gammafeldern verlässlich zu funktionieren.

Der sensitive Teil des Detektors besteht aus einer Mischung aus silber-dotiertem Zinksulfid-Szintillator (ZnS:Ag) in Pulverform und einem transparenten Epoxidharz, welche von Wellenlängenschieberfasern (WLSF) durchzogen wird. Schnelle Neutronen werden durch ihre elastische Streuung an Wasserstoff-Atomen im Epoxidharz detektiert. Die aus der Streuung resultierenden Rückstossprotonen regen das ZnS:Ag an und die WLSF sammeln einen Teil des resultierenden Szintillationslichts. SiPMs (von engl. silicon photomultipliers) werden benutzt, um das Licht aus den Faserenden auszulesen. Ein digitaler Filteralgorithmus basierend auf der Erkennung und dem Zählen einzelner Photonen wird benutzt, um Gruppen von optischen Photonen zu identifizieren, die durch die Interaktion mit einem Neutron erzeugt wurden.

Die Arbeit beinhaltet die Beschreibung der umfassenden Messungen, die durchgeführt wurden, um den Detektor zu charakterisieren. Der hauptsächlich verwendete Prototyp hatte eine Dicke von 3 cm und ein sensibles Volumen von 3 cm^3 mit 196 WLSF, die in einem Raster mit einem Abstand von 0.7 mm zueinander angeordnet waren. Die WLSF wurden von vier SiPMs ausgelesen. Der Fokus für die Charakterisierung des Detektors lag auf den Eigenschaften und der Effizienz des Detektors in der Gegenwart von starker Gammastrahlung, da dies die Art von Umgebung ist, die für den Detektor während den angestrebten Messungen von abgebrannten Brennelementen erwartet wird. Zunächst wurden die Parameter des Filteralgorithmus so gewählt, dass der Detektor sowohl eine gute Effizienz für Neutronen als auch eine starke Blindheit gegenüber Gammastrahlung aufweist. Mit diesen Parametern erreichte der Detektor eine intrinsische Effizienz (detektierte Neutronen pro auf das sensitive Volumen auftreffendes Neutron) von $\sim 1\%$ für schnelle Neutronen von einer ^{252}Cf Quelle. Gleichzeitig wurden nur wenige (weniger als 0.01 s^{-1}) Gammastrahlen von einer ^{60}Co Quelle bei einer geschätzten Gamma-Flussdichte von $\sim 5 \cdot 10^6 \text{ cm}^{-2}\text{s}^{-1}$ fälschlicherweise als Neutronen detektiert. Zusätzlich wurde der Schaden durch die Gammastrahlung am Detektor charakterisiert. Nach längerer Bestrahlung in einem starken Gammafeld ($1.8 \cdot 10^{13} \text{ cm}^{-2}$ akkumulierte Gamma-Flussdichte von einer ^{60}Co Quelle) wurde eine Reduktion von $\sim 40\%$ in der Effizienz für Neutronen festgestellt.

Die Charakterisierung des Detektors wurde auf Umgebungen mit weniger starker Gammastrahlung ausgeweitet. Damit soll das Fundament für Weiterentwicklungen des Detektors für

andere Anwendungsgebiete (zum Beispiel bildgebende Verfahren oder Überwachung von Neutronenstrahlung) gelegt werden. Durch die reduzierten Anforderungen an die Blindheit des Detektors für Gammastrahlen war es möglich die Parameter des Filteralgorithmus so anzupassen, dass eine intrinsische Effizienz für Neutronen von über 11% erreicht werden konnte. Wiederum eine andere Wahl der Parameter erlaubte eine Bestimmung der Ankunftszeit der Neutronen mit einer Genauigkeit von ~ 60 ns.

Des Weiteren enthält die Arbeit eine Beschreibung einer Messkampagne in der der Detektor, zusammen mit bereits existierender Infrastruktur, die für Gammastrahler-Messungen gebaut wurde, eingesetzt wurde um die Neutronenstrahlung von vier abgebrannten Brennelementsegmenten, deren Eigenschaften bereits aus vorherigen Messungen bekannt sind, zu messen. Der Abbrand der Brennelemente deckte eine grosse Spanne von Werten ab und die Abklingzeit der Segmente war ~ 25 Jahre. Die gemessenen Neutronenstrahlungswerte sind in Einklang mit den Resultaten, die zuvor mit einem anderen Verfahren gemessen wurden. Die relative Neutronenstrahlung der Segmente zueinander stimmt mit den vorherigen Messungen bis auf zwei Standardabweichungen überein und die absolute Neutronenstrahlung stimmt mit den vorherigen Messungen bis auf 2.5 Standardabweichungen überein. Für eines der Segmente wurde die axiale Verteilung der Emitter von schnellen Neutronen rekonstruiert wobei eine Auflösung von 2.5 cm erzielt wurde.

In einem letzten Teil enthält diese Arbeit Informationen zu den laufenden Arbeiten zur Entwicklung einer neuen Version des Messsystems und einen Ausblick auf zukünftige Arbeiten dazu. Ein Grossteil der Entwicklung ist bereits abgeschlossen. Die neue Version des Messsystems soll unter anderem eine bessere Kollimation der Neutronen ermöglichen, um die Auflösung zu verbessern und es erlauben abgebrannte Brennelemente mit kürzeren Abklingzeiten zu messen.

Contents

Acknowledgements	i
Abstract (English/Français/Deutsch)	iii
1 Introduction	1
1.1 Spent Fuel Analysis	1
1.1.1 Destructive Techniques	3
1.1.2 Non-Destructive Techniques	3
1.1.3 PSI Hot-Laboratory Gamma Emission Measurements	3
1.1.4 Neutron Emission Measurements	4
1.2 The NEWS Project and the Scope of the Thesis	6
1.2.1 Choice of Detector	6
2 Detector Design and Manufacturing	9
2.1 General Design and Working Principle	9
2.1.1 Sensitive Volume	9
2.1.2 Light Guides	12
2.1.3 Neutron Event Filter	12
2.2 Manufacturing of Detector Probes	14
2.2.1 Manufacturing Steps Common to All Detectors	14
2.2.2 Hot-Lab Prototype 1	15
2.2.3 Single Channel Detectors	18
2.2.4 Crosstalk Prototype	18
2.3 Electronics Details	21
2.3.1 Front End Electronics	21
2.3.2 Back End Electronics	24
2.4 Control Software	25
2.4.1 Control Software for the Logic Analyzer	25
2.4.2 Control Software for the FPGA	27
3 Detector Properties	31
3.1 Characterization of the Reference ^{252}Cf Source	32
3.1.1 Neutron Output	32
3.1.2 Gamma Output	36

Contents

3.2	Performance in High Gamma Environments	40
3.2.1	Choice of MSD Parameters	40
3.2.2	Gamma Blindness	44
3.2.3	Neutron Detection Efficiency	44
3.2.4	Degradation under Irradiation	51
3.3	Performance in Low Gamma Environments	58
3.3.1	Conservative Gamma Equivalence for the ^{252}Cf Source	58
3.3.2	Measurement Setup	59
3.3.3	MSD Parameter Optimization and Efficiency	60
3.4	Performance for Timing Applications	62
3.4.1	MSD Parameter Optimization	62
3.4.2	Timing Accuracy Interpretation	62
3.4.3	ZnS:Ag Light Output Decay	66
3.5	Crosstalk Between Nearby Fibers	66
3.5.1	Measurement Setup	68
3.5.2	Results and Discussion	68
3.6	Energy-Dependent Efficiency Measurement	72
3.7	Simulation of Inner Processes of the Detector	76
4	Spent Fuel Measurement Campaign	77
4.1	Measurement Setup	77
4.2	Measured Spent Fuel Samples	81
4.3	Setup Characterization	82
4.3.1	^{252}Cf Point Spread Function	83
4.3.2	Energy-Dependent Efficiency	85
4.3.3	^{244}Cm Point Spread Function	87
4.4	Spent Fuel Measurements	87
4.4.1	Absolute Neutron Emission Formula	88
4.4.2	Total Neutron Emission	91
4.4.3	Axial Emission Distribution	94
4.5	Detector Degradation	98
5	Ongoing Development and Outlook	99
5.1	Other Envisioned Detector Applications	99
5.1.1	Fast Neutron Imaging	99
5.1.2	Fast Neutron Monitoring	101
5.2	Improvement of the Hot-Lab Measurement Station	101
5.2.1	New Collimator and Sample Positioning System Design	102
5.2.2	New Detector	112
5.3	Electronics and Software Development	113
5.3.1	SPIDER Project	114
5.3.2	Alternative Digital Filter Algorithms	114

6 Conclusion	117
6.1 Detector Development	117
6.2 Spent Fuel Neutron Emission Measurements	119
6.3 Development of an Improved Measurement System	120
A Drawings	121
A.1 Spacers	121
A.2 Hot-Lab Prototype 1	124
A.3 Single Channel Detectors	132
A.4 Crosstalk Prototypes	136
B Electronics Schematics	139
B.1 SiPM_PS+PreAmp_1 Board	139
B.2 SiPM_amplifier_discriminator_LVDS_5_1 Board	143
C Hot-Lab Campaign Measurement Lists	147
D SPIDER	149
D.1 Structure of the SPIDER System	149
D.2 Front End Crate	149
D.3 MEG Crate	150
Bibliography	161

The scientific method is the best method humanity has developed to gather knowledge. Its ability to produce useful, precise, and testable models of reality is not only unmatched by anything else, it plays in its own league: No other approach can even hope to compete with it.

1 Introduction

The topic of this thesis is to develop a new method for post irradiation examination (PIE) of nuclear fuel based on the neutron emission of the fuel. Section 1.1 describes the motivation for spent fuel analysis and the main methods that currently exist, including the reasoning behind the decision to develop a new method based on neutron emission. Section 1.2 describes in more detail the topic of the thesis and closely related previous work.

1.1 Spent Fuel Analysis

Knowing the content of nuclear fuel is important both during and after its use in a reactor. This information is crucial for predicting the reactor behavior and optimizing profitability as well as mitigating and preventing accidents. After being removed from the reactor, the fuel must be kept sub-critical and its impact on the environment (heat and radiation) has to be limited. To achieve this with as few resources as possible, detailed knowledge of the content of the spent fuel is necessary. The most relevant isotopes depend on the aspect under investigation.

For radiation protection considerations, elements that are incorporated by organisms are of special interest. For severe accidents, isotopes with a short half-life are important due to their high activity and the potential for short times between production and their release to the environment. Of special interest for geological final repositories are the long-lived isotopes that migrate most quickly in the host rock the repository is built into, as well as isotopes that produce a significant amount of decay heat. For transport and intermediate storage, isotopes that emit fast neutrons or high energy gamma rays are important to consider since these radiation types are highly penetrating (e.g. see [1] for a list of the relevant isotopes).

For criticality considerations, burn-up credit is a useful quantity for optimizing safety and efficiency of spent nuclear fuel storage facilities and transport systems. It describes the negative change of reactivity of nuclear fuel relative to the reactivity it had as fresh fuel. The reactivity change is caused by a change in the fuel composition. For most reactors and fuel types, the burn-up credit increases during operation as fissile atoms are being split to keep

the chain reaction going and produce energy. However, there are also effects which negatively impact the burn-up credit of the fuel, such as new fissile material being bred and built-in neutron poisons being depleted. It is important to be able to quantify all of these processes as precisely as possible to fully utilize the potential of the burn-up credit concept [2, 3].

The content of nuclear fuel is strongly dependent on its history. It is, for example, influenced by its initial composition, the amount of time it spent in the reactor, the local neutron field (i.e. flux density and spectrum) during this time, and (if applicable) the cooling time afterwards. This means that the content of the fuel can vary quite significantly for different fuel elements and also over time. It would not be feasible to perform measurements covering all relevant scenarios. Computational models (for simplicity, the combination of calculation methods, data libraries, and geometry descriptions are referred to collectively as a model in this thesis) are therefore used to calculate the contents of nuclear fuel based on known parameters of its history. These models are complex and frequently use simplifications to be feasible to compute. Additionally, they require detailed information on the different materials in the reactor core (such as fuel, moderator, and structural elements), including their geometry, reaction cross sections, and temperature and density distributions. Depending on the model, some parameters are directly calculated by the code (for example coolant density if the model includes thermal hydraulics calculations). The models themselves as well as the input data can contain errors. It therefore can not be assumed that the results produced by the models are accurate in all cases. They therefore have to be validated frequently against measurements. Such measurements of fuel content are easiest to perform on spent fuel, as the fuel does not need the fuel to be measured inside the reactor or reinserted back into the reactor after the measurements. Additionally, spent fuel analysis is ideal for checking and predicting the content of fuel in the back end of the fuel cycle (any time after discharge of the fuel) since no more in-core irradiation will take place. The uncertainties associated with the processes occurring in spent fuel (mainly radioactive decay) are in general lower than the uncertainties associated with how the fuel changes during irradiation inside a reactor, where the changes induced by the neutron field have a large impact. This means that if there is accurate knowledge of spent fuel content at one point in time, the fuel composition can be predicted with relatively high accuracy within a long period of time.

The strong dependence of spent fuel content on the neutron field means that spent fuel measurements are useful not only to ensure a good prediction of the fuel content, but also to verify the neutron field predicted by a computational reactor model. Spent fuel analysis can essentially make the fuel act as a type of detector, measuring the neutron field during reactor operation. The distribution of the fuel throughout the entire reactor core means that the detector capabilities of the fuel can be used to gather information on the local environment at almost any point in the reactor core.

There are multiple measurement techniques for spent fuel that have been developed over time. They can be separated into the two categories of destructive and non-destructive techniques. Non-destructive measurements do not alter the fuel under investigation in a meaningful way.

The interpretation of what exactly is meaningful can vary. In the context of this thesis it is taken as leaving the cladding of the fuel pins intact and not subjecting the fuel to strong enough external radiation fields to significantly alter its composition.

1.1.1 Destructive Techniques

Destructive techniques can give direct and detailed information on the content of spent fuel. A good example for this is mass spectrometry coupled with liquid chromatography, which is capable of providing different signals, each corresponding to a different isotope and its concentration in the investigated fuel sample [4, 5]. Another approach is to couple a mass spectrometer to a laser ablation system, allowing for measurements with spatial resolutions on the order of 10 μm [6]. Dissolved nuclear fuel can also be analyzed using alpha and gamma spectrometry [7]. There are also techniques that do not focus on individual isotopes, such as measuring the produced fission gas by puncturing a fuel rod [8].

1.1.2 Non-Destructive Techniques

Non-destructive measurement techniques are especially convenient when analyzing spent fuel. They do not prevent further analysis with different techniques and, contrary to most destructive techniques, generally have a negligible impact on the volume of hazardous radioactive material. As they do not damage the cladding, they can be performed in facilities that cannot handle unclad fuel. This opens up the possibility for non-destructive techniques to characterize a large portion of all produced spent fuel, not only selected samples.

One possible type of experiment is to measure the radiation emitted by spent fuel. The only particles that are produced in significant quantities and are penetrating enough to also leave the cladding are gamma rays, neutrons, and neutrinos. Neutrinos are notoriously hard to detect, limiting their potential usefulness for spent fuel analysis. This leaves gamma rays and neutrons as potential candidates.

1.1.3 PSI Hot-Laboratory Gamma Emission Measurements

At the Hot-Laboratory (AHL) of the Paul Scherrer Institut (PSI), the measurement of gamma rays emitted by spent fuel rods is already a standard procedure. These measurements take place in hot-cell number 1 (HZ1), an overview of which is given in figure 1.1a. HZ1 is the only hot-cell at AHL large enough to accommodate full-length spent fuel rods. Additionally, it is connected to a hot-cell extension via a $\varnothing \sim 30$ cm hole called measurement penetration (Messbankdurchführung in German). The hot-cell extension is long enough to accommodate a full-length fuel rod as well, allowing a rod to be moved in its entirety between the HZ1 and the extension through the measurement penetration. To be moved through the measurement penetration, a fuel rod can be put on a set of rollers and fixed at one end to a remotely controlled sledge. A picture of that system is shown in figure 4.2a. From the outside world, a

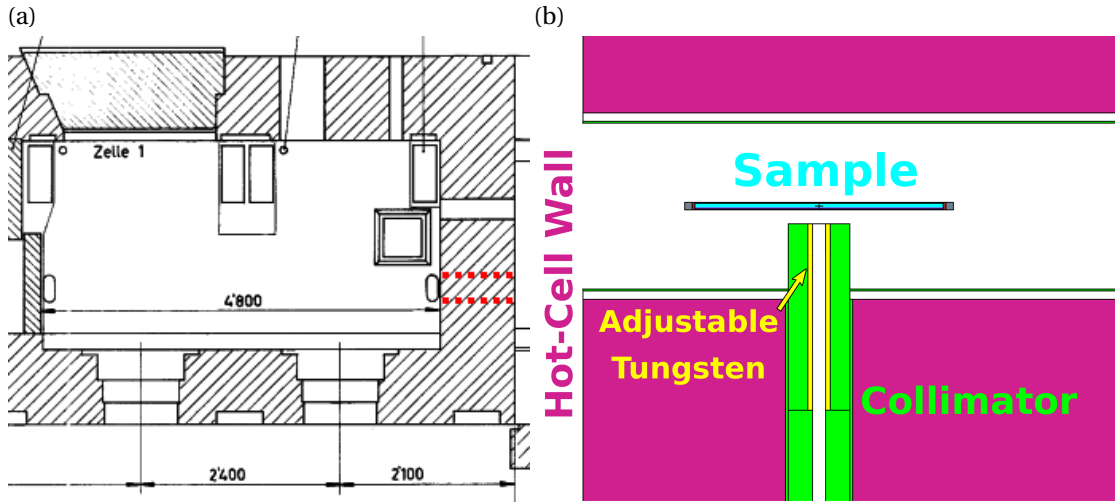


Figure 1.1: (a) A top view technical drawing of the hot-cell number 1 of the PSI Hot Laboratory, length units in mm. The red dashed lines mark the position of the fuel rod channel. On the right side of this channel a hot cell extension is mounted (not shown). (b) A to-scale illustration of the setup in the fuel rod channel. The collimator (green) is mounted in a hole in the concrete walls (violet) of the fuel rod channel. The adjustable tungsten blocks (yellow) at the tip of the collimator are shown in their fully opened configuration (~18 mm apart). The sample under investigation (blue) can be moved past the collimator (shown is a 40 cm fuel segment but up to full-length spent fuel rods are possible).

∅ ~10 cm hole called collimator penetration (Kollimatordurchführung in German) connects to the measurement penetration at a 90° angle (see figure 1.1a).

To perform gamma emission measurements, a collimator is inserted into the collimator penetration and a high-purity germanium (HPGe) is placed behind it. The measured fuel rod is moved through the measurement penetration and past the collimator. This allows the measurement of a space (in the axial direction of the fuel rod) and energy resolved emission profile. The collimator has movable tungsten blocks at its tip (see figure 1.1b). Their distance determines the aperture of the collimator and with that the spatial resolution of the measurement. The aperture has a fixed height of ~2 cm to ensure that the aperture always covers the entire diameter of the fuel rod. By rotating the fuel rod around its axis, additional data about the angular distribution of gamma ray emitters can be extracted (see for example [9]).

1.1.4 Neutron Emission Measurements

There are three main types of reactions producing neutrons in spent nuclear fuel. The first one is spontaneous fission of heavy elements such as ^{242}Pu , ^{242}Cm , ^{244}Cm , ^{246}Cm , and ^{252}Cf . Spontaneous fission usually produces the majority of neutrons in spent fuel (see e.g. [1, figures 16 and 17]). The following numbers are an example for illustration purposes. The numbers depend heavily on parameters like burn-up, initial enrichment, and fuel type. For typical

Swiss spent fuel (uranium oxide PWR fuel with initial enrichment of ~5% and a burn-up of ~60 GWd/tU) and typical cooling times for a spent fuel measurement (~10 y), over 95% of the emitted neutrons are produced by spontaneous fission (excluding neutron induced fission, see below) [10]. For short cooling times (1 – 100 y), ^{244}Cm is the dominant emitter of spontaneous fission neutrons. Small additional contributions come from other minor actinides while the contribution from uranium and plutonium is usually negligible. In the spent fuel example provided before, over 95% of the spontaneous fission neutrons are coming from ^{244}Cm [10]. For longer cooling times ^{242}Pu , ^{246}Cm , and ^{248}Cm become more important [10]. The second interaction to produce neutrons is the (α , n) reaction with light nuclei (usually oxygen in oxide fuels). Typical α -emitters to start such a reaction are americium, plutonium and curium isotopes. The third type of reaction is neutron induced fission. Its influence is strongly dependent on the measurement setup (for example the amount of fuel measured, and the presence of moderators and neutron poisons) not only on the spent fuel content. All three production methods generate neutrons almost exclusively in the fast range.

Typical neutron emission measurement results are mainly influenced by the concentration of spontaneous fission neutron emitters, and especially by the ^{244}Cm concentration. ^{244}Cm is produced, just like the other minor actinides contributing to the spontaneous fission neutron source term, by successive neutron capture starting with the uranium (and depending on the fuel type also plutonium) present in the fresh fuel. This is in contrast to the nuclei relevant for gamma emission measurements, which are fission products. Neutron and gamma ray emission measurements are therefore independent to a certain degree. This is especially beneficial when considering reactor model validation where techniques are more likely to catch mistakes when using more independent measurements.

Neutron emission measurements using a moderator to first thermalize the emitted fast neutrons before detection have already been carried out. Samples ranged from entire spent fuel assemblies [11] down to small sections of individual spent fuel rods [12, 13]¹. The approach to moderate the neutrons before detection has advantages when compared to direct fast neutron detection. Thermal neutron detectors that have high efficiencies and are insensitive to gamma rays are commercially available (such as ^3He detectors or fission chambers). Spent fuel is frequently already stored in a water pool and the moderator is therefore readily available. The main downside of these measurement systems is the poor spatial resolution, since the moderation process causes a loss of information about the initial direction of the neutron. The neutron flux and spectrum in a reactor changes on the order of mm to cm. The composition of some fuel rods also changes on this length scale (i.e. the size of a fuel pellet). For reactor model validation it would therefore be advantageous to have measurements with a resolution as close to that as possible. To the knowledge of the author, no non-destructive technique exists with ~cm or better resolution for neutron emission measurements.

¹It has to be noted though that cutting sections out of spent fuel rods makes these measurements no longer non-destructive

1.2 The NEWS Project and the Scope of the Thesis

The NEWS (Neutron Emission measurements With Scintillators) project is a collaboration between the Paul Scherrer Institut and swissnuclear. Its aim is to develop a method for measuring the neutron emission of full-length spent fuel rods with a fine axial resolution (target is 2 cm). As a basis, the already existing infrastructure for the gamma emission measurements (see section 1.1.3) is used. This facilitates the development significantly since all the infrastructure for handling and accurately positioning the fuel rod is already present. This allows the project to focus on the neutron detection aspect. Alongside the experimental work presented in this thesis many MCNP [14] simulations are included. Generally the conceptualization, geometry definition, and analysis of these simulations were performed by me in close collaboration with PSI scientist Grégory Perret, who generally did the actual implementation of the simulations.

To achieve the targeted resolution, it was decided to use direct fast neutron detection over thermal neutron detection. Thermal neutron detectors would require a moderation process where information about the emission point of the neutron can get lost. The loss of information during moderation would be expected to mandate a collimator design which takes up more space to achieve the same resolution as a collimator for direct fast neutron detection. Since space in the targeted hot-cell environment is limited, direct fast neutron detection was chosen. An example of a measurement system based on a moderator and a thermal neutron detector is a theoretical study done at PSI [15]. The simulated measurement system requires a significant amount of space with a box of 1 m height and 55 cm depth, and the calculated point spread function has a full width at half maximum of about 10 cm. This is significantly larger than the targeted 2 cm resolution of the new system.

The work presented in this thesis is part of the NEWS project. It covers the entirety of NEWS-I and NEWS-II as well as the first part of NEWS-III. Several papers on the project have been published or are in the process of being published (references [16, 17, 18]). Most of the information used to write these papers is re-used throughout the entirety of this thesis. For simplicity, citations will not be given for every part of this thesis where the same data is used again. The descriptions in the thesis are generally as complete or even more complete than the information given in the papers. It should therefore generally not be necessary to refer to the papers for more information. Where this is not the case or where content has been taken directly from one of the papers, citations will be given.

1.2.1 Choice of Detector

There are different types of commercially available fast neutron detectors. They can mainly be separated into five categories: gas based detectors, fission chambers, liquid scintillator detectors, organic solid detectors, and inorganic scintillators with a hydrogen-rich neutron converter. This section evaluates these options with respect to the requirements for the NEWS project.

Due to the low density of the sensitive volume in gas-based detectors and the small interaction cross-section of fast neutrons with any nuclei, gas-based detectors have a low detection efficiency per unit volume. As the space available for the detector is severely limited in the envisioned measurement setup, this would make the measurement time unacceptably long, especially for fuel rod sections with a low burn-up and therefore a low neutron emission. Gas detectors were therefore disregarded as a viable option. For similar reasons, fission chambers are excluded as an option. The main difference is that the limitation of useful neutron interactions to one of the electrodes limits the efficiency instead of the low density of the gas.

Liquid and solid organic scintillator detectors are not only sensitive to fast neutrons but also to gamma rays. However, using a technique called pulse shape discrimination, some detectors are capable of distinguishing neutrons from gamma rays [19]. Pulse shape discrimination works by analyzing the time it takes for a scintillation light flash to fade. It therefore only works if individual events are clearly separated in time from one another. The high gamma environment associated with spent fuel means that gamma ray events will usually occur in quick succession, causing the pulse shape discrimination to stop being able to reliably distinguish them from neutrons. For this reason, liquid and solid organic scintillators were also disregarded as an option.

This leaves inorganic scintillators with neutron converters as the remaining option. While none of the commercially available solutions is satisfactory, a detector with a promising basic concept had been developed shortly before the start of the NEWS project at PSI by the Research with Neutrons and Muons (NUM) division for thermal neutron detection at the Swiss Spallation Neutron Source (SINQ) [20, 21, 22]. This detector uses a silver-activated zinc sulfide scintillator (ZnS:Ag) mixed with ^6Li and with embedded wavelength-shifting fibers (WLSFs). It detects thermal neutrons via a reaction with ^6Li :



The resulting ^4He and ^3H particles then deposit their energy partly in the ZnS:Ag and the WLSFs collect the scintillation light released by the ZnS:Ag. While the ^6Li reaction has a large cross-section for thermal neutrons, the cross-section for fast neutrons is too small for this detection mechanism to be efficient. It was therefore decided to develop a modified version of the detector for the NEWS project where instead of ^6Li , hydrogen is used as a converter. Instead of ^4He and ^3H nuclei from a nuclear reaction, the recoil proton from elastic scattering with hydrogen activates the ZnS:Ag. A detailed description of the working principle can be found in section 2.1.

As it happens, the small quantity of binding material used in the original thermal neutron detector already contains hydrogen, which can act as a converter for fast neutrons. It was therefore possible to already conduct some preliminary measurements using one of the existing detectors and perform a feasibility study based on these measurements before the

start of the NEWS project. This was performed by Marianna Papadionysiou in the context of a master thesis [23, 24]. The preliminary study found that the detector performance is most likely sufficient for the characterization of spent fuel with a longer cooling time (~ 10 y) while measurements at shorter cooling times (~ 1 y) might not be possible. This was deemed a positive enough signal to go ahead with the detector choice, especially with the knowledge that the detector can probably be optimized for the specific task and therefore made to perform better than the thermal neutron detector considered for the feasibility study.

2 Detector Design and Manufacturing

Several detector prototypes were built over the course of this thesis. Since the detector designs as well as the assembly process were refined over time, only the detectors most relevant to this thesis are discussed in this chapter. Information on earlier prototypes can be found in [16] and [25].

Section 2.1 describes the structure of the detector and explains how it detects neutrons. The two sections afterwards go into more details for two of the detector parts. Section 2.2 describes the manufacturing process of the detector probe, which includes the sensitive volume, together with the technical details of the individual detectors. Section 2.3 describes the implementation of the detector electronics. Section 2.4 describes the software used for controlling and reading out the detector.

2.1 General Design and Working Principle

The detector can conceptually be separated into three parts: the sensitive volume where fast neutron interactions generate flashes of light; the light guides, which transport the photons; and the readout electronics which analyze the photons coming from the light guides.

2.1.1 Sensitive Volume

The sensitive volume consists of a mixture of silver activated zinc sulfide (ZnS:Ag) powder and clear epoxy, in which wavelength shifting fibers (WLSFs) are embedded. An electron microscope image of the ZnS:Ag-epoxy mixture is shown in figure 2.1. Incoming fast neutrons can scatter on nuclei in the sensitive volume, transferring some of their energy to the target nucleus. This nucleus then travels through the mixture, depositing the transferred energy along its path. The relevant portion for detection is the part of the energy deposited into the ZnS:Ag grains. Since the energy transfer from neutron to nucleus is more efficient for lighter nuclei, this discussion focuses on hydrogen as the only relevant target (the next lighter nuclei present in significant quantities being ^{12}C , which receives on average an order of magnitude

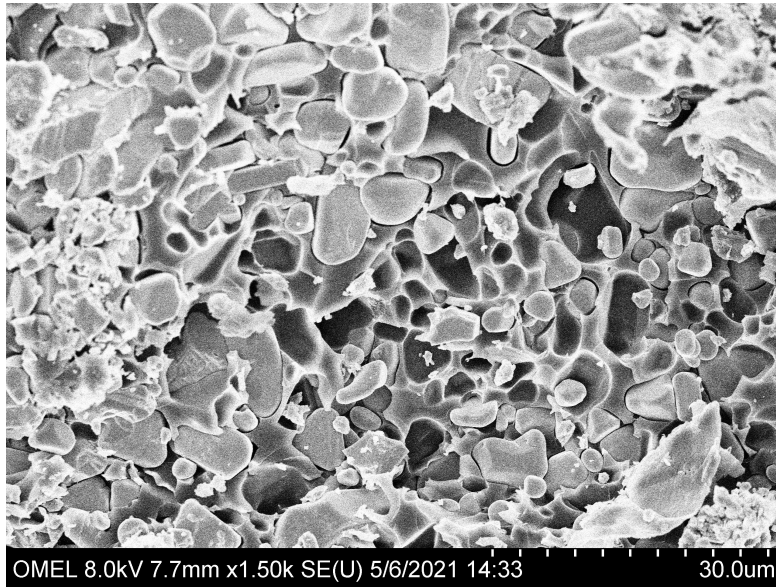


Figure 2.1: Electron microscope image of a cut through the ZnS:Ag-epoxy mixture. The ZnS:Ag grains are the roughly oval shaped objects with the epoxy matrix being visible between the grains.

less energy from neutron scattering). Both the epoxy and the WLSFs contain hydrogen. The contributions of these two sources of hydrogen to the overall performance of the detector have not yet been quantified. The recoil proton range is on the order of $10\text{ }\mu\text{m}$ whereas the WLSF diameter is $250\text{ }\mu\text{m}$, meaning a small fraction of recoil protons produced within the fiber will escape the fiber and reach the ZnS:Ag-epoxy mixture. Therefore those events are neglected in the following discussion, although they may contribute, to the overall sensitivity of the detector.

The scintillation light generated by the ZnS:Ag then travels through the mixture until it is either absorbed in one of the WLSFs or lost (being absorbed in the ZnS:Ag-epoxy mixture or leaving the sensitive volume). The core of the WLSFs contains a dye, which re-emits any absorbed photon at a lower wavelength in a random direction. If the angle between the re-emission direction and the axis of the WLSF is small enough to cause total internal reflection at the fiber cladding, the photon becomes trapped in the fiber and is guided towards one of its ends. The dye has a low absorption probability for the wavelengths at which it emits light, and the re-emitted light can travel through the fiber unhindered. To concentrate all photons at one end of the fiber, a mirror is attached to the other end. This mirror reflects the photons leaving the “wrong” end of the fiber back towards the “right” end. The entire process is illustrated in figure 2.2.

At the end where the photons leave the fiber, the WLSFs are bundled together to allow easier collection of the light from all fibers. For detectors with more than one channel, the WLSFs can be separated into multiple of these bundles instead. In this case, each bundle of WLSFs

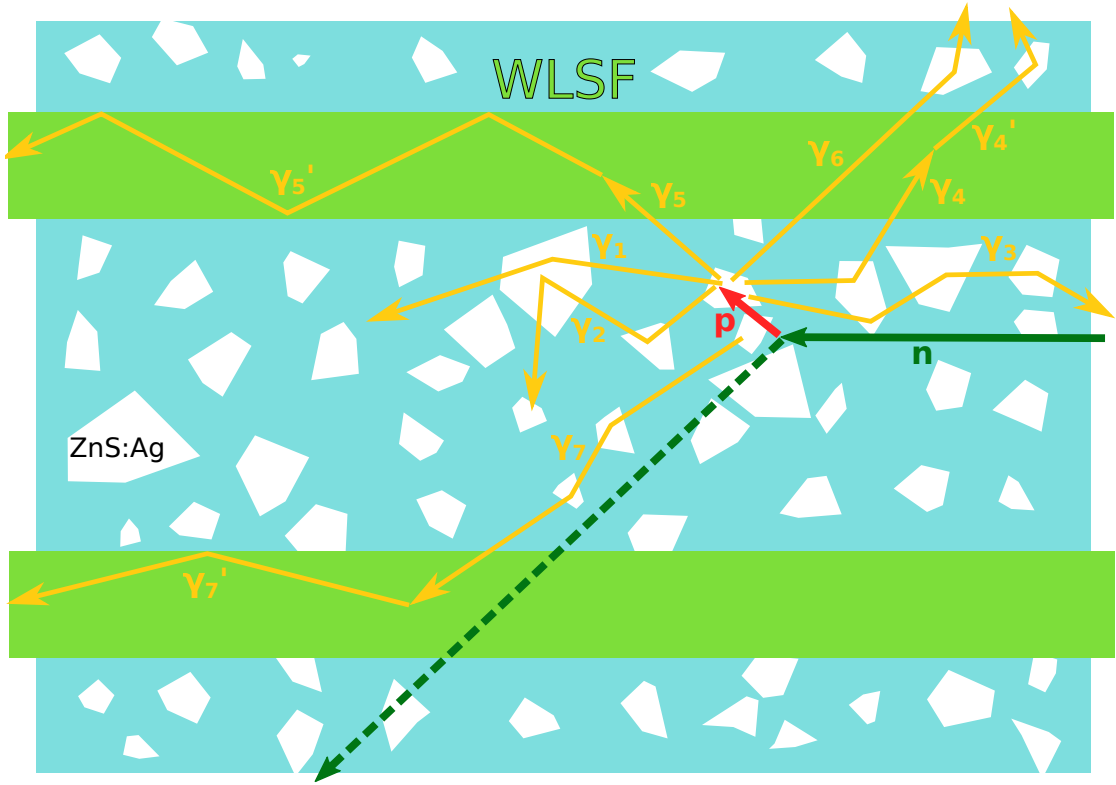


Figure 2.2: Illustration of the working principle of the sensitive volume. The components of the sensitive volume are epoxy (light blue), ZnS:Ag (white), and WLSFs (light green). The neutron path is shown (dark green) with the incoming (solid line) and the scattered (dashed line) part. The recoil proton (red) in this case deposits energy in two ZnS:Ag grains. Several possible paths for the scintillation light are shown. Some photons scatter at ZnS:Ag grains before being absorbed in the epoxy (γ_1) or a ZnS:Ag grain (γ_2), or leaving the detector (γ_3). Other photons eventually reach the WLSF and pass through it (γ_6), are captured (γ_5, γ_5'), or escape after re-emission (γ_4, γ_4'). Some photons are also captured in farther away fibers (γ_7, γ_7').

defines one channel. Details on the exact geometry of the different detectors (thickness, WLSF arrangement in the ZnS:Ag-epoxy mixture, etc.) can be found together with the details of the manufacturing process in section 2.2.

2.1.2 Light Guides

The light guides collect the light from the sensitive volume (more precisely the WLSFs) and guide it towards the readout electronics. In the case of detectors with more than one channel, each channel has its own light guide, which is connected to all WLSFs belonging to its channel. The light guide consists of a $\varnothing 2.5$ mm bundle of many thin optical fibers and has a length of ~ 5 m. At the back end, the light guides have an SMA connector, which is used to connect them to the readout electronics. Optical grease is used at both ends of the fiber to reduce coupling losses. Experience has shown that this method results in a reliable coupling of the light guides to the WLSFs and SiPMs. The packing density of the thin fibers in the light guide is about 90%. Coupling losses, packing density, and losses over the length of the fibers lead to a light transmission of about 70% according to the manufacturer [26].

2.1.3 Neutron Event Filter

The detector uses the so-called moving sum after differentiation (MSD) algorithm to recognize clusters of photons caused by a neutron event and disregard the noise (photons from other sources such as residual light from the environment or gamma rays hitting the detector, as well as electronic noise). The MSD is performed for every channel (i.e. for the light coming from every light guide) separately. In a first step, the measurement time is separated into intervals of length Δt . If the measurement starts at time 0 and ends at time T_{End} , there are a total of $n = \left\lfloor \frac{T_{End}}{\Delta t} \right\rfloor$ intervals $[i\Delta t, (i+1)\Delta t[$ for $0 \leq i < n$. For convenience, these intervals will be numbered by their value of i in the expression above. The number of photons registered on a single channel within the interval i is defined as q_i . The MSD d_i for an interval i is only defined for a subset $V_{MSD} = \{i \mid i \in \mathbb{N}_0, (2m-1) \leq i < n\}$ of all interval numbers.

$$d_i = \sum_{j=i-m+1}^i q_j - \sum_{j=i-2m+1}^{i-m} q_j \quad \forall i \in V_{MSD} \quad (2.1)$$

The summing length m can be fixed to any integer greater or equal to 1. The MSD is simply the difference in the number of photons in two subsequent time windows defined by Δt and m . This is also illustrated in figure 2.3. The intervals for which the MSD is not defined are only the intervals at the very start of the measurement where not all of the q_j values for the two sums are defined (i.e. where at least one of the two time windows of which the difference in the number of photons should be calculated are not entirely within the time of the measurement). Recognition of neutron events happens by setting a threshold k for the MSD value. The time of the event is determined by the first maximum of the MSD after crossing the threshold. The

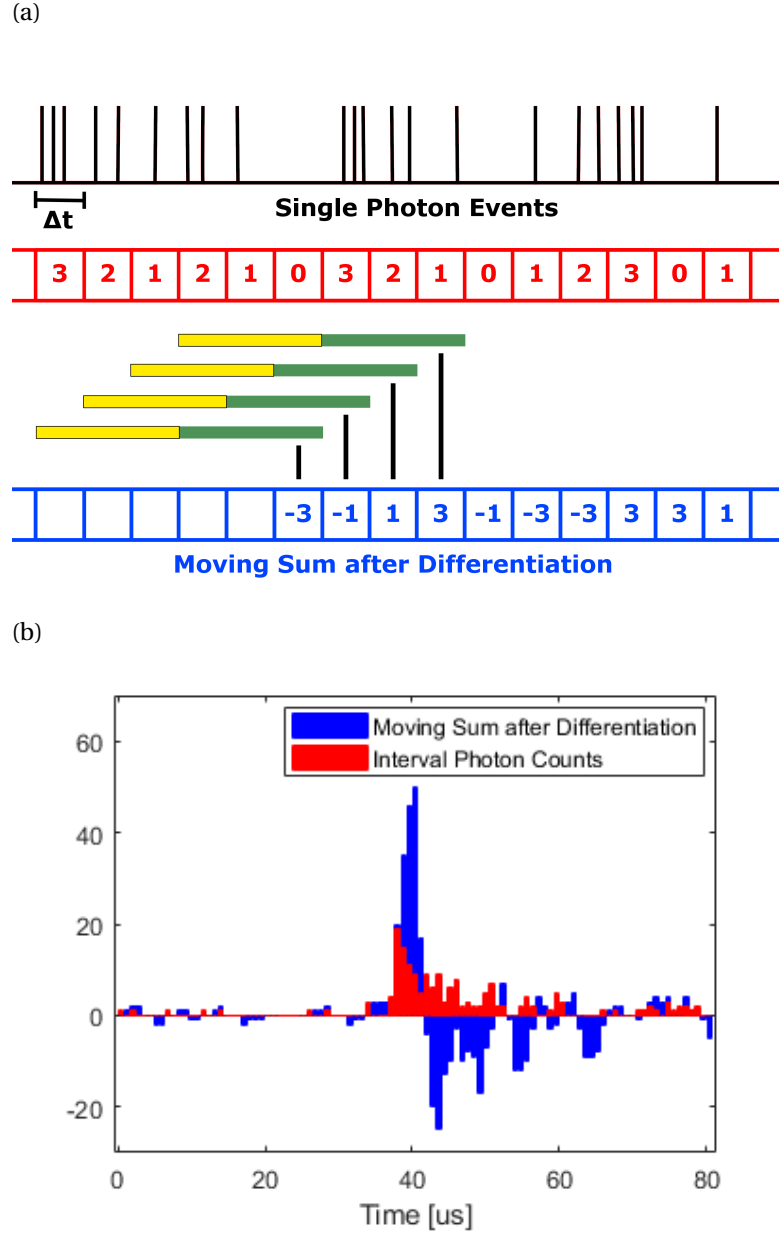


Figure 2.3: (a): Illustration of how the moving sum after differentiation (MSD) is calculated. The vertical black lines indicate the arrival of individual photons. The red numbers indicate the number of photons counted for every Δt interval. The blue numbers are the MSD values calculated for every interval using $m = 3$ as an example. For some MSD values, green and yellow bars are shown. They mark the intervals where the number of photons is added and subtracted respectively to calculate the MSD value. (b): Number of photons counted per interval and the corresponding MSD values for a real neutron event. Taken from [16].

condition for an event to be recognized in an interval i is therefore $(q_i \geq k) \wedge (q_i > q_{i+1})$. After each recognized event, the MSD needs to drop below the threshold value k and a blocking time t_B must elapse before the algorithm looks for another event. This prevents triggering multiple times from the signal of a single neutron. The values of Δt , m , k , and t_B can be tuned to improve the detector performance for specific applications. A set of values for all of these variables is referred to as an MSD setting.

Details on the implementation of the event recognition used for the detectors presented in this thesis can be found in section 2.3.

2.2 Manufacturing of Detector Probes

This section details the manufacturing process of the detector probes. The procedure is similar for all detectors and the steps common to all detectors are therefore described first described using pictures of the Hot-Lab Prototype 1 (see section 2.2.2) for illustration purposes. Information on the unique aspects of each detector is given afterwards.

2.2.1 Manufacturing Steps Common to All Detectors

The first step of the manufacturing process is the fabrication of spacers, which hold the WLSFs in the final positions. The spacers are custom printed circuit boards (PCBs) featuring a 21×21 grid of $\varnothing 0.35$ mm holes with a pitch of 0.7 mm. Drawings for the spacers can be found in appendix A.1. The WLSFs (Y-11(400)MSJ with a diameter of 0.25 mm from Kuraray [27]) are fed through these spacers. The layout of the WLSFs is different for each detector (see sections 2.2.2, 2.2.3, and 2.2.4). A picture of a stack of spacers with fibers fed through is shown in figure 2.4a.

The spacers are then drawn apart until there is a 1 cm gap between them, and fixed in a 3D printed holder. The fibers of each channel are bundled together. Which fibers belong to which channel is different for the different detectors and indicated in the sections dedicated to the individual detectors. Each bundle of WLSFs is fed individually through holes in a piece made from aluminum and plastic at the back of the detector probe (see figure 2.4b). To fix everything in this configuration, the fibers are glued first to the spacer at the front, then to the spacer closest to the back, and finally to the aluminum and plastic piece at the back using clear epoxy (EPO-TEK 301 [28]). After mixing the two epoxy components (but before applying it), the epoxy is heated for ~ 30 s in a ~ 60 °C water bath. The time in the water bath can be extended to increase the viscosity of the epoxy (this can make it easier to apply the epoxy). The epoxy also seals holes, effectively creating two molds, which are sealed off from each other. The mold in front consists of several 1 cm long compartments between the spacers while the mold at the back is the region from the last spacer to the aluminum and plastic piece at the end (see figure 2.4b). Several layers of epoxy are usually necessary to ensure that all holes are properly sealed.

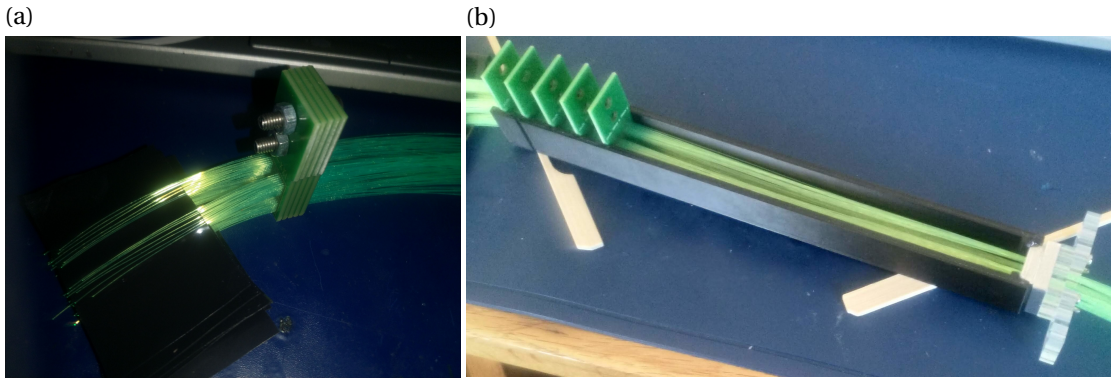


Figure 2.4: (a): A stack of spacers (dark green) with WLSFs (bright green) fed through in four separate bundles. The depicted arrangement of the fibers is for the Hot-Lab Prototype 1. (b): The spacers are drawn apart and held in place by a 3D printed holder (black). At the back, the fibers of each channel are bundled together in a block of aluminum and acrylic. Additional acrylic pieces are mounted at the back, sticking out on each side. Their purpose is to facilitate the assembly and they are removed later.

The first mold to be filled is the one at the back. Black potting epoxy is used for this to minimize potential crosstalk between the WLSFs of different channels. The mold at the front is filled in two steps. First, the compartment between the spacer in the front and the spacer immediately behind it is filled with clear epoxy (EPO-TEK 301 [28]). Before casting, the epoxy is again heated for ~ 30 s in a ~ 60 °C water bath (contrary to before, the time should not be extended). To prevent any epoxy from spilling into the rest of the front mold, the detector is hung with its front towards the ground and tape is used to form a mold (to facilitate this step, the top of the corresponding spacer PCBs, which has been used for aligning the spacers while feeding fibers through them, are cut off). Figure 2.5a shows a picture of this configuration. The remaining compartments of the front mold are then filled with a mixture of clear epoxy (EPO-TEK 301 [28]) and ZnS:Ag powder (EJ-600 [29]). Before mixing, the clear epoxy is heated for ~ 30 s in a ~ 60 °C water bath. The two components are mixed in a mass ratio of 2 parts epoxy to 3 parts ZnS:Ag. A picture of the result after this final casting step is shown in figure 2.5b.

In a next step, the 3D printed holder is milled away. After that, the front part filled with clear epoxy is cut away, leaving only 1 mm of clear epoxy. The resulting surface is polished and a mirror is glued to it (see figures 2.7b and 2.7c). The WLSFs coming out of the back are cut and polished as well (see figure 2.7a). Finally, the sensitive volume is surrounded by a casing to block environmental light.

2.2.2 Hot-Lab Prototype 1

The Hot-Lab Prototype 1 is built, as the name suggests, for measurements of spent fuel in the PSI Hot-Lab. Its detector probe is designed as an insert for the current gamma collimator.

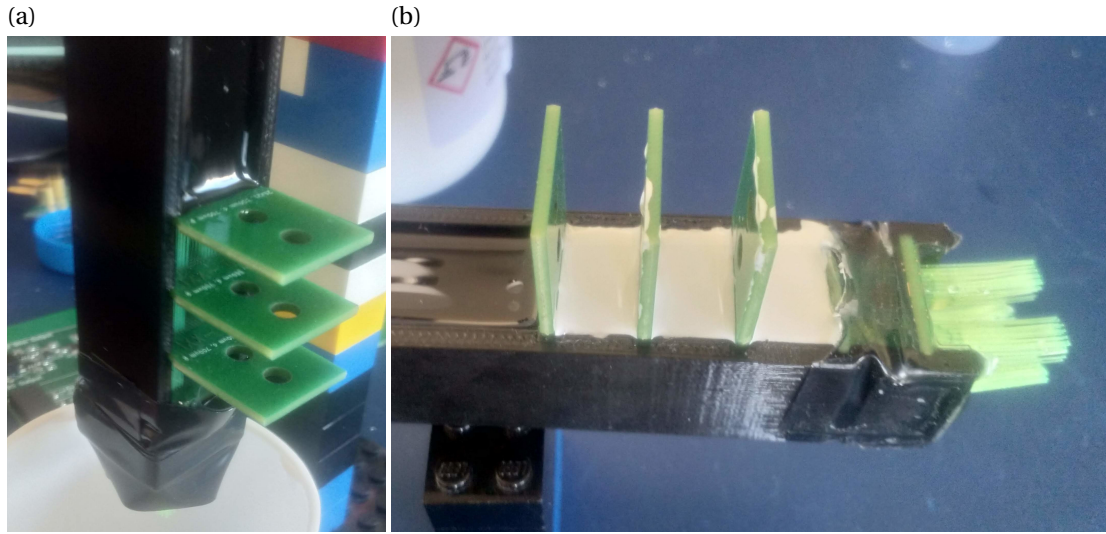


Figure 2.5: (a): A picture of the setup used to fill the front part of the detector probe with clear epoxy. Black tape is wrapped around to form a mold for casting. (b): All parts of the detector probe are filled: in the left of the picture, part of the black epoxy filled volume can be seen; in the center are the three white regions filled with the ZnS:Ag-epoxy mixture; and to the right is the small part filled with clear epoxy.

Details on this setup and the measurements can be found in chapter 4. The measurement setup and especially the collimator dimensions inform to a large extent the design of this detector. Technical drawings of the final detector as well as of individual components can be found in appendix A.2.

The probe of the Hot-Lab Prototype 1 has four channels, defined by the arrangement of the WLSFs embedded in the ZnS:Ag-epoxy mixture. Each of the channels has 49 WLSFs arranged in a 7×7 grid with a pitch of 0.7 mm. The channels have 5 empty grid positions between them (4.2 mm center to center distance between the outermost fibers). The exact arrangement is illustrated in figure 2.6. They are embedded in the mixture for a length of 3 cm, divided into 3 sections with a length of 1 cm each. At the back of the probe, the fibers of each channel are bundled together (the bundle diameter being about 2.4 mm). Pictures of this structure are shown in figure 2.7.

The probe is enclosed in an aluminum casing, as shown in figure 2.8. This casing has a provision for fixing tungsten plates to its front, which is located 10 cm from the front of the sensitive volume. These optional tungsten plates can be used to reduce the gamma intensity at the detector. The 10 cm distance to the sensitive volume is to reduce the scattering of gamma rays from the tungsten into the sensitive volume. To facilitate inserting the detector into the collimator, a long aluminum piece is connected to the back of the probe.

	0	0	0	0	0	0	0						3	3	3	3	3	3	
	0	0	0	0	0	0	0						3	3	3	3	3	3	
	0	0	0	0	0	0	0						3	3	3	3	3	3	
	0	0	0	0	0	0	0						3	3	3	3	3	3	
	0	0	0	0	0	0	0						3	3	3	3	3	3	
	0	0	0	0	0	0	0						3	3	3	3	3	3	
	0	0	0	0	0	0	0						3	3	3	3	3	3	
	1	1	1	1	1	1	1						2	2	2	2	2	2	
	1	1	1	1	1	1	1						2	2	2	2	2	2	
	1	1	1	1	1	1	1						2	2	2	2	2	2	
	1	1	1	1	1	1	1						2	2	2	2	2	2	
	1	1	1	1	1	1	1						2	2	2	2	2	2	
	1	1	1	1	1	1	1						2	2	2	2	2	2	
	1	1	1	1	1	1	1						2	2	2	2	2	2	

Figure 2.6: The fiber arrangement of the Hot-Lab Detector 1 when looking from the back towards the front. Each cell in the table corresponds to a $0.7 \text{ mm} \times 0.7 \text{ mm}$ part of the sensitive volume. The cells with numbers indicate parts of the volume with a WLSF in the center. The number indicates which channel this WLSF belongs to.

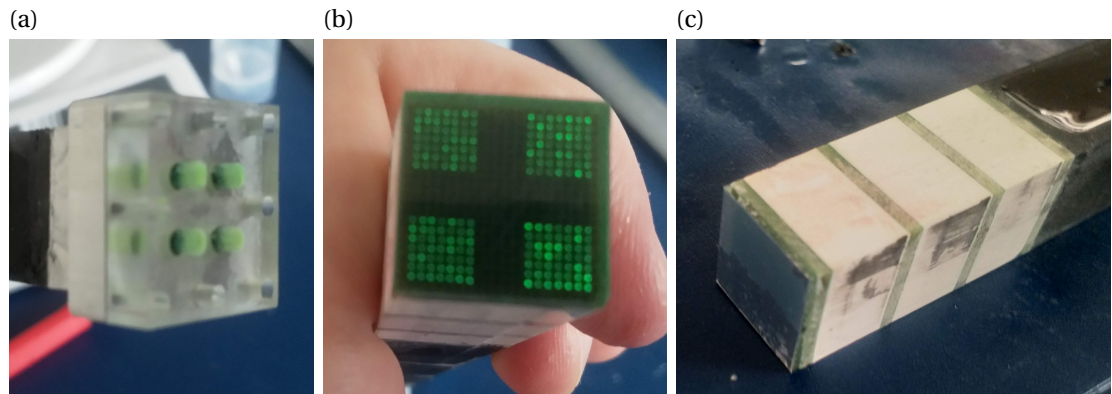
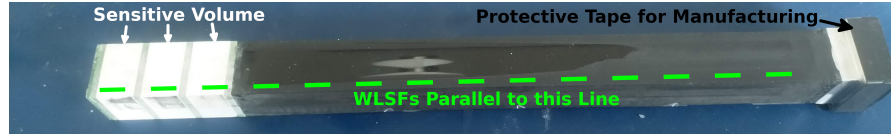


Figure 2.7: Pictures of parts of the Hot-Lab Prototype 1 detector probe (without aluminum enclosure). (a): Back of the sensitive volume. The WLSFs of each channel are bundled together. (b): Front of the sensitive volume. The front end of the WLSFs are visible in a grid with four distinct rectangles, one for each channel. (c): Side view. The three white blocks of the ZnS:Ag-epoxy mixture, separated from each other by spacers, are clearly visible. Compared to (b), a mirror is glued to the front, hiding the front ends of the WLSFs.

(a)



(b)

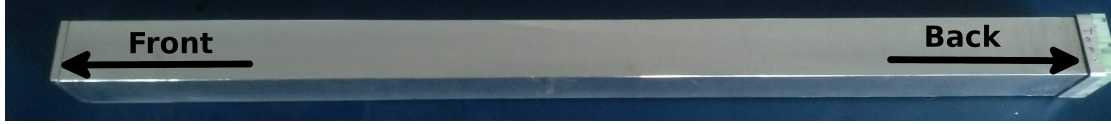


Figure 2.8: Picture of the detector probe of the first Hot-Lab prototype without (a) and with (b) the aluminum enclosure. The two pictures have roughly the same scale. The black tape around the right end of the detector in (a) is only for protecting that part of the detector during manufacturing and was removed after encapsulation, as can be seen in (b).

2.2.3 Single Channel Detectors

The single channel detectors are intended for radiation damage measurements (see section 3.2.4 for details on the experiments). To allow different irradiation environments to be tested as well as to have a reference detector and some spare ones in case of a failure, a total of five of these detector probes were built. The design resembles the Hot-Lab Prototype 1, with only a single 7×7 WLSFs channel placed in the center of the sensitive volume. The exact arrangement is illustrated in figure 2.9. In addition, the dimensions of several structural elements is slightly changed for easier handling since these detectors do not have to fit into a collimator. Figure 2.10 shows a picture of the detector probes.

2.2.4 Crosstalk Prototype

The crosstalk prototype is designed to measure the crosstalk between WLSFs that are right next to each other (on the 0.7 mm grid imposed by the spacer). The crosstalk prototype has two single fiber channels on adjacent positions on the spacer grid. Additional channels are placed 2 and 3 positions away respectively to measure how the crosstalk falls off over distance. To decrease the required measurement time, the structure of the 4 single WLSF channels is repeated several times at a distance of 4 grid spaces. This distance was deemed unlikely to produce a significant crosstalk between the structures. They can therefore be thought of as independent measurements. The exact configuration is shown in figure 2.11.

To further decrease the measurement time, the volume of each channel is increased by embedding the WLSFs in the ZnS:Ag-epoxy mixture for 10 cm (instead of 3 cm as in the other detectors), as can be seen in figure 2.12.

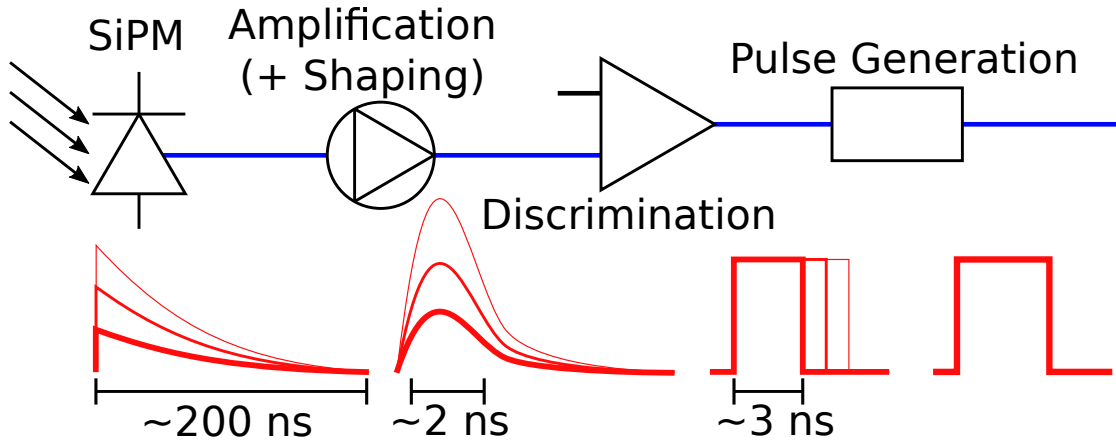


Figure 2.13: An illustration of the signal processing chain to generate digital pulses from photons. The first set of red lines represent the signals generated by the SiPM, with the thickest line being a single photon pulse and the higher thinner lines multi photon pulses. The second and third set of red lines represent the signal after amplification and shaping, and after discrimination respectively. The last red line is the output of the front end electronics.

2.3 Electronics Details

The detector electronics is comprised of two stages. The front end electronics generates a digital pulse for every incoming photon that is recognized by the SiPM. It is described in section 2.3.1. The back end electronics reads these pulses and, depending on the configuration, either performs the MSD algorithm or saves the timestamps of each photon. It is described in section 2.3.2. Section 5.3.1 describes the currently ongoing development of a new version of the detector electronics.

2.3.1 Front End Electronics

The purpose of the front end electronics is to create digital pulses of a fixed width for every photon coming from the light guides. The different stages in that process are illustrated in figure 2.13. In a first step an SiPM generates a weak and relatively long (order of ~ 100 ns) analog pulse for an incoming photon. The highest probability is for the SiPM to produce a so called single photon pulse but sometimes it also creates multi-photon pulses. These multi-photon pulses have the same shape as the single photon pulses but are scaled by an integer factor. The SiPM pulses are then amplified (amplitude of ~ 100 mV for single photon pulses) and shortened to about 2 ns. Afterwards a discriminator generates a digital pulse from the amplified signal and a pulse generator fixes the length of the pulses to a predetermined value. The entire front end processing chain is separated on two custom boards, which were developed specifically for this project and are described in the following sections.

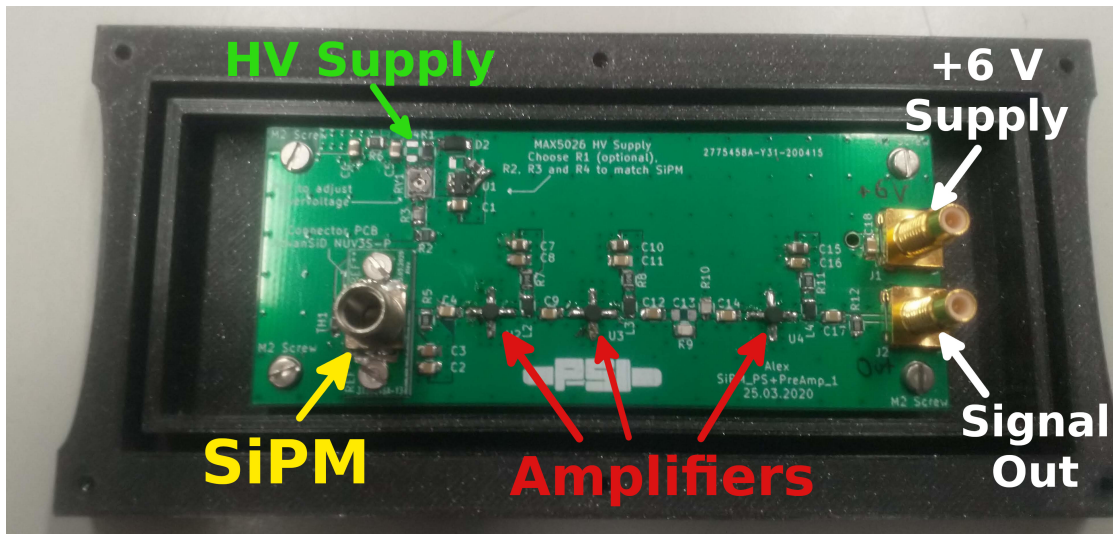


Figure 2.14: Picture of the SiPM_PS+PreAmp_1 board. The SiPM sits below an SMA connector. From there the signal goes to the right through 3 amplifier stages to the signal output. The additional capacitors and resistors to shorten the pulse are placed between the second and the third amplifier. The integrated HV supply for the SiPM is located at the top. The amplifiers and the HV supply are powered by +6 V, supplied to the connector directly above the signal output. The board is mounted in the lower half of its black enclosure.

Silicon Photomultiplier and Preamplifier Unit

Each optical light guide (see section 2.1.2) is connected to an ASD-NUV3S-P [30] SiPM made by AdvanSiD, which converts photons into an electrical signal. Every SiPM is mounted on its own custom board (board name SiPM_PS+PreAmp_1, a schematic and technical details can be found in appendix B.1), containing a high voltage (HV) supply for the SiPM as well as a chain of amplifiers and a pulse shaping stage. The entire board is mounted inside a 3D printed box to prevent light from the environment reaching the SiPM. A picture of this board is shown in figure 2.14.

The core of the on-board HV supply is a MAX5026 [31] DC-to-DC converter, which can generate an adjustable voltage up to 36 V. The exact output voltage is determined by a resistor network. On the SiPM_PS+PreAmp_1 board, this resistor network consists of several resistors with a fixed resistance determined by the intrinsic characteristics of the SiPM (such as the breakdown voltage), a ERT-J1VR332G thermistor [32] to compensate for temperature fluctuations, and a potentiometer to adjust the desired overvoltage. The temperature compensation is especially interesting since there are two main effects the temperature has on an SiPM. With rising temperature, the SiPM produces more dark counts and its breakdown voltage increases. If the HV supply is kept constant, the breakdown voltage increase leads to a decrease of the overvoltage. A reduced overvoltage in turn leads to a decrease in the SiPMs photon detection efficiency. For this reason, the temperature compensation on the SiPM_PS+PreAmp_1 board aims to make the supply voltage follow the breakdown voltage to get a constant overvoltage

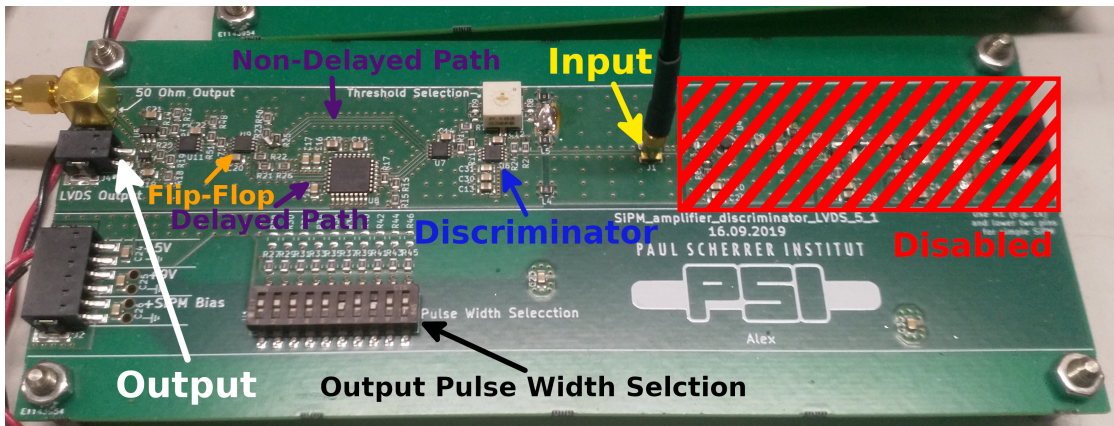


Figure 2.15: Picture of the PCB used to generate digital pulses from analog ones. The input where the analog signal enters the board is marked in yellow. The amplifiers before it are disabled. After the discriminator (blue), the signal splits into a delayed and a non-delayed one (both purple). The delay can be adjusted using a set of switches (black). Both paths enter the flip-flop (orange) and the resulting signal goes to two outputs (using two different signal standards to provide flexibility when further processing the output)

and thereby a constant detection efficiency. As a side effect of this approach, the dark count rate increases significantly if the temperature rises. However, the neutron detection algorithm is very good at filtering out background noise and can therefore be trusted to deal with this effect at a later stage.

For the amplification, three MAR-6SM+ [33] amplifiers are used for a total amplification of a factor of ~ 1000 . The input of the third amplifier is connected to the output of the second amplifier via a 22 pF capacitor. This shortens the relatively long pulses coming from the SiPM to about 2 ns (full width at half maximum). Additionally, the input of the third amplifier is connected to ground via a 6.8 pF capacitor. This suppresses very fast signal components, which could otherwise induce too much noise in the rest of the processing chain.

Discrimination and Pulse Generation Unit

The second board (called SiPM_amplifier_discriminator_LVDS_5_1 or simplified discrimination and pulse generation board) in the readout chain prepares the signal for digital processing by transforming the analog pulses from the SiPM_PS+PreAmp_1 board into digital pulses with a fixed length. A picture of the board is shown in figure 2.15. The analog signal is fed into a discriminator with a threshold of about half of the height of a single photon pulse. A pulse generator is used to fix the length of the pulse. The signal is first split up and one of them is delayed by an adjustable delay line. The delayed and non-delayed signals are then fed into a D flip-flop. The non-delayed signal is connected to the clock input and the delayed signal to the reset input of the flip-flop. The data input is tied to a high signal. The output of the flip-flop is therefore set to high when the non-delayed signal arrives and reset to low once the

delayed signal arrives. The width of each output pulse can be controlled by setting a delay value for the delay line. The discrimination and pulse generation board originally contained a preamplification stage as well. However, this part of the board has been disabled since the amplification is already done on the SiPM_PS+PreAmp_1 board. The nominal pulse width (i.e. the delay of the delay line) is set to 3.465 ns, which has been experimentally determined to be adequate for a pulse to be recognized by the following electronics.

2.3.2 Back End Electronics

There are two different types of back end electronics used to process the signals from the discrimination and pulse generation boards. The first one uses a logic analyzer, which records the timestamps of individual pulses for later analysis in post-processing. The second one uses an FPGA with a custom firmware for online processing of the signal.

Logic Analyzer

The logic analyzer (Logic Pro 8 [34]) has a small internal buffer to store photon timestamps before transferring them to the memory of a connected computer. The logic analyzer can only record the signal for a finite amount of time before memory space runs out, or its buffer overflows because it can not write to the memory fast enough. Depending on the rate of pulses which are recorded, the maximum recorded time can vary but it is usually between 0.1 s and 10 s. After such a segment, the data needs to be saved on some medium with a higher capacity (usually a hard drive) to free up space for the next segment. A measurement using the logic analyzer setup consists of multiple segments. The data collection electronics remains idle for an extended period of time between segments due to the raw data being saved, which leads to a measurement taking significantly longer than the effectively recorded time. The useful measurement time varies with the circumstances but it is usually between 10% and 20% of the total time. Additionally, a considerable volume of data is being generated. Despite these drawbacks, the logic analyzer setup can be very useful. Saving the timestamps of each individual photon makes it possible to use the same data multiple times in post processing. It is therefore invaluable for tasks such as optimizing parameters of the MSD algorithm or testing new algorithms.

FPGA with Custom Firmware

The FPGA processes data online, using the MSD algorithm (see section 2.1.3) with MSD parameters that can be set by the user at the start of a measurement. The FPGA relays the information about each event it found (the channel on which it occurred, its strength (maximum of the MSD value), and the time at which it occurred) to a computer via a microprocessor. Since this method is capable of continuous measurements for very long times and its output requires far less space to be saved, this is usually the preferred option.

The FPGA firmware and microprocessor program were developed and tested in the context of a Master thesis by Lorenz Becker-Sander [35]. For details on the implementation, the reader is referred to the thesis.

2.4 Control Software

There are two different sets of software, depending on whether a measurement is based on the Logic Analyzer (see section 2.3.2) or the FPGA (see section 2.3.2). An overview of both of them is given in this section. With a few exceptions (which are marked accordingly), all of the software consists of custom programs developed specifically for the detector, and written in MATLAB for an easy interface with data analysis and data presentation tools.

2.4.1 Control Software for the Logic Analyzer

The different pieces of software used with the logic analyzer are illustrated in figure 2.16. In this configuration, the logic analyzer is the last part of the detector electronics chain. A proprietary software (Logic 1.2.18 [36]) is provided by the vendor of the logic analyzer which allow controlling the logic analyzer by custom user software. The logic analyzer control is such a custom software written for the detector. It receives user input about the measurement to be carried out (such as the measurement duration, the duration of each segment, and where the data should be saved), and some metadata to be saved together with the data from the detector. The logic analyzer control saves the individual photon data, which it receives from the logic analyzer, leading to large data sets (more than 10 TB of this type of data have been accumulated during the thesis). During the measurement, the program displays information on the current status and history of the measurement.

After the measurement, the gathered data can be analyzed in post processing. In a first step, a filter algorithm is applied to the data. For this, two different programs are provided, which are explained below in detail. Both programs take the same type of objects (so-called filter algorithm objects) as inputs. These objects specify the filter algorithm which should be used. There is an object for the MSD algorithm explained in section 2.1.3 and used throughout this thesis, but there are also objects implemented for more advanced filters that could be used in the future. Among them are the continuous ordinary least squares (COLS) filter, which should use information about the decay shape of the ZnS:Ag scintillation light to better filter out events, and the dead time corrected MSD (DTC MSD) algorithm, which seeks to eliminate the influence of the photon rate on the neutron detection efficiency (see section 3.2.3 for details on this effect). Both of these algorithms are described in detail in section 5.3.2. These advanced algorithms are currently still being tested, which is why no results using any of them are presented in this thesis. The structure of the programs, which has the filter algorithms easily exchangeable and usable for both programs, facilitates the investigation of new algorithms. Due to the large data sets, both of these programs have large computational requirements and are therefore usually executed on a cluster for several hours or even days. To avoid unnecessary

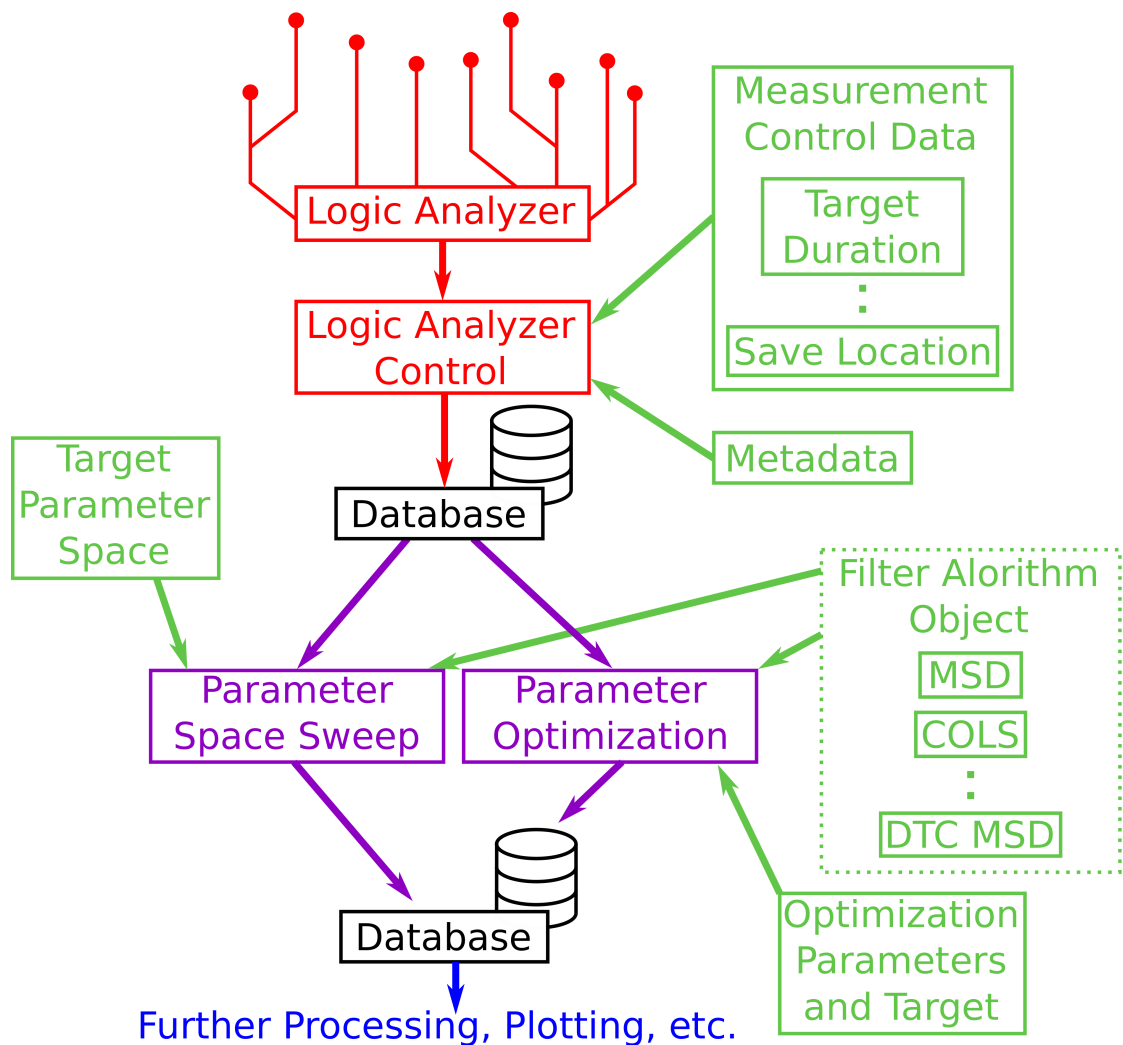


Figure 2.16: Illustration of the pieces of software used to control the detector during a logic analyzer measurement, and to perform the most common processing steps for the gathered data. The red section runs during the measurement. The violet and blue sections are performed in post-processing. The light green sections mark inputs to the different programs.

repetitions of these expensive computations, their results are stored for further use by other programs.

The first of the two programs performs the filter algorithm on the saved data for different values set for the filter parameters. The part of the filter parameter space to be used is specified by the user. Some of the calculations are the same for different parameter combinations. Instead of performing these calculations multiple times, the program saves the results of these common calculation steps and re-uses them for the calculations for other parameter combinations. This speeds up computation significantly if results on large parts of the filter parameter space are requested.

The second program performs a custom variant of the hill climbing algorithm [37] to optimize the filter parameters. This algorithm starts with an arbitrary point in the parameter space as the current position. It then checks points in the immediate vicinity in the parameter space for their performance. Of all the checked points in the parameter space it takes the best performing one and repeats all the steps with this point as the new current position. The algorithm stops once the best performing candidate is not better than the current position. The algorithm will only find a local maximum. This can be an issue especially for experimentally gathered data where random noise can create a lot of small local maxima. This issue can be reduced by enlarging the portion of the parameter space checked at every step. By checking a larger parameter space, the algorithm is more likely to capture longer ranged parameter changes and prioritize them over searching small maxima. This can also reduce the number of necessary steps, allowing the algorithm to take big steps when it is far away from a maximum. However, checking every possible point in a big part of the parameter space makes the algorithm slow, usually more than negating any potential speed gain from reducing the number of steps. As a compromise, the algorithm checks points in a large part of the parameter space but these points are not uniformly distributed. The checked points are strategically chosen with large gaps far away from the current position to capture long range trends, and closer to each other when approaching the current position for fine tuning once it is close to a maximum. The optimization target for the algorithm together with some parameters (such as the starting point) can be provided by the user.

2.4.2 Control Software for the FPGA

The different pieces of software used with the FPGA are illustrated in figure 2.17. A custom FPGA control software communicates with the FPGA via the microcontroller. The software takes user inputs such as the MSD setting that should be used for the measurement and the targeted duration. The user can also specify any metadata to be saved alongside the measured data. The program relays the relevant information to the FPGA and gives the signal to start and stop the measurement. During the measurement, the FPGA control software gathers the data sent by the FPGA and saves them at regular intervals as well as once at the end of the measurement. The program also displays information on the current status and history of the

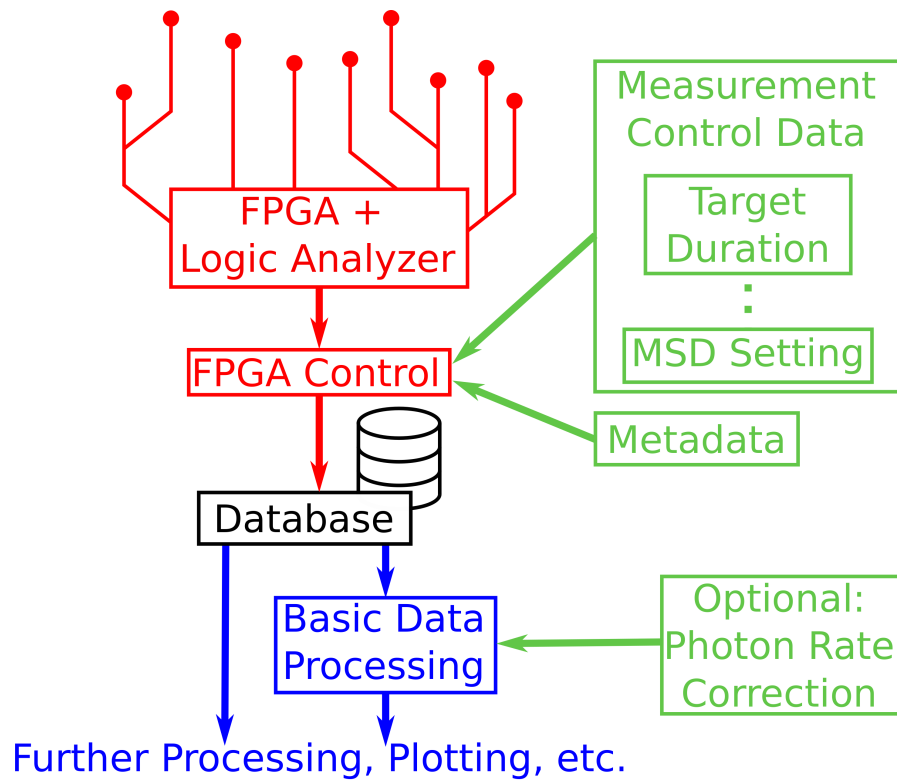


Figure 2.17: Illustration of the pieces of software used to control the detector during an FPGA measurement, and to perform the most common processing steps for the gathered data. The red section runs during the measurement. The blue section is performed in post-processing. The light green sections mark inputs to the different programs.

measurement while it is running. If information on the photon rate (defined in section 3.2.1) is desired, the logic analyzer can be connected to the FPGA control software for a short time before the start of the actual measurement with the FPGA. During this time the photon rate is recorded and is then used as an approximation for the photon rate during the entire measurement. This only works well if the photon rate is not expected to change significantly over the measurement and the short time before the measurement is representative of the entire measurement.

To facilitate the analysis of the saved data, a basic data processing software is provided. It performs tasks that are frequently needed such as calculating count rates, providing a list of all captured events arranged by channel, and applying a photon rate correction that can be supplied by the user.

3 Detector Properties

This chapter focuses on the characterization of the Hot-Lab Prototype 1 (see section 2.2.2), which is the detector that has been characterized most thoroughly due to it being used during the hot-lab campaign (see chapter 4). Some specialized measurements were carried out with other detectors. Where other detectors are used, this is indicated explicitly.

This chapter first presents the characterization of the source (section 3.1) and the detector in a strong gamma environment (section 3.2), both being necessary to interpret the measurements performed at the Hot-Laboratory (section 2.2.2). Because the performance of the detector depends on the parameters chosen for the MSD algorithm (see section 2.1.3), section 3.2 focuses first on choosing adequate MSD settings for a high gamma-ray environment before characterizing the detector more thoroughly. Additionally, the chapter presents investigations of the detector degradation under irradiation (section 3.2.4). The energy-dependent efficiency measurement described in section 3.6 would also have been of great value for the spent fuel measurements described in chapter 4, but unfortunately there were problems during the measurements that prohibited the extraction of useful data.

Apart from the characterization with respect to high gamma environments, other properties of the detector of general interest for future detector applications were investigated as well. Together with the high gamma environment results, they also show the versatility of the detector. Section 3.3 presents an optimization of the set of MSD parameters to quantify the maximum efficiency of the detector when the gamma background is low. Section 3.4 instead presents an optimization of the MSD parameters for neutron event timing resolution.

Section 3.5 presents crosstalk measurements between individual WLSFs, which give information useful for the design of the sensitive volumes of future detectors. Finally, section 3.7 presents the attempt to build a complete computational model of the detector.

3.1 Characterization of the Reference ^{252}Cf Source

This section describes the characterization of the ^{252}Cf source (PSI source number 1154) that was used as an absolute reference for several of the measurements described in this thesis.

3.1.1 Neutron Output

Important Impurities

According to its certificate, the source was manufactured in April 1988. The neutron output of the source is reported to have been $1.12 \cdot 10^8 \text{ s}^{-1}$ on the April 22, 1988 [38]. However, as shown in [38] and further illustrated in this section, the measured initial neutron output or the related ^{252}Cf content is not reliable. Further difficulties when reconstructing the neutron output of the source arise from its old age. Due to the difficulty in separating different isotopes of Californium, ^{252}Cf sources usually contain some amount of other Californium isotopes. While these are usually not relevant for a fresh ^{252}Cf source, the ^{250}Cf isotope can give a significant contribution for older sources due to its long half life of 13.1 y [39] and its relatively high branching ratio for spontaneous fission of 0.077% (compared to for example $5 \cdot 10^{-7}\%$ for ^{251}Cf) [39]. The age when ^{250}Cf contributions become relevant varies dependent on the source and the desired accuracy, but typically after ~ 20 years the ^{250}Cf contribution is high enough to be relevant. At the same time, decay products build up over time and they can have a significant contribution for old sources as well. The most important one for the neutron output is ^{248}Cm , which is the product of the α -decay branch of ^{252}Cf and builds up in the source due to its long half life of $3.48 \cdot 10^5 \text{ y}$ [39]. Its high spontaneous fission branching ratio of 8.39% [39] makes it a significant contributor for old sources.

The ^{248}Cm content of the source can be calculated based on the initial ^{252}Cf content using the Bateman equation:

$$n_{\text{Cm}248}(t) = n_{\text{Cf}252,0} \frac{\lambda_{\text{Cf}252}}{\lambda_{\text{Cf}252} - \lambda_{\text{Cm}248}} br_{\text{Cf}252,\alpha} \left(e^{-\lambda_{\text{Cf}252} \cdot t} - e^{-\lambda_{\text{Cm}248} \cdot t} \right) \quad (3.1)$$

Here, $\lambda_{\text{Cf}252}$ and $\lambda_{\text{Cm}248}$ are the decay rates of ^{252}Cf and ^{248}Cm , respectively, $n_{\text{Cf}252,0}$ is the initial ^{252}Cf content, $br_{\text{Cf}252,\alpha} = 96.898\%$ [39] is the branching ratio of ^{252}Cf for the α -decay, and t is the time since the source manufacturing. In contrast to ^{248}Cm , the amount of ^{250}Cf is not closely linked to the amount of ^{252}Cf at the beginning, it represents an independent contribution to the neutron emission of the source.

Comparison to Reference Source

To accurately measure the neutron output of the source, it was compared to a well known reference ^{252}Cf source (PSI source number 1077, referred to as the reference source here) with a neutron output of $1.78 \cdot 10^7 \text{ s}^{-1}$ at the time of the calibration. This calibration was performed

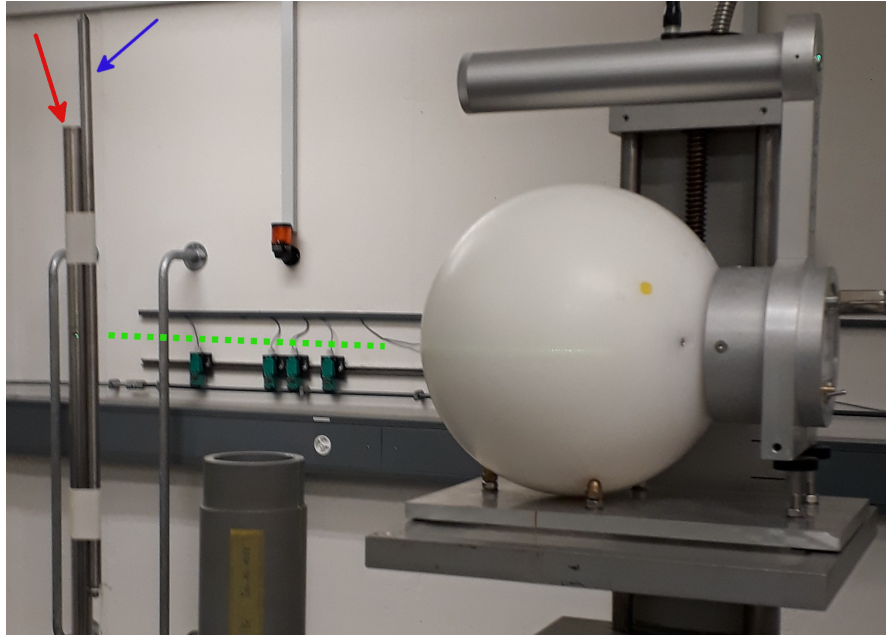


Figure 3.1: Picture of the setup at the PSI Eichstelle which was used to calibrate the ^{252}Cf source. The reference ^{252}Cf source can be inserted into the thicker metal tube (marked by the red arrow). The slightly thinner tube (marked by the blue arrow) containing the source that is being calibrated is taped to the front of it. The green dashed line marks the measurement height, which is the height at which both sources are placed in their respective tube. The calibration detector (shown is the SmartREM detector) is clearly recognizable by its white spherical moderator, which is centered on the measurement height.

on the 11th of September, 2020, directly before the measurements in the PSI Hot-Laboratory described in chapter 4.

The measurements were performed at the calibration laboratory (Eichstelle) of the ASI (Abteilung Strahlenschutz und Sicherheit) division at PSI. The measurements were performed with two different detectors (LB 6411 [40] and SmartREM [41]) for cross validation. The measurement system consists of a vertical tube for the neutron source and a horizontal rail on which a detector can be placed. The reference source can be inserted into and retracted from the vertical tube automatically. For measurements with the source that is being calibrated, it is taped to the front of the vertical tube. A picture of the setup is shown in figure 3.1. Multiple measurements are conducted, switching between the two detectors and varying the distance between the detector and the source. Each of these measurements is performed once with the reference source and once with the source that is being calibrated. Since the source that is being calibrated is taped to the front of the tube, it is 1.25 cm closer to the rail holding the detector. This is compensated by moving the detector 1.25 cm towards the source when measuring with the reference source, thereby keeping the same distance between detector and source. The different measurement arrangements and the measured count rates are shown in table 3.1.

Chapter 3. Detector Properties

Detector	Distance	Count Rate C	Count Rate R	Ratio
LB 6411	38.75 cm	$10.27 \pm 0.04 \text{ s}^{-1}$	$1219.9 \pm 1.2 \text{ s}^{-1}$	118.8 ± 0.5
SmartREM	38.75 cm	$18.81 \pm 0.13 \text{ s}^{-1}$	$2316.8 \pm 2.3 \text{ s}^{-1}$	123.2 ± 1.0
LB 6411	58.75 cm	$4.99 \pm 0.02 \text{ s}^{-1}$	$562.4 \pm 0.6 \text{ s}^{-1}$	112.7 ± 0.4
SmartREM	58.75 cm	$9.17 \pm 0.06 \text{ s}^{-1}$	$1050.8 \pm 1.1 \text{ s}^{-1}$	114.6 ± 0.4
LB 6411	66.10 cm	$4.13 \pm 0.02 \text{ s}^{-1}$	$450.8 \pm 0.3 \text{ s}^{-1}$	109.3 ± 0.5
Average				113.6 ± 4.8

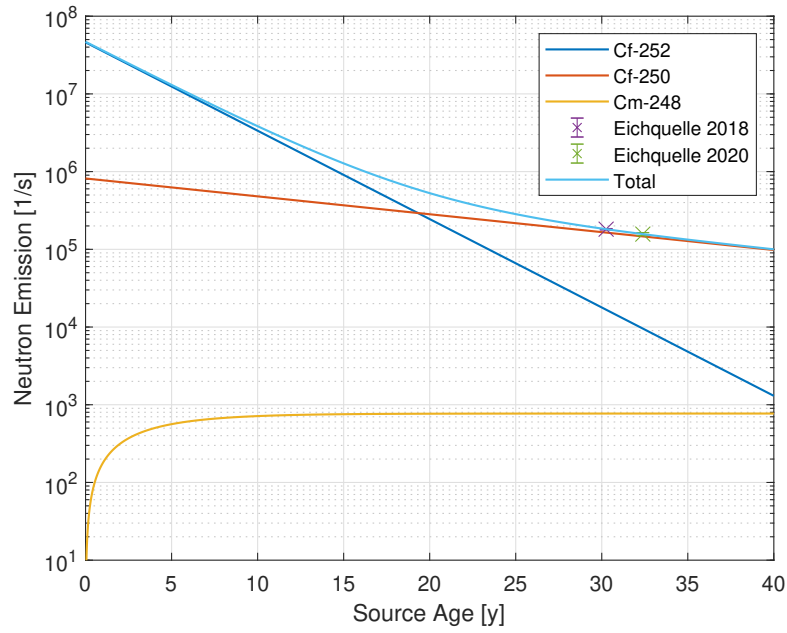
Table 3.1: Results for the ^{252}Cf source calibration measurements. The count rates for the source that is being calibrated are marked “C” and the ones for the reference source are marked “R”. The uncertainties represent a single standard deviation.

The ratio of the count rates when measuring with the two different sources allows calculating the neutron output of the source that is being calibrated by applying the same ratio to the known neutron output of the reference source. However, as can be seen from table 3.1, the ratios for the different measurement arrangements are different and their spread is significantly larger than the uncertainties on the individual ratios. The reason for this remains unknown. A similar calibration measurement for the same source has already been done in the context of the CASQUADES project in 2018. The change of the ratio of the count rates with the distance between detector and source was not observed during the 2018 measurement [42, 12]. The geometry was also modeled using MCNP 6.2 [14], the results of which showed no significant change in the count rate ratio with distance. A possible explanation is the presence of an unknown background signal, which is not subtracted. For the calculation of the neutron emission, the weighted average of all ratios is taken and the standard deviation of the values is taken as the uncertainty. This gives a neutron output of $(1.57 \pm 0.07) \cdot 10^5 \text{ s}^{-1}$ for the source being calibrated. Since the calibration took place immediately before the measurements at the PSI hot laboratory described in chapter 4, this value and uncertainty is taken for the interpretation of the results of these measurements. For the interpretation of other measurements, the decay of the source needs to be taken into account. This is detailed in the next section.

Source Content and Neutron Emission Reconstruction

Using the results of the two measurements in 2018 and 2020, it is possible to reconstruct the initial ^{252}Cf and ^{250}Cf content of the source. The 2018 calibration measured a neutron emission of $(1.817 \pm 0.036) \cdot 10^5$ on the 24th July 2018 [12, 42]. The resulting initial contents are $4.75 \cdot 10^{16}$ atoms of ^{252}Cf and $1.79 \cdot 10^{17}$ atoms of ^{250}Cf . The resulting neutron emission is shown in figure 3.2a. When comparing the ^{252}Cf to ^{250}Cf ratio of about 2 : 8 to what has been found for other sources (ratios between 8 : 2 and 8.5 : 1.5 [43]), there is a large discrepancy. Possible problems with this approach are the measurements being relatively close to each other when compared to the age of the source, and the issue with the 2020 measurement potentially being unreliable due to the unexplained spread in the results. Another approach is to take a fixed ratio of ^{252}Cf to ^{250}Cf in accordance with the literature and determine the initial

(a)



(b)

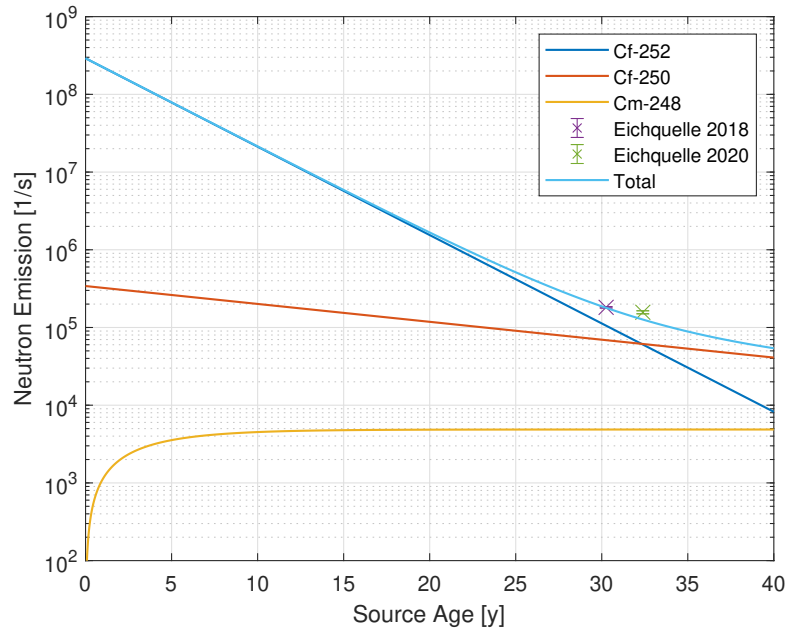


Figure 3.2: Neutron emission of the ^{252}Cf source in total as well as separated by isotope. Additionally, the two measured values are shown. The emission in (a) is based on the reconstruction which agrees with both measurements and (b) is based on the reconstruction using a ^{252}Cf to ^{250}Cf ratio which agrees with literature values.

content only using the probably more reliable results from the measurement in 2018. The initial contents using that method and a ratio of 8 : 2 are $3 \cdot 10^{17}$ atoms of ^{252}Cf and $7.5 \cdot 10^{16}$ atoms of ^{250}Cf . The resulting neutron emission is shown in figure 3.2b. At the time of the 2020 calibration, this method would give a neutron emission of $1.27 \cdot 10^5 \text{ s}^{-1}$ (compared to the measured $1.57 \cdot 10^5 \text{ s}^{-1}$).

No nuclear database or other publication containing information on the neutron spectrum for spontaneous fission of ^{250}Cf and ^{248}Cm was able to be located despite significant effort searching. For this reason, the source is always treated as if it had a pure ^{252}Cf spectrum. While there is still a large uncertainty in the composition of the source, it is clear that at least the contribution of ^{250}Cf to the neutron output is significant (see figure 3.2). If the neutron spectrum of ^{250}Cf is therefore significantly different from the one of ^{252}Cf , that could influence the results of the calibration and of subsequent measurements with the source.

Overall, there is not enough information available to deduce the neutron emission rate and spectrum of the source with a high degree of confidence. For further use in the thesis, the neutron output is assumed to be the one predicted by the two measurements in 2018 and 2020, and which is shown in figure 3.2a. The idea of this choice is to have a better accuracy for the measurements of the hot-lab campaign (chapter 4) which was conducted close to the 2020 calibration measurements. While the possible bias in the neutron source emission is not detrimental for the interpretation of the results in this thesis, it is vital to have a better characterized source (best would be a fresh ^{252}Cf source) for high accuracy measurements in the future.

3.1.2 Gamma Output

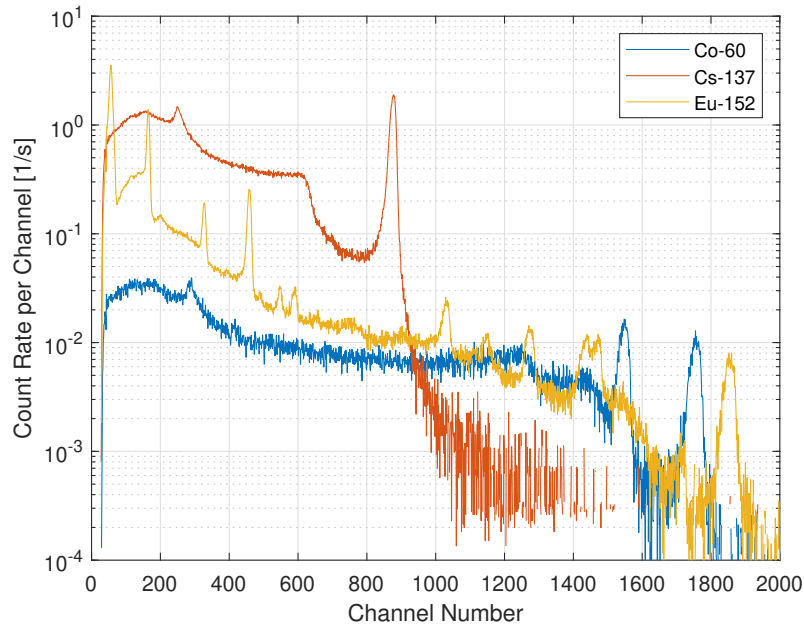
This section describes the measurement of the gamma emission of the ^{252}Cf source. This is mostly interesting when trying to determine what influence on the detector the gamma rays could have had during a measurement with the ^{252}Cf source. A Kromek-GR1A CZT gamma detector [44] was used for the measurements.

Gamma Detector Calibration

The detector is calibrated using a 48 kBq ^{60}Co source, a 2.1 MBq ^{137}Cs source, and a ^{152}Eu source with an unknown activity. The spectrum for each of these calibration sources is recorded as well as a background spectrum with no sources present. Care was taken to have each source at the same position relative to the detector. The results are shown in figure 3.3a.

The calibration was only done for counts in the photopeaks, and is therefore of course also only valid to interpret photopeak data. The calibration was performed using custom scripts and is split into two parts: A function to relate the position of a photopeak to the energy of the gamma rays producing it, and a function for the energy-dependent efficiency. To get the position and the count rate of a photopeak, it is first fit to a Gaussian function for the peak

(a)



(b)

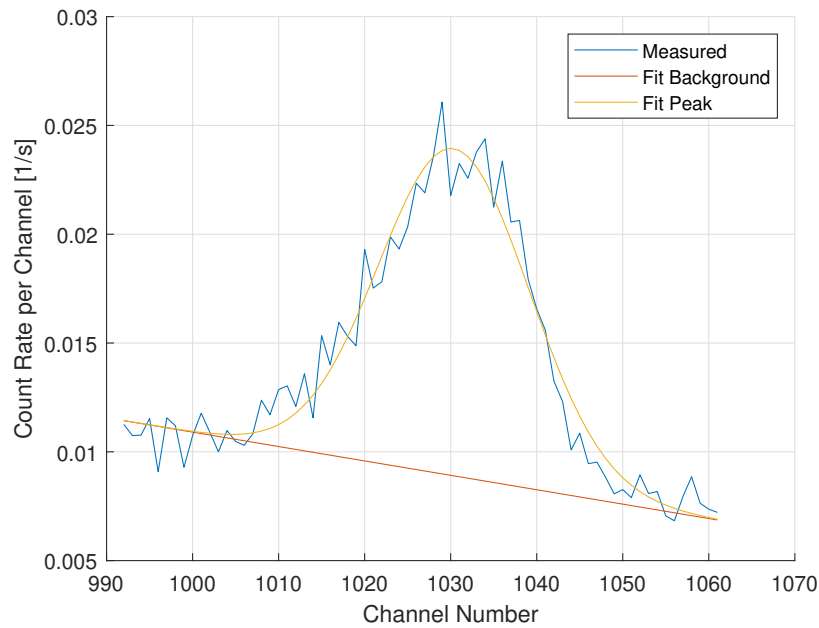
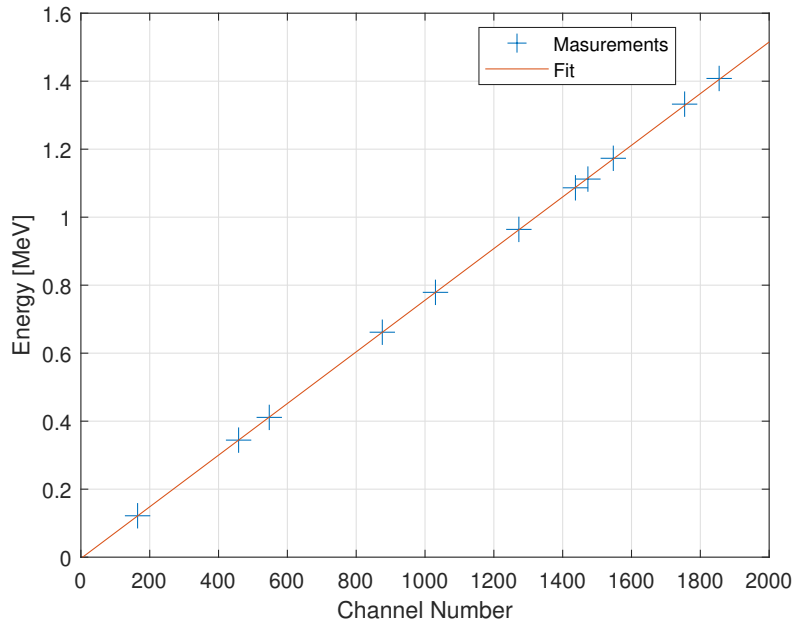


Figure 3.3: (a): Spectrum measured by the Kromek detector for the different calibration sources. The background spectrum recorded with no source present is already subtracted. (b): Close-up of the spectrum measured for the ^{152}Eu 779 keV photopeak is shown as an example. Also shown is the fit for the background (red) and the photopeak (yellow). The total count rate in the photopeak is estimated by integrating the region between the red and the yellow line.

(a)



(b)

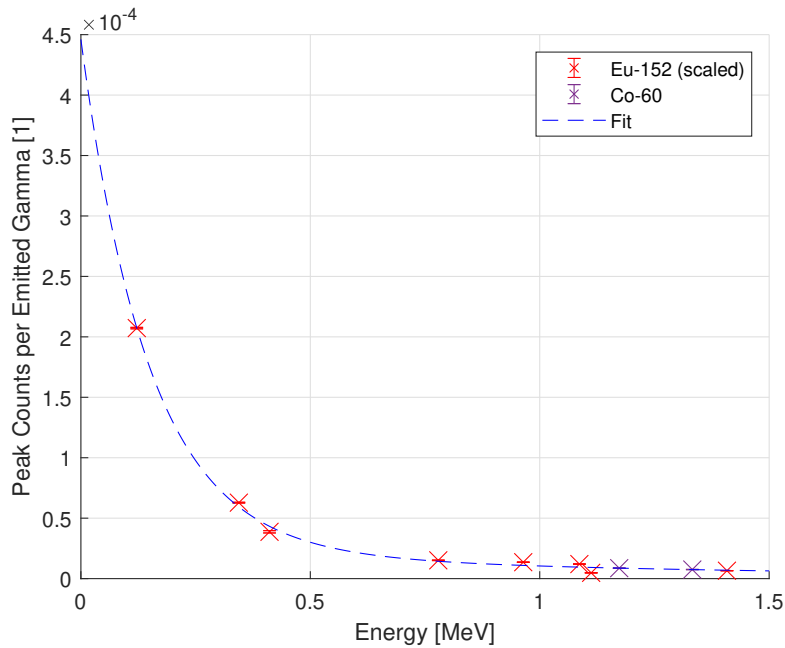


Figure 3.4: The results of the calibration of the Kromek gamma detector. (a): channel number of the photopeak position against the energy of the corresponding gamma line of the calibration sources. (b): Energy of the gamma lines plotted against the count rate in the photopeak divided by the emission rate for the corresponding gamma line. The error bars show the uncertainty due to counting statistics, uncertainties of the nuclear data is not taken into account for the error calculation. The double exponential fit through the data points is shown as well.

itself and a linear function for the background. An example of this is shown in figure 3.3b. For the position of the photopeak, the maximum position of the Gaussian function is taken. The count rate of the photopeak is estimated as the area under the Gaussian function and above the linear background function.

The energy calibration is done by plotting the position of each clearly recognizable photopeak in the recorded spectra for the three calibration sources against the energy of the corresponding gamma line (data from [45]). A linear fit through the obtained values is then taken as the relation between photopeak position and the corresponding gamma energy (see figure 3.4a). The energy-dependent efficiency for photopeak counts is determined in two steps. Since the activity of the ^{152}Eu source is not well known, this data cannot be used directly to determine the absolute efficiency. Instead, the count rate of every clearly recognizable photopeak in the measured ^{152}Eu spectrum is divided by the corresponding gamma emission rate per ^{152}Eu decay to get a relative efficiency as a function of gamma energy. A complete function is derived by fitting the data points to a double exponential function. This relative efficiency function is then scaled to match the photopeak count rates divided by the corresponding gamma emission rates for the two gamma lines (1.17 and 1.33 MeV) of the ^{60}Co source. The result is shown in figure 3.4b.

^{252}Cf Source Measurement

The ^{252}Cf source was placed at the same position relative to the Kromek detector as the calibration sources to record its spectrum. The recorded spectrum with the background subtracted is shown in figure 3.5. The positions and count rates for the individual photopeaks are determined the same way as for the calibration sources. This is only done for the clearly visible photopeaks above 200 keV since below that energy the photopeaks were hard to distinguish from each other and from the background. The gamma energy and emission rate for each of these photopeaks is determined using the calibration presented in the previous section. The result is shown in figure 3.5.

Isotope Analysis

Based on the gamma energies, three isotopes can be determined which are most likely emitting these gamma rays. These are ^{137}Cs , ^{249}Cf , and ^{251}Cf (see table 3.2). The presence of all these isotopes in the source is expected. Separation of the different californium isotopes during the production of such sources is difficult and it is therefore expected that other isotopes apart from ^{252}Cf are present in the source (as already discussed in section 3.1.1). Both ^{249}Cf , and ^{251}Cf being present in similar quantities is also what is expected from literature [43]. It is also interesting to compare these values to the initial quantities of ^{252}Cf determined in section 3.1.1. The result is much closer to the literature values when imposing the literature ^{252}Cf to ^{250}Cf ratio than when only using the measured results. Regarding ^{137}Cs , it is a fission product with a high cumulative fission yield ($\sim 5.0\%$ [46]) and a long half life (30.1 years). It is therefore

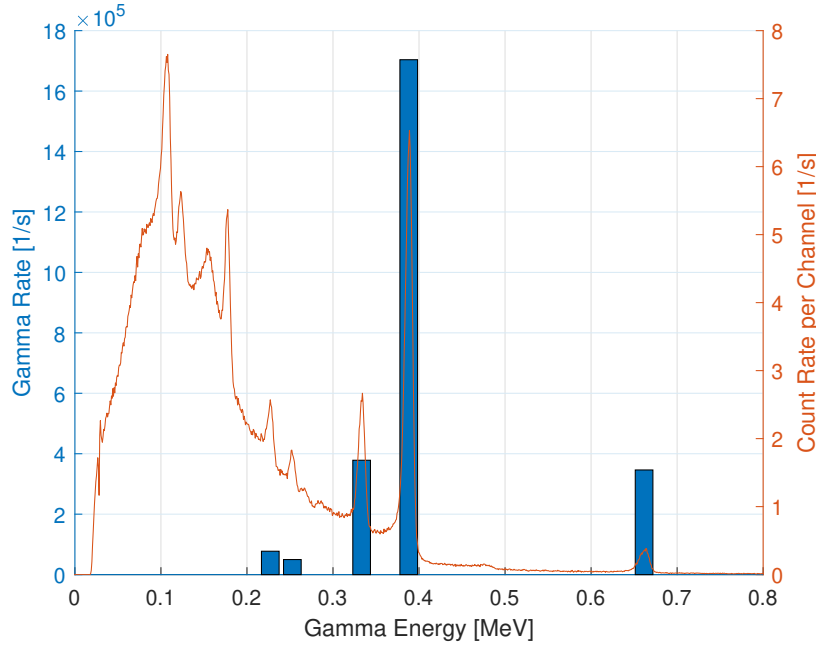


Figure 3.5: Measured spectrum and the deduced gamma emission lines for the ^{252}Cf source. For the x -axis of the spectrum, every channel is converted to the energy a gamma ray would need to produce a photopeak centered on that channel.

expected to be present in large quantities as a result from the spontaneous fission of ^{252}Cf (and to a lesser degree spontaneous fission of other nuclei).

3.2 Performance in High Gamma Environments

3.2.1 Choice of MSD Parameters

Due to the strong gamma background present when measuring spent fuel, it is important to choose the MSD parameters (see section 2.1.3) in such a way that gamma rays are not producing false counts in the detector (for example via pile-up). Measurements to optimize the MSD parameters were performed at the PSI Fast Neutron Lab (FNL) using a ~ 120 MBq ^{60}Co source. The detector was put in a lead cavity together with the source to maximize the flux density of gamma rays in the sensitive volume. A picture of the setup is shown in figure 3.6 (the ^{252}Cf source shown in figure 3.6a was not present for this measurement).

Since the characterization of the gamma environment in this setup is rather complicated and would include a lot of uncertainties, the detector itself is used to quantify the gamma environment. More precisely, the rate of pulses coming from the SiPMs (before the filter algorithm), measured over a long period of time (more than 1 s), is used. Further on, this quantity is called “photon rate”. Since the photon rate is connected to an SiPM, it is defined for each detection channel individually. Using the photon rate as the metric for the gamma

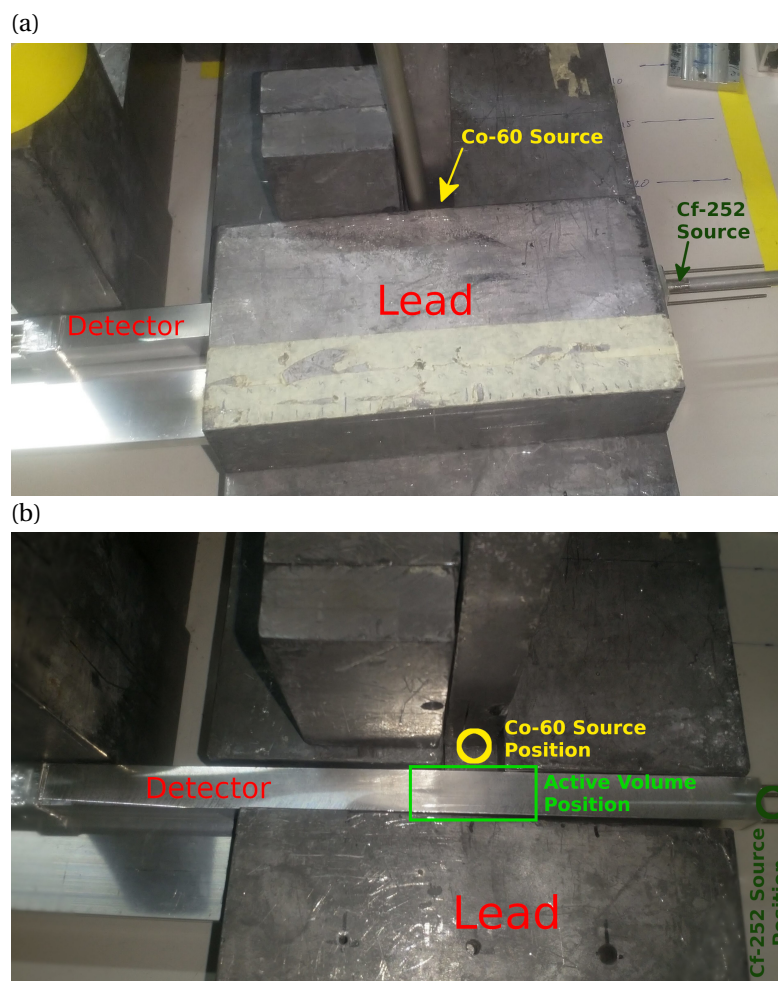


Figure 3.6: Two pictures of the setup at the FNL used to subject the detector to a high gamma environment. (a): The detector is inserted from the left into a cavity where its sensitive volume is surrounded by lead. The ^{252}Cf source is placed at the front of the detector, ~ 10 cm away from the sensitive volume. The ^{60}Co source is at the tip of a steel rod and inserted from the top into the same cavity. Only one of the sources is used at a time for the measurements described here. (b): The setup without the sources and with the top lead block of the cavity removed. The position where the sources would be placed during a measurement is marked. Right next to it is the sensitive volume of the detector.

Chapter 3. Detector Properties

γ -Energy	Isotope	Activity	Atoms	Atoms at T_0
662 keV	^{137}Cs	0.40 MBq	$5.54 \cdot 10^{14}$	-
388 keV 333 keV 253 keV	^{249}Cf	2.56 MBq	$4.09 \cdot 10^{16}$	$4.37 \cdot 10^{16}$
227 keV	^{251}Cf	1.13 MBq	$4.61 \cdot 10^{16}$	$4.74 \cdot 10^{16}$

Table 3.2: Main gamma lines in the ^{252}Cf source spectra with corresponding isotope activities and atom numbers. Where applicable, the number of atoms at the time of manufacturing (T_0) is also given.

environment has the added benefit of providing a quantity that can easily be measured in any circumstances (e.g. also when the source is unknown and a theoretical calculation of the gamma environment is impossible). By its nature, the photon rate depends on different aspects of the gamma environment (such as flux density, spectrum, and gamma directions). When making the approximation that all of the SiPM pulses from gamma rays are uncorrelated to each other¹, the effect of a change of the gamma environment on the detector can be perfectly represented by the associated change in the photon rate. This is because the SiPM signals used to calculate the photon rate are the same SiPM signals also used by the detector to find the neutron events, and the distribution of random uncorrelated pulses is perfectly described by its average rate. There are other contributions to the photon rate apart from gamma rays. Most important are pulses generated by the SiPM if there is no incident photon (these are called dark counts). Second is stray light from the environment that manages to reach the SiPM through the enclosure. Together, the dark counts and the stray light produce a contribution to the photon rate which is usually between $5 \cdot 10^5 \text{ s}^{-1}$ and $10 \cdot 10^5 \text{ s}^{-1}$, depending on the light in the environment and the temperatures of the SiPMs. In principle, the neutron flux also has an influence on the dark count rate but this has so far always been an extremely small influence and is therefore disregarded. Assuming, as before, that the SiPM pulses from these contributions are uncorrelated, characterizes the full impact of the gamma rays, dark counts, and environmental light on the detector performance. I.e. if two different gamma environments lead to the same photon rate, their effect on the detector behavior is the same. If the photon rate is monitored and its influence on detector performance used to interpret the detector output, no other extra steps have to be taken to account for possible changes in the dark count rate or stray environmental light. In high gamma environments the photon rate is dominated by the contribution from the gamma rays. For this reason it can still be used as a good indicator of gamma intensity in high gamma environment and also the vast majority of the false positive counts (i.e. counts not due to neutrons) will be due to gamma rays.

¹Strictly speaking, it is only necessary for the SiPM pulses to always have the same correlation to each other. This means that correlations that are introduced for all SiPM pulses in the same way, such as the afterpulse effect of the SiPM or discretization of the pulses in the electronics, do not negate the argument. The idealization of uncorrelated events is used here only simplify the argumentation.

3.2 Performance in High Gamma Environments

Channel	Photon Rate	Counts
Ch 0	$10 \cdot 10^6 \text{ s}^{-1}$	2
Ch 1	$9 \cdot 10^6 \text{ s}^{-1}$	1
Ch 2	$7 \cdot 10^6 \text{ s}^{-1}$	0
Ch 3	$6 \cdot 10^6 \text{ s}^{-1}$	0

Table 3.3: The results of the gamma-blindness measurements with only the ^{60}Co source present for the Hot-Lab Prototype 1 detector. The number of counts is for the MSD parameters which were chosen to be used in the end. The photon rate shown is the measured rate of pulses from the SiPMs. The effective measurement time was 100 s.

Channel	Counts
Ch 0	232
Ch 1	50
Ch 2	291
Ch 3	198

Table 3.4: Raw count results obtained during the neutron efficiency measurements with the ^{252}Cf source for the Hot-Lab Prototype 1 detector. The number of counts is for the MSD parameters which were chosen to be used in the end. The effective measurement time was 500 s.

Apart from ensuring a low number of false positive counts from gamma rays, the choice of the MSD parameters should also maximize the efficiency to detect neutrons. Measurements for this have been performed using the same setup but without the ^{60}Co source. Instead, a ^{252}Cf source (see section 3.1 for its characterization) was placed directly in front of the detector (at 10.5 cm from the sensitive volume), just outside of the cavity. Figure 3.6a shows a picture of this setup (the ^{60}Co source not being present). Deriving a neutron efficiency from measurements in this setup is difficult since there is a significant contribution to the detector response coming from scattered neutrons in the surrounding lead. However, this is acceptable here since qualitative information is enough for choosing the MSD parameters.

To allow different MSD parameters to be tested easily, the logic analyzer setup was used as the detection electronics (see section 2.3.2), allowing the MSD algorithm to be performed in post processing using different MSD settings to try and find the best performing one.

The parameters which were chosen after testing several combinations are an interval length of $\Delta t = 400 \text{ ns}$, a summing length of $m = 5$, a threshold of $k = 35$, and a blocking time of $\delta t_B = 10 \mu\text{s}$ (see section 2.1.3). The results of the measurements when using these parameters are shown in tables 3.3 and 3.4. Unfortunately, due to time constraints, the data set is quite limited. The effective measurement time is only 100 s and not all channels have been exposed up to the same level of gamma radiation. However, with the chosen parameters, a more accurate gamma-blindness measurement has been carried out (see section 3.2.2). The neutron

Channel	Photon Rate	Counts	Run Time	Event Rate
Ch 0	$10 \cdot 10^6 \text{ s}^{-1}$	454	16 h	0.0079 s^{-1}

Table 3.5: Gamma-blindness measurement results for the Hot-Lab detector 1

efficiency has also been measured again with better accuracy and in an environment with reduced scattering to allow a quantitative result in section 3.2.3. The significant difference in the number of neutrons measured is discussed there as well.

3.2.2 Gamma Blindness

As already mentioned previously, it is important to know that the count rate in the detector due to gamma rays (for example through pile-up) is small. To test this, the detector has been exposed to a $\sim 120 \text{ MBq } ^{60}\text{Co}$ source. The source was placed at the side of the detector. A picture of the setup is shown in figure 3.7a. Due to time constraints, the gamma-blindness was measured only for channel 0. The gamma-blindness of all other channels is assumed to be similar for the same photon rate (see section 3.2.1). This approach is justified as the photon rate should capture the main influence of the gamma rays at the point in the processing chain directly before the MSD algorithm. Since the MSD algorithm is identical for every channel, the same photon rate should also produce the same number of false counts. The results of this measurement is shown in table 3.5. They show that the false counts from gamma rays can be ignored at a photon rate of $10 \cdot 10^6 \text{ s}^{-1}$, if a count rate error of 0.0079 s^{-1} is acceptable. The false counts are expected to be dominated by gamma pile-up [16]. Since pile-up results in a strong non-linearity in the relationship between gamma flux and counts, the false counts are expected to be much lower at lower photon rates.

3.2.3 Neutron Detection Efficiency

Dependency on Gamma Background

During the initial tests of the detector, it was observed that its efficiency decreases in the presence of strong gamma fields (high photon rates, see section 3.2.1 for definition). This is likely due to the way in which the MSD algorithm detects events. In an idealized model, it would be possible to separate the counts q_j in every time interval (see equation 2.1) into contributions from neutron events $q_{n,j}$ and background (gammas, dark counts, etc.) $q_{B,j}$: $q_j = q_{n,j} + q_{B,j}$. This would modify equation 2.1 into

$$d_i = \sum_{j=i-m+1}^i (q_{n,j} + q_{B,j}) - \sum_{j=i-2m+1}^{i-m} (q_{n,j} + q_{B,j}) \quad \forall i \in V_{\text{MSD}} \quad (3.2)$$

In reality, SiPM signals from the neutron event and from the background are sometimes so

close to each other that they actually only generate a single detectable pulse. These combined pulses are counted twice in the simplified equation above. Therefore the number of these coincidence signals $q_{C,j}$ has to be subtracted ($q_j = q_{N,j} + q_{B,j} - q_{C,j}$), giving

$$d_i = \sum_{j=i-m+1}^i (q_{n,j} + q_{B,j} - q_{C,j}) - \sum_{j=i-2m+1}^{i-m} (q_{n,j} + q_{B,j} - q_{C,j}) \quad \forall i \in V_{\text{MSD}} \quad (3.3)$$

This can be rearranged into

$$d_i = \left(\sum_{j=i-m+1}^i q_{n,j} - \sum_{j=i-2m+1}^{i-m} q_{n,j} \right) + \left(\sum_{j=i-m+1}^i q_{B,j} - \sum_{j=i-2m+1}^{i-m} q_{B,j} \right) - \left(\sum_{j=i-m+1}^i q_{C,j} - \sum_{j=i-2m+1}^{i-m} q_{C,j} \right) \quad \forall i \in V_{\text{MSD}} \quad (3.4)$$

The content within the first pair of braces (i.e. $\sum_{j=i-m+1}^i q_{n,j} - \sum_{j=i-2m+1}^{i-m} q_{n,j}$) is almost independent from the photon rate (as stated previously, no measurable change in photon rate was ever observed by changing the neutron flux). The content of the second pair of braces (i.e. $\sum_{j=i-m+1}^i q_{B,j} - \sum_{j=i-2m+1}^{i-m} q_{B,j}$) is some random number, the probability distribution of which is symmetric around 0 and gets wider the higher the photon rate is. If an event is detected it is purely dependent on the maximum value of the MSD during this event. If the MSD maximum is above the chosen threshold, the detector triggers. Experience has shown that there are generally more events for which the maximum MSD is slightly below the set threshold than events for which the MSD is higher than the threshold by the same amount. This random contribution is therefore expected to slightly raise the detection efficiency when it gets wider (i.e. with a higher photon rate). The content of the third pair of braces (i.e. $\sum_{j=i-m+1}^i q_{C,j} - \sum_{j=i-2m+1}^{i-m} q_{C,j}$) is the most interesting part. With an increasing photon rate, all $q_{C,j}$ are expected to increase. On average, $q_{C,j}$ will be roughly proportional to $q_{n,j} \cdot q_{B,j}$. This means that the increase with a higher photon rate will be more pronounced in the intervals with a higher $q_{n,j}$. For an event to trigger $\sum_{j=i-m+1}^i q_{n,j}$ is expected to be much higher than $\sum_{j=i-2m+1}^{i-m} q_{n,j}$. It is therefore expected that the content of the third pair of braces increases with higher photon rates, resulting in an overall reduction of the MSD value and a lower chance of triggering on an event. The reduction of the neutron detection efficiency with increasing photon rate is therefore likely due to the effect of the third part being stronger than the one of the second part.

The neutron detection efficiency depends therefore on the environment. The photon rate has already been identified as an adequate metric to describe the combined effect of gamma rays, dark counts, and stray environmental light on the detector (see section 3.2.1). It is therefore used again here to measure the neutron detection efficiency as a function of the photon rate. The idea is again that the entire relevant influence of the non-neutron environment is captured in the photon rate and that therefore the measured efficiency at a given photon rate is independent of the exact causes that lead to that photon rate.

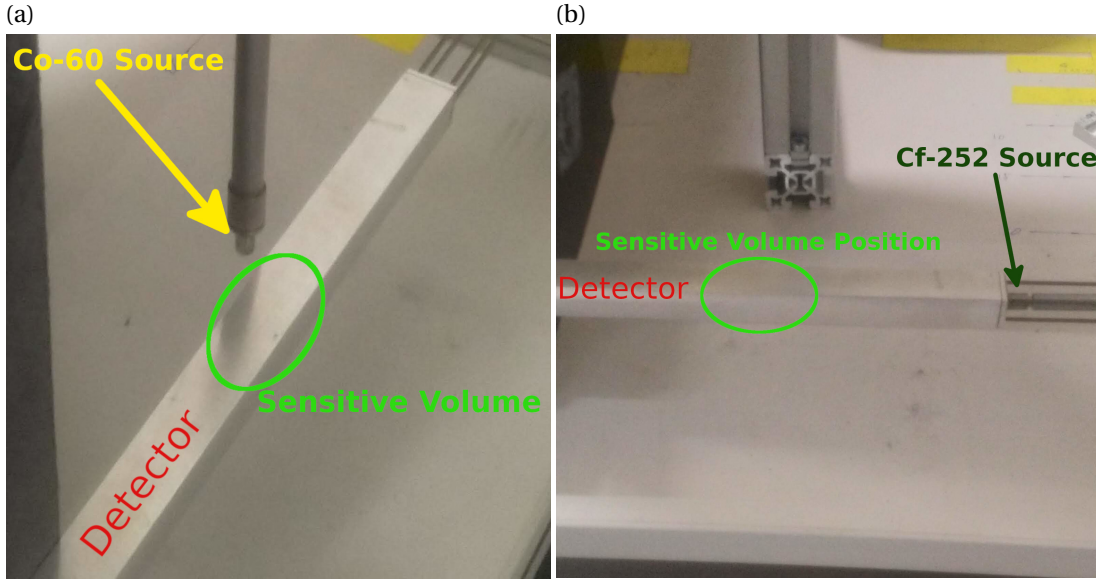


Figure 3.7: Pictures of the setup used to measure the gamma-blindness and gamma-background dependent efficiency. (a): View from the top. Shown is the ^{60}Co source next to the detector. The ^{252}Cf source is not present. (b): View from the side. Shown is the ^{252}Cf source in front of the detector. The ^{60}Co source is not present.

Measurement with a ^{252}Cf and a ^{60}Co Source

The intrinsic neutron detection efficiency in this work is considered to be the count rate divided by the neutron flux through the sensitive volume of a channel or the entire detector. The sensitive volume is approximated as the combined volume of all WLSFs and their immediately surrounding ZnS+Ag-epoxy mixture. The surrounding is considered for each fiber to be the mixture within a square prism with a cross section of a $0.7\text{ mm} \times 0.7\text{ mm}$ centered around the WLSF.

This intrinsic efficiency was measured at different photon rates at the PSI Fast Neutron Laboratory (FNL) using the ^{252}Cf source characterized in section 3.1 and a ^{60}Co source. The ^{60}Co source was placed next to the detector, close to the position of the sensitive volume. The ^{252}Cf source was placed directly in front of the detector, 10.5 cm away from the sensitive volume. Figure 3.7 shows pictures of the setup. It is similar to that described in section 3.2.1 but without the lead cavity. The position of the ^{60}Co source relative to the detector was used to control the photon rate of the different channels. With the ^{60}Co source on the side, one channel receives a higher gamma flux than the others, which are farther away from the source. By rotating the detector between measurements, different photon rates are achieved for each of the channels. Additional data points with lower photon rates are measured with the ^{60}Co source farther away from the detector. One measurement was also conducted without the ^{60}Co source. A linear fit was made for each channel. The results of these measurements together with the fits are shown in figure 3.8a.

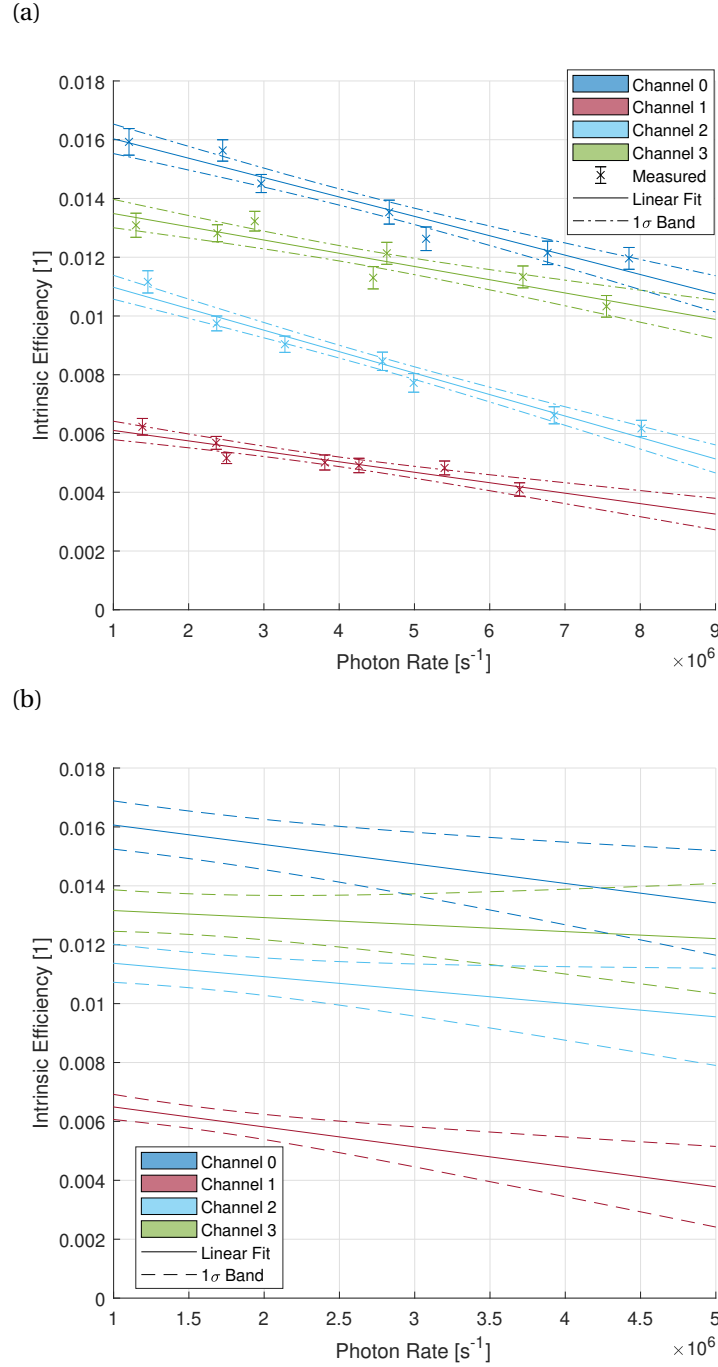


Figure 3.8: The intrinsic neutron detection efficiency as a function of the rate of photons detected by the SiPM of each channel. Shown is a linear fit as well as the band representing a single standard deviation. For (a), the efficiency measured with a ^{252}Cf neutron source and a ^{60}Co gamma source at the FNL. The measured points are shown with an error bar representing a single standard deviation. For (b), a relative efficiency was measured using neutrons and gamma rays from spent fuel at the AHL and put on an absolute scale by comparison with a measurement using a ^{252}Cf source at a photon rate of 10^6 . No measurement points are shown since it is not a direct fit of measurement data.

The efficiency varies significantly between the channels. Channel 0 is over 2.5 times more efficient than channel 1 at a photon rate of 10^6 s^{-1} . The measurement at the lowest photon rate has been repeated several times, switching the light guides and the electronics for the different channels. This did not lead to a change of the measured efficiency. The cause for the difference in the channels is therefore the detector probe. It is likely that some step in the assembly process is not well controlled and leads to variations between the different channels (e.g. formation of air bubbles during the casting process or damage to the WLSFs during assembly). The efficiency of the individual channels varies by about 30% – 40% over the measured photon rate range.

The efficiency fits can be used to determine the neutron flux for a measured count rate at a given neutron flux. However, strictly speaking, this is only valid if the neutron flux has the same spectrum as the ^{252}Cf source used to measure the efficiency.

While the photon rate is a useful quantity for checking the detector condition during a measurement, it is less useful when trying to compare it to calculations or measurements with other detectors. As stated previously, the photon rate (and even more prominently the change in the photon rate) is dominated by the gamma influence for high gamma environments. It is therefore possible to loosely associate a photon rate with a gamma spectrum and flux density at the detector. In the measurements with the ^{252}Cf and the ^{60}Co source, the gamma spectrum is almost entirely the one from the ^{60}Co source (i.e. with a roughly equal amount of gammas with an energy of 1.17 MeV and an energy of 1.33 MeV). Due to the close proximity of the ^{60}Co source to the detector, the flux density is harder to calculate and it varies significantly over the volume of a single channel. When the channel is closest to the source, the received gamma flux density is between $\sim 10^6 \text{ cm}^{-2}\text{s}^{-1}$ and $\sim 10^7 \text{ cm}^{-2}\text{s}^{-1}$, depending on the position within the sensitive volume of the channel. The photon rate scale shown in figure 3.8a can therefore loosely be thought of as representing a gamma flux density from $0 \text{ cm}^{-2}\text{s}^{-1}$ at a photon rate of 10^6 s^{-1} to a gamma flux density of $\sim 5 \cdot 10^6 \text{ cm}^{-2}\text{s}^{-1}$ at a photon rate of $9 \cdot 10^6 \text{ s}^{-1}$.

Measurement with Spent Fuel

The photon rate dependent efficiency was also measured at the PSI hot laboratory (AHL) using spent fuel, which has a different gamma spectrum from that of ^{60}Co (mainly ^{137}Cs for the fuel used here). This measurement allows investigating if there is a strong dependency of the efficiency on the gamma spectrum that is not captured by the photon rate.

These measurements were performed as part of a measurement campaign at the PSI hot laboratory. The details on this measurement campaign and the setup are presented in chapter 4. The measurement setup is the same as that of section 4.1 for the far position and the M4 spent fuel rod segment (described in section 4.2) at the axial zero position. In addition, the measurement was repeated with plates of tungsten added in front of the detector to vary the gamma flux at the detector. The thickness of tungsten used for the different measurements were 0 mm (the original setup), 5 mm, 10 mm, 15 mm, and 50 mm.

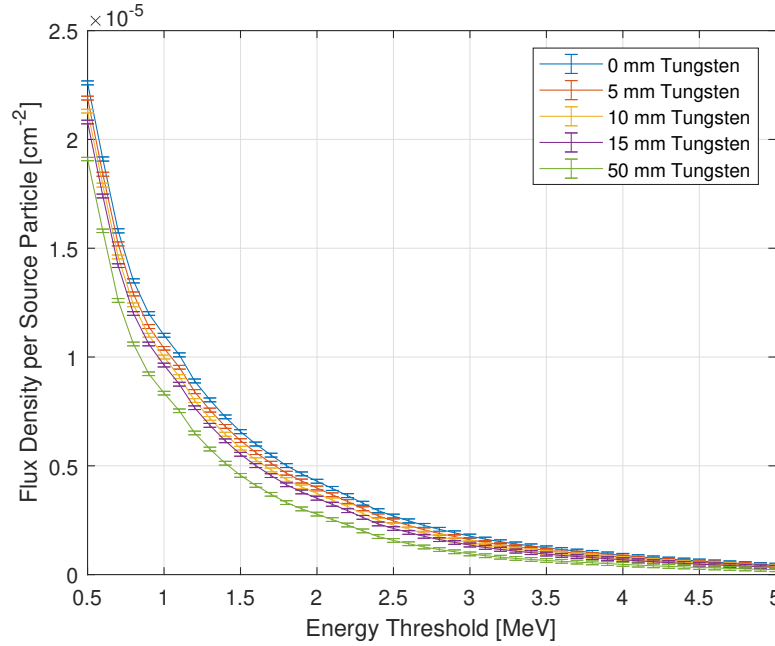


Figure 3.9: Neutron flux density through the detector above an energy threshold simulated with different thicknesses of tungsten plates in front of the detector. The error bars show a single standard deviation.

In the measurement with the ^{60}Co and the ^{252}Cf sources, the neutron flux at the detector did not change when varying the gamma intensity. Contrary to that, the tungsten filter also affects the neutron flux. To correct for this, the effect of the tungsten filter on the neutron flux was simulated using MCNP-6.2 [14] and the ENDF/B-VII.0 [47] nuclear data library. The spent fuel rod segment is assumed to contain ^{244}Cm as the only neutron emitter. The number of particles was increased up to 10^9 to yield uncertainties below 2% for the flux density integrated above a threshold of 1.5 MeV. Figure 3.9 shows the result of this simulation.

The important information to get out of this simulation is the count rate change caused by the change in the neutron spectrum and intensity. When this is known, the remaining change in the count rate can be attributed to the change in the gamma environment. To calculate the count rate from the neutron spectrum, the energy-dependent efficiency of the detector is needed. Since the neutron emission from the fuel sample is a priori unknown, the measurement can in the end only yield a relative efficiency as a function of the photon rate. The scaling of the energy-dependent efficiency used to calculate the count rate from the different simulated neutron spectra is therefore not relevant, only the shape is important. The approximation that the energy-dependent efficiency is constant above 1.5 MeV and zero for lower energies (derived in section 4.3.2) can therefore be used. The relative count rate change due to the neutron spectrum and intensity change can then directly be read from figure 3.9 as the values for an energy threshold of 1.5 MeV. The remaining change observed in the measurement is assumed to be the relative efficiency change due to the gamma influence.

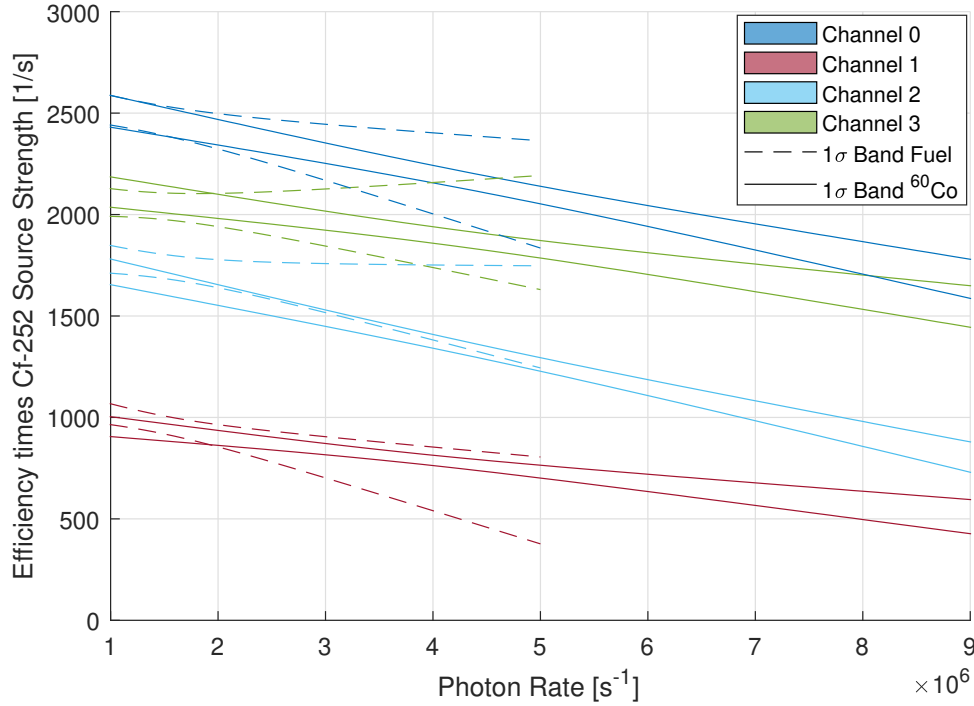


Figure 3.10: Comparison of the gamma-induced efficiency loss measured with a ^{252}Cf and a ^{60}Co source to the one measured with a spent fuel sample. Plotted is the neutron detection efficiency for a ^{252}Cf spectrum multiplied by the emission of the reference source against the rate of photons detected by the SiPM for each channel. For clarity, only the lines indicating a single standard deviation are shown.

To get an absolute efficiency, the relative efficiency was scaled to match the absolute efficiency measured with the method described in section 3.2.3 around a photon rate of 10^6 s^{-1} . At this photon rate, the influence of the gammas should be negligible as the photon rate is dominated by the dark counts and stray environment light, and the two methods should therefore be comparable. The resulting absolute efficiency is shown in figure 3.8b.

The efficiencies measured using spent fuel, and ^{60}Co and ^{252}Cf sources are compared in figure 3.10. To eliminate the influence of the uncertainty on the activity of the ^{252}Cf source (which affects both efficiency curves in the same way and would therefore make the curves appear to agree more than they actually do), the quantity which is used for the comparison is the efficiency multiplied by the ^{252}Cf source strength. The efficiencies agree well within the single standard deviation boundaries, supporting the assumption that the influence of the gamma spectrum on the detector is captured well by the photon rate.

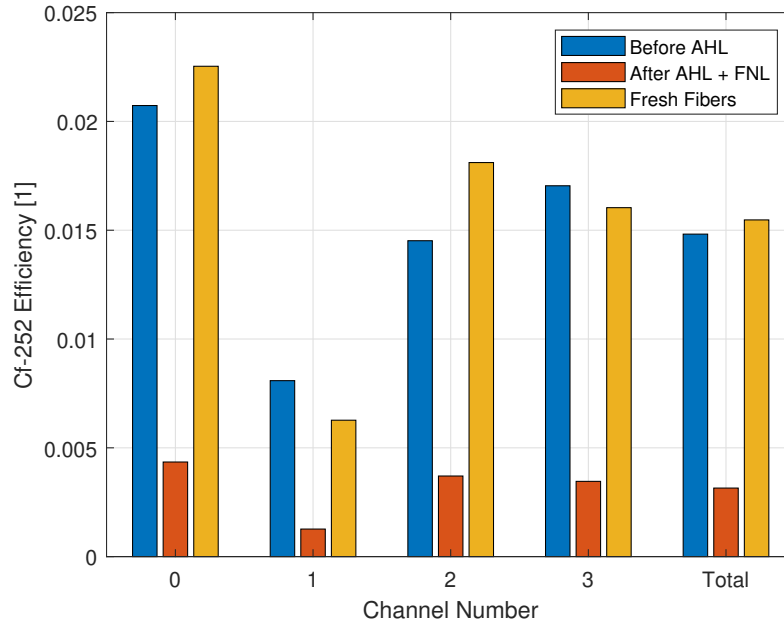


Figure 3.11: Measured intrinsic neutron detection efficiency for ^{252}Cf neutrons before the hot-lab campaign (blue), after the hot-lab campaign and additional measurements (red), and with the fresh light guides (yellow).

3.2.4 Degradation under Irradiation

During the measurement campaign at the PSI Hot-Laboratory (AHL) described in chapter 4, a drop of the detection efficiency of the detector was observed (see section 4.5 for details). An even stronger decrease of the efficiency was observed after additional measurements at the PSI Fast Neutron Lab (FNL). This is illustrated in figure 3.11 which compares the efficiency measured before and after the AHL campaign and additional FNL measurements. All three measurements used the setup described in section 3.2.3 (version without ^{60}Co source). Ionizing radiation is well known for causing damage in optical and electronic equipment. The detector efficiency degradation is therefore likely due to irradiation. The detector components in which irradiation damage is most likely to have occurred in a way which influences the working of the detector are the sensitive volume (section 2.1.1) and the light guides (section 2.1.2).

Degradation of the Light Guides

To investigate potential damage in the light guides, they were replaced with freshly manufactured ones and the measurement with the ^{252}Cf source was repeated again. The result of this measurement is shown in figure 3.11 alongside the results of the previous measurements.

The replacement of the fibers increased the efficiency significantly, raising it slightly above the efficiency measured before the campaign at AHL (~5% higher). It is hard to do a quantitative

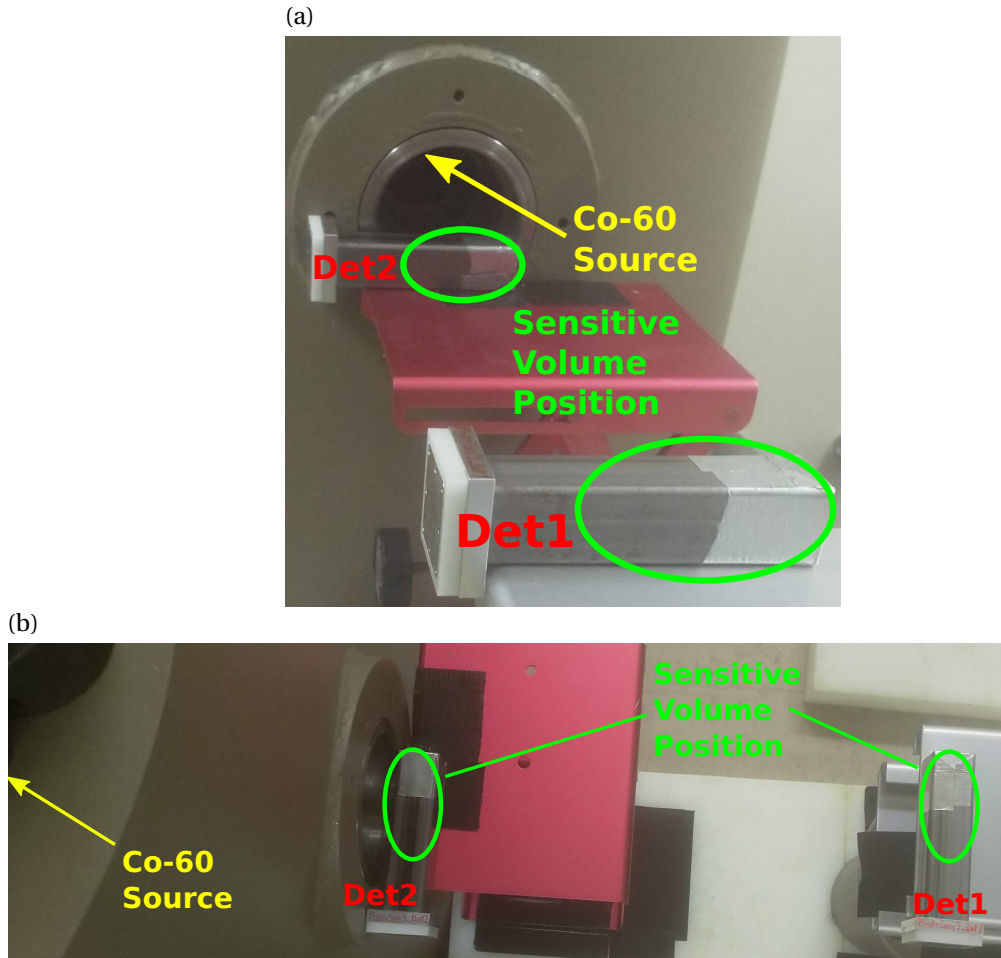


Figure 3.12: Pictures of the setup used to irradiate the detector probes in the LOTUS main cavity. While irradiation is ongoing, the ^{60}Co source is positioned inside the beige container at the position marked by the yellow arrows. Det2 was placed in such a way that the sensitive volume is completely inside the irradiation cone defined by the ^{60}Co source collimator, leaving the back of the detector probe less exposed.

analysis of the result since the light guides used in the experiment before the campaign at AHL were not fresh at the time of the measurement but already irradiated during several earlier measurements. However, it is clear that radiation damage in the light guides is a significant factor for the efficiency of the detector. For this reason, it is important to investigate possibilities for more radiation resistant fibers for future detectors.

Degradation of the Detector Probe

To investigate potential radiation damage to the sensitive volume, 5 identical detector probes were manufactured. They are simplified versions of the Hot-Lab Prototype 1, having only a single channel each (see section 2.2.3 for details). Two of these detector probes were irra-

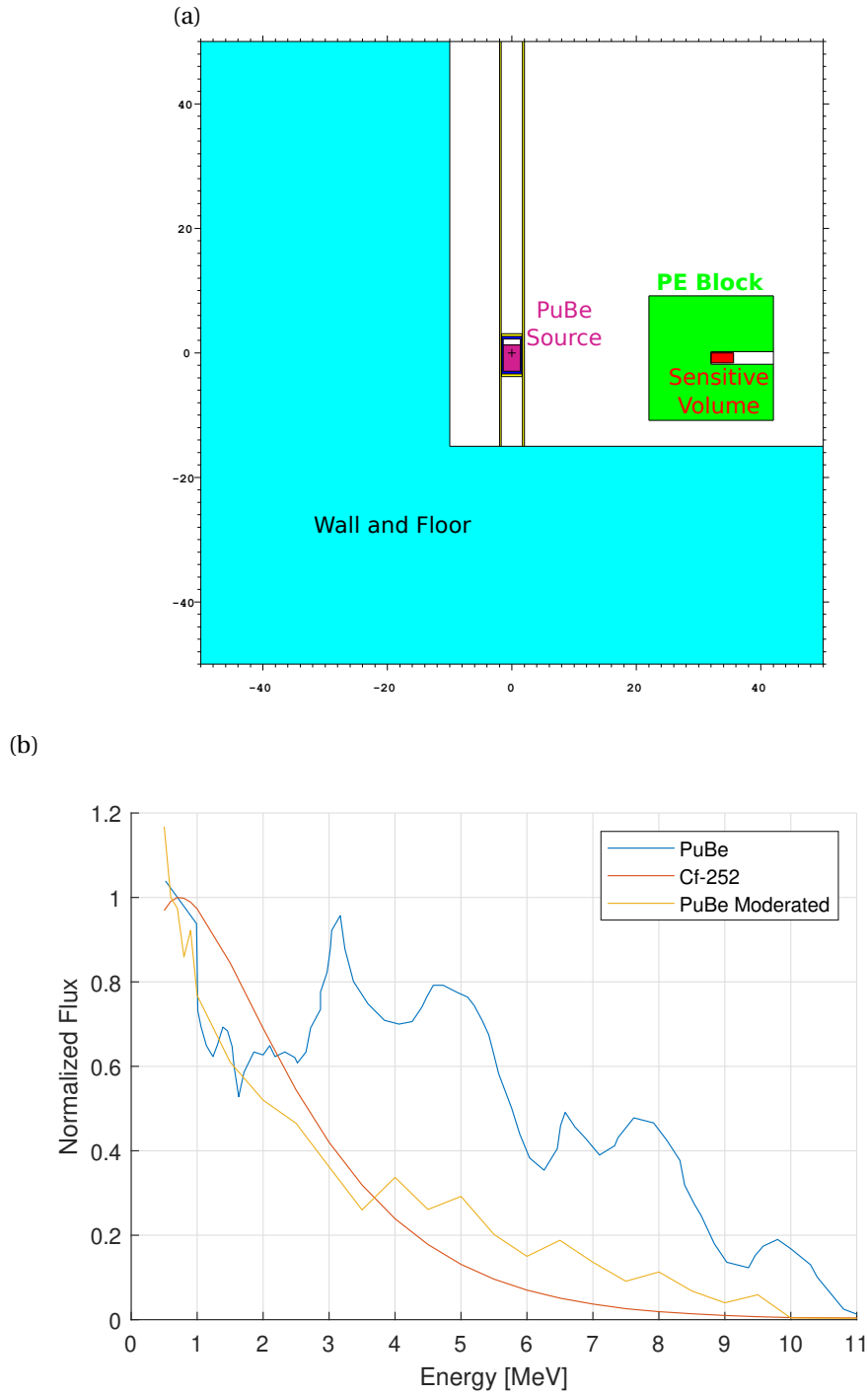


Figure 3.13: (a): Illustration of the measurement setup for the detector between irradiation sequences at LOTUS (MCNP input geometry). The distances are given on the x and y axes in cm. (b): Simulated neutron spectrum at the sensitive volume position during measurements with the PuBe source. As a comparison, the unmoderated PuBe and the ^{252}Cf spectra are shown as well. Adapted from [17].

diated with a strong ^{60}Co source at the LOTUS facility at EPFL to test if that influences the performance of the detectors.

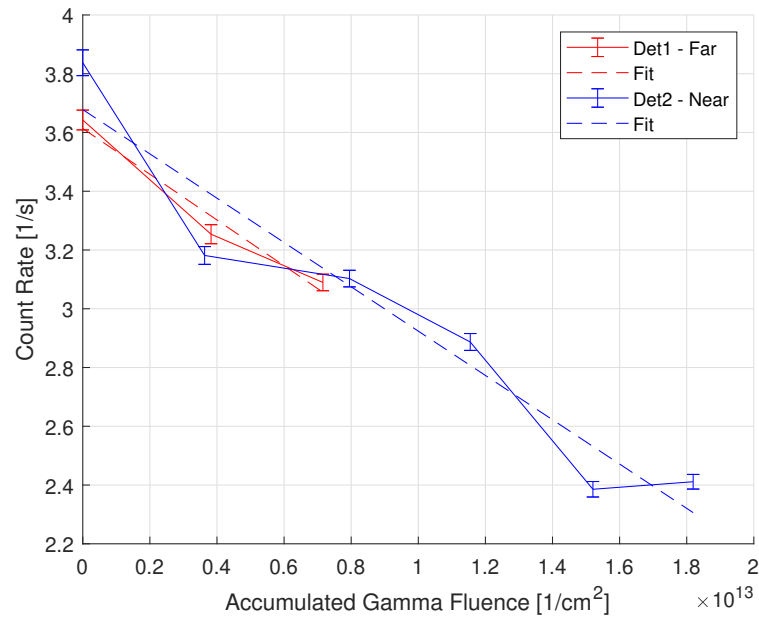
The LOTUS facility at EPFL has a cavity with a 165 GBq (at time of measurement) ^{60}Co source installed. A collimator limits the radiation to a cone inside the cavity in which objects for irradiation can be placed. The ^{60}Co source is automatically retracted into a storage position between irradiation times to avoid exposure of people setting up the experiments. The cavity housing the source is shielded by thick concrete walls. [48]

The two detector probes to be irradiated were placed in different positions inside the cavity. The first one (called Det1) was placed at a distance of 50 cm from the ^{60}Co source and the second one (called Det2) was placed directly in front of the collimator at a distance of 23 cm from the ^{60}Co source. The setup is shown in figure 3.12. Det1 was placed at a slightly higher elevation than Det2 to allow the irradiation of both detectors at the same time without having Det2 shielding Det1. Although Det2 was too close to the collimator to be entirely exposed, it was placed in such a way that the sensitive volume was completely inside the irradiation cone defined by the ^{60}Co source collimator. The sensitive volume therefore receives the full flux (and only the back of the detector probe is less exposed.)

The irradiation was carried out in short sequences with the detector probes being taken out of the cavity and their performance checked between each sequence. There was no ^{252}Cf source available at EPFL, which would have yielded the best comparability to other measurements with the detector. A PuBe source was used instead. To make the spectrum of the PuBe source closer to the spectrum of a ^{252}Cf source, the detector was surrounded with a polyethylene moderator block during the measurements with the PuBe source. An illustration of the measurement setup is shown in figure 3.13a. The setup was simulated with MCNP-6.2 [14], using the ENDF/B-VII.0 [47] library and the PuBe neutron spectrum measured in [49]. The result of this simulation is shown in figure 3.13b. The moderated PuBe spectrum resembles the ^{252}Cf spectrum better than its unmoderated output, but there is still a significant difference in the high energy tail (above ~ 4 MeV).

The measured count rates of the detectors between the irradiation segments are shown in figure 3.14a. The decrease in count rate is very similar for both detector probes for the same gamma fluence accumulated over the irradiation sequences. The count rate of Det1 decreased by about 15% at an accumulated gamma fluence of $7 \cdot 10^{12} \text{ cm}^{-2}$ at the end of the irradiation campaign, and the one of Det2 decreased by about 35% at a total gamma fluence of $18 \cdot 10^{12} \text{ cm}^{-2}$. Before and after the irradiation campaign, the neutron detection efficiency for both detector probes was measured at FNL using the ^{252}Cf source. The efficiency was measured again one month after the end of the irradiation campaign to see if there is a recovery effect. As a consistency check, a non irradiated detector probe (called Det4) is measured each time as well. The results are shown in figure 3.14b. The efficiency of the non-irradiated detector probe did not change over time, as expected. The efficiency of Det1 drops by about 30% after the irradiation campaign, which is double the effect measured with

(a)



(b)

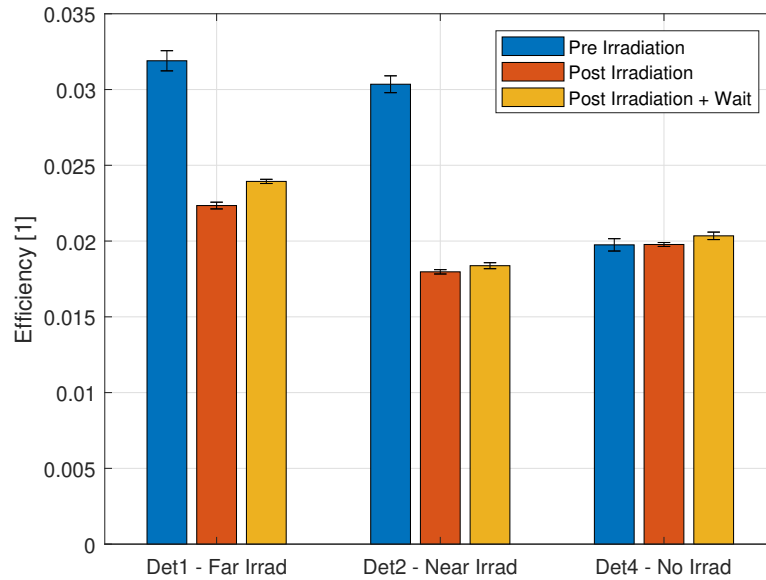


Figure 3.14: (a): Count rate recorded with the PuBe source between sequences of irradiation at LOTUS as a function of the total accumulated gamma fluence during irradiation at the detector position. The error bars mark a single standard deviation. A linear fit is provided for each detector as well. (b): Efficiency measured using the ²⁵²Cf source before and after the irradiation campaign at LOTUS as well as one month after the irradiation campaign. The error bars mark a single standard deviation (only from counting statistics). Adapted from [17].

the PuBe source. With an efficiency drop of 40%, the results from Det2 are more in line with what was measured with the PuBe source. Det1 experienced a small but noticeable recovery of efficiency after a waiting time of one month while the efficiency of Det2 did not recover.

The most likely explanation for the differences between the PuBe and the ^{252}Cf source measurements is that the change of efficiency due to irradiation is energy dependent. Theoretically, this is expected as neutron interactions that deposit more energy in the sensitive volume (which are more likely for the moderated PuBe source as it has a bigger high-energy tail than the ^{252}Cf source, see figure 3.13b) are more likely to still be detected even if some photons are lost to defects caused by irradiation. Another interesting point is the recovery seen in Det1 but not in Det2, for which no explanation was found.

The measurements show that the detector probe degrades significantly when exposed to an accumulated gamma fluence higher than 10^{12} cm^{-2} . For the use in high gamma environments it would therefore be advantageous to find solutions to reduce or eliminate this degradation. The most likely components of the detector probe to be causing this degradation are the epoxy in the ZnS:Ag-epoxy mixture and the WLSFs. For both materials, there are currently measurements being set up and conducted to test their radiation stability. It is much harder to modify these components than the light guides (see section 3.2.4). For the WLSFs, new fibers would have to be ordered and tested. For the epoxy there are some more options. The addition of radical suppressants to the epoxy could improve its radiation hardness. Another option would be to replace the epoxy completely. It could even be possible to replace it with a liquid. In this case, the ZnS:Ag grains are not fixed in their positions after detector construction. It is therefore possible that the local distribution of changes over time. One method to combat this is to have the ZnS:Ag grains in the mixture densely packed and only fill the remaining gaps with liquid. To investigate this option, tests with water, isopropyl alcohol, and ethanol were conducted. To measure the volume ratio of liquid to ZnS:Ag for densely packed grains, ZnS:Ag powder was mixed with the liquid and was left for the ZnS:Ag grains to settle. A picture of the result is shown in figure 3.15. The overall volume of the mixture increases by $\sim 0.5 \text{ ml}$ when adding the ZnS:Ag, with the region containing the ZnS:Ag grains taking up a volume of $\sim 1.5 \text{ ml}$ for all three liquids. The region containing the settled grains therefore contains about 0.5 ml of ZnS:Ag and 1 ml of liquid. This is similar to the volume mixing ratio of ZnS:Ag grain and epoxy in the current detectors. Together with the high hydrogen density in the liquids, this result suggests that detectors with liquids as recoil proton providers could achieve higher efficiencies than detectors with epoxy as a recoil proton provider. The use of liquids would be mechanically more challenging but could eliminate radiation damage almost completely.

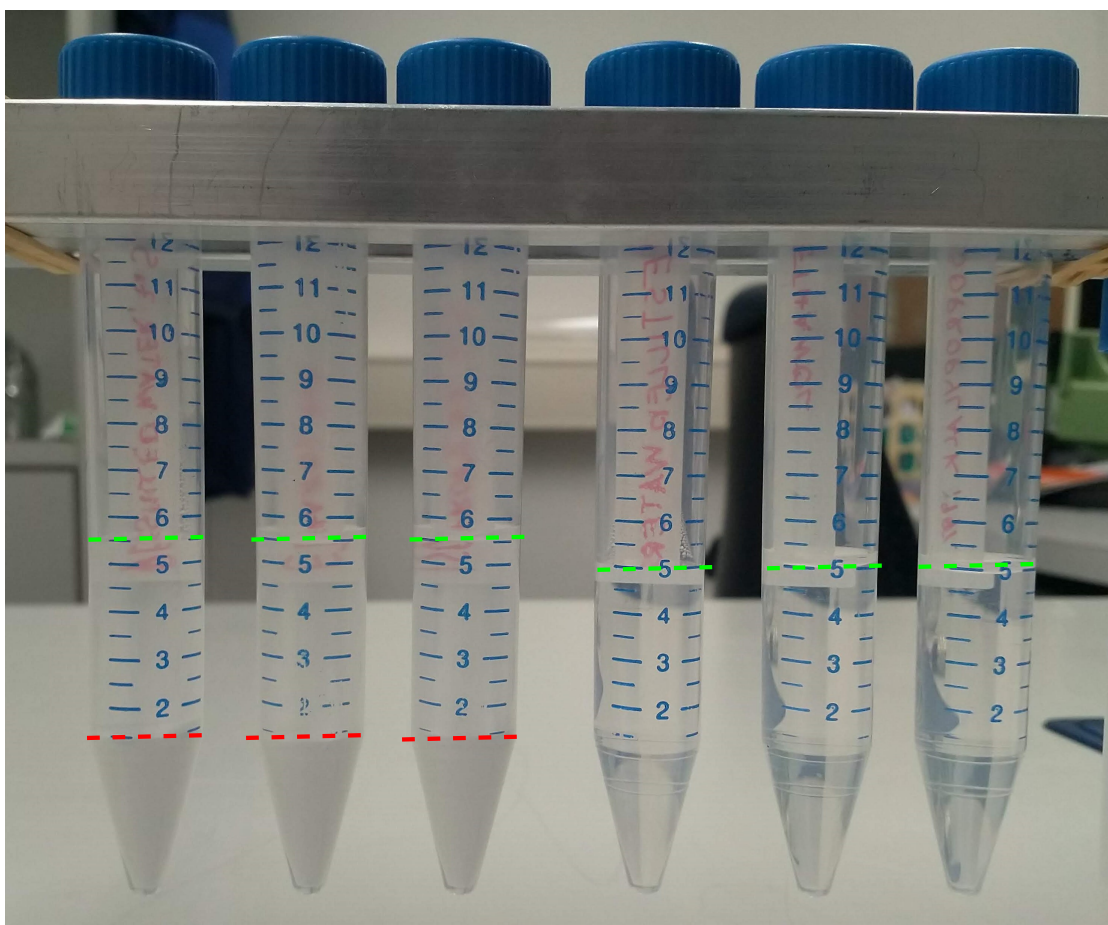


Figure 3.15: Mixing of ZnS:Ag powder in water, ethanol, and isopropyl alcohol (3 tubes on the left, from left to right). As a reference, 3 tubes with the same amount of liquid but without the ZnS:Ag powder added are shown on the right. For better visibility, the liquid level is marked in green and the level of the mixed phase is marked in red.

3.3 Performance in Low Gamma Environments

While the main target for the detector in the context of the NEWS project is to operate in a high gamma environment, the detector design is also interesting for other applications. Some of these applications, such as homeland security or fast neutron imaging, might not involve a gamma background which is as strong as during spent fuel analysis. Neutron detection efficiency is a major concern in most applications involving fast neutrons. This section aims to provide a basis on which the usefulness of the detector design for applications with low gamma background can be evaluated and investigated further.

3.3.1 Conservative Gamma Equivalence for the ^{252}Cf Source

One of the concerns when trying to measure the performance of the detector with the ^{252}Cf source is that gamma rays from the source could create false counts in the detector, making the efficiency for neutrons appear higher than it actually is. To check whether this happens, the detector can be exposed to a pure gamma environment that creates at least the same number of counts in the detector as only the gamma contribution from the ^{252}Cf source (i.e. a conservatively equivalent gamma environment to the ^{252}Cf source gamma environment). This section explains the methodology used to derive such a pure gamma environment.

The comparison between the gamma environment created by the ^{252}Cf source and the targeted pure gamma environment relies on the assumption that gamma interactions that deposit more energy in the sensitive volume of the detector are more likely to lead to a detector count. If for every gamma interaction in the ^{252}Cf source environment there is one interaction in the pure gamma environment which deposits at least the same amount of energy, the condition of creating at least the same number of detector counts in the pure gamma environment should be fulfilled. The deposited energy from gamma rays can be calculated from the ^{252}Cf source spectrum measured in section 3.1.2 and the spectrum of any pure gamma source which would be a candidate to create the pure gamma environment. For the ^{252}Cf source, only the gamma lines which were measured in section 3.1.2 (see figure 3.5 and table 3.2) are considered here.

The highest energy a gamma can deposit in the sensitive volume is its full energy via photoelectric absorption. The pure gamma environment therefore has to contain gamma rays with an energy of at least the highest gamma ray energy of the ^{252}Cf source. Since the ^{252}Cf source does not emit significant quantities of gamma rays above the 662 keV line of ^{137}Cs , a ^{137}Cs source would be a good candidate to create the pure gamma environment. Since in that case all gamma energies are below 1.022 MeV, pair production is not possible and the only gamma interactions which deposit energy in the sensitive volume are photoelectric absorption and Compton scattering. Disregarding edge effects, the deposited energy resulting from photoelectric absorption is always the full gamma energy and the deposited energy from Compton scattering can be approximated using energy-momentum conservation and the

Klein-Nishina formula [50] (differential scattering cross-section for a free electron):

$$E'_\gamma(\theta) = E_\gamma \cdot \frac{1}{1 + \frac{E_\gamma}{m_e c^2} \cdot (1 - \cos(\theta))} \quad (3.5)$$

$$\frac{d\sigma}{d\Omega} = \frac{1}{2} \alpha^2 \bar{\lambda}_c^2 \cdot \left(\frac{E'_\gamma(\theta)}{E_\gamma} \right)^2 \left(\frac{E'_\gamma(\theta)}{E_\gamma} + \frac{E_\gamma}{E'_\gamma(\theta)} - \sin(\theta)^2 \right) \quad (3.6)$$

Here, E_γ is the initial energy of the incoming gamma ray, m_e is the electron mass, c is the speed of light, θ is the scattering angle, $E'_\gamma(\theta)$ is the resulting energy of the outgoing gamma ray, α is the fine structure constant, $\bar{\lambda}_c = \frac{h}{m_e c}$ is the reduced Compton wavelength of the electron (with h the reduced Planck constant), and $\frac{d\sigma}{d\Omega}$ the differential scattering cross-section.

Summing up the Compton scattering and photoelectric absorption contribution for all gamma lines, an interaction rate distribution $r_X(E_D, d)$, where $r_X(E_D, d)dE$ is the rate of gamma interactions caused by the source X (^{252}Cf or ^{137}Cs source) at a distance d to the detector and depositing an energy in the infinitesimal range between E_D and $E_D + dE$, is calculated. Here, a 1D approach using the flux generated by the source at the distance to the center of the sensitive volume is used for the calculation of the interaction probabilities. This means that multi-scattering and variation of the flux density inside the sensitive volume due to different distances to the source is disregarded, but self-shielding is taken into account.

For the comparison of the ^{252}Cf and the ^{137}Cs environment, the total rate $R_X(E_D, d)$ of interactions depositing more than E_D in the sensitive volume is calculated for every energy E_D .

$$R_X(E_D, d) = \int_{E_D}^{\infty} r_X(E, d) dE \quad (3.7)$$

The result for the ^{252}Cf source at 10.5 cm and for a 2.1 MBq ^{137}Cs source at 7.5 cm is shown in figure 3.16. As can be seen, the interaction rate with the ^{137}Cs source is at least as high as the one with the ^{252}Cf source for every minimum energy deposited E_D in the sensitive volume. This is exactly the requirement to ensure at least the same count rate in the ^{137}Cs environment as only from the gammas in the ^{252}Cf environment that was introduced above. For comparison: the radiation of the ^{137}Cs source corresponds to a dose rate of about $20 \mu\text{Sv/h}$, which is about 200 times average natural background radiation.

3.3.2 Measurement Setup

Three measurements were carried out to determine the neutron detection efficiency in low gamma environments. The first one was a measurement with the ^{252}Cf source in front of the detector at a distance of 10.5 cm. This is the same setup as previously used for the measurements in high gamma environments and shown in figure 3.7b. The second one was with the ^{137}Cs source 7.5 cm away from the detector, as determined in section 3.3.1. This setup is shown in figure 3.17. The last one was a background measurement with no sources

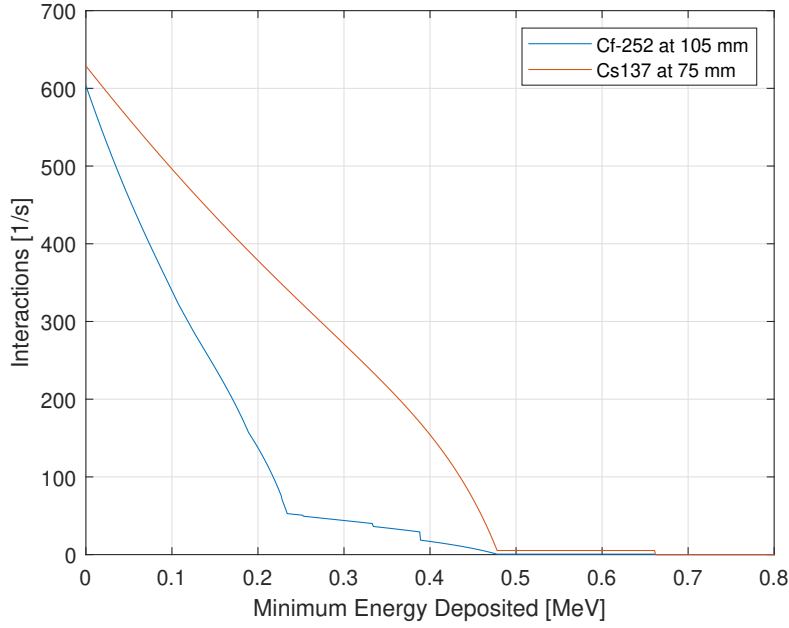


Figure 3.16: For every energy the number of gamma interactions which deposit at least this amount of energy in the sensitive volume is plotted. The line for the ^{137}Cs source at 7.5 cm distance is always at least as high as the one for the ^{252}Cf source at 10.5 cm distance. Adapted from [17]

present. To minimize the number of measurements while trying out several MSD settings, the MSD algorithm was performed in post processing. As such the logic analyzer setup (see section 2.3.2) was used.

3.3.3 MSD Parameter Optimization and Efficiency

The gathered data was analyzed in post processing to find a good choice of parameters. The data sets are too large and the possible parameter combinations too extensive to test all combinations with a reasonable use of computational resources. Instead, a custom variant of the hill climbing algorithm was employed (see section 2.4.1 for details). The optimization target for the algorithm was set to the highest count rate during the measurement with the ^{252}Cf source while neither the count rate during the ^{137}Cs measurement nor the one during the background measurement is allowed to be higher than 1% of the counts with the ^{252}Cf source. The initial start point was set to $\Delta t = 400$ ns, $m = 5$, $k = 35$, and $\delta t_B = 10$ μs , which is known from previous measurements (see section 3.2.3) to produce good results. The algorithm was allowed to change all of the parameters except δt_B . A blocking time of 10 μs should not have a significant impact on the measured count rate and allowing the algorithm to reduce it would risk counting some events more than once.

The best parameter combination the algorithm found was $\Delta t = 195$ ns, $m = 42$, and $k = 30$. The

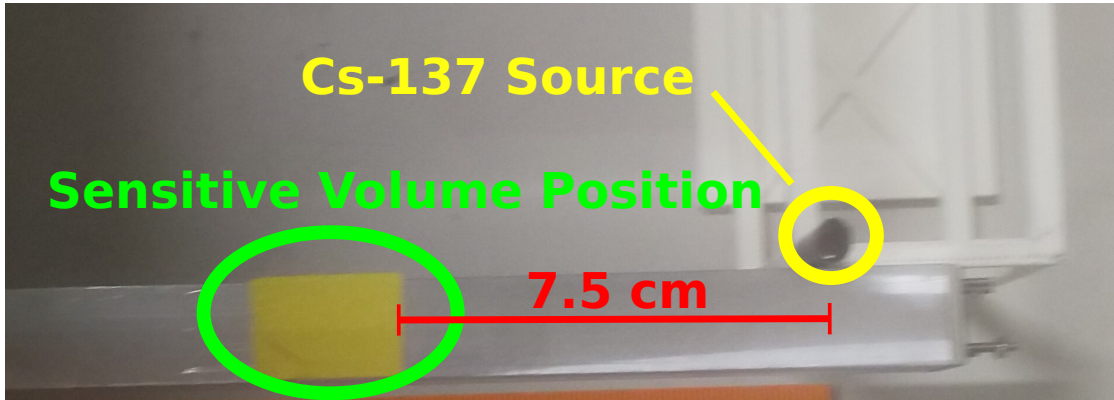


Figure 3.17: Measurement to determine the possible influence of the ^{252}Cf source gammas by a conservatively equivalent ^{137}Cs setup. The ^{137}Cs source had to be placed on the side of the detector to reach a distance of 7.5 cm due to the detector geometry. Adapted from [17]

Channel	cps ^{252}Cf	cps ^{137}Cs	cps Background	Efficiency
0	1.91 ± 0.3	< 0.001	0.040	$13.5\% \pm 0.2\%$
1	1.10 ± 0.2	< 0.001	0.022	$7.8\% \pm 0.2\%$
2	1.70 ± 0.3	< 0.001	0.0025	$12.0\% \pm 0.2\%$
3	1.75 ± 0.3	< 0.001	< 0.001	$12.4\% \pm 0.2\%$
Average	1.618 ± 0.013	< 0.001	0.016	$11.42\% \pm 0.09\%$

Table 3.6: Results of the measurements in low gamma environment. The errors indicate a single standard deviation. The error on the intrinsic efficiency only accounts for the error due to counting statistics. Adapted from [17]

results using this combination are shown in table 3.6. The count rate for either the ^{137}Cs or the background measurement does not exceed 2% of the count rate during the ^{252}Cf measurement for any given channel. Averaged over all channels, the count rate for either the ^{137}Cs or the background measurement does not exceed 1% of the count rate during the ^{252}Cf measurement (as required by the optimization target). The overall intrinsic efficiency (neutron counts per neutron entering one of the detector channels) is high at 11.42%. The fact that the background and ^{137}Cs count rates can reach up to 1% of the ^{252}Cf count rate reduce the 11.42% efficiency by 0.1% at most. Similar as for the previous results shown in section 3.2.3, significant differences between the channels can be observed with channel 0 having the highest efficiency and channel 1 the lowest.

The reason why the count rate during the background measurement was higher than the one during the ^{137}Cs measurement is unclear. Intuitively, the count rate should have been lower during the background measurement. A difference in environmental light or temperature could explain this trend (as the measurements were performed several months apart). It would be good to repeat these measurements in direct succession and paying attention to these potential influences on the measurement. If the count rate really declined due to the

introduction of extra gamma rays from the ^{137}Cs , the premise of the gamma equivalence calculation for the ^{252}Cf source in section 3.3.1 would be invalid.

3.4 Performance for Timing Applications

Some applications such as coincidence, time of flight, and neutron noise measurements require precise timing information for individual neutron events. The exact requirements vary greatly between different applications. It is nevertheless interesting to investigate the achievable timing precision of the detector, which is the purpose of this section.

Section 3.4.1 describes the metric used to measure the timing accuracy and explains how the MSD parameters were optimized. The interpretation of the physical meaning of the achieved timing accuracy is presented in section 3.4.2. In section 3.4.3 a measurement using the high timing accuracy to determine the shape of the decay of the scintillation light from ZnS:Ag is presented.

3.4.1 MSD Parameter Optimization

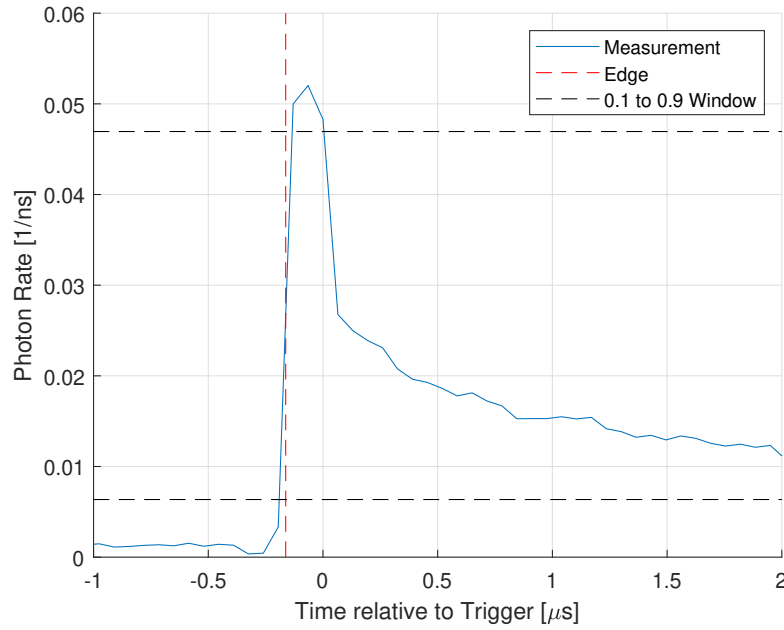
The data gathered during the measurement described in section 3.3.2 is used again. A custom hill climbing algorithm (see section 2.4.1 for details) is used for the analysis. The optimization target for the hill climbing algorithm is set to an estimate of the timing precision for the events. The timing precision is estimated by averaging the shape of all recognized events and calculating the time it takes for the rising edge to go from 10% to 90% of the peak value. This is illustrated in figure 3.18a.

The best results were obtained with an MSD setting of $\Delta t = 65 \text{ ns}$, $m = 3$, $k = 9$, and $k_B = 10 \mu\text{s}$ (see section 2.1.3). With this setting, the 10% to 90% rise time of the averaged event shape (shown in figure 3.18a) was 57 ns.

3.4.2 Timing Accuracy Interpretation

If the time of the neutron interaction with the sensitive volume would be known without any uncertainty for every event, it would be possible to average the event shape (density of pulses from the SiPM) relative to this known neutron interaction time. This is illustrated in figure 3.19a. For this discussion, it is assumed that the resulting average event shape has an infinitely sharp rising edge (more on this below). The time when the trigger occurs will have some kind of distribution relative to the neutron interaction time. If the time of the trigger is fixed instead, the time of the neutron interaction is distributed (relative to the trigger time) according to a mirrored version of the distribution of the trigger time before. This is illustrated in figure 3.19b. The distribution of the neutron interaction time relative to the trigger is the description of the timing accuracy we are interested in.

(a)



(b)

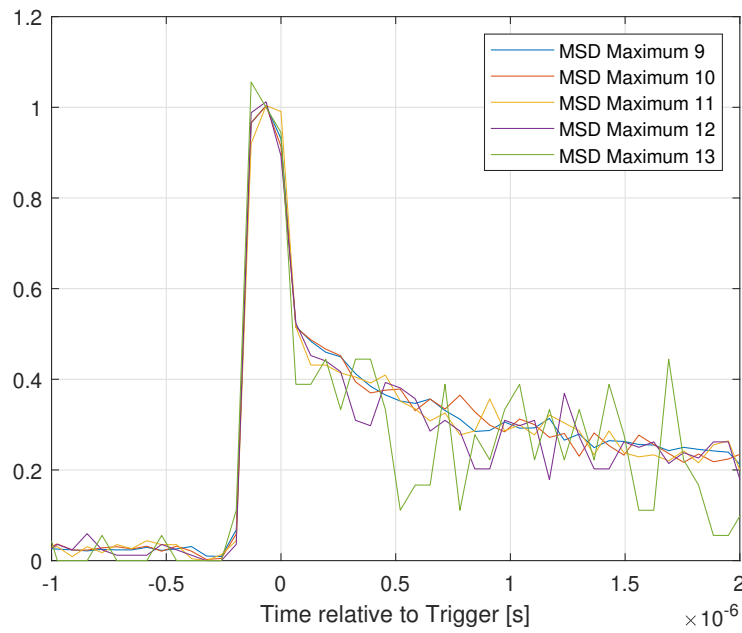


Figure 3.18: (a): Average pulse shape of the events focused on the region of the rising edge. Also shown is the center of the rising edge and the 10% to 90% window used to estimate the timing precision. (b): Normalized average event shapes for different MSD maximum values.

In reality, we do not know the interaction time of the neutron, and it is therefore impossible to directly extract the desired information. However, the average event shape is deformed when switching from averaging relative to the neutron interaction time to averaging relative to the trigger, as illustrated in figure 3.19. Assuming that the individual event shapes that were averaged are uncorrelated with the difference between neutron interaction time and trigger of the corresponding event, the deformation that occurs is simply a convolution with the distribution of the neutron interaction time relative to the trigger. If the average event shape relative to the neutron interaction time is known, it can be used in a deconvolution to extract the neutron interaction time distribution.

In reality, the average event shape relative to the neutron interaction time is not known. However, it can be estimated by (1) assuming that the neutron interaction time relative to the trigger follows a Gaussian distribution, (2) assuming that the average event shape relative to the neutron interaction time has an infinitely sharp rising edge, and (3) making an educated guess about the decay tail after the sharp rising edge (from the measured event shape shown in figure 3.18a). The result of this estimation is a Gaussian distribution of the neutron interaction time relative to the trigger where the 57 ns measured as the 10% to 90% rise time represents the $\pm 1\sigma$ region of the distribution. This means that a fraction of ~ 0.7 of all neutron interactions occur within a 57 ns window relative to the trigger.

It should be noted that if instead of the educated guess for the decay tail of the average event shape all possible decay shapes are considered, the 57 ns interval corresponds to $\pm x \cdot \sigma$ region of the Gaussian distribution where x is between 0.9 and 1.3. The assumed decay shape does therefore not have a large impact on the result.

As a check, the estimated fraction of ~ 0.7 of neutron events within the 57 ns time window can be compared to the maximum possible fraction of neutron events that could be within this time window. With the chosen MSD setting, the trigger for an event can only occur every $\Delta t = 65$ ns. Since the neutron interactions with the detector are not correlated with this discretization in time, the maximum fraction of neutrons in the 57 ns time window is 0.87. A fraction of ~ 0.7 is therefore possible.

Two major assumptions were made for the derivation of this result. The first one is the choice of the average event shape relative to the neutron interaction time, and especially its infinitely sharp rising edge. The second assumption is that the shape of a single event is not correlated with the timing precision of that particular event. Both of these assumptions are violated in reality.

The de-excitation of the ZnS:Ag scintillator happens via a chain of events. The average light output from ZnS:Ag therefore has some finite rise time. The rise time is further increased by the de-excitation of the dye in the WLSFs and to some limited extent by the path length difference for different scintillation photons. The detector electronics introduces additional deformation of the signal, but in a way which is less directly linked to the fundamental working principles of the detector and therefore can be changed more easily. The first assumption is

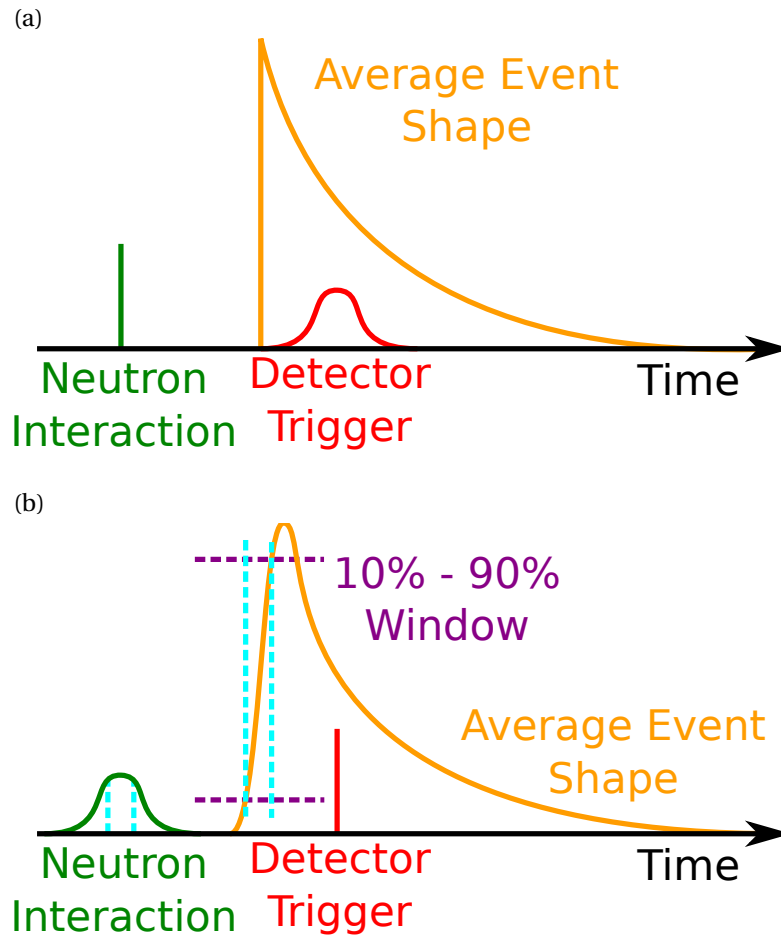


Figure 3.19: (a): Illustration of the average event shape and distribution of trigger times relative to the neutron interaction time. The timing difference between the neutron interaction and the rising edge of the average event shape is exaggerated for clarity. Most likely, this timing difference is negligible. (b): Average event shape and distribution of neutron interaction times relative to the trigger time. The deformation of the average event shape when compared to (a) leads to a finite rise time (indicated by cyan dashed lines). This rise time corresponds to a certain section of the neutron interaction time distribution.

therefore violated. However, a finite rise time would make the timing accuracy determined above worse than the actual timing accuracy (i.e. it would still be valid as a conservative estimate).

Far more serious is the violation of the second assumption. The shape of any individual event is exactly what is used by the algorithm to produce a trigger. The individual event shape therefore is almost certainly correlated with the timing precision of the corresponding event. Since the MSD algorithm is likely to favor earlier detection of events where more light is detected at the beginning of the event, this effect makes the timing precision appear better than it actually is. It therefore does not allow the measured timing precision to be used as an upper bound. This effect is also expected to favor earlier and more precise detection of stronger events (i.e. events that generate more photons that are detected by the SiPM). The impact of this effect might therefore be investigated by looking at events of different strengths. The average event shapes for different event strengths (estimated by the maximum of the MSD) is shown in figure 3.18b. No significant difference between the shapes of different event strengths is visible. While this is not a definite proof that the individual event shape variation has a negligible effect on the timing accuracy, it is an indication that the effect is not strong enough to dominate the result.

In the future, one could perform measurements of the timing accuracy in which the intrinsic rise time effect and the individual event shape variation effect are not relevant. This could for example be achieved by a coincidence measurement of two neutrons emitted at the same time by a ^{252}Cf spontaneous fission event. A detector which has a very good timing accuracy (such as some plastic scintillator detectors) could be used as the second detector in this case to provide a reference trigger against which the trigger of the detector under investigation can be measured.

3.4.3 ZnS:Ag Light Output Decay

The precise timing of the detector allows the measurement of the shape of the ZnS:Ag scintillator light output decay including fast components (decay time of ~ 100 ns). The measured decay tail including a 5-exponential fit is shown in figure 3.20. The coefficients for the 5-exponential fit are shown in table 3.7.

3.5 Crosstalk Between Nearby Fibers

To optimize the detector sensitive volume, it is advantageous to know how the scintillation light travels from the ZnS:Ag to the surrounding WLSFs. This is especially important if the surrounding WLSFs do not all belong to the same channel and their light therefore ends up at different SiPMs. Such situations occur more frequently for detectors with smaller and more densely packed channels (as in this case a higher fraction of the WLSFs will be close to WLSFs of other channels). This section tries to estimate the behavior of light in the sensitive volume

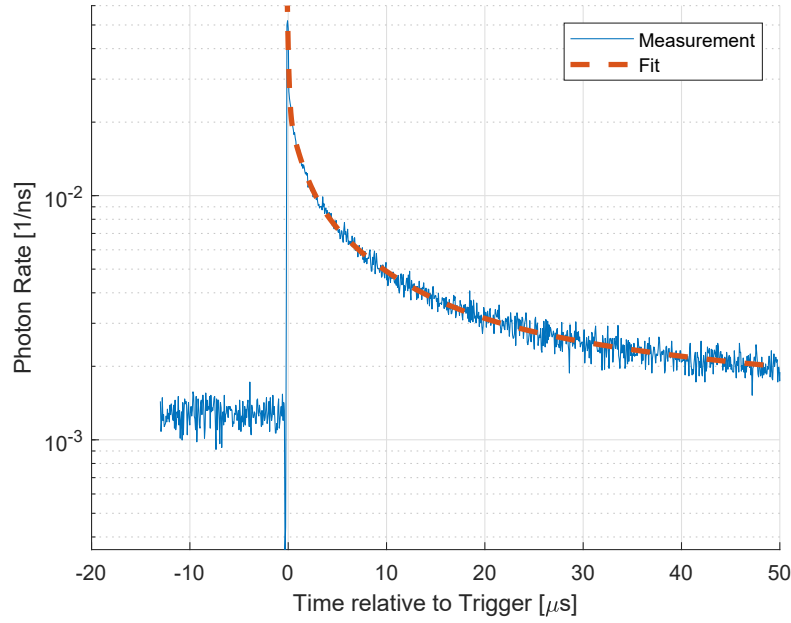


Figure 3.20: The measured average pulse shape of the events. A 5-exponential fit for the tail region is shown as well.

Decay Constant (λ_i) [μs^{-1}]	Amplitude (a_i) [ms^{-1}]
0.0054 ± 0.0006	0.023 ± 0.004
0.036 ± 0.004	0.15 ± 0.02
0.16 ± 0.02	0.46 ± 0.03
0.76 ± 0.07	0.68 ± 0.03
8.3 ± 0.3	4.21 ± 0.11
0 (Background)	1283.6

Table 3.7: The values for fit parameters used to approximate the photon rate decay of the events. The fit function used is $f(t) = \sum_{i=1}^5 (a_i \cdot e^{-\lambda_i t}) + b$ with t being the time relative to the center of the rising edge. The background b is not a fit parameter but instead is deduced from the average photon rate away from the events. The given uncertainties represent the 95% confidence interval. The R^2 value of the fit is 0.98. Adapted from [17]

by measuring the crosstalk between channels. Here, crosstalk is considered to be between the counts of different channels, not between the photons captured by the WLSFs of different channels.

There are two main reasons for trying to build detectors with smaller channels. The first one is that smaller channels reduce gamma pile-up and therefore can help with operating the detector at a stronger gamma background. In this case a dense WLSFs packing is desirable to minimize dead volume between the channels. Here, the main concern with having the light from a single event traveling to WLSFs of different channels, is that the individual channels capture less light from individual neutron events. Some neutron events that would have been detected if all the light had traveled to WLSFs of a single channel might therefore not be detected. It is also not desirable to simply combine the light of multiple channels when looking for neutron events, as this would negate the gamma influence reduction that is the reason for the smaller channels. The second reason for smaller and more densely packed channels is the potential to use multi-channel detectors in imaging applications. In this case, the target is to enhance the spatial resolution. If scintillation light of a single event is shared between channels, this can lead to crosstalk. Having strong crosstalk between a large number of detector channels limits the resolution improvements that can be achieved by reducing the channel size further (although some amount of crosstalk is usually desirable to allow sub pixel resolution).

This section presents a crosstalk measurement for individual WLSFs in close proximity to each other. The results can be used to estimate the effects mentioned above and help with the design of new sensitive volumes.

3.5.1 Measurement Setup

A specifically designed detector was used for the crosstalk measurement. The detector consists essentially of four channels, each channel having only a single WLSF. These four channels are placed directly adjacent to each other. Details on the specifications and construction can be found in section 2.2.4. The detector was exposed to a ^{252}Cf source (see section 3.1). The arrangement is shown in figure 3.21. The MSD setting used during the measurement were $\Delta t = 400 \text{ ns}$, $m = 5$, $k = 35$, and $\delta t_B = 10 \mu\text{s}$ (the same as for the high gamma environment analysis in section 3.2). The timestamps of the registered events were saved to allow identification of coincidences.

3.5.2 Results and Discussion

The number of coincidence counts between the channels was estimated using the Pearson correlation formula. The channels were compared pairwise to each other, each time calculating the correlation for different time offsets between the channels to allow for slight imperfections in the timing accuracy of the event detection. The formula for the correlation



Figure 3.21: Picture of the measurement setup used to measure the crosstalk between individual WLSFs.

Channel	Counts	Count Rate	Occupied Interval Fraction
0	12386	0.67 s^{-1}	$0.27 \cdot 10^{-6}$
1	16858	0.92 s^{-1}	$0.37 \cdot 10^{-6}$
2	17533	0.95 s^{-1}	$0.38 \cdot 10^{-6}$
3	18498	1.01 s^{-1}	$0.40 \cdot 10^{-6}$

Table 3.8: Time-averaged values for the individual channels during the crosstalk measurement. The occupied interval fraction is the fraction of all intervals of length Δt in which events were recognized by the MSD algorithm.

$\rho_{v,w}(\Delta i)$ between the two channels v and w with a time offset of Δi intervals (see section 2.1.3 for the definition of the intervals in the MSD algorithm) is given in equation 3.8.

$$\rho_{v,w}(\Delta i) = \sum_i \frac{(s_v(i) - \mu_v) \cdot (s_w(i + \Delta i) - \mu_w)}{N \sigma_v \sigma_w} \quad (3.8)$$

$$n_u = \sum_i s_u(i) \quad (3.9)$$

$$\mu_u = \frac{n_u}{N} \quad (3.10)$$

$$\sigma_u = \sqrt{\frac{n_u \cdot (1 - \mu_u)^2 + (N - n_u) \cdot \mu_u^2}{N}} \quad (3.11)$$

Here, $s_u(i)$ is 1 if an event has been detected by the MSD algorithm on channel u in the interval number i . The sum over i only goes over the interval numbers for which all the outputs of all channels is valid (this depends on Δi), with N as the number of these valid intervals. The total number of counts n_u , the channel average μ_u , and the standard deviation σ_u of a channel u are defined in equations 3.9, 3.10, and 3.11.

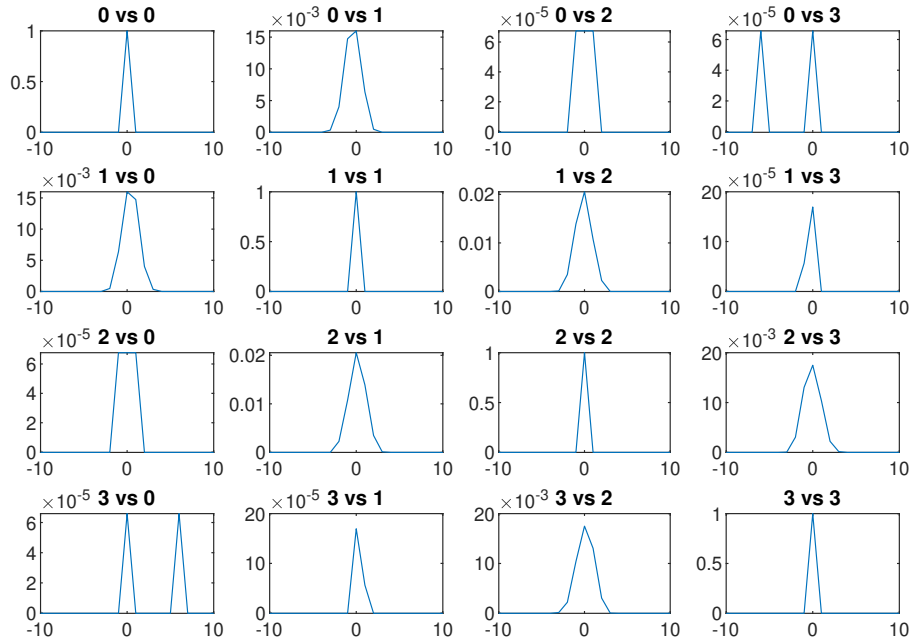


Figure 3.22: Correlation of neutron events measured in individual fibers. Every plot contains the correlation between two fibers with the x -axis being the number of intervals between the trigger of coincident events and the y -axis being the Pearson correlation coefficient.

The resulting correlations for all channel combinations are shown in figure 3.22. For easier interpretation of the results, equation 3.8 can be simplified when using the approximation that the count rate is equal on all channels and that the fraction of intervals in which events are detected is small: $n_v = n_w \ll N$.

$$\begin{aligned}
 \rho_{v,w}(\Delta i) &= \frac{1}{N\sigma_v\sigma_w} \sum_i s_v(i)s_w(i+\Delta i) - s_v(i)\mu_w - s_w(i+\Delta i)\mu_v + \mu_v\mu_w \\
 &= \frac{1}{N\sigma_v\sigma_w} \left(\left(\sum_i s_v(i)s_w(i+\Delta i) \right) - 2\frac{n_v n_w}{N} + \frac{n_v n_w}{N} \right) \\
 &= \frac{1}{N\sigma_v\sigma_w} \left(\left(\sum_i s_v(i)s_w(i+\Delta i) \right) - \frac{n_v n_w}{N} \right) \\
 &\approx \frac{1}{n_v} \left(\left(\sum_i s_v(i)s_w(i+\Delta i) \right) - \frac{n_v^2}{N} \right) \\
 &= \frac{1}{n_v} \left(\sum_i s_v(i)s_w(i+\Delta i) \right) - \frac{n_v}{N}
 \end{aligned} \tag{3.12}$$

The first part is the fraction of events on one of the channels which are coincident with events on the other channel. Subtracted from that is the fraction of intervals occupied by events. If the fraction of occupied events is small, this is approximately the probability of events being coincident assuming completely uncorrelated channels. The correlation coefficient ρ can therefore be interpreted as roughly the fraction of events which are coincident above the level of coincidence expected from randomness.

The correlation of 1 without any timing difference is expected when comparing one channel to itself (plots on the main diagonal in figure 3.22). The correlation between adjacent fibers (plots adjacent to the main diagonal in figure 3.22) is significant but not high. The results are equivalent to about 4% to 5% of the counts in any given fiber also being measured in the fiber right next to it. The correlation between fibers which are farther away is small. The results in figure 3.22 only represent a few counts which were coincident over the entire measurement. Apart from some residual crosstalk between fibers at these distances, these counts could also be random coincidences, the result of multiple neutrons being released from a single spontaneous fission event in the source, or the result of multi-scattering in the sensitive volume.

The results demonstrate that the individual WLSFs that have centers separated by 0.7 mm operate relatively independently. It is therefore expected that reducing the number of WLSFs in a channel while keeping a 0.7 mm pitch between the fibers (i.e. reducing the channel size) only has a small impact on the intrinsic detection efficiency, even when considering the extreme case of a single fiber per channel. For imaging applications, it would probably be desirable to move the WLSFs closer together to take better advantage of the possibility for sub-pixel resolution. It is important to keep in mind that this result depends on the MSD setting, which could also be optimized for a specific targeted application.

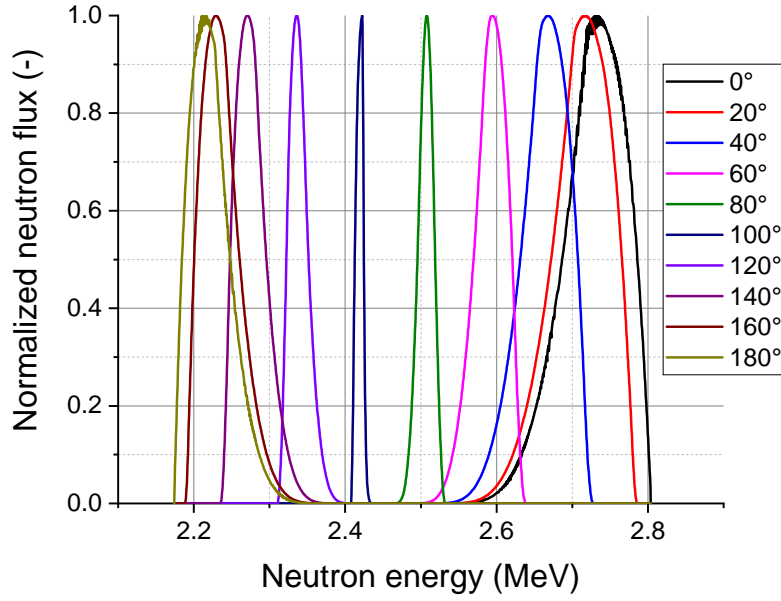


Figure 3.23: Simulation of the neutron generator spectra at different angles relative to the forward direction. A deuterium ion impact energy of 80 keV is assumed here. Adapted from [51].

3.6 Energy-Dependent Efficiency Measurement

The response of the the detector to neutrons of different energy is an important characteristic. It is important when comparing measurements for which the neutron spectrum is different, but can for example also help to estimate how efficiently the detector can be used in an application with a known spectrum. With respect to the application of spent fuel measurements, there is for example the question of the difference between a reference ^{252}Cf source spectrum and the spent fuel spectrum for the detector (see also section 4.3.3), or how to arrange moderator materials for effective neutron collimation (see also section 5.2.1). This section gives an overview of a measurement system developed to measure the energy-dependent efficiency of the detector. The system was developed in the context of a semester project by Vincent de Buys, which I co-supervised. For details on the development, characterization, construction, and use of the measurement system, the reader is referred to the semester work thesis [52].

The measurements rely on the fast neutron generator at the PSI Fast Neutron Lab (FNL). This generator uses deuterium-deuterium fusion to produce neutrons (see equation 3.13).



The fusion reaction is initiated by accelerating deuterium ions up to a set energy (usually between 80 keV and 100 keV) such that they impact a titanium target which is loaded with

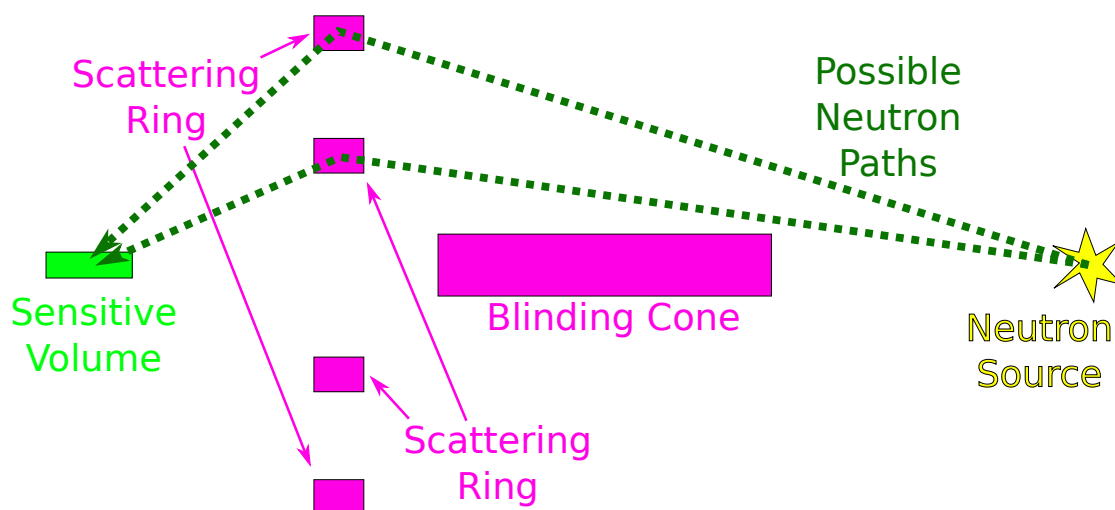


Figure 3.24: Illustration of the functioning of the scattering rings. Two scattering rings are shown for illustration purposes, there are never multiple rings present at the same time during a measurement. The blinding cone blocks the direct path to the sensitive volume, leaving mostly neutrons which scattered from the scattering ring into the sensitive volume.

deuterium at the surface by the incoming deuterium beam. Since the center of mass frame for the fusion reaction is not the same as the lab frame, the energy of the neutron which is released in the reaction depends on the emission direction, relative to the traveling direction of the deuterium nuclei hitting the target. The highest neutron energy is achieved in the forward direction where the neutron is emitted in the same direction as the deuterium nuclei was traveling (~ 3 MeV). With an increasing emission angle (relative to the forward direction) the neutron energy steadily decreases, reaching its minimum at 180° (~ 2 MeV). Figure 3.23 shows the neutron spectra at different angles. [51, 53, 54]

By exposing the detector to the generator flux at different angles, the neutron detection efficiency in the region between ~ 2 MeV and ~ 3 MeV can be measured directly (with an energy resolution better than 200 keV). An investigation of energies lower than this region is more difficult. In order to obtain information on the lower energies with the same neutron source, a technique involving scattering rings has been developed. This is illustrated in figure 3.24. The direct flux from the neutron generator to the sensitive volume is blocked by a 20 cm thick blinding cone in this configuration. The scattering ring is made of polyethylene and was placed between the the sensitive volume and the generator. The rings used had outer diameters between 12 cm and 24 cm. Neutrons can scatter off the hydrogen inside the polyethylene. For the scattered neutrons to hit the sensitive volume (ignoring the possibility of further scattering), they have to scatter in a specific angle defined by the size and position of the ring. Since the generator produces neutrons of a specific energy at every angle, the energy of the neutrons reaching the sensitive volume is fully defined by this initial energy and the scattering angle.

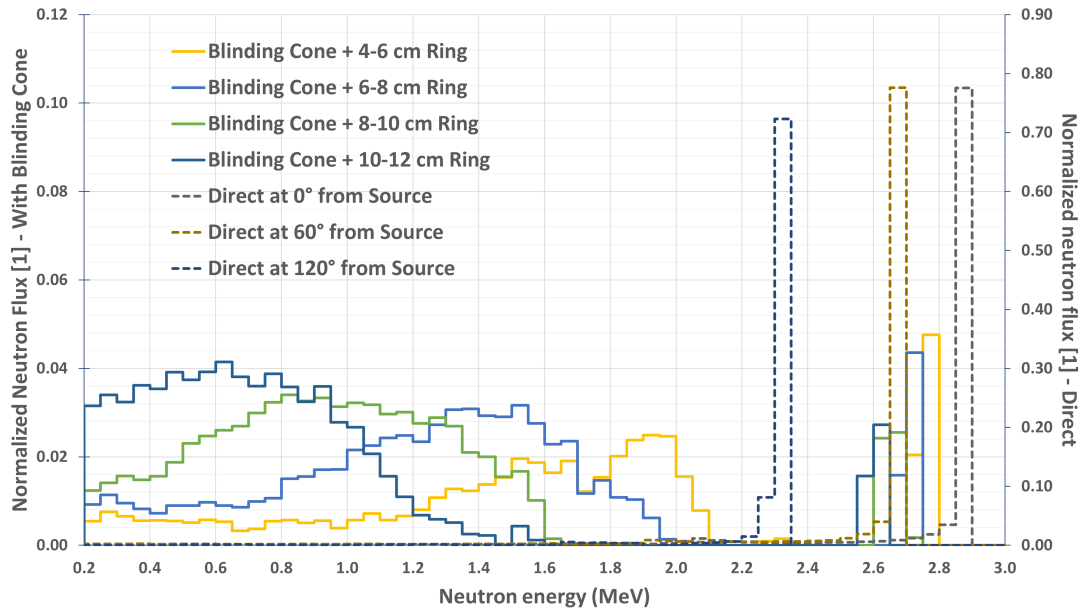


Figure 3.25: Simulation of the background corrected neutron spectrum for the different measurements. The first 4 measurements are conducted with the blinding cone and scattering rings with different radii (denoted by their inner and outer radius in the legend). The following 3 measurements are conducted with direct exposure to the neutron generator at different emission angles. Adapted from [52].

In reality, the neutrons reaching the detector have some distribution caused by the output of the generator which is only quasi-monoenergetic (see figure 3.23), and the finite sizes of the scattering rings and sensitive volume. Additionally, some neutrons can scatter off carbon atoms contained in the polyethylene, thereby losing less energy, and some neutrons can take entirely different scattering paths, potentially even via some structures in the surrounding room. The measurements can therefore not simply all be evaluated to an efficiency at a certain energy. Instead, the energy-dependent efficiency has to be reconstructed using the information from multiple measurements. To find a function which can be used to extract the energy-dependent efficiency from the count rate of multiple measurements, a simulation of the neutron spectrum at the sensitive volume is performed with MCNP. The results of such a simulation is shown for illustration purposes in figure 3.25.

Three measurements with direct flux from the neutron generator at varying angles relative to the forward direction were performed as well as four measurements in the forward direction with different sized scattering rings. The ring sizes and positions, and the angles were exactly the same as the ones of the simulations shown in figure 3.25. Pictures of the setups are shown in figure 3.26. In addition, a background measurement with only a blinding cone between the generator and the sensitive volume was performed for every angle. This was used as a correction for the measurements to reduce the influence of the scattering paths involving structures in the room that were not simulated.

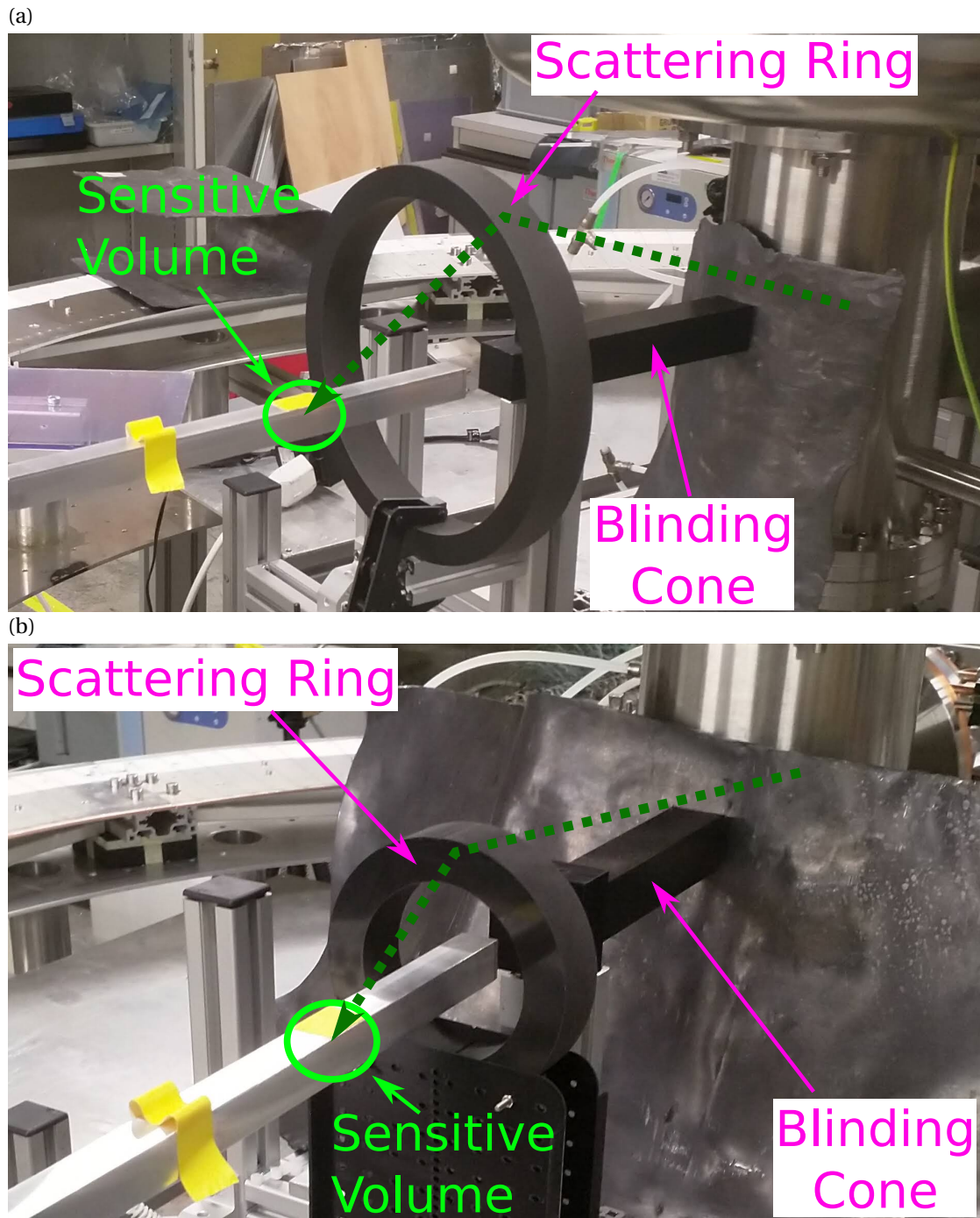


Figure 3.26: Pictures of the measurement setup using the scattering rings. Possible neutron paths are illustrated by dashed green lines. The emission spot of the neutron generator is inside the vertical metal cylinder on the right side of the pictures, at the start point of the dashed dark green line.

Unfortunately, with this initial test series it was not possible to extract meaningful energy-dependent efficiency data from the measurement results. During the measurements the strong degradation of the detector light guides described in section 3.2.4 was observed. It is likely that the reconstruction was not possible due to a significant portion of this degradation occurring during the measurements, changing the detector properties between the measurements. This is the reason why the estimation measured at AHL from the point spread function (see section 4.3.2) is used in this thesis whenever an energy-dependent efficiency is necessary. The measurement should be repeated when a more radiation resistant replacement for the light guides is found. An alternative would also be to couple the sensitive volume directly to the SiPMs without a light guide. Finally, to validate the measurement system itself, the measurements and subsequent reconstruction could be repeated with a more established detector whose energy-dependent efficiency is known.

3.7 Simulation of Inner Processes of the Detector

There was a considerable amount of work done in an attempt to build a complete model of the detector that could be used to predict the detector output under different circumstances and for different sensitive volume geometries. This work was done in the context of several student projects. These are the Master thesis of Enrico del Re [55], the semester project of Caroline Seyffert [56], and the Bachelor thesis and semester project of Nicolas König [57, 58]. All of these, except for the semester project of Caroline Seyffert, were co-supervised by me.

The most challenging aspect of the simulation was the light propagation through the ZnS:Ag-epoxy mixture. Other difficult areas were the deposition of energy in the ZnS:Ag from protons and electrons, and the capturing of light by the WLSFs. No reliable model for the neutron detector could be built in the end. However, a lot of important work towards such a model has been made. This also includes measurements of individual pieces of the detector (such as light transmission measurements through thin sheets of ZnS:Ag-epoxy mixture [57, 58]). For information on the different methods of simulating the detector and the respective outcomes, the reader is referred to the student theses.

4 Spent Fuel Measurement Campaign

A first version measurement system for spent fuel was built up at the Hot-Laboratory (AHL) of the Paul Scherrer Institut (PSI) and first measurements were carried out. Large parts of the existing infrastructure for gamma emission measurements (see section 1.1.3) were used for this measurement system. The measurements are intended as a proof of concept as well as an opportunity to gather additional data on the behavior of the combined system of detector, collimator, and spent fuel positioning devices to detect possible pitfalls before building a more sophisticated measurement system (see section 5.2).

This chapter is organized as follows. It first gives an overview of the measurement system (section 4.1) and of the relevant properties of the spent fuel sample selected for the measurements (section 4.2). Preparatory measurements and simulations of the setup that are necessary for the interpretation of the main neutron emission measurements are then presented in section 4.3. The main neutron emission measurements (including total emission and axial distribution) are then presented and their results discussed in section 4.4. Finally, section 4.5 shows some evidence of the degradation of the detector during the measurement campaign.

4.1 Measurement Setup

An illustration of hot-cell number 1 and the extension in which the measurements were performed is shown in figure 4.1. A significant part of the infrastructure used for the gamma emission measurements (described in section 1.1.3) is reused for the neutron measurement setup described here. The same measurement penetration is used, including the sledge and supports used to move samples through it. The axis on which the samples are aligned and can be moved is called the center axis. A pictures of the hot cell interior with the sledge and supports is shown in figure 4.2a. The collimator for the gamma measurements is used as well, opened to its maximal width of 18 mm. Instead of the HPGe detector, the Hot-Lab Prototype 1 (see section 2.2.2) is used. Contrary to the HPGe detector, which is always positioned behind the collimator during gamma measurements, the Hot-Lab Prototype 1 is inserted into the collimator opening. A picture of this is shown in Figure 4.2b. Unless explicitly stated, all results

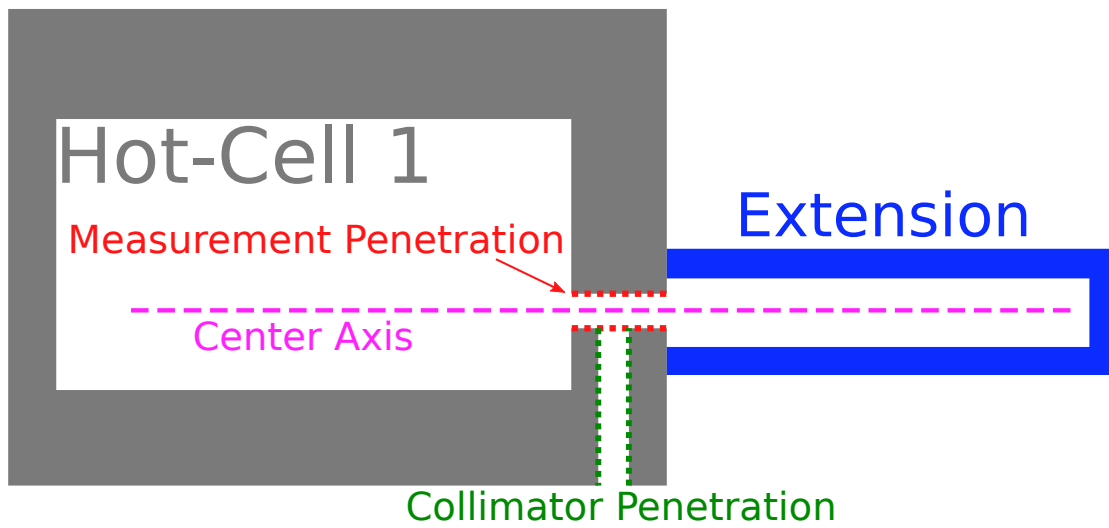


Figure 4.1: Horizontal cross section illustration of hot-cell number 1 and the attached extension (not to scale). The center axis goes through the center of the measurement penetration. Adapted from [18]

presented in this chapter were obtained using the FPGA electronics (see section 2.3.2) with the MSD settings presented in section 3.2 for high gamma environments.

Two parameters of the measurement setup were changed over the course of this measurement campaign. These are the depth to which the detector was inserted into the collimator opening (or the distance between the detector and the measured sample), and the thickness of tungsten put in front of the detector for gamma shielding (see section 2.2.2). Two combinations of these parameters are used frequently for the measurements and are described here for easy reference. The first combination has the detector probe inserted into the collimator such that the distance between the front of the sensitive volume and the center axis is 200 mm. In this setup, a block of tungsten with a thickness of 20 mm is attached to the front of the detector probe, 10 cm away from the sensitive volume. This setup is referred to as the “Near” setup. The second setup has the sensitive volume at a distance of 367 mm from the center axis. No tungsten plate is attached to the front of the detector probe. This setup is referred to as the “Far” setup. Schematic representations of the two setups are shown in figure 4.3.

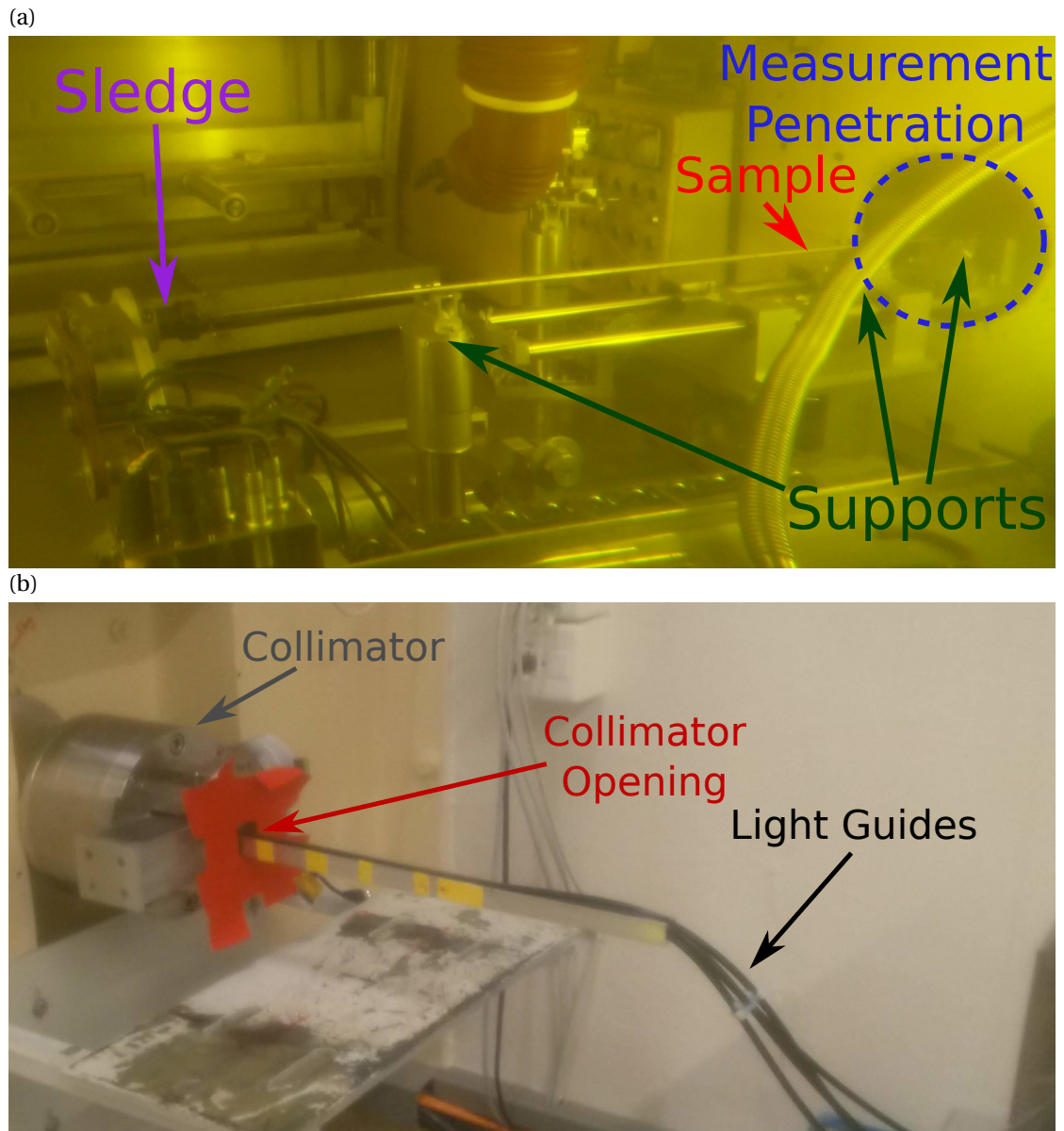


Figure 4.2: (a): View into hot-cell number 1 with the entrance to the measurement penetration (marked dashed blue). A fuel sample (red arrow), fixed at one end on a sledge (purple arrow) and supported by rollers, is being inserted into the measurement penetration. (b): Outside view of the collimator penetration with the gamma collimator inserted. The neutron detector is inserted into the collimator opening with black light guides leading to the readout electronics. Adapted from [18].

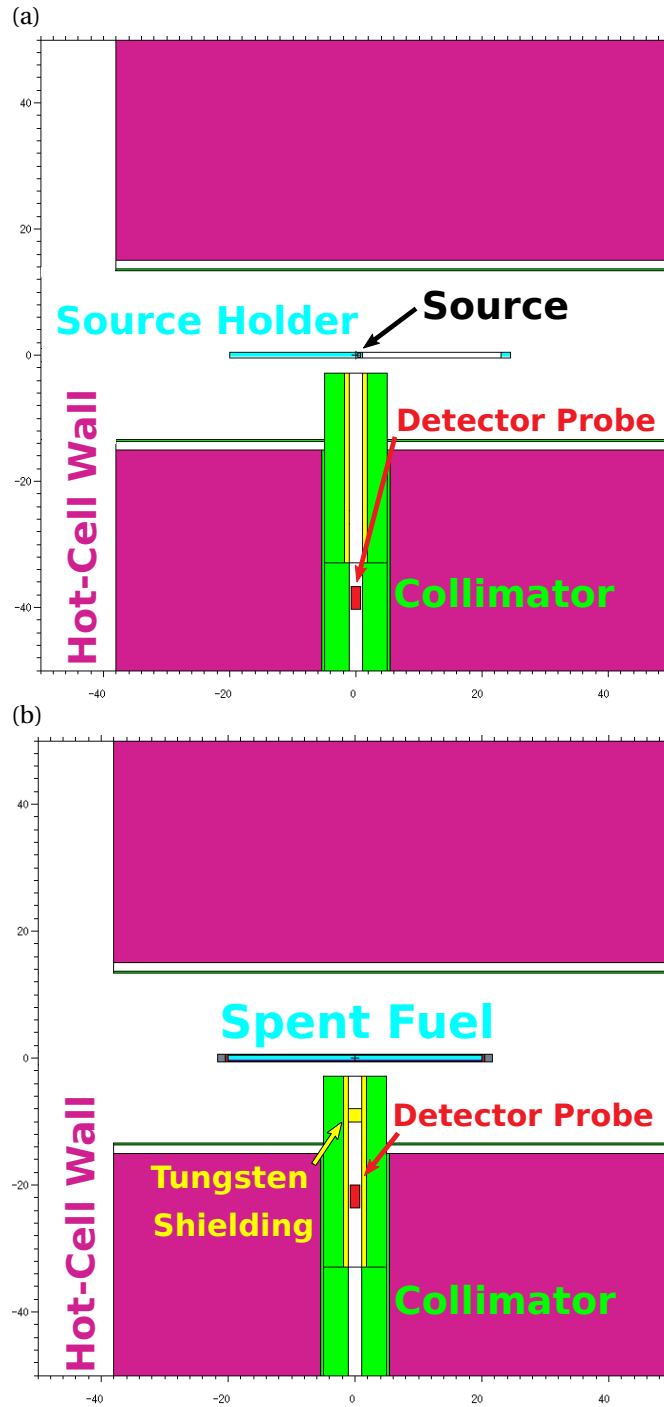


Figure 4.3: Representations (MCNP input geometries) of the measurement setup (dimensions in cm). The measurement penetration goes from the left (inside of the hot-cell number 1) to the right through the hot-cell wall. (a): The encapsulation (blue) for the source (marked by black arrow) is at the zero position. The source is roughly in the center of the encapsulation, at the position where the the source holder changes from being solid to being hollow. The detector is shown in the far configuration. (b): A spent fuel sample is shown in blue in the zero position. The detector is shown in the near configuration. Adapted from [18].

Sample ID	Fuel Type	Burn-up	Shutdown Date	Active Cycles
M4	MOX	~70 GWd/t	2001-07	4
U1	UO ₂	~40 GWd/t	1996-06	2
U3	UO ₂	~70 GWd/t	1995-06	5
U6	UO ₂	~90 GWd/t	1995-06	7

Table 4.1: Properties of the spent fuel samples selected for neutron measurements from the LWR-Proteus Phase II program. [61, 62] Adapted from [18].

4.2 Measured Spent Fuel Samples

During the measurement campaign, four fuel samples with a length of 40 cm each were measured. They were cut from spent fuel rods from the Swiss nuclear power plant in Gösigen (KKG) [59] as part of the LWR-PROTEUS Phase II program [60]. Sections in the middle of the rod and away from spacer grid positions were chosen to have uniform neutron flux over the entire length of the sample during irradiation inside the reactor, and therefore axially uniform composition. Before cutting the fuel rods, their axial ^{137}Cs gamma-ray distribution were measured and found to be flat over the sample location confirming the axial uniform composition of the sample. Table 4.1 shows an overview of the most relevant properties of the samples.

As part of the LWR-PROTEUS program, the composition of each sample was measured. Small parts about the size of a single fuel pellet were cut from the original fuel rods right next to the locations the samples were taken from. These were then dissolved and the composition analyzed using a mass spectrometry and liquid chromatography, as well as gamma spectrometry for selected nuclides [63, 64, 65]. Additionally, the neutron emission of the samples was measured using the source amplification technique. The samples were inserted in the PROTEUS zero-power reactor, which was configured to be slightly sub-critical. The effects on the over all neutron level was measured and compared to measurements using a calibrated ^{252}Cf source [66].

In the context of the CASQUADES project, the neutron emission of each sample was measured using a BF_3 thermal neutron detector in the hot-cell number 5 of the PSI hot laboratory. Each fuel sample was in turn inserted into a polyethylene block. The thermal neutron detector was inserted into the same block at some distance from the fuel sample and the neutron emission relative to each other was measured. In addition, a calibrated ^{252}Cf source (the same that is used here) was inserted in place of the sample and used as a reference to calculate absolute neutron emissions [62].

As detailed above, the neutron emission of the samples has been derived several times using different methods, making the samples a good reference set to test the detector capability. Since the measurements in the context of CASQUADES were the most recent, comprehensive and direct measurements of the neutron emission, they will be used for comparison further

Chapter 4. Spent Fuel Measurement Campaign

Sample ID	Neutron Emission		
	Relative [1]	Absolute [s^{-1}]	Decay Adjusted [s^{-1}]
M4	3.85 ± 0.06	$(2.7 \pm 0.1) \cdot 10^6$	$(2.5 \pm 0.1) \cdot 10^6$
U1	0.0578 ± 0.0005	$(4.1 \pm 0.1) \cdot 10^4$	$(3.7 \pm 0.1) \cdot 10^4$
U3	1	$(7.0 \pm 0.2) \cdot 10^5$	$(6.4 \pm 0.2) \cdot 10^5$
U6	2.02 ± 0.01	$(1.41 \pm 0.05) \cdot 10^6$	$(1.28 \pm 0.05) \cdot 10^6$

Table 4.2: Neutron emission of the different spent fuel samples from the LWR-Proteus Phase II program based on the CASQUADES measurements. The relative neutron emission is relative to the U3 sample. The decay adjusted neutron emission is the one calculated for the time of the measurements reported here. The uncertainties represent a single standard deviation. [62] Adapted from [18].

on. However, the measured absolute emissions first have to be adjusted for the time difference between the CASQUADES measurements (performed in May 2018) and the measurements presented in the following sections (performed in September and October 2020). Since the neutron emission for these fuel samples is almost exclusively due to ^{244}Cm , the adjusted emission is calculated by following the exponential decay of ^{244}Cm (half life of 18.1 years [39]) and the relative emission of the samples (i.e., ratios between samples) does not need to be adjusted. The original and adjusted results from the CASQUADES measurements are shown in table 4.2.

In addition to the spent fuel samples, the ^{252}Cf source described in section 3.1 was used during the measurement campaign. The ^{252}Cf source was encapsulated to avoid contamination of the source and to enable using the same positioning system as for the spent fuel samples. The back part of the encapsulation was a solid cylinder and the front part was a hollow tube. The ^{252}Cf source was sitting to the front of the solid part, inside the tube part.

During a measurement, one of the samples is placed on the center axis. The samples are always aligned with the center axis (i.e. the center axis coincides with the rotational symmetry axis of the sample). The samples can be moved along the center axis, the exact positions are given with the descriptions of the individual measurements. The zero position for the spent fuel samples is defined as the position where the center of the 40 cm long fuel segment is directly in front of the center of the collimator opening. Similarly, the zero position for the ^{252}Cf source is defined as the position where the center of the active part of the encapsulated ^{252}Cf source is directly in front of the center of the collimator aperture. Both zero positions are illustrated in figure 4.3.

4.3 Setup Characterization

Several measurements and simulations were carried out to characterize the detector and the measurement setup. These are necessary to properly interpret the results of the measurements

described in section 4.4.2 and 4.4.3. Section 4.3.1 describes the derivation of point spread functions for the measurement setups for the ^{252}Cf source. In section 4.3.2, these results are then compared to simulations to get an approximate model of the energy-dependent efficiency of the detector. Section 4.3.3 finally describes the simulation of point spread functions for the ^{244}Cm spectrum emitted by the spent fuel samples.

4.3.1 ^{252}Cf Point Spread Function

The point spread function (PSF) is defined as the probability of a neutron being detected as a function of its emission location on the center line. The PSF accounts for the neutron transport from the emission point to the detector as well as the probability of detecting a neutron entering the sensitive volume of any channel of the detector (intrinsic efficiency). The PSF depends on the detection setup (such as location of detector and geometry surrounding materials) and the emission spectrum. Because the intrinsic efficiency of the detector depends on the photon rate (see section 3.2), the PSF is also dependent on the photon rate (this effect can be corrected for, see section 4.4.1 for details). Two PSFs, one with the detector in the near configuration and one with it in the far configuration, were measured with the encapsulated ^{252}Cf source. The ^{252}Cf source was placed in the measurement penetration at different axial positions between -20 cm $+2\text{ cm}$. Due to limited availability of measurement time and technical constraints, it was not possible to measure in the entire range from -20 cm to $+20\text{ cm}$. To get the entire point spread function between -20 cm and $+20\text{ cm}$, the measured values between -20 cm and -2 cm were mirrored at the 0 position. The results are shown in figure 4.4.

The most prominent feature in the PSF is the center region. There, the neutrons can reach the detector unhindered by the collimator. In both the near and far setups, the full width at half maximum of the center region peak is $\sim 25\text{ mm}$. While neutrons from the center region have the highest probability to be detected, the PSFs also feature a significant detection probability for the sides of the central peak. The height of these side regions, relative to the central peak, is much higher for the near setup, as is expected from the shorter useful collimator length. Interesting features of this off-center contribution are the secondary peaks occurring at a distance of $\pm 125\text{ mm}$. They correspond to the neutrons traveling to the detector through the region where the outer surface of the collimator meets the surface of the measurement penetration (see figure 4.3). For this path, the distance through the collimator is relatively short due to the angle while the distance through the hot-cell wall is not yet significant. Within the measured region, the PSF does not fall off to 0 at the sides. This is acceptable when measuring the total neutron emission of small samples that do not extend past the measured region (see section 4.4.2), but it is a problem for the reconstruction of the axial distribution of neutron emitters (see section 4.4.3). For this reason, an extended PSF had to be simulated (see section 4.3.3).

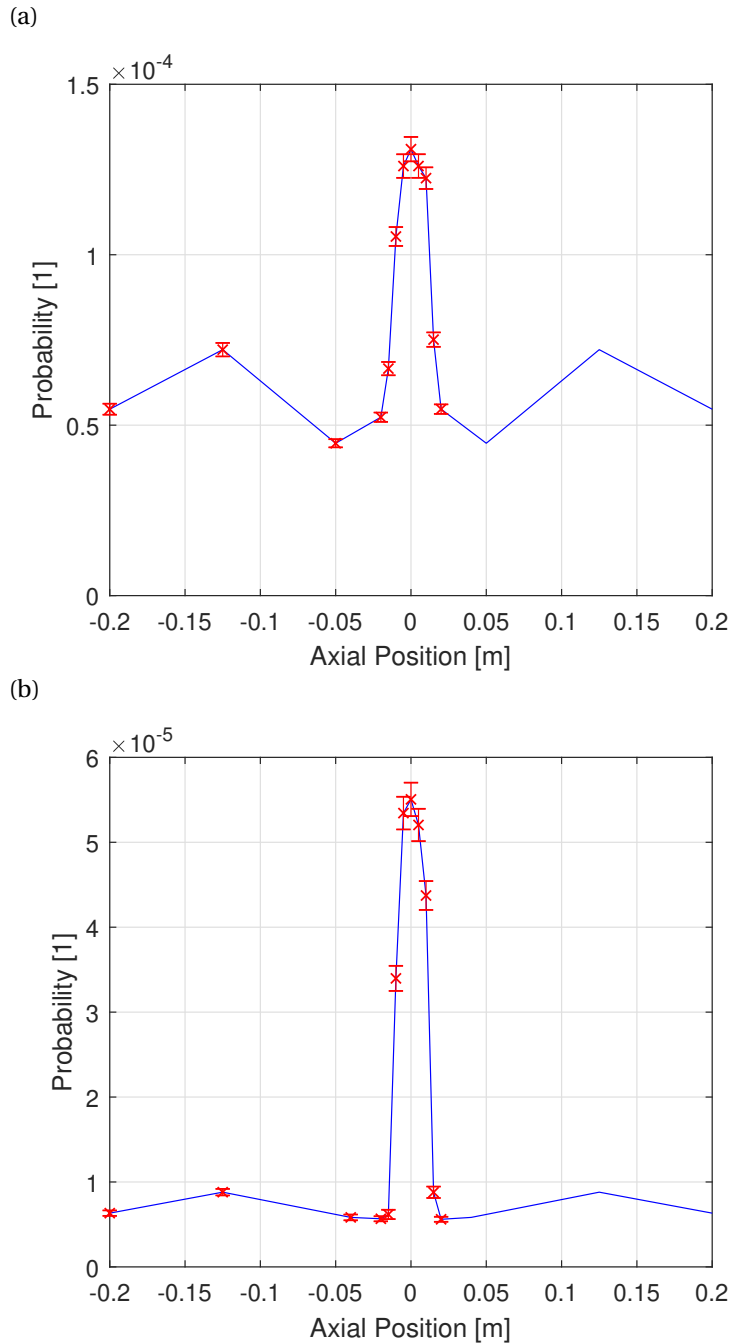


Figure 4.4: Point spread function (PSF) measured with the ^{252}Cf source for the near configuration (a), and the far configuration (b). The x -axis is the axial position of the ^{252}Cf source. The y -axis is the probability of an emitted neutron to reach the detector. The measured points are shown in red with an error bar indicating a single standard deviation. The blue line represents a PSF which has been extended by mirroring data from the left side at $x = 0$. Adapted from [18].

4.3.2 Energy-Dependent Efficiency

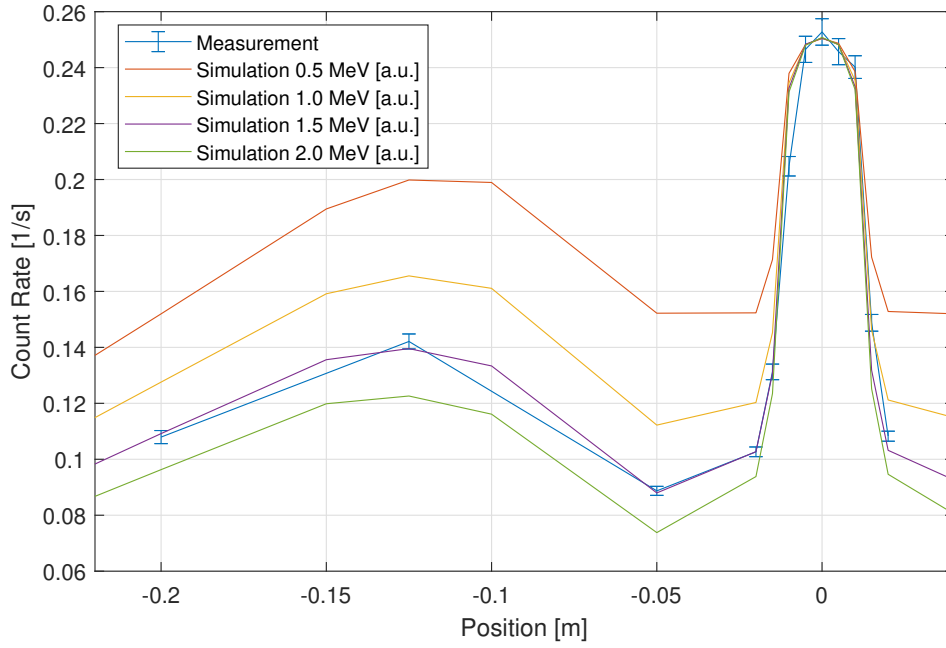
One of the parameters necessary to correct for the difference in the neutron spectrum between the spent fuel and the ^{252}Cf source is the energy-dependent neutron detection efficiency η_E of the detector. More precisely, only the shape of the energy-dependent efficiency function is important, the scaling is not necessary. The energy-dependent efficiency function was estimated by first assuming that $\eta_E(E)$ has the form of $a \cdot \Theta(E - E_{Th})$. Where Θ is the Heaviside step function, and a and E_{Th} are parameters to be determined. This is an approximation which was used in the absence of more detailed knowledge (see also section 3.6 for a more sophisticated approach to measure the energy-dependent efficiency). Since the scaling a is not of primary interest, the only parameter left to determine is E_{Th} . This was done by comparing the PSF measured with the ^{252}Cf source and presented in section 4.3.1 with simulations.

MCNP-6.2 [14] and ENDF/B-VII.0 [47] were used for the simulations. They include a section of the wall at the entrance of hot-cell number 1, the measurement penetration, the collimator penetration, and the existing gamma ray collimator. A representation of the geometry is shown in figure 4.3. In these simulations, the source was modeled as a hollow stainless steel cylinder containing a 0.5 cm long active volume with a diameter of 0.5 cm, emitting neutrons isotropically with the spontaneous fission spectra of ^{252}Cf . The source encapsulation that was used in the experiments was also modeled. The detector was not explicitly modeled. Instead a point detector (F5 tally [14]) located in the middle of the detector's sensitive volume was used to tally the neutron flux density per source particle at that position. The tally was segmented in energy to obtain the flux spectrum and aggregated to yield the integrated flux above several threshold energies (E_{th}). Simulations were performed for the near and far configurations. For both detector geometries, the source was located at different axial positions between -1 m and $+1$ m. Typically, 10^8 particles were sufficient to yield uncertainty ranging from about 1% to 7% from the center to the periphery of the investigated axial range (i.e. uncertainties significantly lower than the experimental ones).

Figure 4.5 shows the comparison between the simulated PSFs with a few representative values for E_{Th} and the measured ones. Since the scaling of the energy-dependent efficiency function is not relevant, the simulated functions are scaled to ease the comparison. The shape of the simulation with $E_{Th} = 1.5$ MeV matches the measured data well. This justifies to some degree the approximation of the shape of the energy-dependent efficiency. The function $\eta_E(E) = a \cdot \Theta(E - E_{Th})$ with $E_{Th} = 1.5$ MeV is used for the energy-dependent efficiency of the Hot-Lab Prototype 1.

The real energy-dependent efficiency is likely significantly different and the scope where this approximation can reliably be applied is limited. Within this thesis, the derived energy-dependent efficiency function is only used for modeling geometries similar to the one with which it was derived and only for modeling the response to the ^{252}Cf source it was derived with, or to ^{244}Cm which has a similarly shaped spectrum as ^{252}Cf . These two restrictions allow the use of the approximated energy-dependent efficiency with some confidence.

(a)



(b)

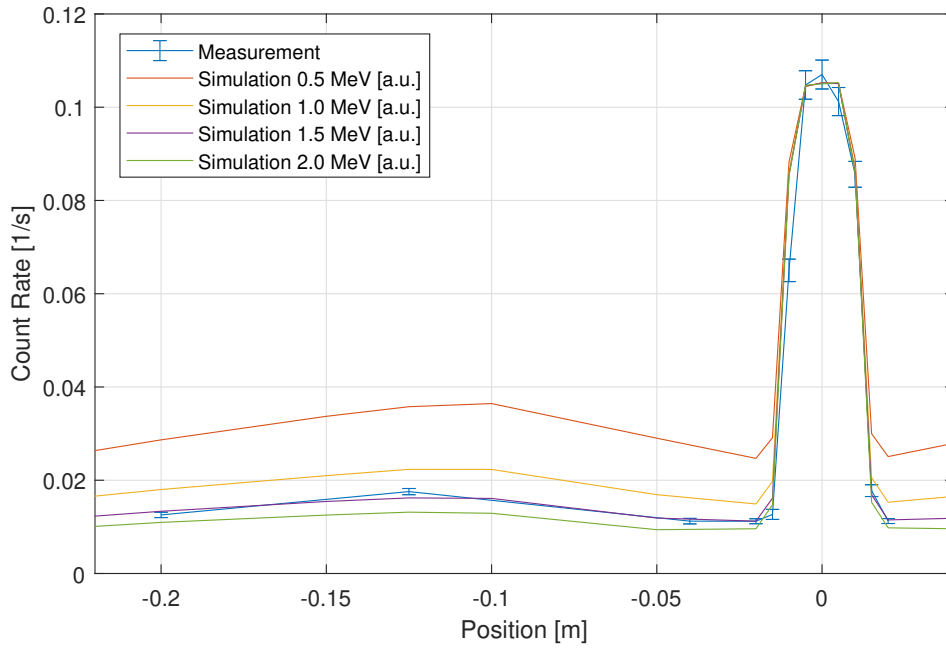


Figure 4.5: Comparison of the measured PSF with simulations for the ^{252}Cf source. In (a) the data for the near setup is shown and in (b) the one for the far setup. The simulations assume a constant detection efficiency above the given neutron energy and 0 efficiency below. They are scaled to match the experimental data in the region around the 0 position. Adapted from [18].

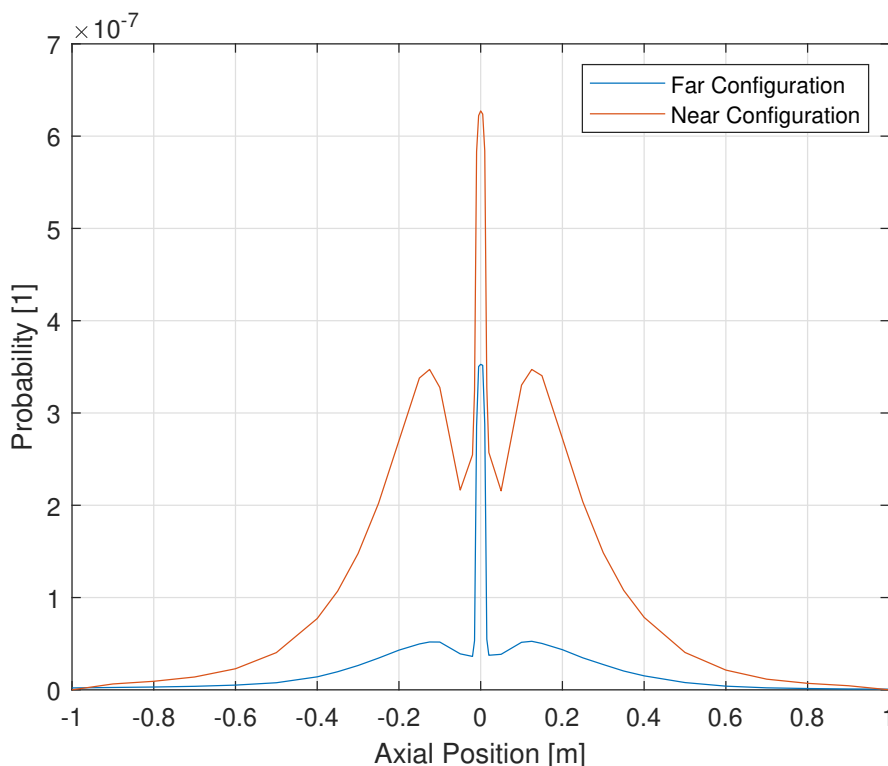


Figure 4.6: Simulated PSF for ^{244}Cm neutrons with the detector in the near and the far configuration. The y-axis is the probability of a neutron emitted at the specified axial position to be counted by the detector (assuming a photon rate of $\gamma = 1 \cdot 10^6 \text{ s}^{-1}$). Adapted from [18].

4.3.3 ^{244}Cm Point Spread Function

The measured PSF presented in section 4.3.1 is only valid for neutrons with the same spectrum as the ^{252}Cf source. The neutron emission of the measured fuel samples is dominated by ^{244}Cm . The PSF therefore has to be adjusted for the ^{244}Cm spontaneous fission spectrum. A simulation using MCNP-6.2 [14] and ENDF/B-VII.0 [47] together with the energy-dependent efficiency η_E derived in section 4.3.2 was used to simulate this PSF. The simulation was extended to positions on the center axis between -1 m and $+1 \text{ m}$ to ensure that the tails go down to a negligible value (as this is important for emission distribution reconstruction, see section 4.4.3). The resulting PSF is shown in figure 4.6. The difference between the simulated PSF for the ^{244}Cm and the ^{252}Cf is $\sim 5\%$, relatively independently of the axial position and also about the same for the near and the far setup.

4.4 Spent Fuel Measurements

This section presents the measurements of the total relative and absolute neutron emission of the samples (section 4.4.2), as well as the axial distribution of the neutron emission of

Chapter 4. Spent Fuel Measurement Campaign

sample M4 (section 4.4.3). In preparation for the analysis of the measured data, section 4.4.1 presents the equations to calculate the absolute neutron emission based on measurement and simulation results presented in the previous sections.

4.4.1 Absolute Neutron Emission Formula

This section describes in detail the derivation of the formula used in section 4.4.2 to calculate the absolute neutron emission of the fuel samples, and which assumptions were made.

The first assumption for this calculation is that no counts are caused by gamma rays (perfect gamma blindness). However, the dependency of the neutron efficiency on the photon rate (which is largely influenced by gamma rays, see section 3.2) is taken into account. The count rate n_X of the detector for a specific sample X can be written as:

$$n_X = \int_{-\infty}^{\infty} \int_0^{\infty} \int_0^{\infty} a_X(x, E) \cdot p(x, E, E') \cdot \eta(E', \gamma_X) dE' dE dx \quad (4.1)$$

Here, $a_X(x, E) dE dx$ is the emission rate of neutrons between the energies E and $E + dE$, and between the axial positions x and $x + dx$. X denotes a sample and its axial position. The expression $p(x, E, E') dE'$ is the probability of a neutron emitted at the axial position x with an initial energy E to end up at the detector position with an energy between E' and $E' + dE'$, and $\eta(E', \gamma_X)$ is the intrinsic detection efficiency for neutrons of energy E' at a photon rate of γ_X (dependent on the sample and its position).

Assuming that the intrinsic efficiency η can be decomposed into a purely energy dependent part η_E and a purely photon rate dependent part η_γ (first order approximation), $\eta(E', \gamma_X)$ becomes $\eta_E(E') \cdot \eta_\gamma(\gamma_X)$ and

$$n_X = \eta_\gamma(\gamma_X) \cdot \int_{-\infty}^{\infty} \int_0^{\infty} \int_0^{\infty} a_X(x, E) \cdot p(x, E, E') \cdot \eta_E(E') dE' dE dx \quad (4.2)$$

To calculate the count rate n_{Cf, x_s} for the ^{252}Cf source at an axial position x_s , the source is approximated as a point source with $a_{Cf, x_s}(x, E) = a_{Cf}(E) \cdot \delta(x - x_s)$, where $a_{Cf}(E)$ is the sources emission rate of neutrons of energy E and δ is the Dirac delta function.

$$n_{Cf, x_s} = \eta_\gamma(\gamma_{Cf, x_s}) \int_0^{\infty} \int_0^{\infty} a_{Cf}(E) \cdot p(x_s, E, E') \cdot \eta_E(E') dE' dE \quad (4.3)$$

Using the total neutron emission rate A_{Cf} of the ^{252}Cf source this becomes:

$$n_{Cf,x_S} = A_{Cf} \cdot \eta_\gamma(\gamma_{Cf,x_S}) \int_0^\infty \int_0^\infty \frac{a_{Cf}(E)}{A_{Cf}} \cdot p(x_S, E, E') \cdot \eta_E(E') dE' dE \quad (4.4)$$

Using this it is easy to calculate the counts per source particle n_{Cf,x_S}^* .

$$n_{Cf,x_S}^* = \eta_\gamma(\gamma_{Cf,x_S}) \int_0^\infty \frac{a_{Cf}(E)}{A_{Cf}} \int_0^\infty \eta_E(E') \cdot p(x_S, E, E') dE' dE \quad (4.5)$$

The neutron emission of the fuel samples is approximately uniform in the axial direction over the entire length of the sample. The fuel sample emission probability $a_{Fuel}(x, E)$ can therefore be written as

$$a_{Fuel}(x, E) = \frac{a_{Fuel}(E)}{x_2 - x_1} \Theta(x - x_1) \Theta(x_2 - x) \quad (4.6)$$

Here, Θ is the Heaviside step function, and x_1 and x_2 are the axial positions of the two ends of the fuel sample. The count rate n_{Fuel} for a spent fuel sample measurement is therefore

$$n_{Fuel} = \eta_\gamma(\gamma_{Fuel}) \int_0^\infty \frac{a_{Fuel}(E)}{x_2 - x_1} \int_0^\infty \eta_E(E') \int_{x_1}^{x_2} p(x, E, E') dx dE' dE \quad (4.7)$$

For the counts per source particle n_{Fuel}^* , this needs to be divided by the total neutron emission A_{Fuel} of the fuel sample.

$$n_{Fuel}^* = \eta_\gamma(\gamma_{Fuel}) \int_0^\infty \frac{a_{Fuel}(E)}{A_{Fuel} \cdot (x_2 - x_1)} \int_0^\infty \eta_E(E') \int_{x_1}^{x_2} p(x, E, E') dx dE' dE \quad (4.8)$$

Combining equations 4.5 and 4.8, we define k_{Fuel} as:

$$\begin{aligned} k_{Fuel} &= \frac{\frac{n_{Fuel}^*}{\eta_\gamma(\gamma_{Fuel})}}{\int_{x_1}^{x_2} \frac{n_{Cf,x_S}^*}{\eta_\gamma(\gamma_{Cf,x_S}) \cdot (x_2 - x_1)} dx_S} \\ &= \frac{\int_0^\infty \frac{a_{Fuel}(E)}{A_{Fuel} \cdot (x_2 - x_1)} \int_0^\infty \eta_E(E') \int_{x_1}^{x_2} p(x, E, E') dx dE' dE}{\int_{x_1}^{x_2} \int_0^\infty \int_0^\infty \frac{a_{Cf}(E)}{A_{Cf} \cdot (x_2 - x_1)} \cdot p(x_S, E, E') \cdot \eta_E(E') dE' dE dx_S} \end{aligned} \quad (4.9)$$

This can be simplified by introducing $\psi_{Fuel}(E) = \frac{a_{Fuel}(E)}{A_{Fuel}}$ and $\psi_{Cf}(E) = \frac{a_{Cf}(E)}{A_{Cf}}$ the neutron emission spectrum of the fuel sample (almost exclusively ^{244}Cm spontaneous fission for the samples used) and the one of the ^{252}Cf source (assumed to be the pure ^{252}Cf spectrum)

respectively.

$$k_{Fuel} = \frac{\int_0^\infty \frac{\psi_{Fuel}(E)}{x_2 - x_1} \int_0^\infty \eta_E(E') \int_{x_1}^{x_2} p(x, E, E') dx dE' dE}{\int_0^\infty \frac{\psi_{Cf}(E)}{x_2 - x_1} \int_0^\infty \eta_E(E') \int_{x_1}^{x_2} p(x_S, E, E') dx_S dE' dE} \quad (4.10)$$

The factor k_{Fuel} does not depend on the background-dependent efficiency η_γ nor on the emission rate of the samples A_{Cf} and A_{Fuel} . It can be interpreted as the ratio of the count rates detected from a spent fuel sample and a sample of ^{252}Cf with the same geometry, total neutron emission, and gamma emission. The value of k_{Fuel} will later be deduced using data from simulations.

Using the definition of k_{Fuel} together with equation 4.7, the count rate for the spent fuel sample can be rewritten as:

$$n_{Fuel} = \frac{A_{Fuel}}{A_{Cf}} \cdot \eta_\gamma(\gamma_{Fuel}) \cdot k_{Fuel} \cdot \frac{1}{x_2 - x_1} \int_{x_1}^{x_2} \frac{n_{Cf, x_S}}{\eta_\gamma(\gamma_{Cf, x_S})} dx_S \quad (4.11)$$

This can be rearranged to get an expression for the activity of the fuel:

$$A_{Fuel} = \frac{1}{k_{Fuel}} \cdot \frac{\frac{n_{Fuel}}{\eta_\gamma(\gamma_{Fuel})}}{\frac{1}{x_2 - x_1} \int_{x_1}^{x_2} \frac{n_{Cf, x_S}}{\eta_\gamma(\gamma_{Cf, x_S})} dx_S} \cdot A_{Cf} \quad (4.12)$$

The activity of the ^{252}Cf source A_{Cf} and the background-dependent efficiency η_γ are known from sections 3.1.1 and 3.2.3. The integral $\int_{x_1}^{x_2} \frac{n_{Cf, x_S}}{\eta_\gamma(\gamma_{Cf, x_S})} dx_S$ can be calculated from the point spread function measurements described in section 4.3.1. The only quantity which is still missing to link the count rate n_{Fuel} to the activity of a fuel sample is k_{Fuel} (equation 4.10).

The value of k_{Fuel} was estimated using MCNP-6.2 [14] and ENDF/B-VII.0 [47], and the approximation for the detector's energy-dependent efficiency η_E described in section 4.3.2. The nominator (expression 4.13) and denominator (expression 4.14) in the formula for k_{Fuel} were both simulated individually.

$$\int_0^\infty \frac{\psi_{Fuel}(E)}{x_2 - x_1} \int_0^\infty \eta_E(E') \int_{x_1}^{x_2} p(x, E, E') dx dE' dE \quad (4.13)$$

$$\int_0^\infty \frac{\psi_{Cf}(E)}{x_2 - x_1} \int_0^\infty \eta_E(E') \int_{x_1}^{x_2} p(x_S, E, E') dx_S dE' dE \quad (4.14)$$

For the denominator, the data from the simulations in section 4.3.2 was reused. The values at the individual axial positions were integrated using linear interpolation between the points. The nominator can be seen as the counts per source particle for a fuel sample measurement

Measurement	Time [h]	Counts	Count Rate [s^{-1}]
M4 Near	1.86	9835	0.461 ± 0.005
U1 Near	15.69	1464	0.0081 ± 0.0002
U3 Near	5.92	8379	0.1222 ± 0.0013
U6 Near	3.28	9238	0.243 ± 0.003
M4 Far	27.32	21063	0.0668 ± 0.0005
U1 Far	20.75	266	0.00110 ± 0.00007
U3 Far	27.25	5793	0.0184 ± 0.0002
U6 Far	22.39	9652	0.0371 ± 0.0004

Table 4.3: Results of the measurements of the different fuel samples in the axial zero position for the near and the far setup. The number of counts and the count rate are the sum over all four detector channels. The count rate is given with a single standard deviation. Adapted from [18].

divided by the length of the fuel sample. It was simulated using MCNP-6.2 [14] and ENDF/B-VII.0 [47] together with the energy-dependent efficiency η_E derived in section 4.3.2. The basic geometry for the simulation is the same as in section 4.3.2. The only difference is that instead of the source with its encapsulation at a variable axial position, a fuel sample was placed in the measurement penetration at a fixed position centered on the collimator. A representation of the geometry is shown in figure 4.3a. The fuel sample is modeled as a 40 cm long neutron emitter with a ^{244}Cm spectrum. A total of 10^8 source particles were used for the simulation. The simulation was performed for the near and the far setup (see section 4.1). The results are $k_{Fuel} = 1.014 \pm 0.013$ for the far setup, and $k_{Fuel} = 1.014 \pm 0.004$ for the near setup. This therefore only represents a small correction factor when compared to the assumption that the fuel and the ^{252}Cf source have the same neutron spectrum (which would mean $k = 1$).

4.4.2 Total Neutron Emission

For the measurement of the total neutron emission of the samples, the near setup and the far setup (see section 4.1) were used. Each of the four 40 cm long fuel samples M4, U1, U3, and U6 (see section 4.2) are placed in turn in front of the collimator in the axial zero position. The count rate for each of these measurements is recorded and used to calculate the relative neutron emission (section 4.4.2) and the absolute neutron emission (section 4.4.2). The measured count rates are shown in table 4.3. To reach the same relative uncertainty, measurements using the far setups took about 7 times longer than for the near setup.

Relative Neutron Emission

The recorded count rates are adjusted one time using the photon rate dependent efficiency measured at the FNL with ^{252}Cf and ^{60}Co (see section 3.2.3) and another time adjusted using the photon rate dependent efficiency measured at the AHL with spent fuel (see section 3.2.3).

Chapter 4. Spent Fuel Measurement Campaign

Sample ID	Relative Neutron Emission			
	Near, AHL	Near, FNL	Far, AHL	Far, FNL
M4	3.85 ± 0.09	3.88 ± 0.07	3.72 ± 0.08	3.75 ± 0.06
U1	0.062 ± 0.003	0.061 ± 0.002	0.056 ± 0.004	0.055 ± 0.004
U3	1	1	1	1
U6	2.04 ± 0.04	2.06 ± 0.03	2.06 ± 0.04	2.08 ± 0.04

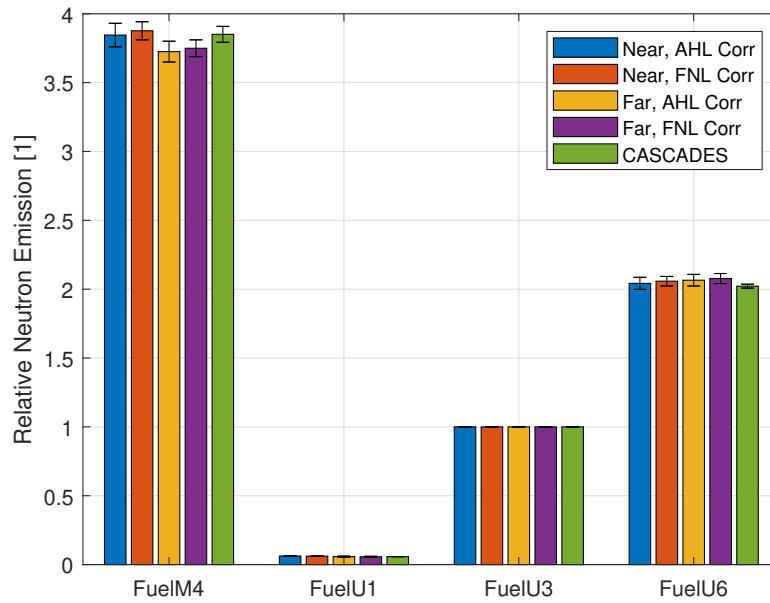
Table 4.4: Total neutron emission of the different measured spent fuel samples relative to the emission of the U3 sample. Each sample is measured with the near and the far setup. For each measurement, the analysis is performed once with the gamma-background correction measured using spent fuel (marked “AHL”) and once with the correction measured using the ^{252}Cf and ^{60}Co sources (marked “FNL”). The errors indicate a single standard deviation.

Since the geometry, neutron emitter distribution (all samples have a flat burn-up profile), and the neutron emission spectra (all samples are almost exclusively emitting ^{244}Cm spontaneous fission neutrons) are the same for all fuel samples, the ratio of the adjusted count rates is equal to the ratio of their total neutron emissions. The results for the relative neutron emissions are shown in figure 4.7a and table 4.4. For the uncertainty calculations, the uncertainty on the photon rate correction function and the uncertainties due to the counting statistics during the measurements are considered. The agreement of the different setups and the different corrections is good. The results are within one standard deviation, with the single exception of the near measurement with the correction measured at FNL when compared to the far measurement with the correction measured at AHL. The results also agree within 2 standard deviations with the values obtained during the CASQUADES project for the same samples.

Absolute Neutron Emission

Equation 4.12 is used to calculate the total activity of each fuel sample from the corresponding measured count rate in both configurations and with both photon rate corrections. The results are presented in table 4.5 and in figure 4.7b together with the emission rates from the CASQUADES project. For the uncertainty calculations, the uncertainties due to the counting statistics during the measurement, the simulations of k_{Fuel} , the ^{252}Cf source activity, the PSE, the photon rate dependent efficiency have all been taken into account. The agreement between the near and far measurements and the two photon rate dependent efficiencies is good, all four values being within one standard deviations for each fuel sample, with the single exception of the near measurement with the correction measured at FNL when compared to the far measurement with the correction measured at AHL. However, it has to be noted that a significant part of the uncertainty is due to the uncertainty in the calibration of the ^{252}Cf source (see section 3.1.1), which affects all measurements in the same way. The uncertainties are therefore not completely uncorrelated and just comparing the standard deviations can therefore be misleading. When only taking uncertainties into account which are not due to the uncertainty on the ^{252}Cf source output, the values agree within two standard deviations.

(a)



(b)

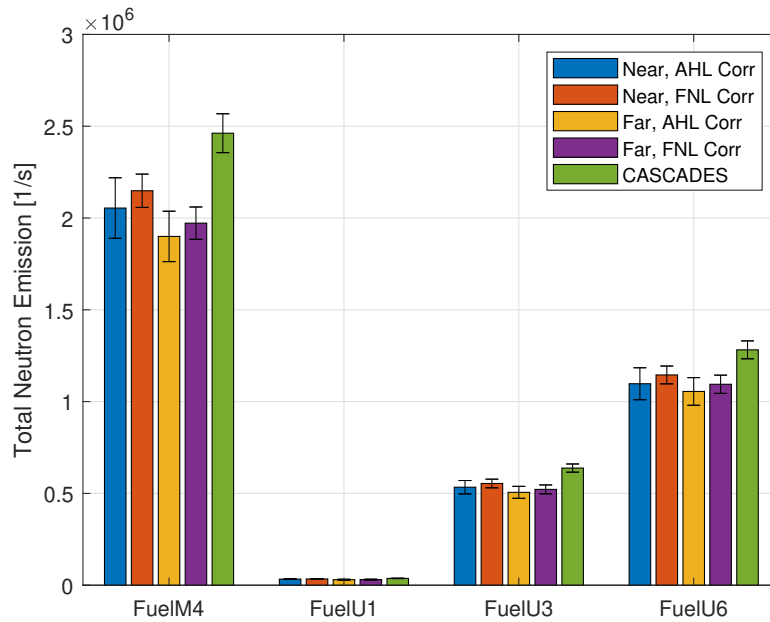


Figure 4.7: The neutron emission of each fuel sample relative to the U3 sample (a) and as absolute values (b). Each sample is measured with the near and the far setup. For each measurement, the analysis is performed once with the photon rate correction measured using spent fuel (marked “AHL correction”) and once with the correction measured using the ^{252}Cf and ^{60}Co sources (marked “FNL Correction”). As a comparison, the results obtained in the context of the CASQUADES project are plotted as well (see section 4.2). The error bars indicate a single standard deviation.

Sample ID	Absolute Neutron Emission [10^5 s^{-1}]			
	Near, AHL	Near, FNL	Far, AHL	Far, FNL
M4	21 ± 2	22 ± 1	19 ± 1	20 ± 1
U1	0.33 ± 0.02	0.34 ± 0.02	0.29 ± 0.02	0.30 ± 0.02
U3	5.3 ± 0.4	5.5 ± 0.3	5.1 ± 0.3	5.2 ± 0.3
U6	11.0 ± 0.9	11.5 ± 0.5	10.6 ± 0.8	11.0 ± 0.5

Table 4.5: Total absolute neutron emission of the measured spent fuel samples. For each measurement the analysis is performed once with the photon rate correction measured using spent fuel (marked “AHL”) and once with the correction measured using the ^{252}Cf and ^{60}Co sources (marked “FNL”). The errors indicate a single standard deviation.

There seems to be a trend towards the far setup data yielding systematically lower values than the near setup data. This could be an indication that the point spread function was not measured accurately enough. However, the difference is small compared to the uncertainties and the indication therefore only weak. Similarly, the efficiency correction measured with spent fuel seems to give systematically lower results than the one measured with ^{252}Cf and ^{60}Co . This could indicate some imperfections in the photon rate dependent efficiency, but this effect is too small (compared to the uncertainties of the measurements) to give a clear indication.

The agreement with the CASQUADES data is not as good as for the relative results presented in section 4.4.2. The agreement is within two standard deviations for the near setup data and within 2.5 standard deviations for the far setup data. The CASQUADES results are consistently higher than all values measured in this thesis, indicating a systematic error. A possible source for this discrepancy is detector degradation (see section 4.5), although this effect should be limited as the measurement was performed soon after the point spread function and gamma-background correction measurements. A more likely issue is the activity of the ^{252}Cf source. The calibration process showed unexplained deviations in the source activity results obtained with different measurement setups (see section 3.1.1). Although the dispersion was accounted for in the source uncertainty, some doubts remain as to the accuracy of the averaged value of the source activity.

4.4.3 Axial Emission Distribution

The aim of this measurement is to estimate the capability of the measurement setup to reconstruct the axial distribution of the neutron emission of a sample. All of the samples have a flat burn-up profile and are therefore also expected to have a uniform neutron emission over the entire length. While it is important to see if the flat region in the middle can be reconstructed, the most interesting part for estimating the capabilities of the technique are the regions around the edges of the sample. By comparing the reconstructed edges to the known real edges, the resolution can be estimated.

For this measurement, the M4 fuel sample was moved through the measurement penetration past the collimator with the far detector setup (see figure 4.3). At selected positions the count rate of the detector was recorded. A ^{252}Cf equivalent neutron flux (i.e., neutron flux with a ^{252}Cf spectrum that would produce the same count rate) is derived as the ratio of the measured count rate and the photon rate dependent efficiency obtained in section 3.2.3). The ^{252}Cf equivalent neutron flux can be used later in conjunction with the detector point spread function to reconstruct the sample emission profile (see below). Due to technical and time constraints, only a limited number of positions were measured. Since the problem is roughly symmetric with respect to the fuel sample position mirrored on the zero position, additional values can be generated by mirroring measured values at the zero position. Additional values were also added for the positions further away from the center than any measurement was taken by extrapolating the trend of the measured values. The measured, mirrored and extrapolated flux values are shown in figure 4.8.

The reconstruction was performed between -50 cm and $+50$ cm relative to the center of the fuel sample. The sample itself covers only the region from -20 cm to $+20$ cm within the reconstructed region. Without any uncertainties, the reconstruction could be done by solving a linear equation $Ax = b$ where b is a vector containing the measured neutron fluxes, x is a vector of neutron emissions at different positions, and A a matrix which can be constructed from the point spread function (see section 4.3.3). However, when introducing noise, this equation usually does not have a solution, so an approximate solution has to be found by minimizing $\|Ax - b\|_2^2$. Additionally, minimizing this expression usually amplifies the noise and therefore leads to low quality results. One method to mitigate this effect is called Tikhonov regularization [67]. Instead of minimizing $\|Ax - b\|_2^2$, the following expression is minimized:

$$\|Ax - b\|_2^2 + \|Tx\|_2^2 \quad (4.15)$$

Where T is the Tikhonov matrix which can be any matrix suitable to solve the problem. $\|Tx\|_2^2$ can be thought of as a penalty term which discourages certain outcomes defined by T . Independent of the choice of T (except in some edge cases), Tikhonov regularization also favors solutions that are scaled down by a scalar factor as this reduces the second term of equation 4.15. This behavior is unwanted since we are interested in the absolute emission. Therefore, the Tikhonov regularization was modified, resulting in the following expression to be minimized:

$$\|Ax - b\|_2^2 + \frac{\|Tx\|_2^2}{\|x\|_1^2} \quad (4.16)$$

This ensures that the scaling of the solution is the one which best fits the original data. In other words: If $x = x^*$ minimizes expression 4.16, there does not exist a scalar α such that $\|A(\alpha x^*) - b\|_2^2 < \|Ax^* - b\|_2^2$. This can easily be seen through a proof by contradiction: We

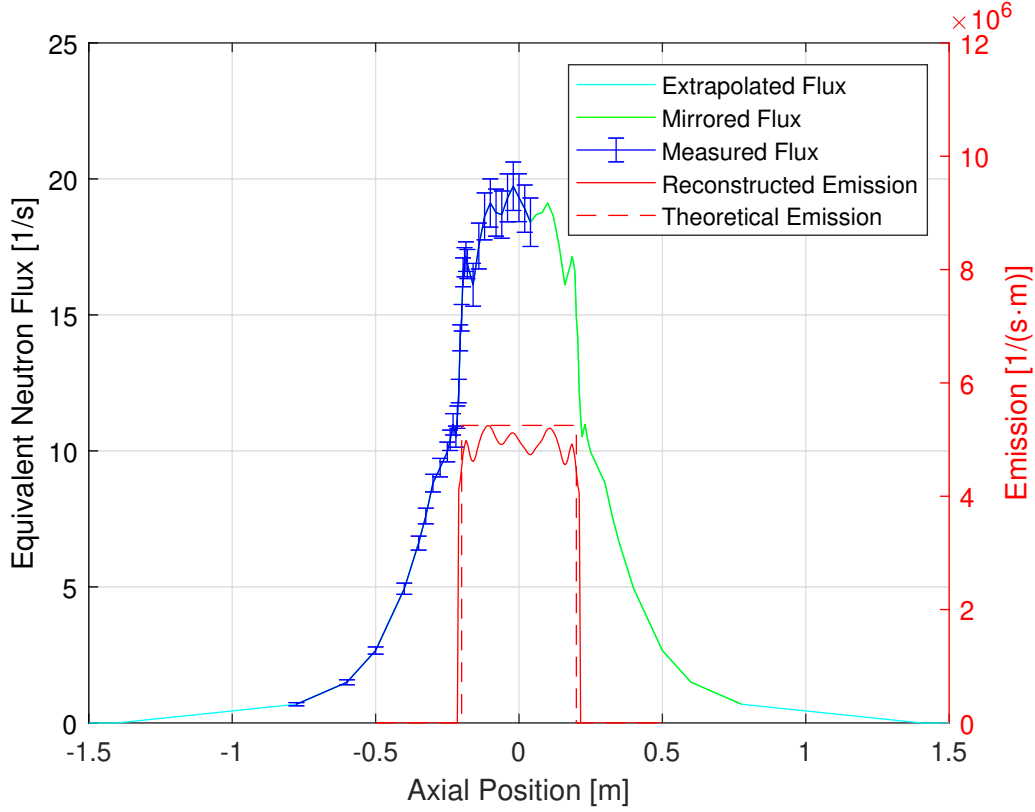


Figure 4.8: Measured ^{252}Cf equivalent neutron flux through the detector and the sample neutron emission reconstructed from that flux. For the flux, the axial position is the sample position. For the reconstructed emission, the axial position is measured relative to the center of the fuel sample. The blue line indicates the measured values. The individual measurements are marked together with their standard deviations. The green line represents the measured points that were mirrored at $x = 0$. The cyan line represents the flux extrapolated outside the measured range. Adapted from [18].

assume that such an α exists for a solution x^* . Since x^* minimizes expression 4.16 it follows that:

$$\begin{aligned} \|Ax^* - b\|_2^2 + \frac{\|Tx^*\|_2^2}{\|x^*\|_1^2} &\leq \|A(\alpha x^*) - b\|_2^2 + \frac{\|T(\alpha x^*)\|_2^2}{\|\alpha x^*\|_1^2} \\ \Rightarrow \|Ax^* - b\|_2^2 + \frac{\|Tx^*\|_2^2}{\|x^*\|_1^2} &\leq \|A(\alpha x^*) - b\|_2^2 + \frac{\|Tx^*\|_2^2}{\|x^*\|_1^2} \\ &\Rightarrow \|Ax^* - b\|_2^2 \leq \|A(\alpha x^*) - b\|_2^2 \end{aligned}$$

which contradicts the assumption.

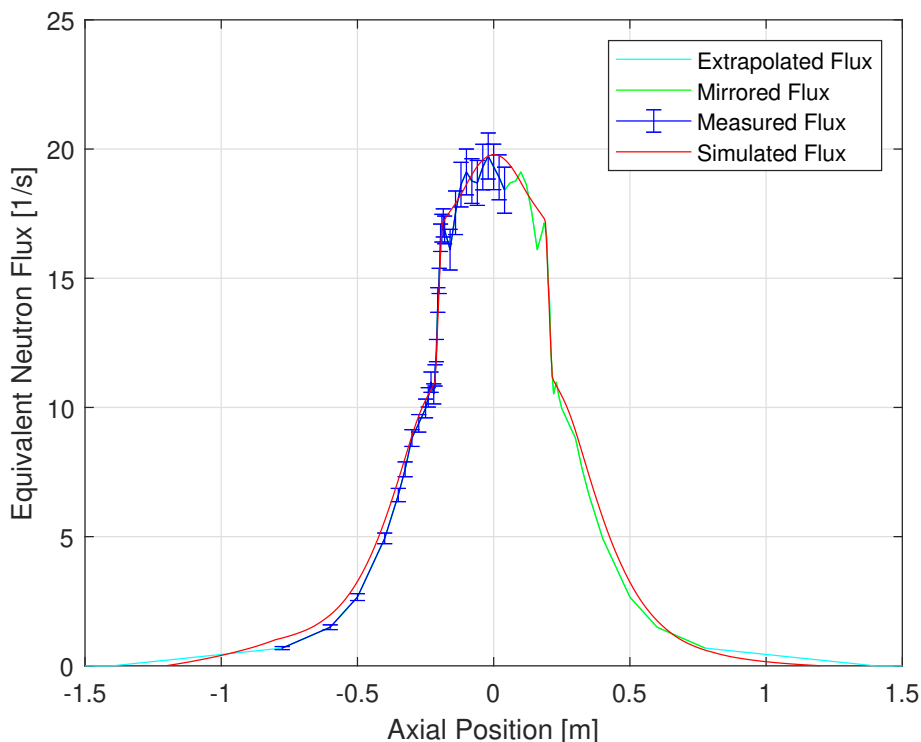


Figure 4.9: Measured and simulated ^{252}Cf equivalent neutron flux through the detector.

For the Tikhonov matrix, a multiple of the identity matrix was chosen: $T = \alpha \cdot I$ with $\alpha = 40$. The resulting emission is plotted in figure 4.8 together with the theoretical emission of the sample. The two edges of the fuel sample are captured quite well. They reach 90% of the full height in about 1.5 cm. There is a slight bias in the positioning with the reconstructed edges being about 1 cm further away from the center of the rod than they theoretically should be. The shape of the region between the two edges is captured quite well, oscillating around a constant value. However, the absolute value of the emission is about 5% lower than the theoretical value (the theoretical value being calculated by averaging the measurements of the total neutron emission of the sample in section 4.4.2 and assuming a uniform distribution of neutron emitters). One factor in this discrepancy is the outwards bias in the reconstruction of the edges. When integrating the reconstructed emission profile, the result is within 2% of the average total emission measured in section 4.4.2. This is within a single standard deviation.

Another comparison which can be made is between the measured neutron flux, and the neutron flux obtained by calculating the convolution of the theoretical neutron emission distribution (flat between $\pm 20\text{cm}$ and zero otherwise) and the simulated point spread function (see section 4.3.3). This comparison is shown in figure 4.9. The simulated and measured fluxes agree well, indicating a good match of the different measurements and the simulated point spread function.

4.5 Detector Degradation

The entire Hot-Laboratory measurement campaign was performed over the course of 1.5 months. Towards the beginning and the end, the M4 sample was measured in the same configuration (using the near setup). This allows to check for possible degradation in the detector leading to a lower detection efficiency. The count rate measured at the start of the campaign is $0.461 \pm 0.005 \text{ s}^{-1}$ and the one measured at the end of the campaign is 0.394 ± 0.002 . This corresponds to a reduction of approximately 15%, which is significant enough to require the detector to be re-calibrated several times during a long measurement campaign. The implications of this degradation for the detector are discussed in section 3.2.4. It should be noted here that the influence on the results presented in this chapter should be limited. Absolute results were always obtained by comparison to the ^{252}Cf source and data which was compared to each other was measured within relatively short time intervals (usually within a week). Details on the time of individual measurements can be found in appendix C. Unfortunately, the radiation exposure of the detector was not logged well enough over time to attempt a quantitative correction using these results.

5 Ongoing Development and Outlook

5.1 Other Envisioned Detector Applications

Fast neutron detection is useful for a number of applications apart from spent fuel characterization such as fast neutron imaging and tomography, homeland security, radiation protection, and nuclear reactor instrumentation. This section details some applications where the type of detector developed in this thesis could be used.

5.1.1 Fast Neutron Imaging

The most prevalent method of fast neutron imaging is currently to use a thin screen of plastic mixed with ZnS:Ag and a camera located at the back of the screen to capture the scintillation light [68]. Due to the opacity of the screen material (similar to the ZnS:Ag-epoxy mixture used in this thesis for the detector, but it depends on the ZnS:Ag content), only thin screens (thickness on the order of 1 mm) are feasible in this configuration. This severely limits the efficiency of such imaging devices. The small efficiency of the detectors is one of the main issues of fast neutron imaging.

As shown in section 3.5, the scintillation light of an event is concentrated on the WLSFs immediately around the neutron scattering position. This makes it possible to use the detector as an imaging screen. Individual neighboring fibers have a low crosstalk. Reading out every fiber individually should lead to largely independent pixels with a size of 0.7 mm. Further resolution improvements can be attained by reducing the pitch of the fibers. Doing so reduces the pixel size and also increases the crosstalk between neighboring channels allowing sub-pixel resolution by analyzing the distribution of the total light of an event between neighboring fibers. The thickness of the detector is essentially unlimited, allowing a much higher efficiency for neutron detection than the traditional approach with a thin screen and a camera. The WLSFs can also be used to guide the light towards the readout electronics. Depending on the exact layout, this can improve light collection significantly when compared to the traditional fast neutron imaging method.

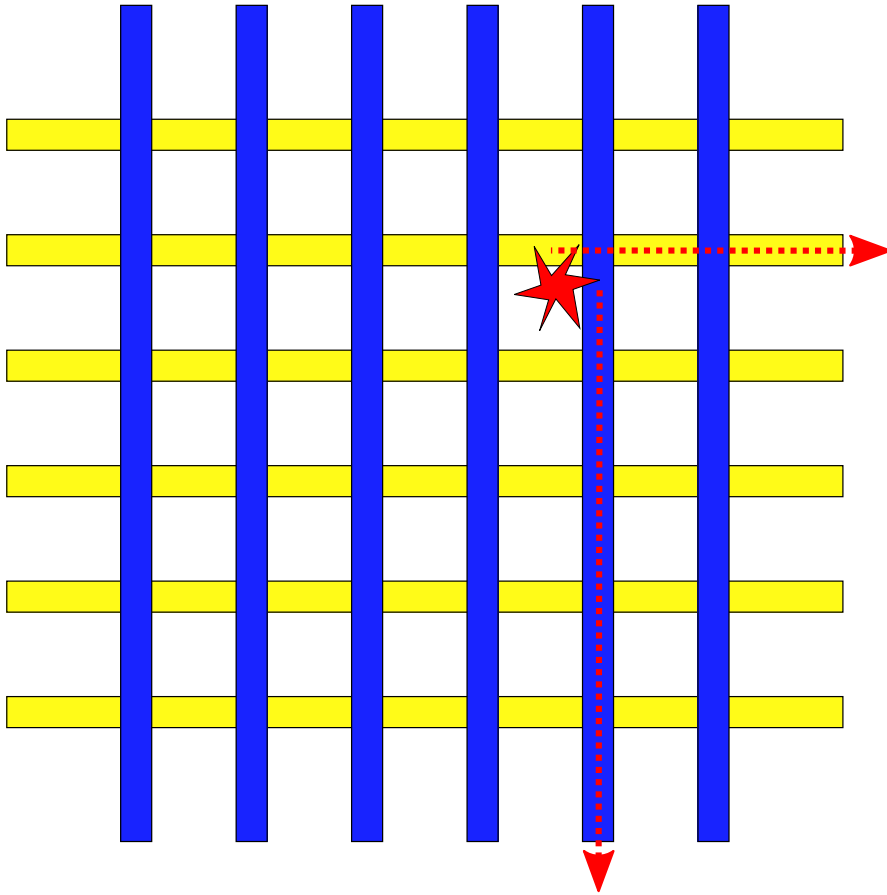


Figure 5.1: Illustration of the proposed imaging detector with crossed WLSFs (view in the direction of the neutron beam). The WLSFs marked blue are in front of the ones marked yellow. A neutron interaction in the ZnS:Ag mixture is marked in red. It is registered by one horizontal and one vertical fiber (marked by the red arrows).

One method of reducing the number of readout channels necessary for an imaging detector is to use coincidences. Instead of all of the WLSFs being parallel to the incoming neutron beam, a layout with two rows of WLSFs that run perpendicular to the neutron beam and to the fibers of the other row can be used. This layout is illustrated in figure 5.1. Neutron interactions which occur close to the crossing of two fibers can be detected in the channels for both fibers at the same time and the neutron interaction position can be reconstructed. For increased efficiency, this grid structure can be stacked along the direction of the neutron beam. WLSFs which have the same direction and are directly behind one another can be combined into a single channel to reduce the number of detection channels, or read out individually to get 3D information on the interaction position.

5.1.2 Fast Neutron Monitoring

Neutron monitoring frequently needs to be distributed over large areas or volumes. For such an application the detector design is well suited. The sensitive volume of every channel can have complex structures and extend over large areas and volumes while maintaining a uniform detection efficiency. The main limitation of the size of the sensitive volume of a single channel is the photon rate induced by the gamma ray interactions in the sensitive volume (see section 3.2.1). However, when using the MSD settings derived for high gamma environments in section 3.2.1 at natural background gamma levels, the size of a single channel sensitive volume is expected to be (almost) unlimited (extrapolation suggests more than 1 m³), but practical limitations like the length of fibers before losses are significant or the number of fibers which can be read out by a single channel still have to be considered. It has to be noted though that this sacrifices some of the intrinsic efficiency gains possible with smaller channels in low gamma environments (see section 3.3).

Another possible application is mobile neutron monitoring, for example using flying drones. The sensitive volume is robust and requires no additional heavy components (such as a moderator or a pressure tank). Large sensitive volumes per channel can be used to reduce the number of channels and thereby also reduce electricity consumption.

A possible application in homeland security is to look for illegal neutron emitting material. In this case, it is necessary to be able to capture as many of the emitted neutrons as possible, as illegal materials might be purposefully shielded to prevent detection. This means that large detectors with a high intrinsic efficiency are required. The high efficiency possible in low gamma environments with the detector design presented in this thesis is demonstrated in section 3.3. As mentioned above, the possible channel size is flexible and mainly limited by the expected gamma background and the desired intrinsic efficiency. Size, intrinsic efficiency, and cost would therefore have to be balanced to achieve optimal results for a homeland security system. In this application very low background rates are desired to avoid false alarms, so that issue would need to be studied in more detail to avoid, for example, any impurities of alpha-emitters within the detector volume which might create false counts.

5.2 Improvement of the Hot-Lab Measurement Station

This section describes improvements of the neutron emission measurement station used for the spent fuel measurements presented in this thesis (see chapter 4). These improvements concern the neutron detector but also the collimator and the sample positioning system. They aim at realizing new measurements at AHL to demonstrate the capability of the technology to measure axial neutron emission distributions with a 2 cm resolution for spent fuel with a shorter cooling time (less than couple of years), which is more representative of the typical spent fuel to be characterized. At the same time, they also aim at making measurements faster, easier to perform, and more reliable.

The current status of development of the different improvements varies. Section 5.2.1 details the improvements that are independent (to a large degree) of the detector development, and that concern the collimator and the sample positioning system. Section 5.2.2 focuses on improvements of, or directly related to, the detector.

5.2.1 New Collimator and Sample Positioning System Design

For the results obtained from spent fuel measurements at the AHL (see chapter 4), the collimator and the sample positioning system of the existing infrastructure for gamma measurements were re-used (see sections 4.1 and 1.1.3). Part of the infrastructure is not ideal for fast neutron measurements and albeit adequate for gamma emission measurements could benefit from an overhaul¹.

This section presents a new version of the collimator and sample positioning system, which has been designed as part of the thesis and is expected to start being manufactured soon. Viktor Boutellier from AHL, who is the primary operator of the gamma emission measurement system, was involved in the design process to ensure that the new system would integrate well in the hot-laboratory environment and yields at least the same level of precision and accuracy for the gamma emission measurements. Patrick Suter from the division of large research facilities (GFA) at PSI and Viktor Boutellier are responsible for the mechanical design. Together with the PSI responsible for the NEWS project Grégory Perret, I was responsible for the conceptualization, initialization and follow-up of the project. We defined in particular a coarse design, and ran particle transport simulations to ensure the adequate shielding of the collimator and adequate properties for the measurement. The following sections detail the individual issues encountered for neutron and gamma measurements and how they are addressed in the new version of the system. The focus here is on the coarse design that I conceptualized (and not on the mechanical details on which I had limited inputs and which are still subject to change at the time of writing).

Sample Position Detection

For repeatable measurements, the absolute position of the sample relative to the collimator has to be known. The sledge to which the sample is attached for a measurement is capable of relative movement with a precision between 0.1 mm and 0.2 mm. It is therefore enough to know the position of the sample at one position (preferably with an accuracy of 0.1 mm or better to take full advantage of the sledge movement accuracy). All other points can then be deduced by the movement of the sledge relative to that position.

The current system uses a laser which is pointing through the collimator opening at a mirror inside the measurement penetration. The mirror reflects the light back which can then be

¹contrary to the neutron measurements, the improvements for the gamma measurements are not primarily aimed at increasing the quality of measured results but improving usability, versatility, and reliability

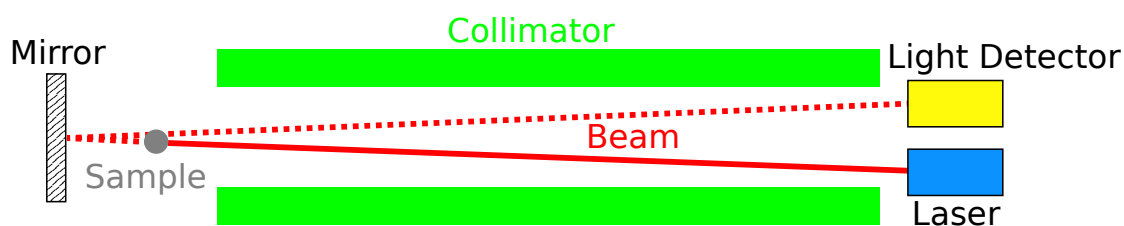


Figure 5.2: Side view of the current system to detect the position at which the sample tip is in front of the collimator. The solid part of the laser beam is always active, but the dashed part is blocked if a sample is in front of the collimator.

measured. If a sample is positioned in front of the collimator, the path of the laser to the mirror is blocked. The system is illustrated in figure 5.2. By slowly inserting a sample and checking the position at which the reflected laser light vanishes, the position of the tip of the sample can be measured.

This system has several limitations. First, the precision relies on the width of the opening of the collimator (the opening essentially defines the final size of the laser beam). While gamma emission measurements have typically an opening of 0.4 mm and therefore can reach an acceptable positioning accuracy, neutron measurements are intended to have a much wider opening of ~ 2 cm, resulting in an unacceptably low accuracy². Second, because the laser positioning system uses the same collimator opening as the measurement, the position of the sample has to be measured once at the beginning of an emission measurement. As the detector is behind the collimator for the gamma measurements, it is easy to place the laser in front of the gamma detector for the sample positioning and remove it for the measurement. For the neutron emission measurements on the other hand the detector is placed inside the collimator opening for an adequate detection efficiency, making it impossible to use the laser system in this configuration and complicating the measurement campaign³. Third, because the height of the samples is not well controlled, mostly due to varying sample rigidity and diameter, the laser can be slightly misaligned with the sample, which in the case of conic sample tips translates in slight errors in axial positioning. Finally, the system is sensitive to small mechanical deformations. The alignment of the mirror especially can be easily changed accidentally, causing the laser beam to no longer be reflected correctly and making the measurement impossible.

The new system uses a camera based detection of the sample tip. It is illustrated in figure 5.3. The camera looks via a mirror and through a dedicated channel (called camera channel) in the collimator at the inside of the measurement penetration. The introduction of the mirror at the back of the collimator puts the camera out of the direct path of radiation from the sample. A white surface, which is angled to be well illuminated by the light from the normal hot-cell

²Note that for the results obtained in chapter 4, a labor intensive alternative solution was performed to reach a high accuracy in sample positioning. That procedure is not adequate for routine measurements.

³Indeed, for radio protection reasons it is not feasible to remove the detector from inside the collimator for the position measurement

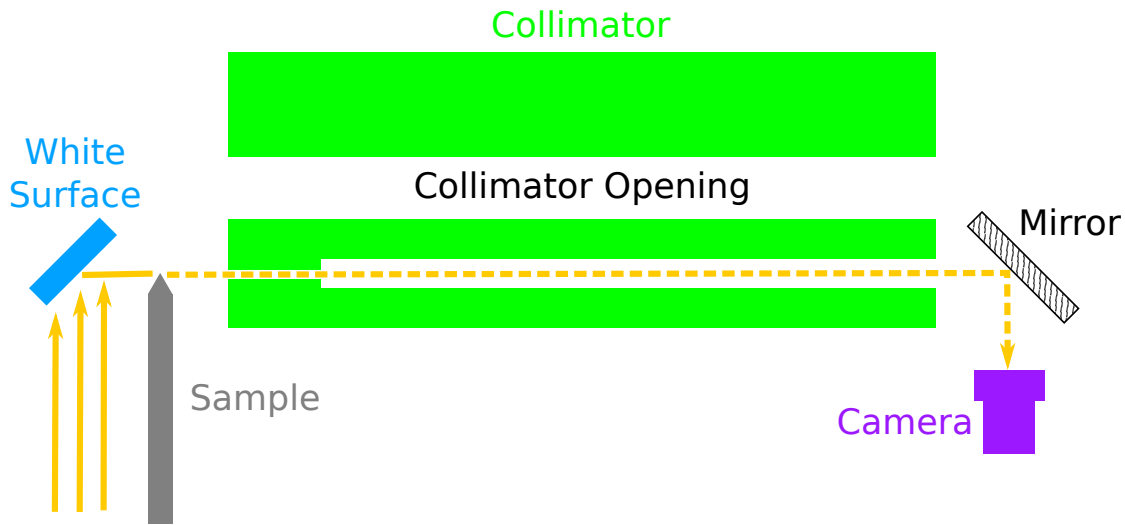


Figure 5.3: Top view illustration of the new camera based tip position detection method. The camera looks via a mirror at a white surface. The white surface is illuminated by light from the already installed normal ho-cell lighting. As soon as the sample moves in the path of the light, the path to the camera (dashed yellow line) is cut.

illumination, acts as a bright background for the camera. The sample, which is either dark or reflects the dark interior of the measurement penetration, gives a clear contrast in front of the white surface. The narrowest region of the camera channel is at the front of the collimator. This defines the slit through which the camera can see the sample. The exact dimension of the slit is not fixed yet but values on the order of 0.1 mm are considered.

Since the camera uses a dedicated channel through the collimator instead of the main collimator opening, this solution is suitable for any measurement, including measurement which could be developed in the future, with little to no adjustment needed. The problem of the varying height of the sample is solved since the camera is not limited to a single spot. The channel to which the camera looks at the sample is 2 cm high. This is significantly more than any expected height variation and should allow the camera to accurately capture the tip of any sample. This system also allows to check the height of a sample during measurement. Although generally not needed, this represents a useful feature in case of heterogeneity of the rod. The angle and position of the white surface is not critical, making the system more robust than the laser based system. While small changes in the camera angle and position can shift the pixels in the image of the sample, it is possible to correct this in the software acquiring the image. A program can for example look for the bright slit in the image, which corresponds to the path of light through the camera channel, and then take all pixels in relation to the slit.

A simplified mock-up of the new positioning system has been built and tested. This mock-up includes a 3D printed replica of the camera channel with a 0.2 mm slit at the front, a white surface as background, a sharp pencil as a sample (approximating the conic sample tip), and the camera foreseen in the real design (a raspberry pi hi quality camera [69] with a

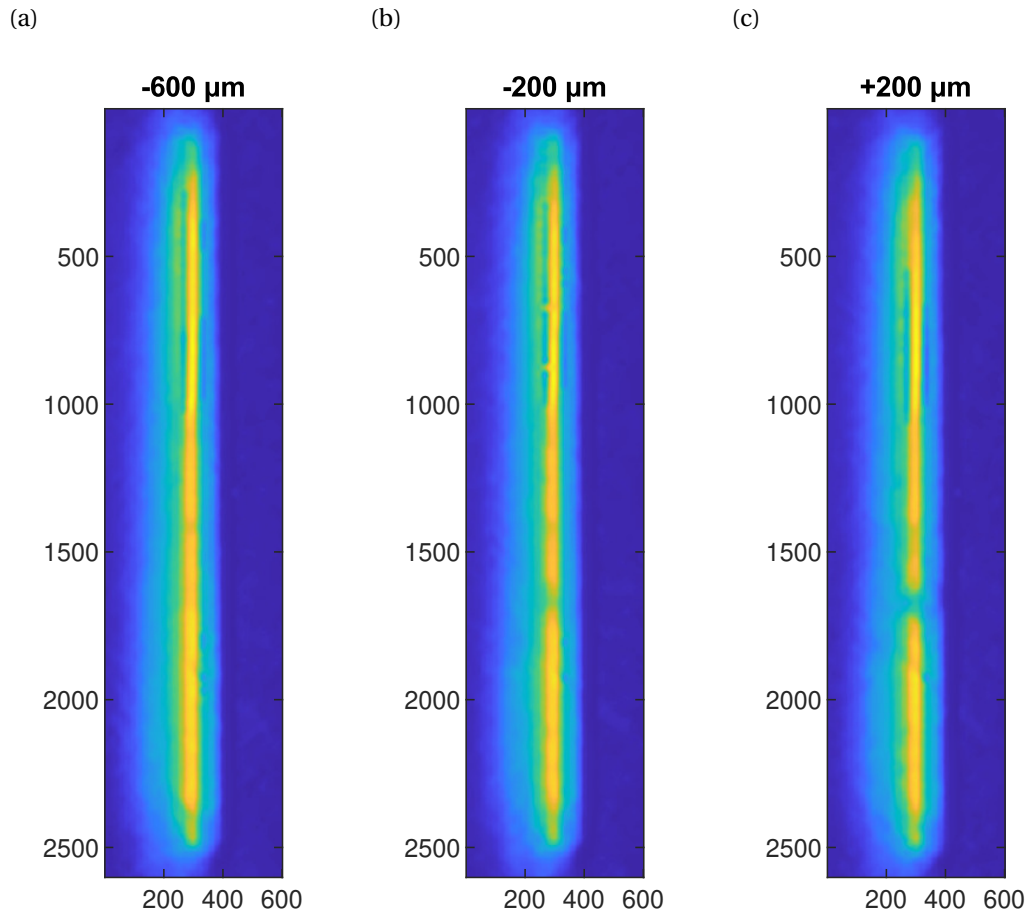


Figure 5.4: Images taken with the mock-up tip detection system with the sample (pencil) at different positions (marked at the top of the image). The zero position is roughly when the tip is directly in front of the camera channel, but only with a precision of ± 0.5 mm. The color indicates the light level from low (dark blue) to bright (yellow). The numbers mark the pixel positions. The dark region from the tip of the sample is faintly visible in (b) and clearly visible in (c) at a height of ~ 1700 pixels.

PT3611614M10MP telephoto lens [70]). The mirror and all other parts of the collimator were not included to simplify the test setup. The sample (pencil) was moved in small steps in front of the camera channel. At each step, a picture was taken. Figure 5.4 shows several images with the sample at different positions. From the images, the sample position can be determined by eye with an accuracy of at least 0.8 mm (probably even 0.4 mm). This is a similar accuracy as for the laser based system. Note that the pencil tip was also much sharper than the tip of a fuel sample, making it likely that the position of a real fuel sample can be determined with better accuracy.

One way of increasing the accuracy of the tip position determination is by using a post-processing algorithm. Such algorithm could have, for example, the following steps. In a first step, the data is limited to the region of the slit, cutting out any noise from the uninteresting region on the sides. The slit is too thin for a realistic chance to get any horizontally resolved data (based on the numerical aperture imposed by the 0.2 mm slit, the maximum possible resolution at the sample position is also about 0.2 mm). In a next step the image pixels are therefore averaged horizontally to get an average light level for every height. The data is then normalized at every height to the light level recorded at the same height without a sample (correcting for potential heterogeneity in the setup), and normalized at every sample position to the overall light level of the picture taken at that position (correcting for any overall light intensity changes). The result of this is shown in figure 5.5.

The deepening of the dip associated with the sample crossing the slit is clearly visible. The main part of the dip lies between pixel positions 1220 and 1320. The change of the total light level in this region as a function of the sample position is shown in figure 5.6. There is a sharp drop of the light level at a sample position of -0.5 mm. Within 0.1 mm the value changes significantly more than any of the noise fluctuations before that. If the start of this drop is used as a reference, the sample position can be determined with a reproducibility of 0.1 mm, which is the best possible value with the current sledge positioning precision. The mock-up system is not precise enough with the absolute sample position to determine if the result is also accurate to 0.1 mm (as the absolute positioning of the mock-up sample was only precise to ~ 0.5 mm). If the positioning has a bias, a reference measurement with a sample with a similarly shaped tip could be used to measure this bias so that it can be corrected for in the future. This would ensure that 0.1 mm accuracy can be reached. This system therefore also represents an improvement on the sample positioning accuracy.

Sample Guiding System

The current system does not feature any supports for a sample on the side of the collimator towards the hot-cell extension. This is not optimal for reliable sample positioning as the stiffness and weight of the sample influences the height at the position in front of the collimator. Additionally, more flexible samples tend to bend more and more downwards when inserting them further into the extension. Another problem is that the distance between the sample and the tip of the collimator is known only with limited precision (~ 5 mm).

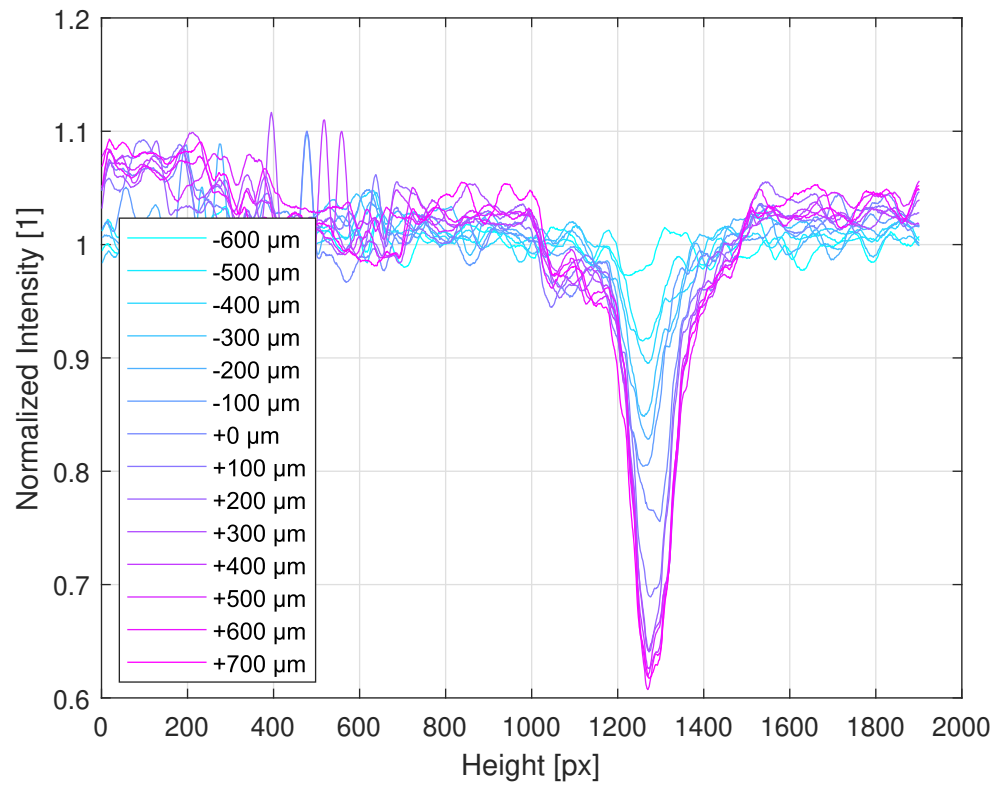


Figure 5.5: Normalized light intensity measured for every height position in the slit and for different sample positions.

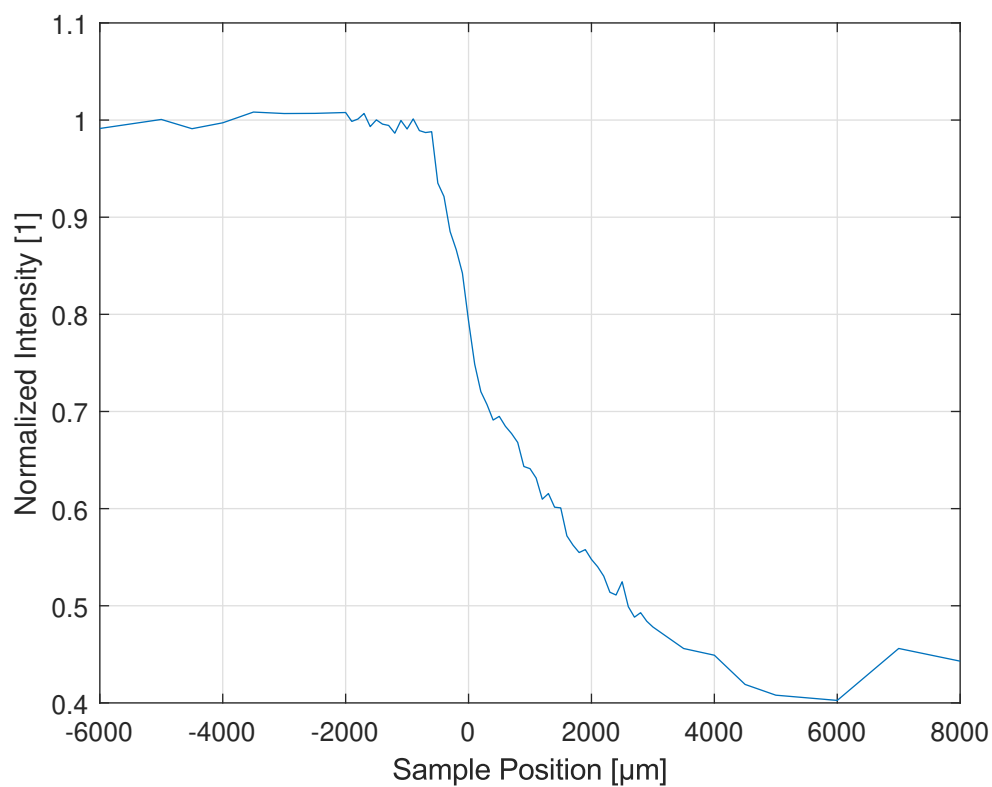


Figure 5.6: Normalized light intensity in the region of the slit that is on the height of the tip of the sample. There is a sharp drop at an axial sample position of $-500 \mu\text{m}$. This drop is significantly larger than the random oscillations for positions $< -500 \mu\text{m}$

The new guiding system has several supports inside the measurement penetration, on both sides of the collimator. This should hold the sample at the same height, independent of weight, flexibility, and its position. All supports are fixed on a plate, which also features a bayonet mount to directly connect the new collimator to the plate. The relative position of the collimator and the sample guiding system is therefore clearly defined.

Improved Neutron Collimation

The current collimator is designed for gamma emission measurements, and its ability to stop neutrons coming from the side of the region of interest is unsatisfactory for a high precision neutron measurement. The current collimator is made of materials with mostly heavy elements such as stainless steel and tungsten. Fast neutrons which scatter with these elements lose very little kinetic energy in the process. Even after multiple scattering interactions, the neutron still has enough energy to be detected.

The new collimator design has thick blocks of high density polyethylene at the sides of the collimator opening. The light elements (most prominently hydrogen) slow down the neutrons much more effectively to a level where they are much less likely to be detected. This improves the collimation significantly. Further improvements are achieved by adding blocks of high density polyethylene to the sides of the collimator, inside the measurement penetration. The geometry is illustrated in figure 5.7. To quantify the effect on the point spread function (see sections 4.3.1 and 4.3.3), the setup was simulated using MCNP-6.2 [14] and ENDF/B-VII.0 [47] together with the energy-dependent efficiency derived in section 4.3.2 (i.e. a constant efficiency with a threshold value of 1.5 MeV). The results are shown in figure 5.8.

The improvement of the point spread function is significant. The contribution to the side of the center region is much lower. This should make the reconstruction easier and therefore more reliable for the same measurement time.

Convenient and Flexible Gamma Collimation

It is a substantial effort to set or check the opening of the current collimator with the required precision for a gamma emission measurement. It necessitates the removal of the collimator from the collimator penetration, and reinsertion afterwards. This is made even more difficult by the fact that the collimator has no significant provisions to help with removal and insertion. There has for some time been the desire to switch to a system that can set the opening width in a more robust way.

The new collimator design has no moving parts to adjust the width of its opening. Instead, it has provisions for inserts into the collimator (similar to the detector for fast neutron emission measurements, see section 5.2.1). For gamma measurements, there will be an insert which narrows the opening to a desired fixed width (e.g. 0.4 mm to match the current default). This makes the opening more precise and reliable. These inserts are easy to handle, and they

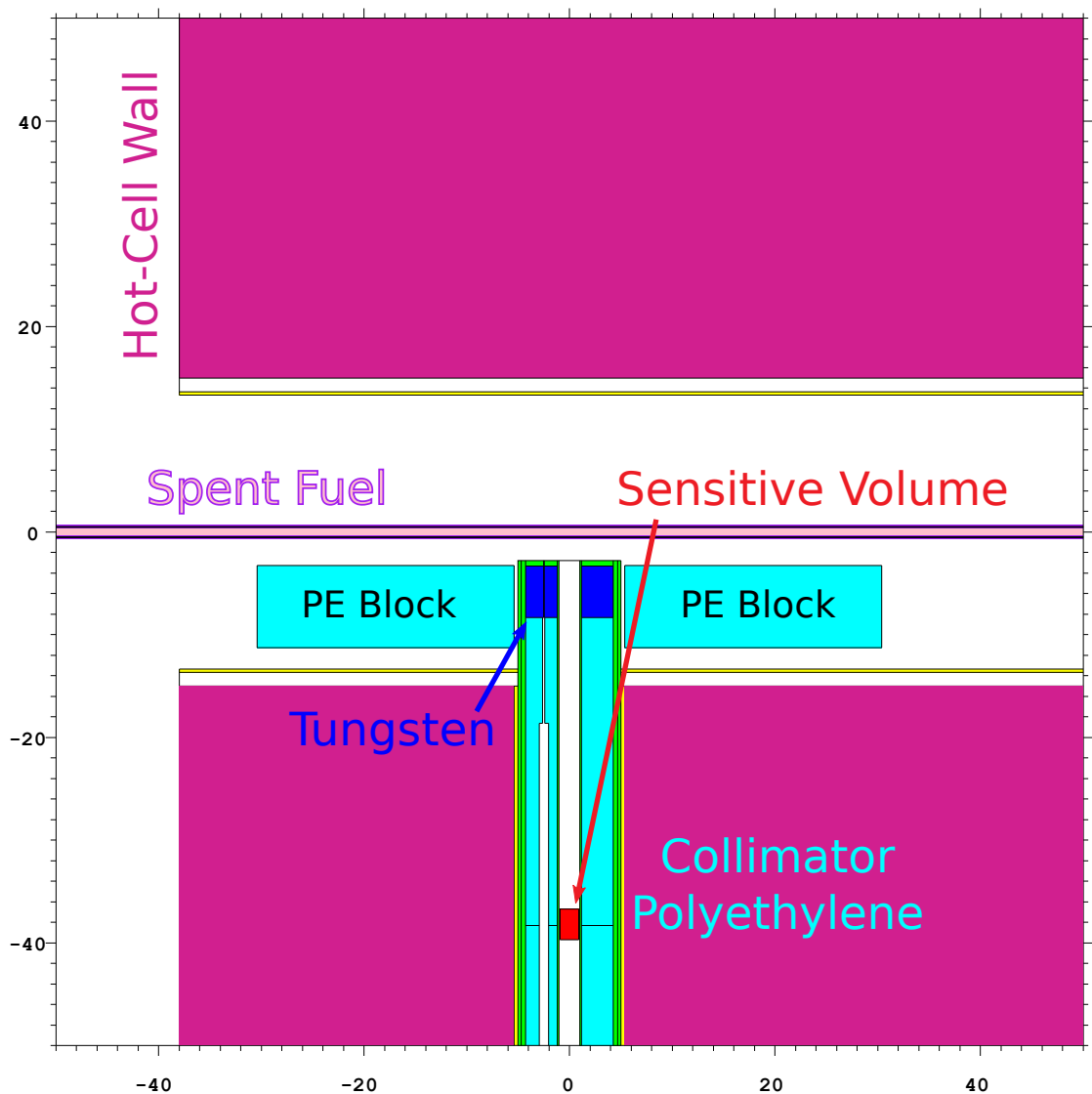


Figure 5.7: Illustration of the moderator layout for the new collimator design with measurements in cm. The polyethylene moderator is present in the collimator and in the form of two blocks inside the measurement penetration. The tip of the collimator is made of tungsten to block gamma rays. An sensitive volume at a distance of 367 mm to the center axis and a spent fuel rod are shown as a reference.

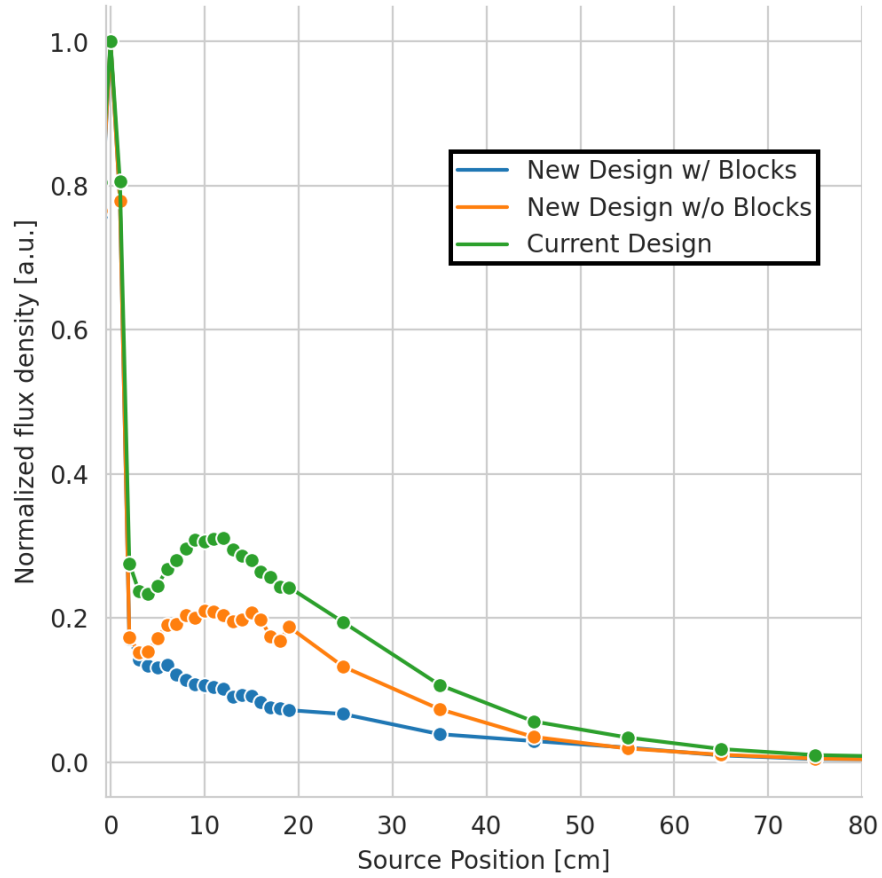


Figure 5.8: Point spread functions for the new collimator with and without the additional moderator blocks in the measurement penetration. As a comparison the point spread function for the current collimator is shown as well. The y -axis is the normalized flux density of neutrons with an energy above 1.5 MeV for a sensitive volume at a distance of 36.7 cm from the center axis.

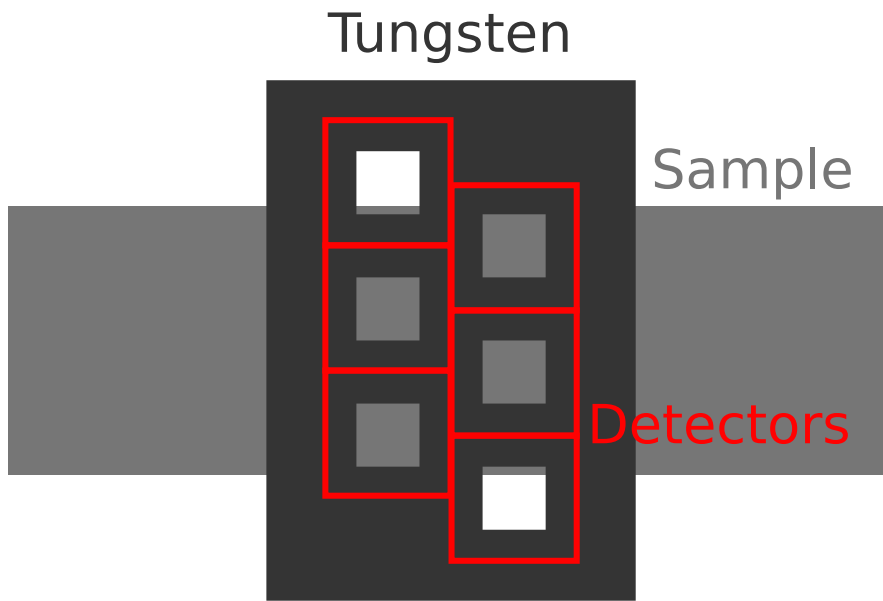


Figure 5.9: Illustration of a possible geometry of a collimator insert for gamma emission tomography.

are easier (and cheaper) to manufacture than a full collimator with a fixed width opening. This allows to have several inserts with different openings to be easily made available should there ever be a need. The individual inserts can easily be removed and inserted between measurements (e.g. for performing successive neutron and gamma emission measurements).

The flexibility of the new collimator also makes investigating new measurement techniques that require a different insert geometry easier. An interesting example is passive gamma emission tomography of a single fuel pin (similar to [71]). A possible geometry for such an insert is shown in figure 5.9. Multiple detectors could be connected to different openings in a tungsten insert. Half of the pixel for the tomography would be blocked for collimation purposes but could be accessed by shifting the sample. Rotating the sample around its axis would yield all the different projection angles needed for the reconstruction.

5.2.2 New Detector

While the Hot-Lab Prototype 1 performed well during the spent fuel measurements (see chapter 4), there are three areas which are intended to be improved for a new detector for spent fuel measurements. These are the fraction of neutrons detected, the radiation damage, and the gamma rejection. The design process of a new detector for spent fuel measurements is currently ongoing. The main reason for this is to wait for the results of the degradation measurements of the WLSFs and the epoxy (see section 3.2.4), and to further test possible replacement materials to improve radiation resistance. The information in this section represents a combination of the current design status and recommendations for its continuation.

The simplest change to the detector design that improves the number of detected neutrons is to increase the solid angle covered by the detector. Space for a detector in the old collimator is limited to about 1.8 cm by 1.8 cm. The new collimator has an opening of 2 cm (width) by 5.5 cm (height), representing an almost 3.5 times larger surface for the detector. The width of 2 cm means that the achievable resolution should be similar to or better than the one of the current collimator setup (see section 4.4.3). The four channels of the Hot-Lab Prototype 1 together only cover an area of $\sim 1 \text{ cm}^2$ due to the significant distance put between the channels. The measurements presented in section 3.5 show that the channels can be packed directly adjacent to each other with manageable crosstalk, or with a single empty fiber position between them for negligible crosstalk. While it is unlikely that the entire 11 cm^2 of the new collimator opening can be used due to the required structural elements, an increase of the covered area by a factor of 9 to 10 is probably possible.

The size of each channel is planned to be reduced. Although the final number of WLSFs per channel is still under investigation, 9 WLSFs are currently targeted (compared to 49 for the Hot-Lab Prototype 1, see section 2.2.2). The smaller channel size reduces the total gamma flux entering each channel, thereby also decreasing the photon rate for each channel (see section 3.2.2). For spent fuel with a short cooling time, this would help to compensate the increased gamma output of the fuel (and the increased photon rate associated with that). For spent fuel with long cooling times, the lower gamma influence could be used to switch to a less strict neutron event filter setting, increasing neutron detection efficiency (see for example sections 2.1.3, 3.2, and 3.3). The increased detector area and decreased channel size lead to a significant increase in the number of channels. To read out all the channels, a new version of the detector electronics is currently being developed (see section 5.3.1).

Regarding the radiation resistance of the new detector, more radiation resistant light guides (see section 3.2.4) can almost certainly be found to replace the current ones. However, it is less likely that the degradation of the detector head (see section 3.2.4) can be mitigated in time for the construction of the next prototype. In that case, frequent checks with a reference source will have to be made during a future measurement campaign to adjust for the reduction in efficiency. If fuel rods with high gamma emissions are measured, additional shielding in front of the detector will likely be required to keep the total damage to the detector limited and keep the measurement times acceptable. One possible target for a measurement campaign would be to limit the total gamma exposure to $\sim 2 \cdot 10^{13} \text{ cm}^{-2}$. This gamma fluence from ^{60}Co lead to a $\sim 40\%$ decrease in efficiency during the measurements presented in section 3.2.4.

5.3 Electronics and Software Development

This section contains information on the current development of the detector electronics and the associated software. These development are not tailored to the spent fuel measurements at the PSI hot-laboratory, but instead are intended to be application independent improvements. Section 5.3.1 gives information on the development of the new detector electronics and

section 5.3.2 discusses the development of new filter algorithms that could replace the MSD algorithm.

5.3.1 SPIDER Project

The SPIDER (Scintillation Particle Identification using Digital Electronics Readout) project has been launched in 2021 to create improved electronics for the detector readout. It is a collaboration with the Electronics for Measurement Systems (EMS) group of the Research with Neutrons and Muons (NUM) division at PSI. The goal is to improve reliability, scalability, and user-friendliness of the electronics. The current electronics (see section 2.3) uses multiple boards with no special provisions to help with cable or space management. This makes them unsuitable for detectors with many channels. The large number of boards and connections which have to be set up and changed manually to perform measurements also makes the current electronics unsuitable for use by a non-expert. Some parts of the current electronics such as the threshold for the discrimination are quite sensitive and have led to problems several times in the past. The new electronics should be more robust. The electronics development is done by Michael Müller, Elmar Schmid, and Urs Greuter from EMS. My responsibilities in the project were to set and review the requirements that the electronics should meet, give inputs from my experience from building and using the current electronics, regularly check on the progress, and solve any issues concerning the interface between the electronics and the rest of the detector or the user. The project is currently ongoing, there is not yet a usable prototype of the electronics. As such none of the results described in other sections were obtained using any part of the electronics described in this section. Additionally, most of the implementation details are not yet fully defined. Details on the SPIDER project and its current status can be found in appendix D.

5.3.2 Alternative Digital Filter Algorithms

This section presents some advanced filtering techniques currently being researched. They have not yet been robustly tested with experimental data and as such no performance evaluation is presented. The purpose of the techniques is to improve on the MSD algorithm (see section 2.1.3) in terms of discrimination between neutrons and noise/gammas, or to remove the dependence of the MSD algorithm output on the photon rate (see section 3.2.3).

Continuous Ordinary Least Squares

The first step of the continuous ordinary least squares is to divide the measurement time into small intervals i of length Δt and to count the number of photon pulses q_i in every interval, just as described for the MSD algorithm in section 2.1.3. At this point it would also be an option to add the single photon dead time correction described in section 5.3.2.

For every interval i , the algorithm takes the m subsequent intervals and tries to fit the decay

shape of the ZnS:Ag scintillator for proton activation to the numbers of photons recorded in these intervals. The value of m can be chosen as any positive integer. It is a filter parameter which can be optimized. The decay shape of ZnS:Ag can for example be extracted from the data shown in figure 3.20. The method used for the fit is ordinary least squares with the scaling of the decay function as the only parameter. If the decay function of the ZnS:Ag is $a(t)$ for a time t after the activation, the scaling d_i^* resulting from ordinary least squares becomes:

$$d_i^* = \frac{\sum_{j=i}^{i+m-1} q_j \cdot a((j-i) \cdot \Delta t)}{\sum_{j=i}^{i+m-1} a((j-i) \cdot \Delta t)} \quad (5.1)$$

The denominator is a constant expression and for simplification a new value d_i can be defined which only includes the nominator:

$$d_i = \sum_{j=i}^{i+m-1} q_j \cdot a((j-i) \cdot \Delta t) \quad (5.2)$$

Implementations of multiplications are expensive in FPGAs. One solution to implement the filter on an FPGA would be to compute the value of $q_j \cdot a(i \cdot \Delta t)$ for all possible q_j and all $0 \leq j < m$ in advance and save them in a lookup table. The filter could then simply extract these values from the lookout table. Another approach would be to use a simplified ZnS:Ag decay function. For the purposes of the filter, the decay of the ZnS:Ag can be approximated as a single exponential decay. This simplifies $a((j-i) \cdot \Delta t)$ to $e^{-\alpha \cdot (j-i) \cdot \Delta t} = (e^{\alpha \cdot \Delta t})^{i-j}$ with a fixed value α .

$$d_i = \sum_{j=i}^{i+m-1} q_j \cdot (e^{\alpha \cdot \Delta t})^{i-j} = (e^{\alpha \cdot \Delta t})^{1-m} \sum_{j=i}^{i+m-1} q_j \cdot (e^{\alpha \cdot \Delta t})^{i+m-1-j} \quad (5.3)$$

Since $(e^{\alpha \cdot \Delta t})^{1-m}$ is a constant, this can be simplified by defining $d'_i = d_i (e^{\alpha \cdot \Delta t})^{m-1}$.

$$d'_i = \sum_{j=i}^{i+m-1} q_j \cdot (e^{\alpha \cdot \Delta t})^{i+m-1-j} \quad (5.4)$$

The filter will receive q_j values with a low value of j first. These are currently at the beginning of the sum. We can change the summation order to put the values which are received later towards the beginning of the sum, i.e. with $j' = i + m - 1 - j$:

$$d'_i = \sum_{j'=0}^{m-1} q_{i+m-1-j'} \cdot (e^{\alpha \cdot \Delta t})^{j'} \quad (5.5)$$

Each value of q_j gets multiplied by $e^{\alpha \cdot \Delta t}$ every time a new q_j is received. Within the range of the sum, all of the values with the accumulated factors of $e^{\alpha \cdot \Delta t}$ are summed up. This means that the calculation of the filter is reduced to summation and multiplication with a factor of $e^{\alpha \cdot \Delta t}$. While multiplication in general is expensive to implement on FPGAs, special cases can be easy to implement. If one of the factors is a power of 2, the multiplication becomes a bit

shift, which is easy to implement. By extension, if one of the factors is a short sum of powers of 2 (e.g. $2.25 = 2 + \frac{1}{4}$), the multiplication becomes a short sum of bit shifted values, which is also easy to implement. If Δt is chosen such that $e^{\alpha \cdot \Delta t}$ becomes an easy factor for multiplication, the filter can be implemented on an FPGA with an acceptable use of resources.

After d_i or d'_i (depending on the chosen implementation) is calculated, a threshold k is set for d_i/d'_i and events are recognized if that threshold is crossed in the same way as for the MSD algorithm presented in section 2.1.3.

Single Photon Dead Time Correction

Single photon dead time correction is a mechanism to reduce the impact of the photon rate on the detector efficiency (see section 3.2.1). It will be explained here by combining it with the MSD algorithm (creating a dead time corrected MSD algorithm), but the method can be added to other filter algorithms as well. As discussed in section 3.2.3, the photon rate influences the event recognition by individual photon pulses arriving too close to each other to be distinguishable. Essentially, each photon pulse creates a dead time within which no other photon pulse can be registered. The expected number of registered pulses q_i over a time interval of length Δt is related to the true number of photon pulses q_i^* by the formula for the paralyzable dead time model [72, 4-VII]:

$$q_i = q_i^* \cdot e^{-\frac{q_i^*}{\Delta t} \tau} \quad (5.6)$$

Here τ is the dead time of each photon pulse. This equation assumes a random distribution of photon pulses which is uniform over the entire length of the interval. The single photon dead time correction mechanism essentially applies the reverse of this equation to the count rate measured within an interval before forwarding the result to the subsequent filter algorithm. The applied function $f_{\Delta t, \tau}$ gives the average number of initial photon pulses for a measured number of pulses. Assuming a low true number of photon pulses ($q_i^* \ll \frac{\Delta t}{\tau}$), f can be approximated as [72, 4-VII]:

$$f_{\Delta t, \tau}(q_i) = q_i^* = q_i \frac{2}{1 + \sqrt{1 - 4 \frac{\tau}{\Delta t} q_i}} \quad (5.7)$$

For the dead time corrected MSD algorithm, equation 2.1 becomes:

$$d_i = \sum_{j=i-m+1}^i f_{\Delta t, \tau}(q_j) - \sum_{j=i-2m+1}^{i-m} f_{\Delta t, \tau}(q_j) \quad \forall i \in V_{\text{MSD}} \quad (5.8)$$

For implementation in an FPGA (where divisions, multiplications and square roots are expensive to compute), the different values $f_{\Delta t, \tau}(q_j)$ can be computed in advance for all possible q_j values. The results can then be saved in a lookup table, read for quick access during execution of the filter algorithm.

6 Conclusion

The main goal of the thesis was to develop a system for neutron emission measurements of spent fuel rods with a fine axial resolution. A novel fast detector was developed for these spent fuel measurements. While the motivation for the detector development was its envisioned application for the spent fuel measurements, it became clear during development that the properties of the detector make it (or variants of it) a suitable candidate for other applications as well. This opened a second line of investigation to characterize more general properties of the detector, as preparation for its anticipated use in other fields.

Section 6.1 summarizes the main results of the detector development. This includes developments aimed at spent fuel measurements as well as other research. Section 6.2 focuses on the main results derived from the development of the spent fuel measurement station in its entirety. Finally, section 6.3 summarizes the current state of the development of an upgraded measurement system to be used in the future.

6.1 Detector Development

The developed detector design uses a sensitive volume made of a mixture of optical epoxy and ZnS:Ag, with WLSFs embedded in it (see section 2.2). This structure is a continued development from previous detector designs that had the WLSFs embedded in machined plastic sheets. The structure allows uniform light collection over large volumes of the ZnS:Ag-epoxy mixture. The readout electronics uses a digital filter algorithm based on single scintillation photon counting (see sections 2.3 and 2.1.3). This approach is versatile. It allowed the filter to be implemented on an FPGA, where the filter algorithm can be changed without any electronics redesign. It also facilitates the development of new and complex filters (see sections 2.4.1 and 5.3.2), since a digital filter can be perfectly simulated without detailed knowledge of the electronics.

The ability to simulate the filter was used extensively during the detector characterization (chapter 3). The moving sum after differentiation (MSD) algorithm was chosen as the basic

filter and many different combinations of its parameters were simulated on measured raw scintillation photon data. This greatly facilitated the search for well performing MSD parameter choices. Test cases for different scenarios were developed and appropriate data sets were gathered.

The most intensively investigated scenario, due to its relevance for the spent fuel measurements, was the one of a measurement with a high gamma background (section 3.2). The detector showed its capability of measuring neutrons from a ^{252}Cf source with an intrinsic efficiency of $\sim 1\%$, while ignoring gamma rays from a 120 MBq ^{60}Co source directly adjacent to the detector (estimated average gamma flux density of $\sim 5 \cdot 10^6 \text{ cm}^{-2}\text{s}^{-1}$). Special care was taken to measure the influence of the presence of gamma rays on the detector efficiency, measuring it once with ^{60}Co and ^{252}Cf sources, and once with gammas and neutrons from spent fuel. As a result of these measurements, a correction function was produced, allowing consistent measurements in different gamma environments. The parameter for this correction function (the photon rate) can be measured directly by the detector itself, the gamma environment therefore does not have to be known from other sources to be able to apply the correction. Another scenario under investigation was the optimization of the neutron detection efficiency in a low gamma environment (tested with a 2.1 MBq ^{137}Cs source at 7.5 cm distance). A combination of parameters for the MSD algorithm was found which lead to a high intrinsic efficiency above 11% for neutrons from a ^{252}Cf source (see section 3.3). The third scenario was an optimization of the timing precision of registered neutron events. Analyzing the time dependency of the light recorded in the time intervals around recorded events, the timing precision was estimated to reach about 60 ns for the chosen MSD parameter values (see section 3.4).

Properties of the detector design that are not associated with an optimization of the MSD parameters were investigated as well. The decay shape of the scintillation light was measured (see section 3.4.3). By reading out individual fibers, the crosstalk between individual WLSFs in the sensitive volume was estimated (see section 3.5). Four fibers were placed in a line to measure the dependency of the crosstalk on the distance. About 5% of the events detected in one fiber were also detected in a directly adjacent fiber (center to center distance of 0.7 mm between the fibers). The measured crosstalk for next-nearest neighbor (center to center distance of 1.4 mm) and farther away fibers was negligible. The detector was subjected to intense continuous gamma fields to measure and isolate radiation damage in the detector materials (see section 3.2.4). Significant radiation damage was observed for the light guides, which can probably be switched out for more radiation resistant versions. Radiation damage in the sensitive volume was observed to cause a loss of $\sim 40\%$ after ^{60}Co irradiation with an accumulated fluence of $1.8 \cdot 10^{13} \text{ cm}^{-2}$. If not addressed in future detectors, this would mean that the sensitive volume would have to be exchanged for fresh ones frequently if the detector is subjected to strong gamma fields. It would, however, not make measurements in strong gamma fields impossible. Investigations to isolate the material in the sensitive volume responsible for the degradation and research into alternatives (some promising possibilities have already been suggested) are currently ongoing (see section 3.2.4).

6.2 Spent Fuel Neutron Emission Measurements

A measurement station for spent fuel pins was set up in the PSI Hot Laboratory (see section 4.1). Its performance was tested using fuel samples with a neutron emission known from previous measurements carried out with a thermal detector, a moderator block and a ^{252}Cf source. The spent fuel samples had a length of 40 cm and were cut from MOX and UO_2 spent fuel rods irradiated at the Swiss nuclear power plant of Gösgen (KKG). The burn-up of the samples covers a range of 40 GWd/t to 90 GWd/t and had a cooling time of ~ 25 y at the time of measurement (see section 4.2). The relative neutron emission of the samples were measured with in two configurations and the results agreed well with each other. These results also agree well with the relative neutron emission measured previously with the thermal neutron detector. Most of the relative neutron emissions agree within a single standard deviation and all of them agree within two standard deviations of each other (see section 4.4.2). For the absolute neutron emission, the agreement is slightly worse and some trends are visible in the measured data, indicating potential imperfections in the measurement setup or its characterization. The agreement between the different measurements is still acceptable, being within two standard deviations when comparing the measurements of this thesis to each other and within 2.5 standard deviations when comparing them to the previously measured values (see section 4.4.2).

The standard deviation of the individual absolute neutron emission values is about 5%. A significant portion ($\sim 4\%$) of this uncertainty comes from the ^{252}Cf source that was used as an absolute reference. The source is almost 35 years old and its activity cannot be determined from its documentation alone. As such its neutron output was measured by comparing it to a well known reference source. Unfortunately, repeated measurements did not produce reproducible results and this dispersion was accounted for by an increased uncertainty (see section 3.1). Future measurements could be significantly improved by using a fresher and better characterized source.

The main goal of the spent fuel measurement station is to be able to gather axially resolved information on the neutron emission of spent fuel pins. The ^{252}Cf source was used to measure a point spread function (i.e. how the neutrons from the sample are collimated). This point spread function had a full width at half maximum of ~ 2.5 cm, indicating that a similar axial resolution can be expected (see section 4.3.1). This was tested using a spent fuel sample, which was moved in small steps, measuring the neutron flux at the detector in each position. From this data, the distribution of the neutron emission in the sample was reconstructed. Based on the reconstructed edges of the sample, the achieved resolution was estimated to be 2.5 cm. This is in accordance with the expectation from the point spread function and is acceptably close to the targeted resolution of 2 cm. The capabilities of the system in terms of axial resolution have therefore been successfully demonstrated (see section 4.4.3).

6.3 Development of an Improved Measurement System

An improved version of the measurement system has been conceptualized (see section 5.2). This new version should improve measurement times, resolution, and ease of use. Its development continues in the context of the running NEWS collaboration between swissnuclear and PSI.

A new positioning system should lead to a better controlled sample position relative to the collimator and any detector used with the system. This is achieved by introducing supports on both sides of the collimator and by a locking mechanism between the collimator and the sample guiding system. The axial position of the sample is determined via a camera setup, which is more robust than the laser based system currently in use. Preliminary tests suggest that the accuracy of the new camera system is at least as good as the one of the laser based system and could reach the limit of 0.1 mm imposed by the sledge moving the fuel rod.

The new system has improved collimation for neutrons by introducing hydrogen-rich moderator regions inside the collimator and in the measurement penetration. This is expected to lead to an improvement in the reconstructed neutron emission profiles. At the same time, the new collimator is designed for larger detectors, which lead to a higher count rate and therefore faster measurement times.

With respect to gamma emission measurements, the new collimator is expected to improve the ease of use with the new positioning system and the use of inserts with fixed apertures. At the same time its modularity also allows easier development of capabilities for new types of gamma measurements such as gamma emission tomography.

Some design considerations for a new neutron detector have also been made. The new detector should utilize the increased space offered by the new collimator design (see above). It should also feature smaller channels to reduce its gamma sensitivity. The new detector will need some shielding to reduce radiation damage. The exact amount of shielding will need to be determined based on the gamma activity of the fuel which should be measured.

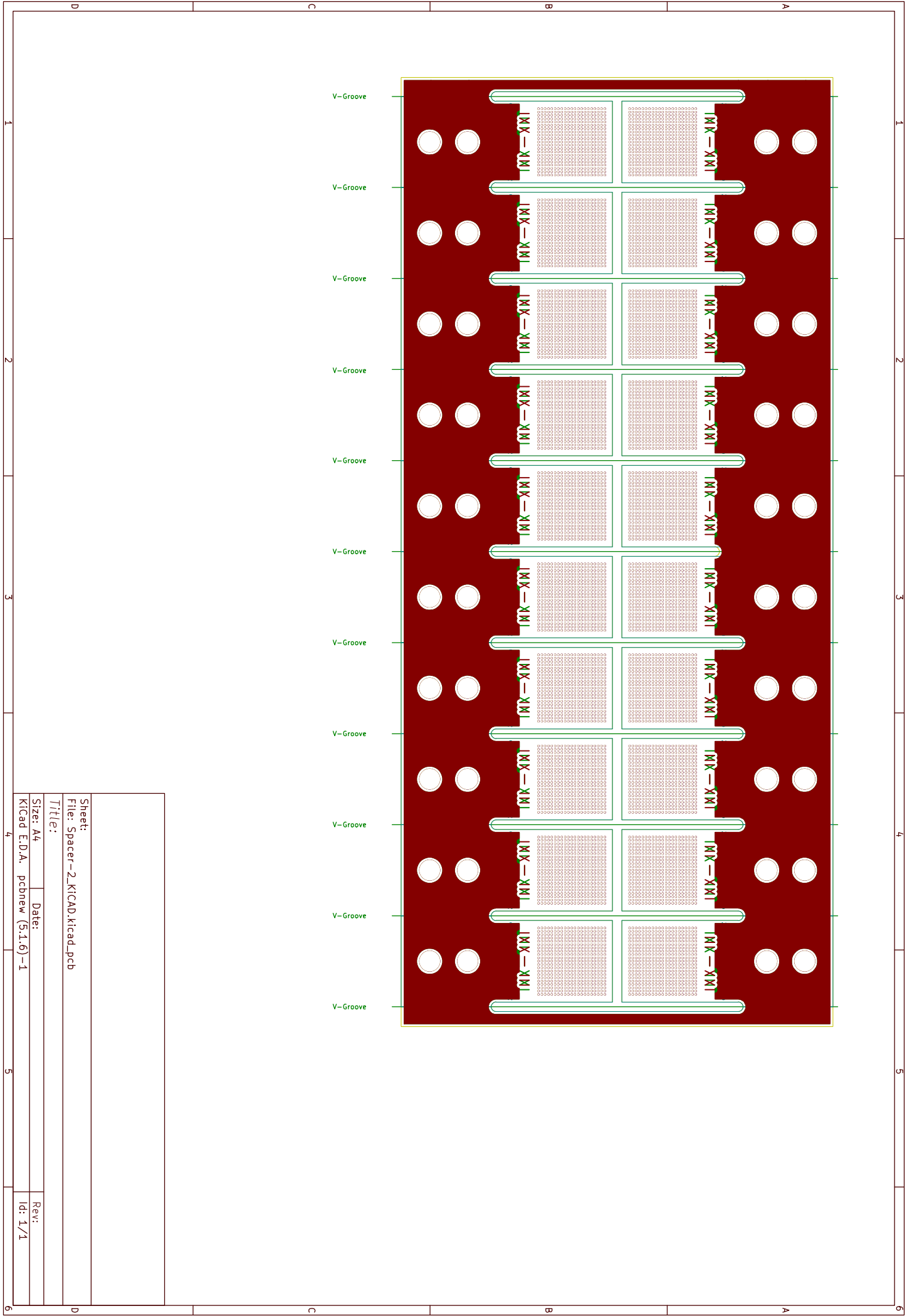
The smaller channels and increased size of the detector necessitates readout electronics with significantly more channels than the current one. To design and build electronics for this, the SPIDER project was started (see section 5.3.1). Its aim is to produce modular detector electronics, which can be used for an arbitrary number of channels (with a single unit featuring 128 channels and the ability to combine multiple units), and which provides improved reliability and user-friendliness.

The design of the collimator and positioning system is finished and their manufacturing is currently being initiated. For the new detector a few more questions need to be investigated before the designing phase can start properly. The SPIDER electronics are currently being designed with prototypes of some of its parts already being tested.

A Drawings

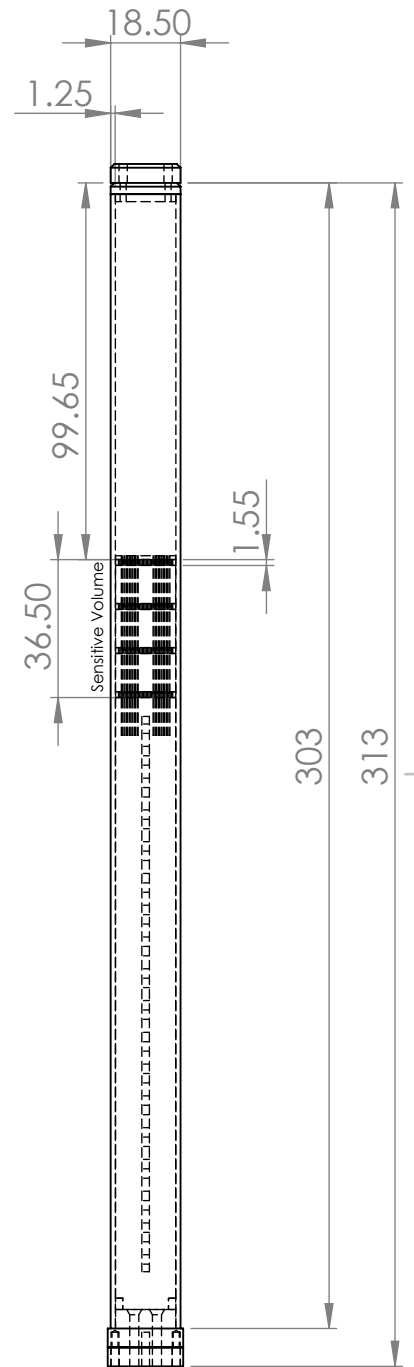
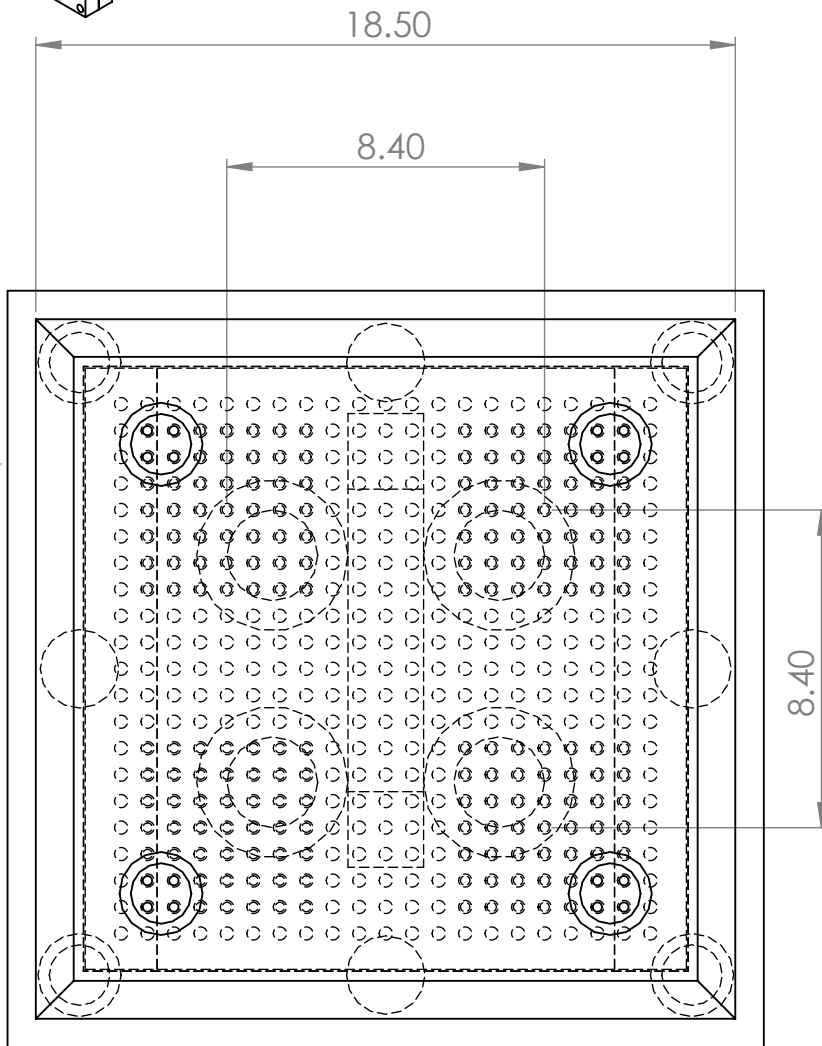
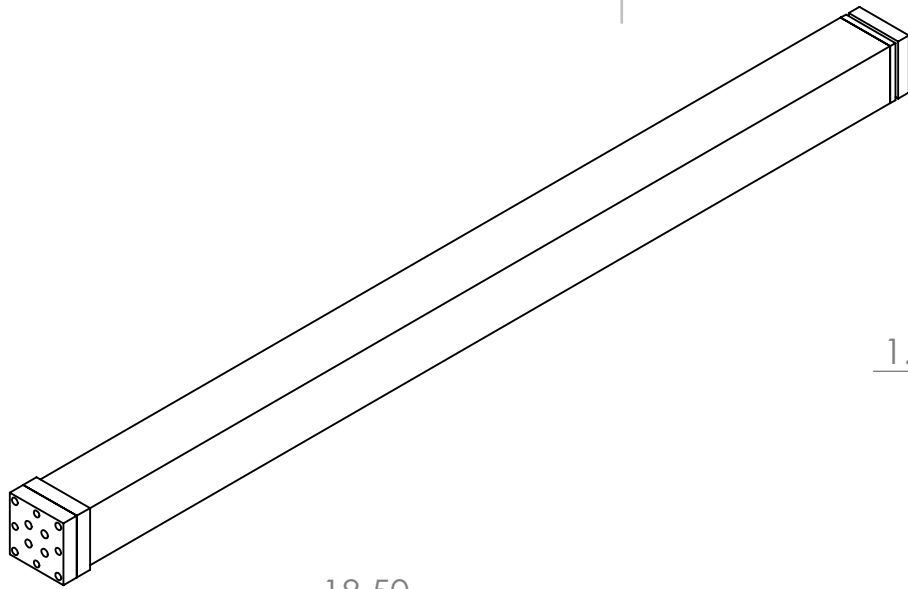
A.1 Spacers

The following pages include drawings of the spacers which are used for the detector construction described in section 2.2.1. The first one is a mechanical drawing of a single spacer while the second one is the arrangement of several spacers in a single PCB board to improve production costs.



A.2 Hot-Lab Prototype 1

This section includes drawings of the Hot-Lab Prototype 1 detector head. On the first one, the head is shown without the slide which is used to insert it into the collimator (for better visibility). The second to fifth drawings are the different components of the slide: The piece which holds the light guides in place, and the outer and inner pieces of the slide which hold the detector tip in place when inserted into the collimator and which have the light guides running through them. The last three drawings are for parts which are used in the construction of the detector head: the 3D printed piece which holds the spacers in place and is milled away after the casting process, and the fiber bundler (aluminum) and WLSFs polishing (acrylic) parts which bundle the WLSFs in according to their channels.



UNLESS OTHERWISE SPECIFIED:
DIMENSIONS ARE IN MILLIMETERS
SURFACE FINISH:
TOLERANCES:
LINEAR:
ANGULAR:

FINISH:

DEBURR AND
BREAK SHARP
EDGES

DO NOT SCALE DRAWING

REVISION

	NAME	SIGNATURE	DATE	
DRAWN				
CHK'D				
APPV'D				
MFG				
Q.A				

MATERIAL:

WEIGHT:

TITLE:

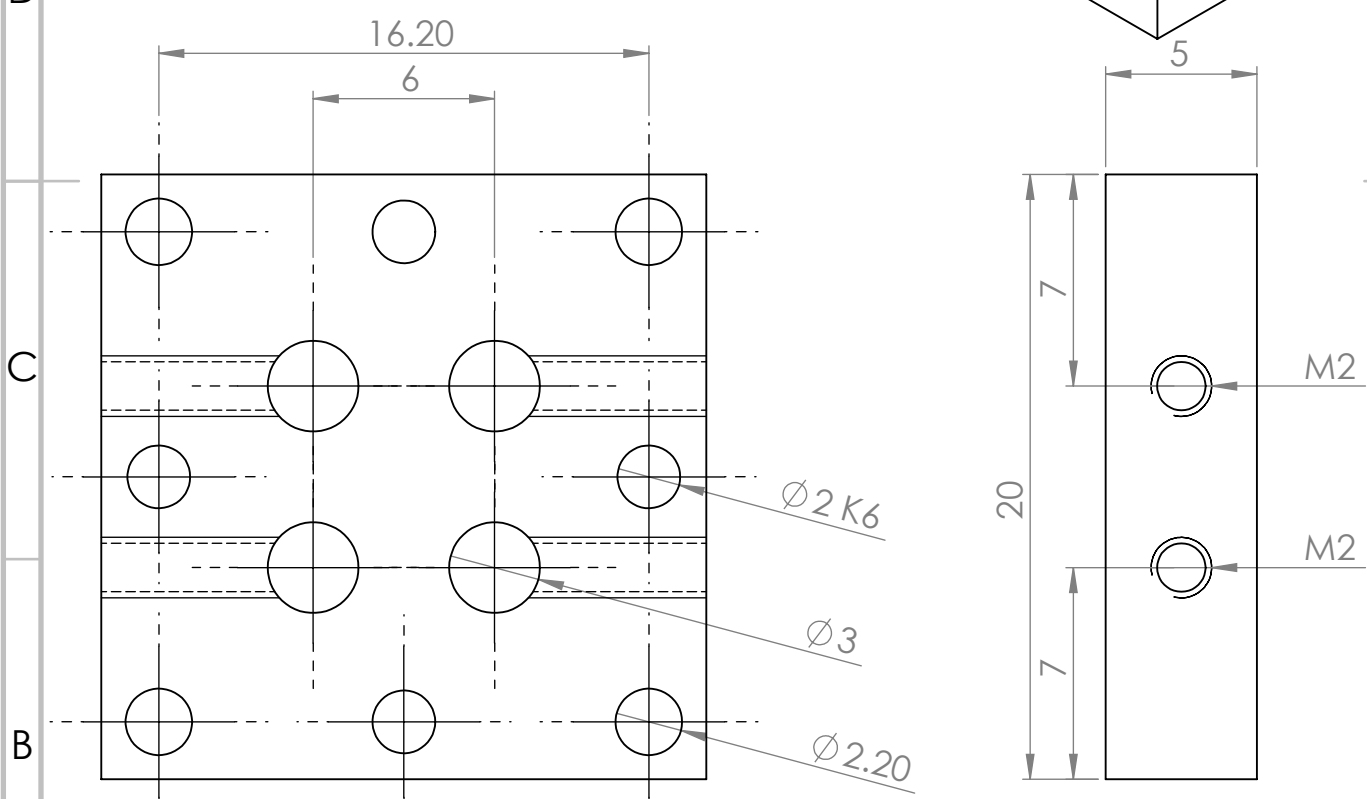
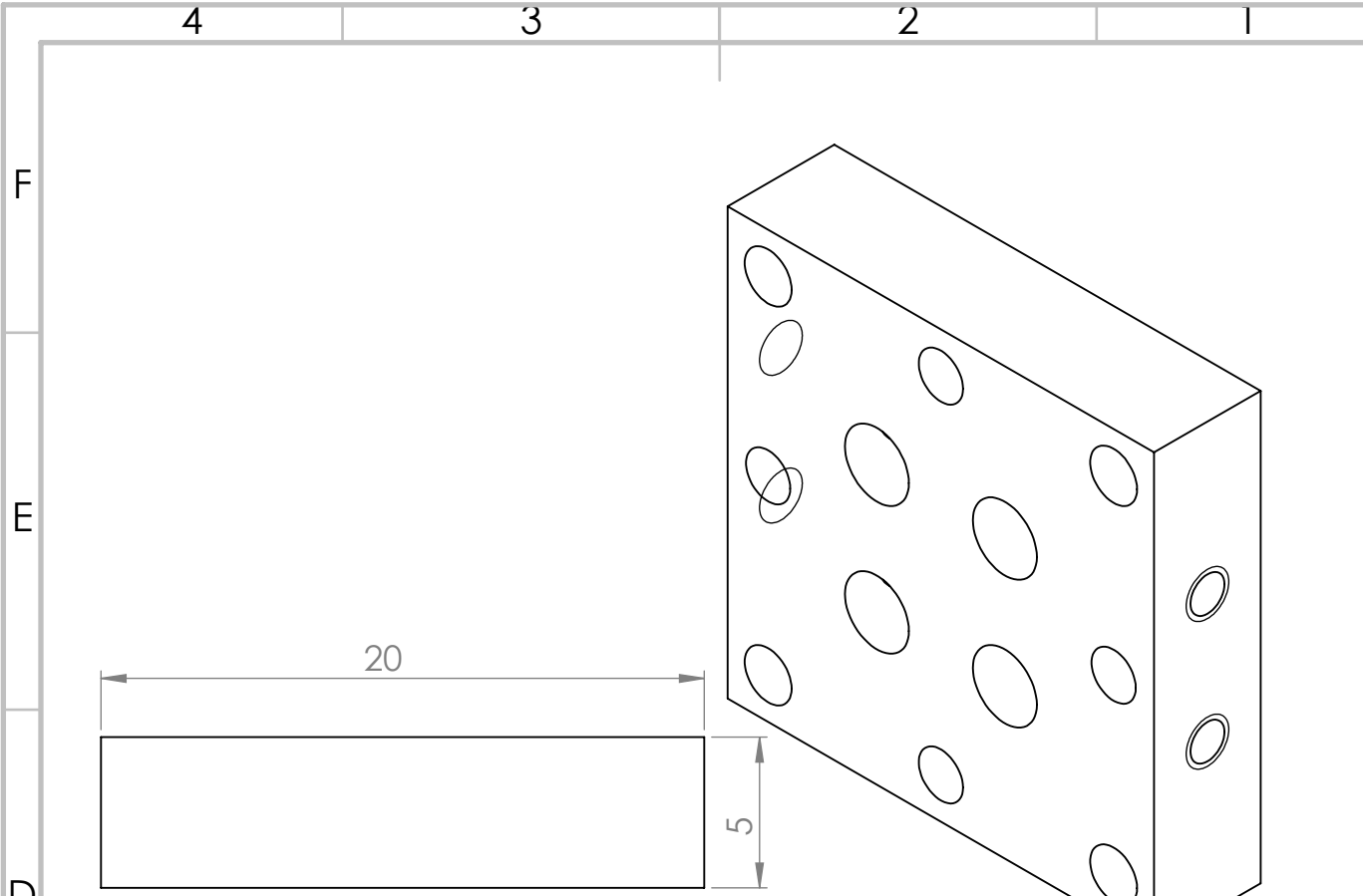
DWG NO.

SCALE:1:2

Head5v2

A4

SHEET 1 OF 1



UNLESS OTHERWISE SPECIFIED:
DIMENSIONS ARE IN MILLIMETERS
SURFACE FINISH:
TOLERANCES:
LINEAR:
ANGULAR:

FINISH:

DEBURR AND
BREAK SHARP
EDGES

DO NOT SCALE DRAWING

REVISION

	NAME	SIGNATURE	DATE		
DRAWN					
CHK'D					
APPV'D					
MFG					
Q.A					

MATERIAL:

WEIGHT:

TITLE:

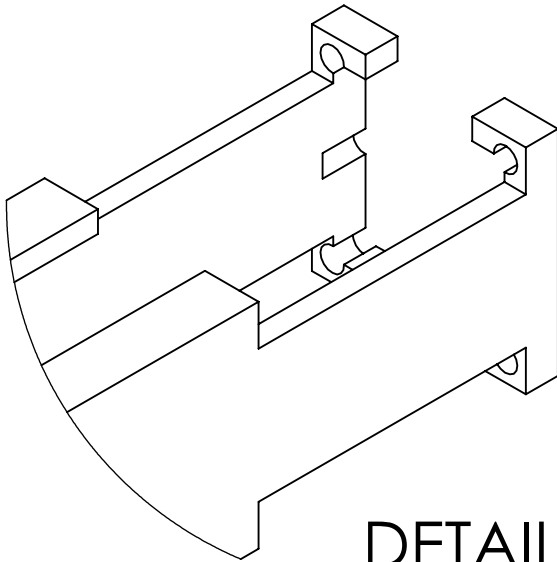
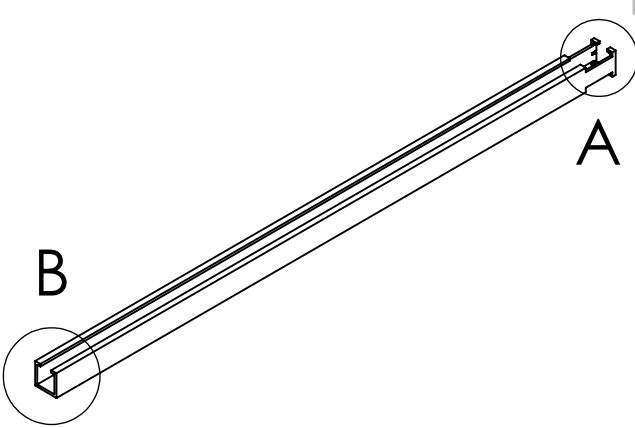
DWG NO.

FiberHolderFront5

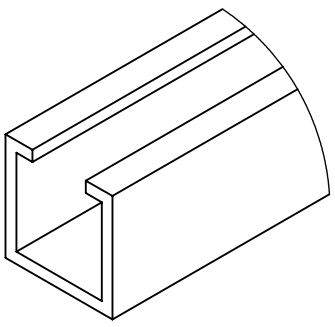
A4

SCALE:4:1

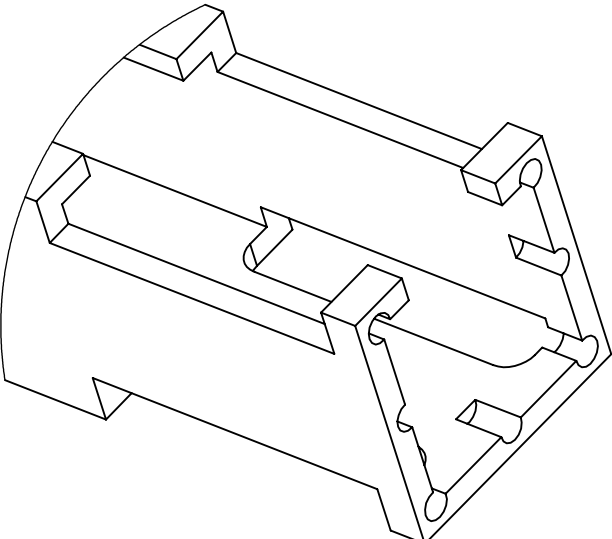
SHEET 1 OF 1



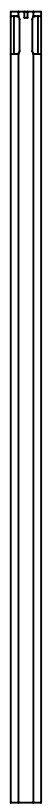
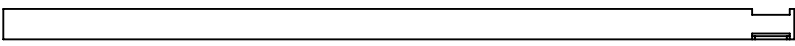
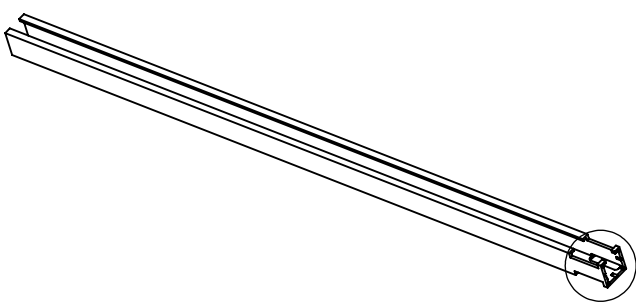
DETAIL A
SCALE 2 : 1



DETAIL B
SCALE 1 : 1



DETAIL C
SCALE 2 : 1



UNLESS OTHERWISE SPECIFIED:
DIMENSIONS ARE IN MILLIMETERS
SURFACE FINISH:
TOLERANCES:
LINEAR:
ANGULAR:

FINISH:

DEBURR AND
BREAK SHARP
EDGES

DO NOT SCALE DRAWING

REVISION

	NAME	SIGNATURE	DATE		
DRAWN					
CHK'D					
APPV'D					
MFG					
Q.A					

MATERIAL:

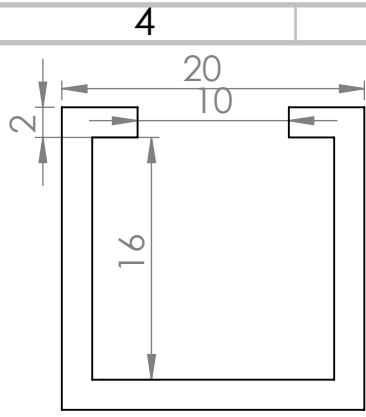
WEIGHT:

TITLE:

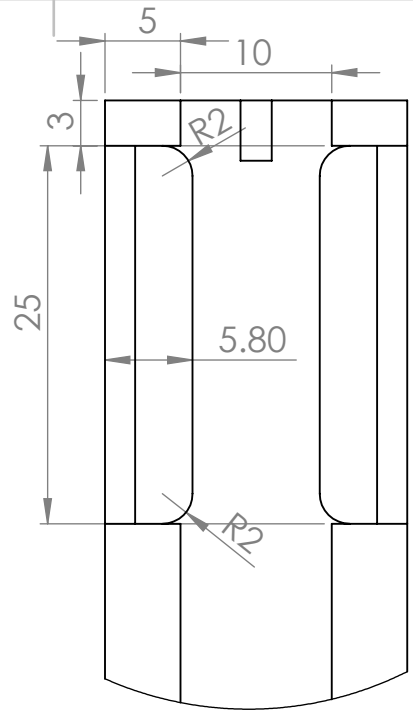
DWG NO. OuterSlide5Sketch A4

SCALE:1:10

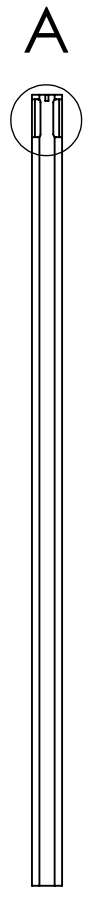
SHEET 1 OF 1



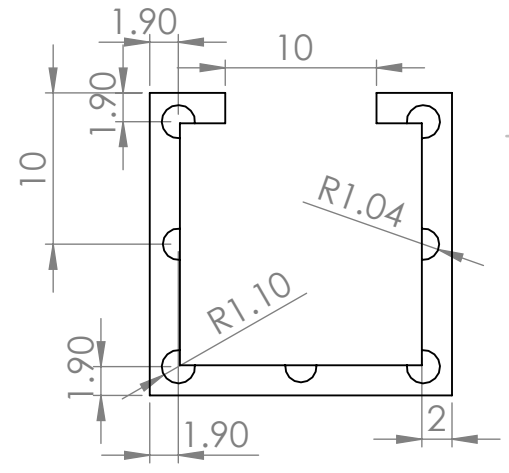
DETAIL C
SCALE 2 : 1



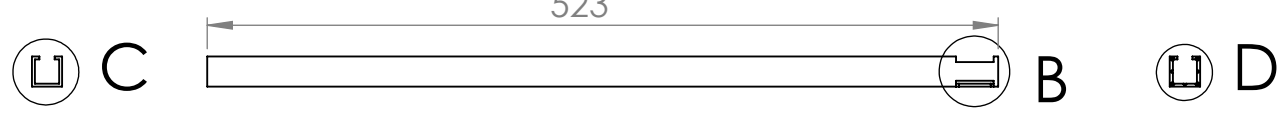
DETAIL A
SCALE 2 : 1



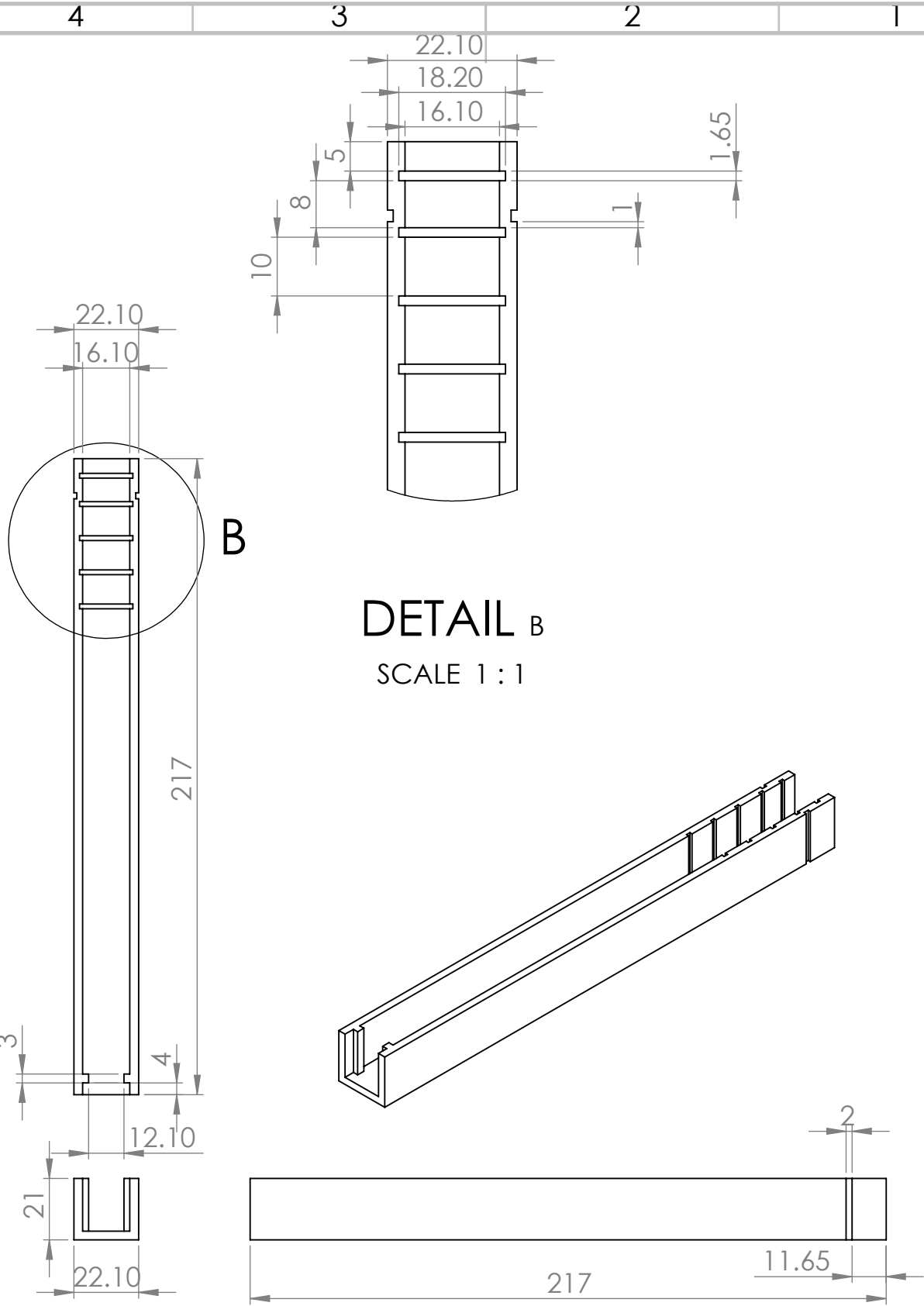
DETAIL B
SCALE 2 : 1



DETAIL D
SCALE 2 : 1



UNLESS OTHERWISE SPECIFIED: DIMENSIONS ARE IN MILLIMETERS SURFACE FINISH: TOLERANCES: LINEAR: ANGULAR:				FINISH:		DEBURR AND BREAK SHARP EDGES		DO NOT SCALE DRAWING		REVISION	
NAME				SIGNATURE		DATE		TITLE:			
DRAWN								OuterSlide5Dimensions			
CHK'D											
APPV'D											
MFG											
Q.A											
						MATERIAL:		DWG NO.			
								SCALE:1:5			
						WEIGHT:		SHEET 1 OF 1			



UNLESS OTHERWISE SPECIFIED:
DIMENSIONS ARE IN MILLIMETERS
SURFACE FINISH:
TOLERANCES:
LINEAR:
ANGULAR:

FINISH:

DEBURR AND
BREAK SHARP
EDGES

DO NOT SCALE DRAWING

REVISION

	NAME	SIGNATURE	DATE		
DRAWN					
CHK'D					
APPV'D					
MFG					
Q.A					

MATERIAL:

WEIGHT:

TITLE:

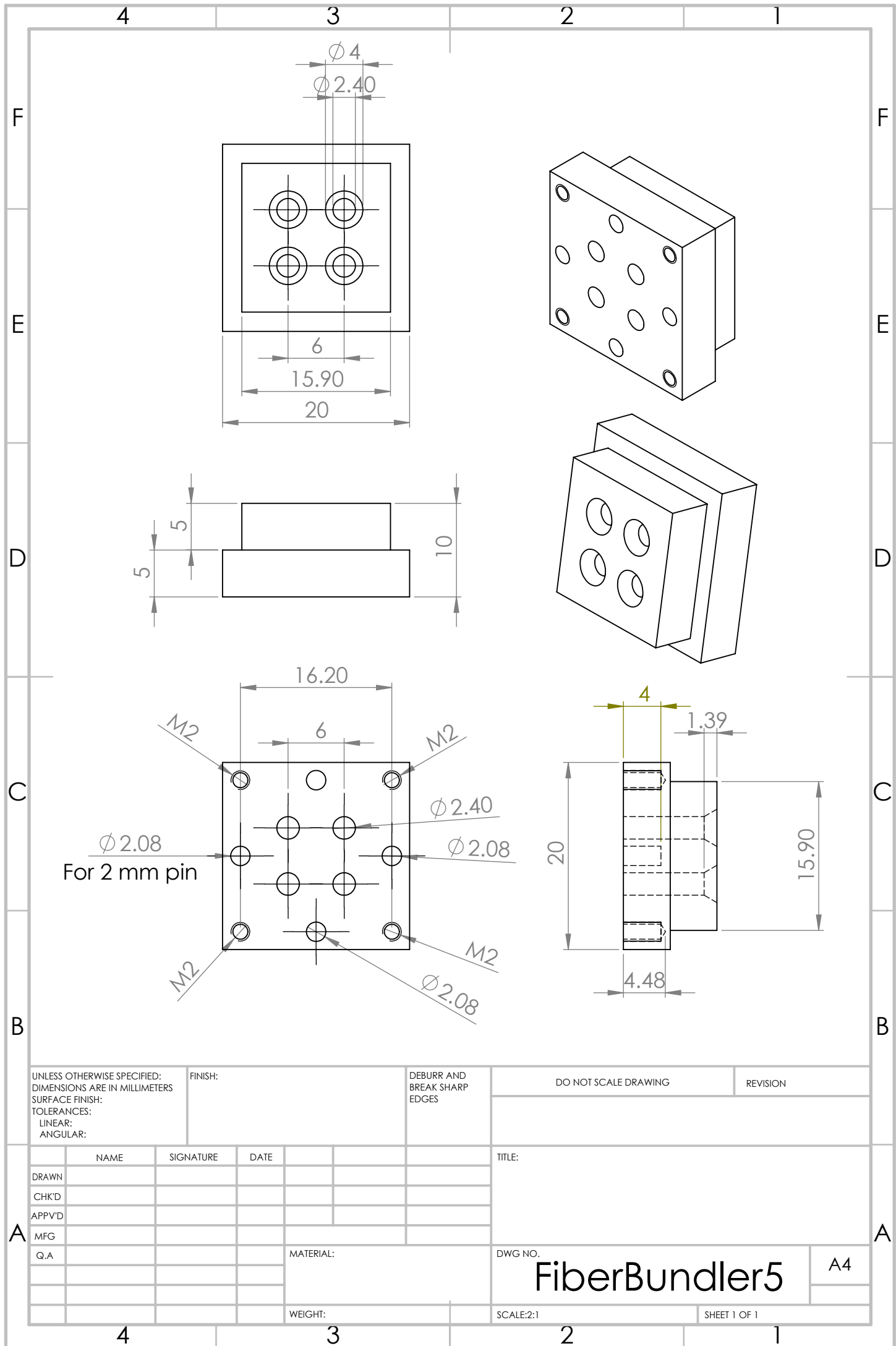
DWG NO.

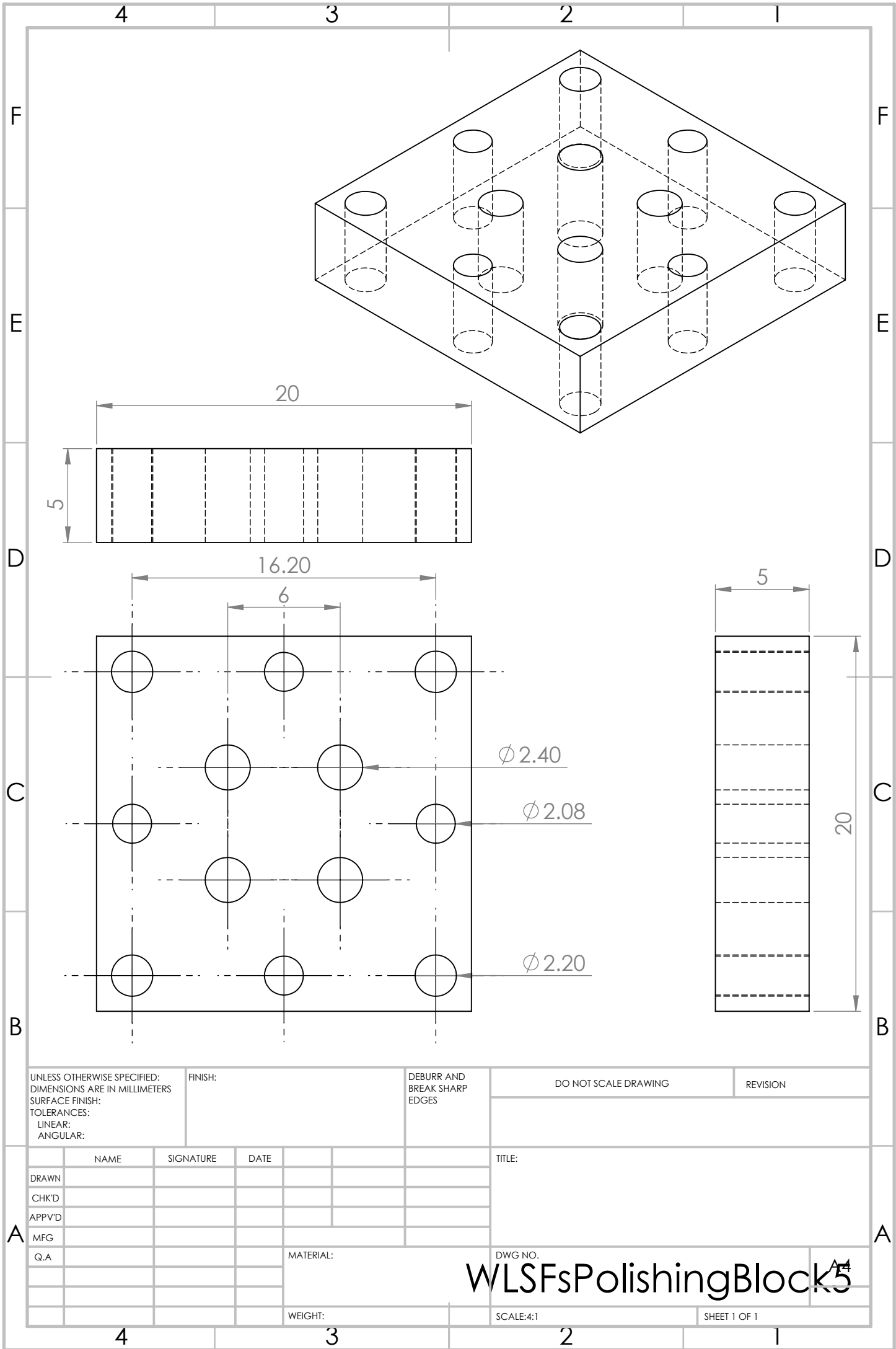
SpacerHolder5

A4

SCALE:1:2

SHEET 1 OF 1





UNLESS OTHERWISE SPECIFIED:
DIMENSIONS ARE IN MILLIMETERS
SURFACE FINISH:
TOLERANCES:
LINEAR:
ANGULAR:

FINISH:

DEBURR AND
BREAK SHARP
EDGES

DO NOT SCALE DRAWING

REVISION

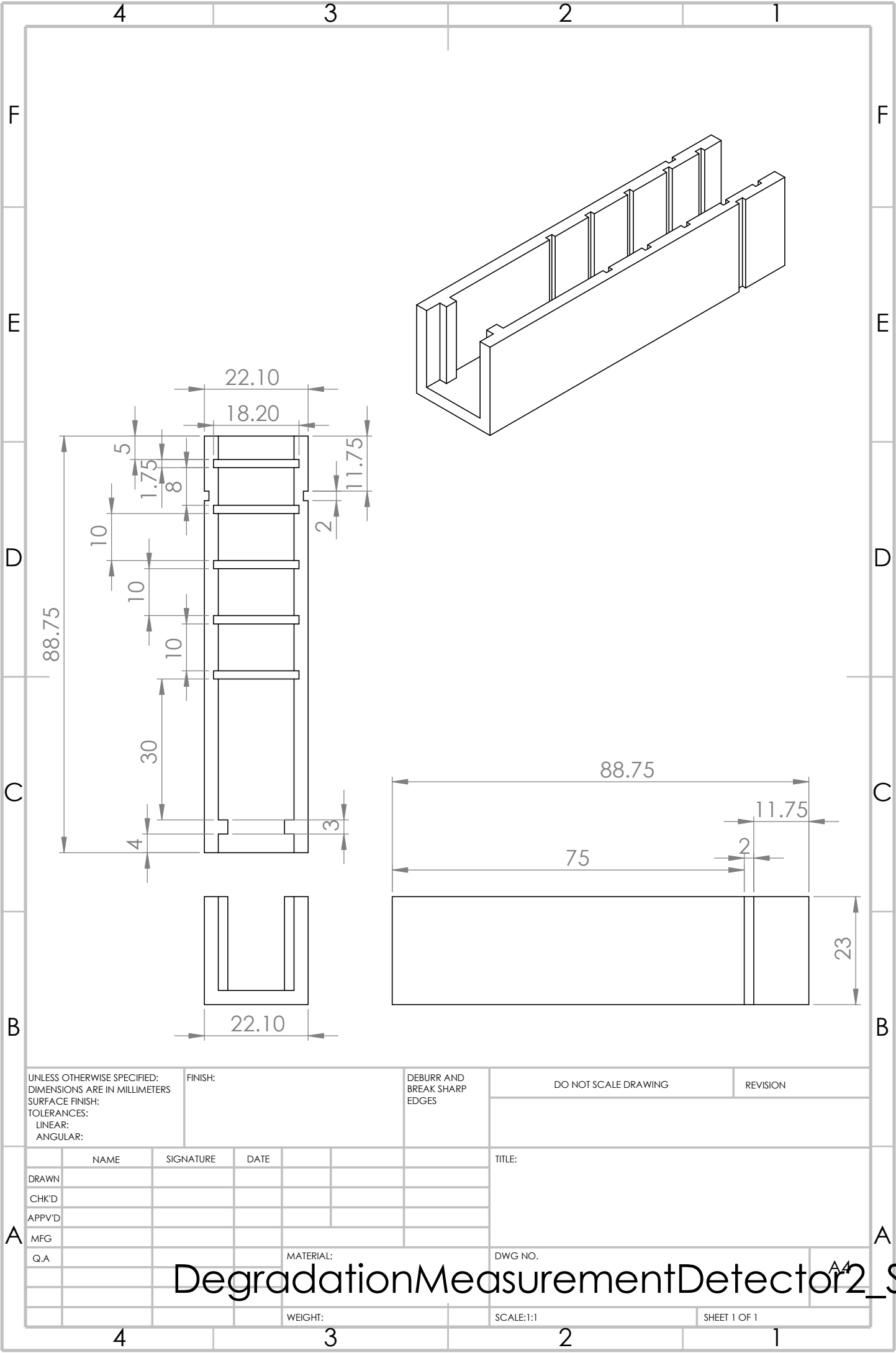
	NAME	SIGNATURE	DATE		
DRAWN					
CHK'D					
APPV'D					
MFG					
Q.A					

TITLE:	
DWG NO.	
MATERIAL:	
WEIGHT:	
SCALE:4:1	
SHEET 1 OF 1	

WLSFs Polishing Block 5

A.3 Single Channel Detectors

This section presents the drawings of the single channel detectors (see section 2.2.3) used for the radiation damage measurements presented in section 3.2.4. The first page is of the 3D printed piece which holds the spacers. The second and third page are the two pieces (aluminum and plastic) which together hold the WLSF at the back of the probe in place. They also provide a surface for polishing and the connection interface for the light guides.



UNLESS OTHERWISE SPECIFIED:
DIMENSIONS ARE IN MILLIMETERS
SURFACE FINISH:
TOLERANCES:
LINEAR:
ANGULAR:

FINISH:

DEBURR AND
BREAK SHARP
EDGES

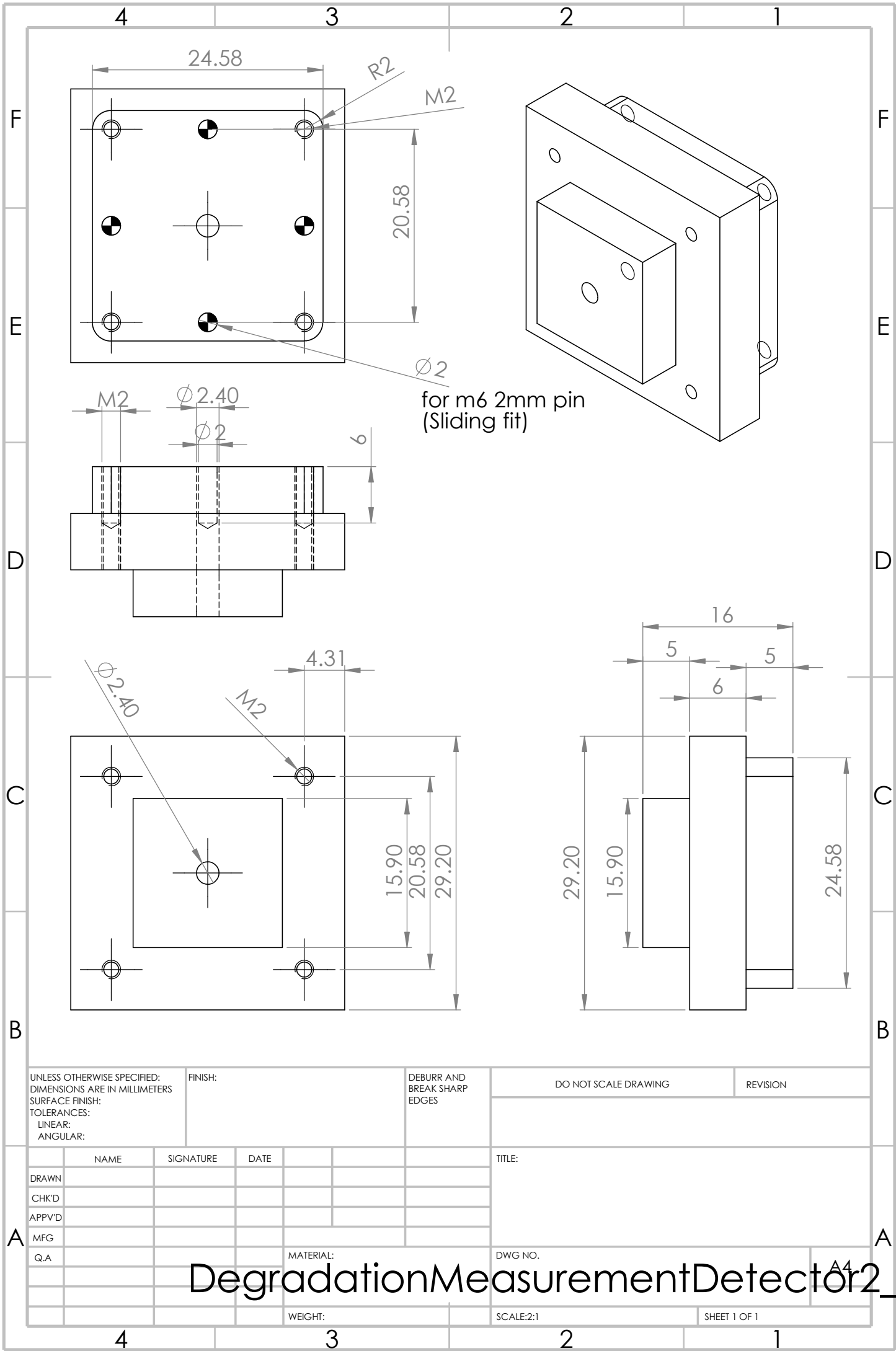
DO NOT SCALE DRAWING

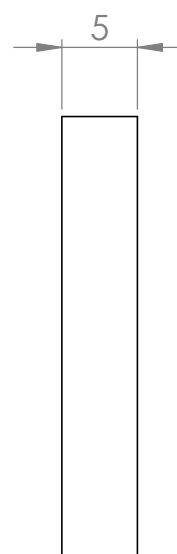
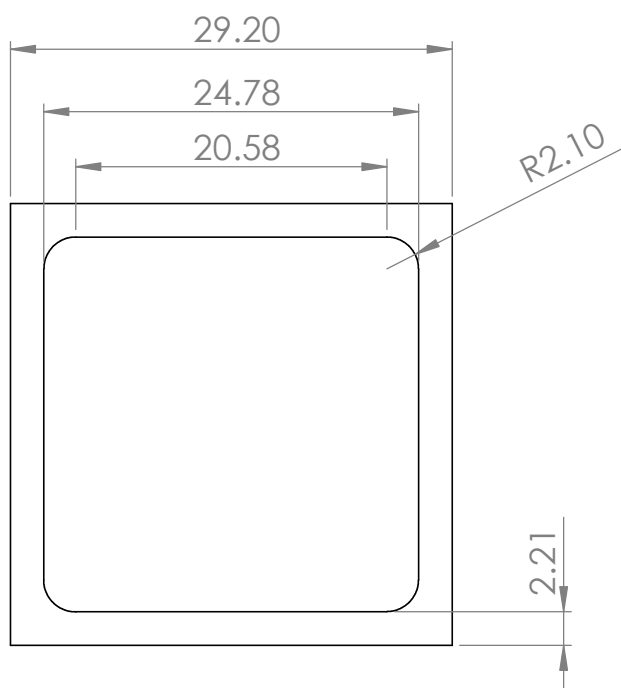
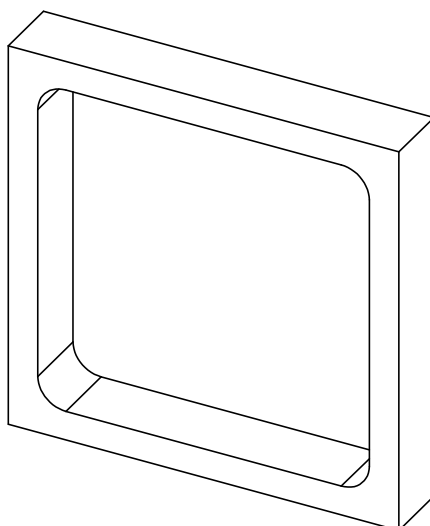
REVISION

	NAME	SIGNATURE	DATE		
DRAWN					
CHK'D					
APPV'D					
MFG					
Q.A					

TITLE:	
DWG NO.	
SCALE:1:1	SHEET 1 OF 1

DegradationMeasurementDetector2_Sp





TITLE:	
DWG NO.	Measurement Detector 2
SCALE: 2:1	SHEET 1 OF 1

DegradationMeasurementDetector2_Po

A.4 Crosstalk Prototypes

This section presents the drawings of the crosstalk detector (see section 2.2.4). The first page is the 3D printed piece that holds the spacers. The second page is the drawing of the aluminum part of the piece that holds the WLSF and provides the interface to connect the light guides. It is combined with the same plastic piece as is used for the single channel detectors (see section A.3).

4 3 2 1

F

F

E

E

D

D

C

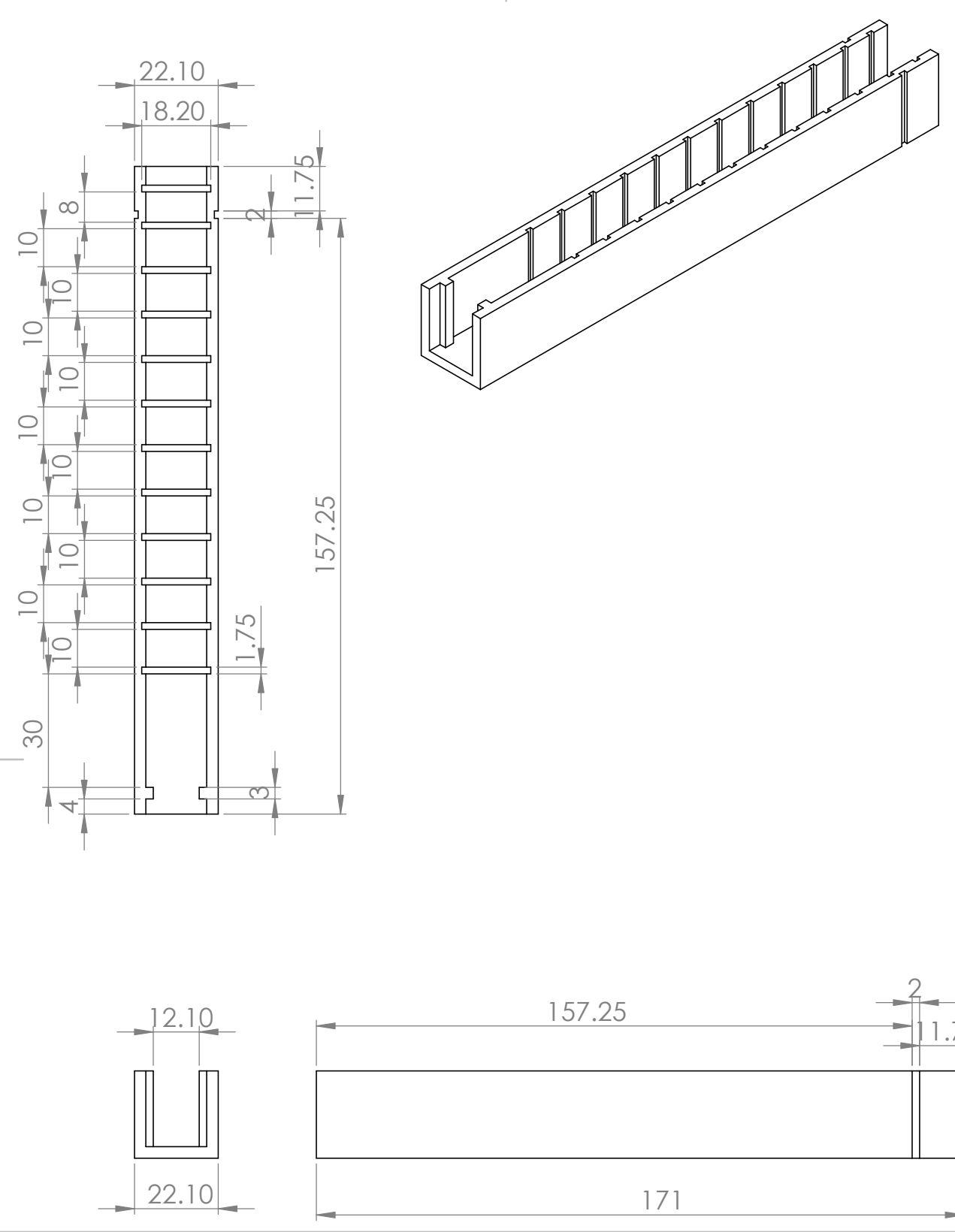
C

B

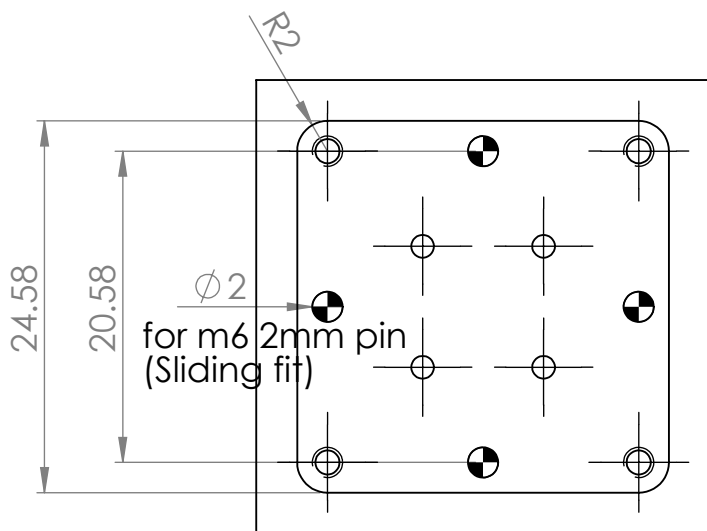
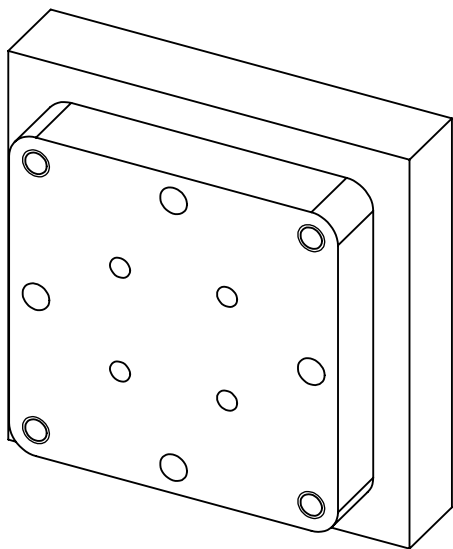
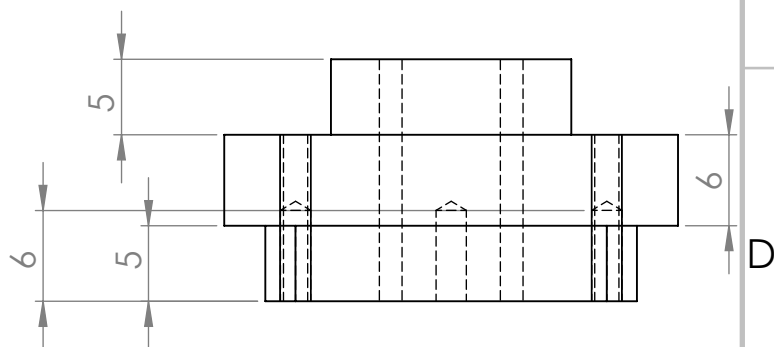
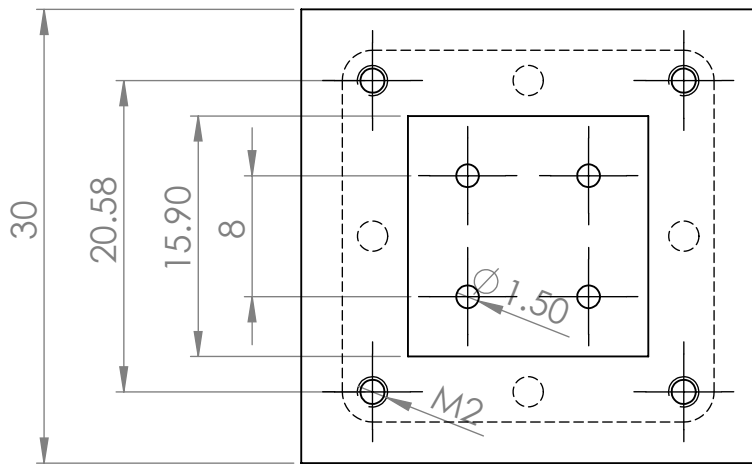
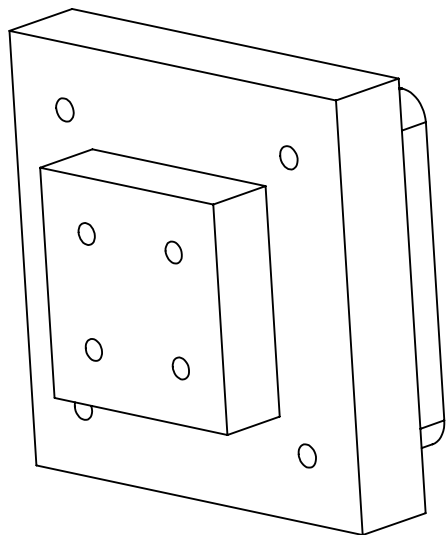
B

A

A



UNLESS OTHERWISE SPECIFIED: DIMENSIONS ARE IN MILLIMETERS SURFACE FINISH: TOLERANCES: LINEAR: ANGULAR:				FINISH:		DEBURR AND BREAK SHARP EDGES		DO NOT SCALE DRAWING		REVISION	
		NAME	SIGNATURE		DATE			TITLE:			
DRAWN											
CHK'D											
APPV'D											
MFG											
Q.A											
							MATERIAL:		DWG NO.		
							CrosstalkDetector1_SpacerH		A4		
							WEIGHT:		SCALE:1:1.5		SHEET 1 OF 1



UNLESS OTHERWISE SPECIFIED:
DIMENSIONS ARE IN MILLIMETERS
SURFACE FINISH:
TOLERANCES:
LINEAR:
ANGULAR:

FINISH:

DEBURR AND
BREAK SHARP
EDGES

DO NOT SCALE DRAWING

REVISION

	NAME	SIGNATURE	DATE	
DRAWN				
CHK'D				
APPV'D				
MFG				
Q.A				

MATERIAL:

WEIGHT:

TITLE:

DWG NO.

SCALE:2:1

SHEET 1 OF 1

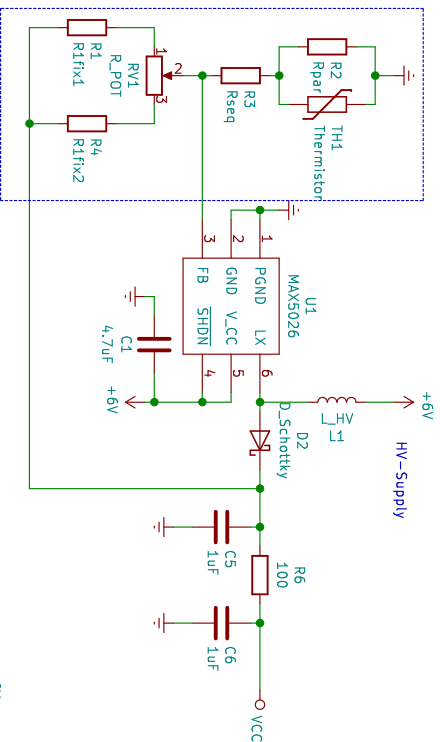
CrosstalkDetector3_FiberBundle

A4

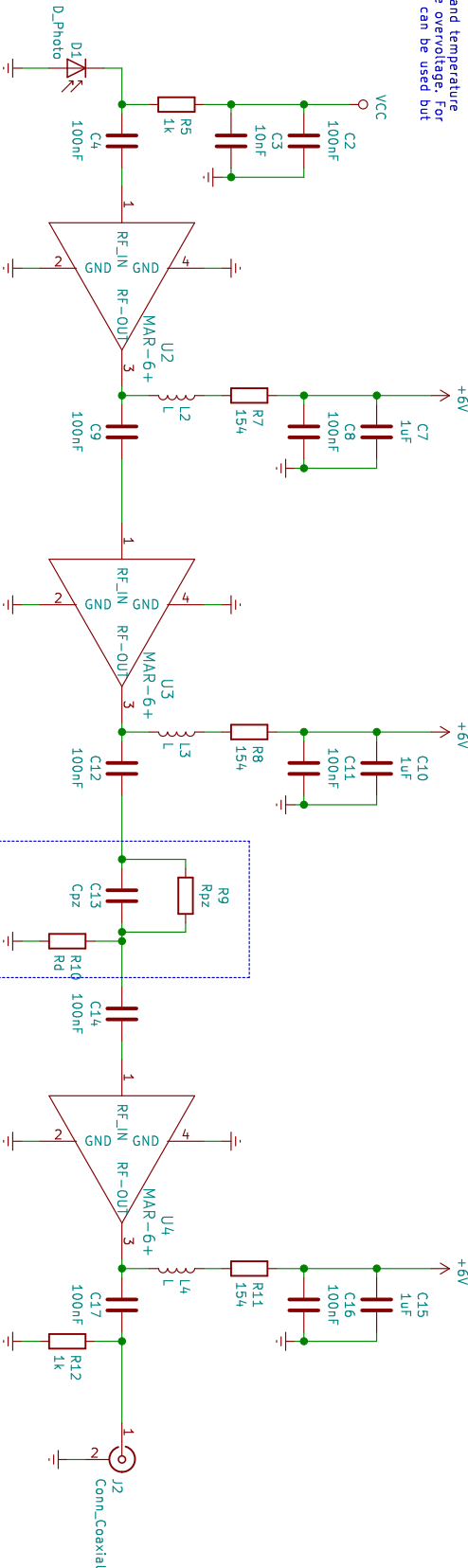
B Electronics Schematics

B.1 SiPM_PS+PreAmp_1 Board

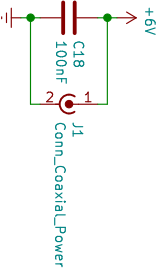
This section contains design information on the SiPM_PS+PreAmp_1 board. The following pages show its schematic and the PCB layout (only the front copper layer is shown for the PCB layout).



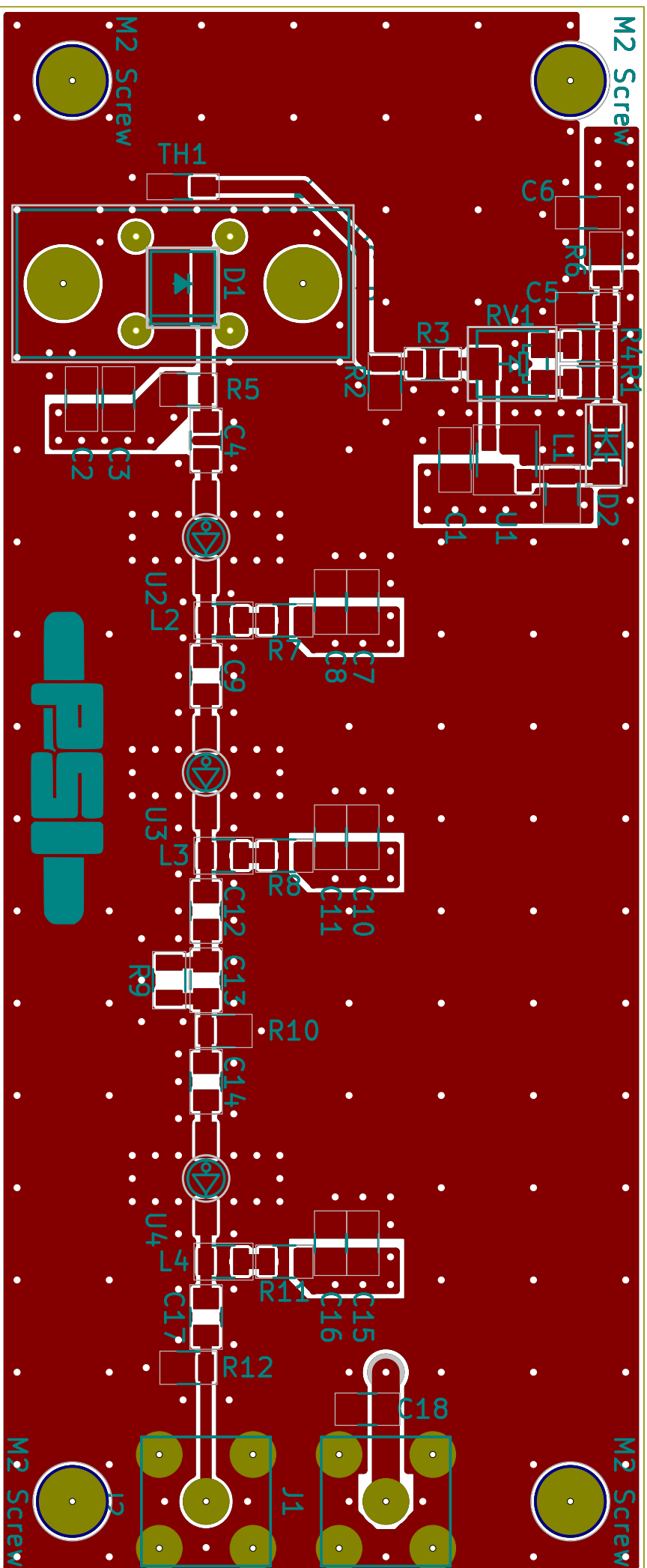
Adjust Resistors to match breakdown voltage and temperature coefficient of SiPM. R_POT is for adjusting the overvoltage. For perfect matching of overvoltage range, Rfix2 can be used but it is not required.



Pole-Zero Cancellation + Differentiation
Rd usually not needed
Use Capacitor in Rd (eg 5 pF) to reduce noise



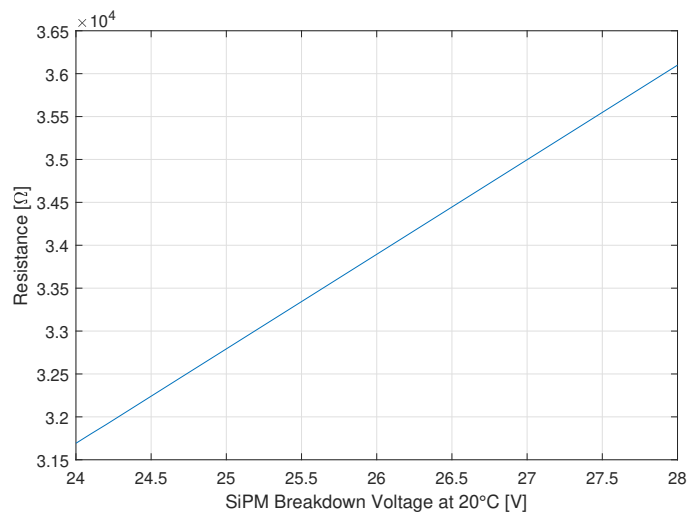
Sheet: /	
File: SiPM_PS+Preamp_1.sch	
Title:	
Size: A4	Date:
Kicad E.O.A. Kicad (5.0.2)-1	Id: 1/1
Rev:	



Appendix B. Electronics Schematics

The values of R_{fix1} , R_{fix2} , R_{seq} , and R_{par} have to be adapted to the mounted SiPM. The following graphs shown in figures B.2 and B.1 have been generated as guidelines for ASD-NUV3S-P [30] SiPMs made by AdvanSiD. R_{fix2} is not used (infinite resistance) in this example. The resulting deviation from the targeted overvoltage is illustrated in figure B.3

(a)



(b)

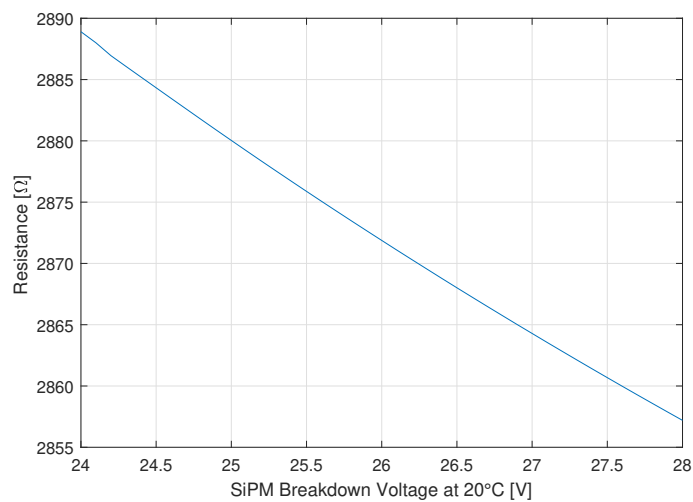


Figure B.1: Suggested resistances for R_{seq} (a) and R_{par} (b).

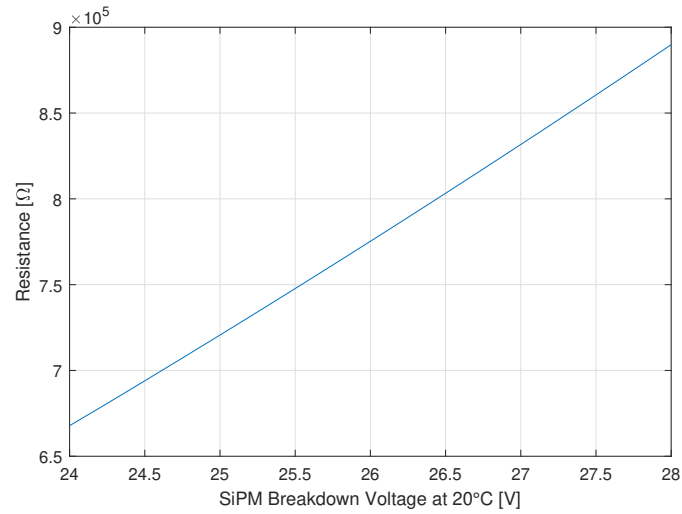


Figure B.2: Suggested resistances for R1fix1, to be used together with a 100 kΩ potentiometer.

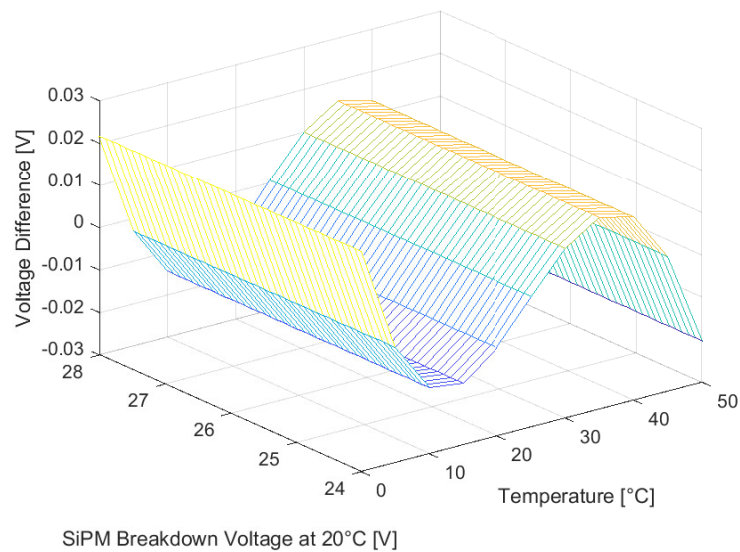


Figure B.3: Calculated deviation from the targeted overvoltage when using the suggested resistors for an example overvoltage of 4.5 V.

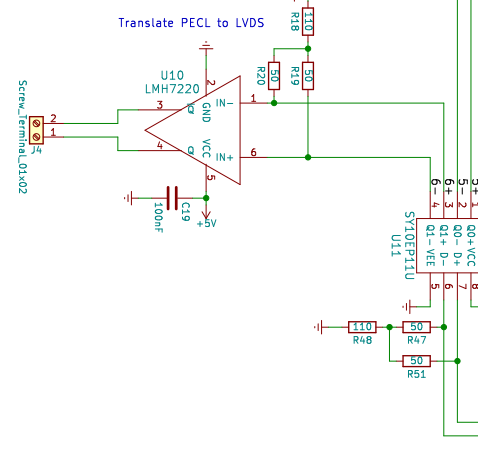
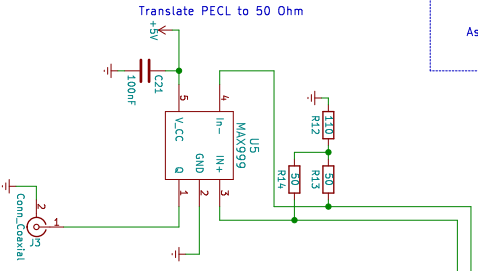
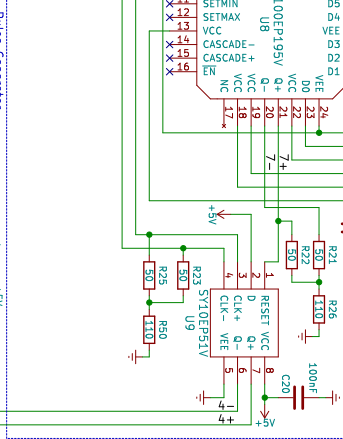
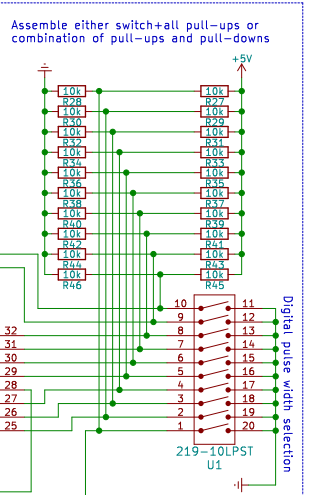
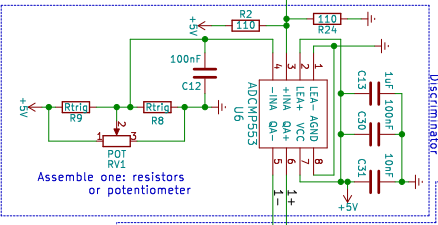
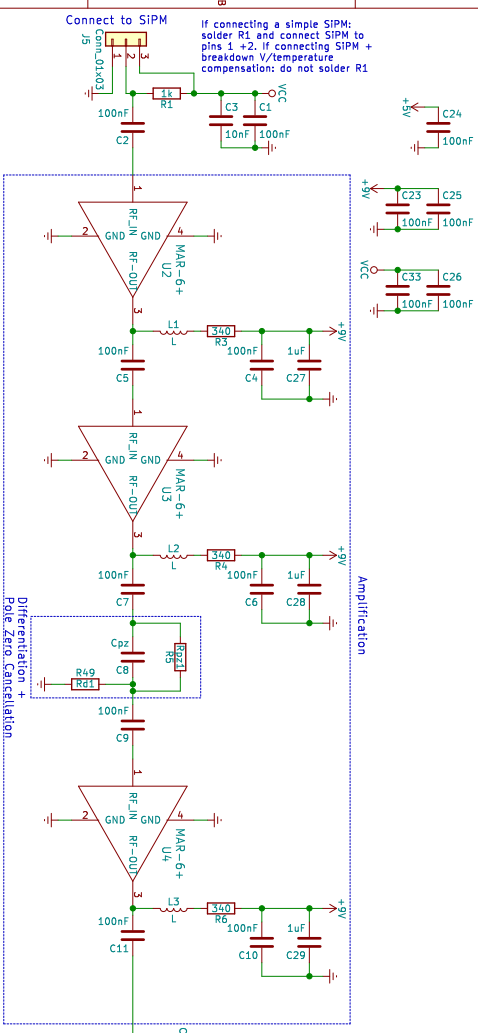
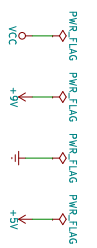
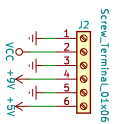
B.2 SiPM_amplifier_discriminator_LVDS_5_1 Board

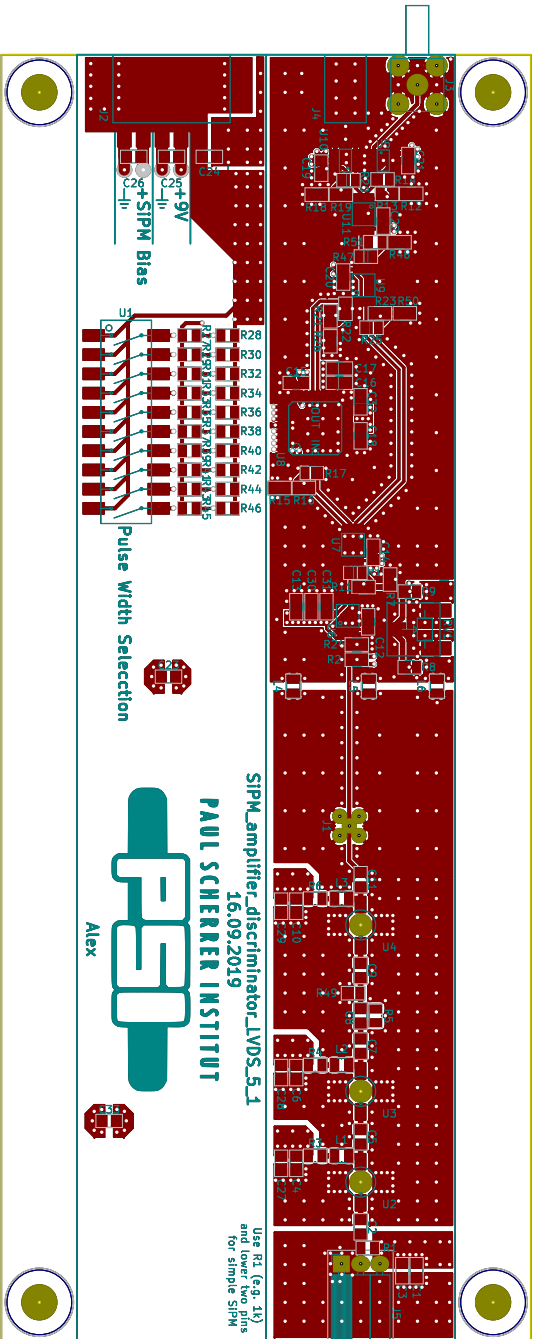
This section contains design information on the SiPM_amplifier_discriminator_LVDS_5_1 board. The following pages show its schematic and the PCB layout (only the front copper layer is shown for the PCB layout). Due to issues with the initial design (noise, feedback loops, and timing issues), several components were changed on the finished boards. These changes are:

Appendix B. Electronics Schematics

- Changed R8 for a capacitor with 2 pF
- Removed C8
- Exchanged R49 for 6.8 pF capacitor
- Exchanged U10 for LTC6754 (modified IC leads to fit the pads on the PCB)
- 15 pF capacitor inserted between R25 and R23 (connecting the two signal lines)

For the use together with the SiPM_PS+PreAmp_1 board, C11 is desoldered and J1 is used as an input for the signal from the SiPM_PS+PreAmp_1 board. This disables the amplifier section before C11 and also makes it unnecessary to provide the SiPM bias voltage and the +9 V supply to the board.





SIPM amplifier discriminator LVDS_5_1
16.09.2019
PAUL SCHERRER INSTITUT



Alex

Use R1 (e.g. 1k)
and lower two pins
for simple SIPM

Sheet:
File: SIPM_amplifier_discriminator_LVDS_5_1.kicad_pcb

Title:

Size: A4

Date:

KiCad E.O.A. KiCad (5.0.2)-1

Rev:

Id: 1/12

C Hot-Lab Campaign Measurement Lists

Measurement ID	Location	Start Date	Time	Samples	Readout
M3	FNL	2020-08-13	~1 h	^{60}Co	Logic
M4	FNL	2020-08-14	~1 h	^{252}Cf	Logic
M5	FNL	2020-08-14	~3 h	^{252}Cf , ^{60}Co	Logic
M7	FNL	2020-09-02	~5 d	^{252}Cf , ^{60}Co	FPGA
H2-1	AHL	2020-09-16	~2 d	Fuel (All)	Logic
H2-2	AHL	2020-09-22	~2 d	^{252}Cf	FPGA
H2-3	AHL	2020-09-24	~5 d	Fuel (All)	FPGA
H3	AHL	2020-09-25	~3 d	^{252}Cf	FPGA
H4-1	AHL	2020-09-28	~7 d	M4, U3, U6	FPGA
H4-2	AHL	2020-10-02	~5 d	^{252}Cf	FPGA
H5	AHL	2020-10-09	~7 d	M4	FPGA
H6	AHL	2020-10-16	~9 d	U1	FPGA
H2-4	AHL	2020-10-27	~6 h	M4	FPGA

Table C.1: An overview of the most important measurements in the context of the spent fuel measurement campaign. Measurements whose ID starts with a “M” were carried out at the FNL and measurements starting with a “H” were carried out at the AHL.

Sections	Samples	Setup	Measurement IDs
3.2.3	M4	Far (Modified)	H4-1
4.3.1	^{252}Cf	Near and Far	H3, H4-2
4.4.2	Fuel (All)	Near and Far	H2-3, H4-1, H5
4.4.3	M4	Far (Moving Sample)	H5
4.5	M4	Near	H2-3, H2-4

Table C.2: Overview over the use of the data from individual measurements for the different sections. The measurement IDs correspond to the ones used in table C.1.

D SPIDER

This chapter contains details about the SPIDER project (see section 5.3.1). The project is currently ongoing, there is not yet a usable prototype of the electronics. Additionally, most of the implementation details are not yet fully defined. This chapter therefore contains only an overview, going as far into details as the current state of development allows. While the main goal of the SPIDER project is to develop electronics for the NEWS project, the design is intended to be modular and should also be useful for other applications which involve digital filter algorithms based on fast photon counting.

D.1 Structure of the SPIDER System

The basic unit of the SPIDER system is a set of 5 crates. Together, these 5 crates contain the electronics to capture and analyze the light of 128 detector channels. Four of the crates are identical units, each containing the SiPMs and amplifiers for 32 channels (for details see section D.2). The fifth one is a crate adapted from the electronics used in the MEG II experiment at PSI [73]. It contains the electronics to discretize the signals coming from all front end boards and to perform the filter algorithm (for details see section D.3). The system is designed to be scalable, allowing multiple of this set of five crates to be used at the same time to support applications where more than 128 channels are needed.

D.2 Front End Crate

Each of the 32 channels in a front end crate can be conceptually separated into 3 elements. The first one is an SiPM, which creates signal pulses for every photon it detects. The second one is the shaping amplification stage. It works similarly to the shaping and amplification stages on the SiPM_PS+PreAmp_1 board 2.3.1, amplifying the signal and shortening each pulse coming from the SiPM. The last part is an AC-DC splitter. In order to simplify the connections of the board, the same connection is used to supply the high voltage necessary for the SiPM to the board and to read the signal pulses generated by the board. The AC-DC splitter couples the

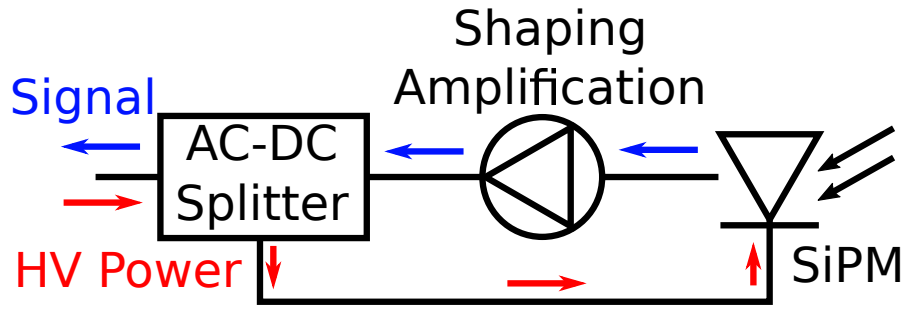


Figure D.1: Illustration of the front end electronics. The SiPM generates a signal (blue arrows) for every photon it detects. The signal is then amplified and shortened. The output for the signal is used at the same time to feed the high voltage for the SiPM. An AC-DC splitter ensures that the amplifier output is not driven by the high voltage and that the SiPM supply is not affected by changes induced by the signal.

amplifier output to the board output via a capacitor to ensure that the high voltage (a pure DC component) is not applied to the amplifier output. At the same time it also couples the SiPM to the board input via an inductor to isolate the SiPM input from the signal (an AC signal with main components of more than 100 MHz). This is illustrated in figure D.1. In the end, the output of the board is a series of short analog pulses (~ 2 ns) for every photon detected by the SiPM.

Apart from the electronics for the individual channels, the crate also contains the power supply for the amplifiers, and 4 temperature sensors to read the temperature of the SiPMs to support temperature compensation (keeping the overvoltage constant, see section 2.3.1 for details). The temperature sensors are distributed evenly between the SiPMs such that each sensor can be thought of to be responsible to read the temperature for 8 SiPMs. Figure D.2 shows 3D renderings of how the finished electronics could look.

D.3 MEG Crate

The adapted MEG crate should take the analog signals from four front end crates as input and recognize neutron events on all of the channels using the MSD algorithm as a filter (see section 2.1.3 for details on the MSD algorithm).

The original system developed for the MEG II experiment [73] is illustrated in figure D.3. It consists of a crate frame with 18 slots in which cards can be inserted. The crate frame contains an active cooling system for the inserted cards, a power supply unit, and other basic electronics to control the crate. For the MEG II experiment, the slots are filled with 16 so-called WaveDREAM boards, a trigger concentrator board (TCB), and a data concentrator board (DCB). The requirements for the SPIDER project are slightly different from the ones of the MEG II experiment. For this reason, the WaveDREAM boards are replaced with custom discrimination boards, which are being developed as part of the SPIDER project.

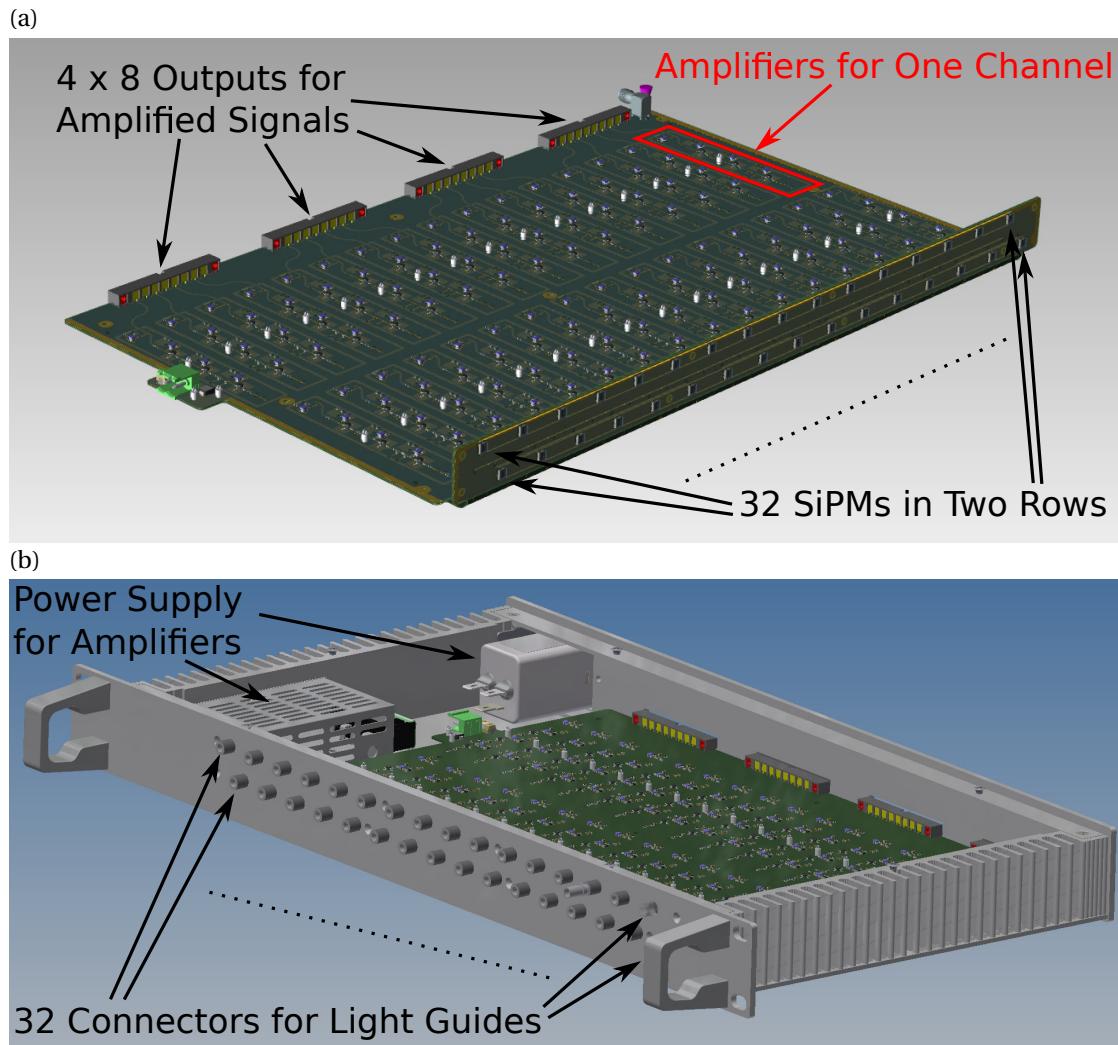


Figure D.2: (a): 3D rendering of the current design of the front end part of the SPIDER electronics. The shaping amplification lines for all channels are arranged in 2 rows of 16 channels each to better utilize the space. The SiPMs are mounted towards the front on a separate part of the PCB, connected via a bent PCB section. The output is arranged in groups of eight, each group with a separate connector combining all its channels for easier cable management. (b): 3D rendering of the front end electronics in its crate enclosure (without the lid). The connectors for the light guides are on the front of the crate with one SiPM behind each of them. The crate power supply is only needed for the amplifiers as the SiPMs are powered via the signal cable. When closed, the crate is completely sealed, all cooling is done via heat conduction through the enclosure, especially through the side panels which have groves designed to enhance heat exchange.

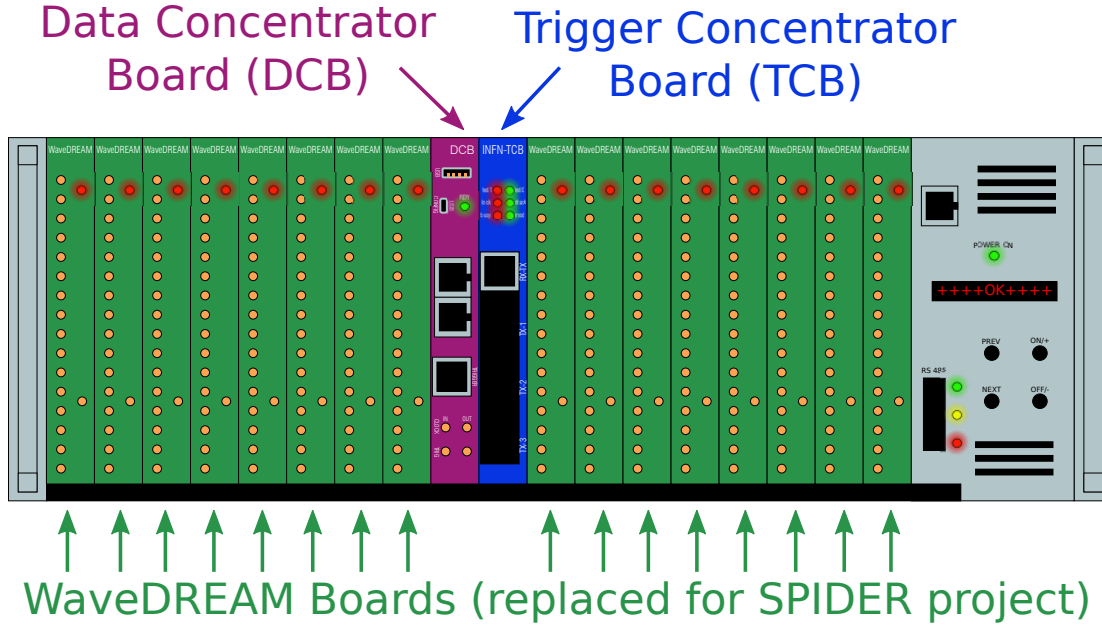


Figure D.3: Illustration of the MEG crate with the cards used for the MEG experiment inserted. The gray panel on the right side is to control the crate frame. Adapted from [73]

The discrimination boards are to some extent equivalent to the discrimination and pulse generation board of the electronics currently employed for the NEWS detectors (see section 2.3.1). Their main task is to generate digital pulses from the pulses on the analog inputs, which are connected directly to the analog outputs of the front end crates. Each of the 16 discrimination boards is responsible for 8 channels, resulting in one discrimination board for every 8 channel connector at the back of the front end crates. Each channel on a discrimination board uses a high speed discriminator with a threshold that is low enough to detect single photon pulses coming from the front end board. The pulse generation stage present on the board currently in use is omitted. Instead, the analog input pulse is tweaked to result in a long enough digital pulse for the subsequent electronics. An additional task of the board is to supply the high voltage for the SiPM to the same pin it receives its input pulses from. This way the discriminator board can directly be connected to the front end electronics without the need of additional connections to supply the high voltage. Similar to the front end electronics, a AC-DC splitter is used to ensure a clean separation of signal and power components. The high voltage generation itself is controlled by a microcontroller, allowing for easy compensation of factors like the SiPM breakdown voltage and temperature (the microcontrollers are connected to the temperature sensors installed in the front end electronics). At the same time, the microcontroller also records all the information, allowing easy analysis and even some fault detection like broken SiPMs that draw too little or too much current.

The TCB of the MEG II experiment is reused and it is where the digital pulses from the discrimination board are sent to. Its FPGA can be programmed to execute the MSD algorithm (or also more advanced triggering algorithms, should better performing ones be found in the

future) in real time, or to save timestamps of the arriving photons for post-processing similar to the logic analyzer solution currently in use (see section 2.3.2). The DCB from the MEG II experiment is re-used as well. It collects all the information from the different microcontrollers on the discriminator boards as well as the data generated by the TCB. The data can then be read from the DCB by connecting it to a computer. The DCB also serves as the communication interface where user input such as the breakdown voltage of the SiPMs, the values of the MSD parameters, and the signal to start a measurement is collected and distributed to the appropriate cards in the crate.

Bibliography

- [1] I. C. Gauld and J. C. Ryman, "Nuclide Importance to Criticality Safety , Decay Heating , and Source Terms Related to Transport and Interim Storage of High-Burnup LWR Fuel - NUREG/CR-6700," Oak Ridge National Laboratory, Oak Ridge, TN 37831-6370, Tech. Rep., 2000.
- [2] *Implementation of Burnup Credit in Spent Fuel Management Systems*, ser. TECDOC Series. Vienna: INTERNATIONAL ATOMIC ENERGY AGENCY, 1997, no. 1013. [Online]. Available: https://www-pub.iaea.org/MTCD/publications/PDF/te_1013_prn.pdf
- [3] *Implementation of Burnup Credit in Spent Fuel Management Systems*, ser. TECDOC Series. Vienna: INTERNATIONAL ATOMIC ENERGY AGENCY, 2001, no. 1241. [Online]. Available: <https://www.iaea.org/publications/6262/implementation-of-burnup-credit-in-spent-fuel-management-systems>
- [4] I. Günther-Leopold, B. Wernli, Z. Kopajtic, and D. Günther, "Measurement of isotope ratios on transient signals by mc-icp-ms," *Analytical and Bioanalytical Chemistry*, vol. 378, no. 2, pp. 241–249, Jan 2004. [Online]. Available: <https://doi.org/10.1007/s00216-003-2226-1>
- [5] I. Günther-Leopold, N. Kivel, J. Kobler Waldis, and B. Wernli, "Characterization of nuclear fuels by icp mass-spectrometric techniques," *Analytical and Bioanalytical Chemistry*, vol. 390, no. 2, pp. 503–510, Jan 2008. [Online]. Available: <https://doi.org/10.1007/s00216-007-1644-x>
- [6] M. Guillon, P. Heimgartner, Z. Kopajtic, D. Günther, and I. Günther-Leopold, "A laser ablation system for the analysis of radioactive samples using inductively coupled plasma mass spectrometry," *J. Anal. At. Spectrom.*, vol. 22, pp. 399–402, 2007. [Online]. Available: <http://dx.doi.org/10.1039/B616364E>
- [7] A. SASAHARA, T. MATSUMURA, G. NICOLAOU, and Y. KIYANAGI, "Isotopic analysis of actinides and fission products in lwr high-burnup uo2 spent fuels and its comparison with nuclide composition calculated using jendl, endf/b, jef and jeff," *Journal of Nuclear Science and Technology*, vol. 45, no. 4, pp. 313–327, 2008. [Online]. Available: <https://doi.org/10.1080/18811248.2008.9711440>

Bibliography

- [8] V. Brankov, G. Khvostov, K. Mikityuk, A. Pautz, R. Restani, S. Abolhassani, G. Ledergerber, and W. Wiesenack, "Analysis of effects of pellet-cladding bonding on trapping of the released fission gases in high burnup kkl bwr fuels," *Nuclear Engineering and Design*, vol. 305, pp. 559–568, 2016. [Online]. Available: <https://www.sciencedirect.com/science/article/pii/S0029549316301819>
- [9] R. Restani, M. Horvath, W. Goll, J. Bertsch, D. Gavillet, A. Hermann, M. Martin, and C. Walker, "On the condition of UO₂ nuclear fuel irradiated in a PWR to a burn-up in excess of 110 MWd/kgHM," *Journal of Nuclear Materials*, vol. 481, pp. 88–100, 2016. [Online]. Available: <https://www.sciencedirect.com/science/article/pii/S0022311516306183>
- [10] J. W. Roddy, H. C. Claiborne, R. C. Ashline, P. J. Johnson, and B. T. Rhyne, "Physical and decay characteristics of commercial lwr spent fuel," 1 1986. [Online]. Available: <https://www.osti.gov/biblio/6105618>
- [11] R. I. Ewing, "Burnup verification measurements at u.s. nuclear facilities using the fork system," 9 1995. [Online]. Available: <https://www.osti.gov/biblio/110688>
- [12] Perret, G., Rochman, D., Vasiliev, A., and Ferroukhi, H., "Neutron emission measurements of pwr spent fuel segments and preliminary validation of depletion calculations," *EPJ Web Conf.*, vol. 247, p. 10004, 2021. [Online]. Available: <https://doi.org/10.1051/epjconf/202124710004>
- [13] S. P, V. M, Z. G, P. Y, P. B, A. G, C. G, G. K, P. J, V. G, and W. R, "A non-destructive method to determine the neutron production rate of a sample of spent nuclear fuel under standard controlled area conditions," no. KJ-NA-30379-EN-N (online), 2020. [Online]. Available: <https://publications.jrc.ec.europa.eu/repository/handle/JRC121586>
- [14] C.J. Werner, et al., *MCNP Version 6.2 Release Notes*, Los Alamos National Lab. (LANL). [Online]. Available: <https://www.osti.gov/biblio/1419730>
- [15] R. Dietler, M. Hursin, G. Perret, K. Jordan, and R. Chawla, "A novel design approach for a neutron measurement station for burnt fuel," *Nuclear Instruments and Methods in Physics Research Section A: Accelerators, Spectrometers, Detectors and Associated Equipment*, vol. 693, pp. 59–66, 2012. [Online]. Available: <https://www.sciencedirect.com/science/article/pii/S0168900212007711>
- [16] A. Wolfertz, R. Adams, and G. Perret, "First tests of a gamma-blind fast neutron detector using a zns:ag-epoxy mixture cast around wavelength-shifting fibers," *Nuclear Instruments and Methods in Physics Research Section A: Accelerators, Spectrometers, Detectors and Associated Equipment*, vol. 971, p. 164003, 2020. [Online]. Available: <https://www.sciencedirect.com/science/article/pii/S0168900220304575>
- [17] A. Wolfertz, R. Adams, G. Perret, and V. Lamirand, "Development of a Multi-Channel Gamma-Blind Fast Neutron Detector Based on Wavelength Shifting Fibers Embedded

- in a ZnS:Ag Epoxy Mixture,” *Submitted to Nuclear Instruments and Methods in Physics Research Section A: Accelerators, Spectrometers, Detectors and Associated Equipment*, 2022.
- [18] A. Wolfertz, G. Perret, and R. Adams, “Non-Destructive Analysis of Spent Fuel Samples using a Gamma-Blind Fast Neutron Detector,” *Submitted to Annals of Nuclear Energy*, 2022.
- [19] G. F. Knoll, *Radiation Detection and Measurement*, 4th ed. Don Fowley, 2010.
- [20] J.-B. Mosset, A. Stoykov, U. Greuter, M. Hildebrandt, N. Schlumpf, and H. Van Swygenhoven, “Evaluation of two thermal neutron detection units consisting of zns/6lif scintillating layers with embedded wls fibers read out with a sipm,” *Nuclear Instruments and Methods in Physics Research Section A: Accelerators, Spectrometers, Detectors and Associated Equipment*, vol. 764, pp. 299–304, 2014. [Online]. Available: <https://www.sciencedirect.com/science/article/pii/S0168900214009188>
- [21] M. Hildebrandt, A. Stoykov, J.-B. Mosset, U. Greuter, and N. Schlumpf, “Detection of thermal neutrons using zns(ag):6lif neutron scintillator read out with wls fibers and sipms,” *Nuclear Instruments and Methods in Physics Research Section A: Accelerators, Spectrometers, Detectors and Associated Equipment*, vol. 824, pp. 204–207, 2016, frontier Detectors for Frontier Physics: Proceedings of the 13th Pisa Meeting on Advanced Detectors. [Online]. Available: <https://www.sciencedirect.com/science/article/pii/S0168900215013418>
- [22] J.-B. Mosset, A. Stoykov, U. Greuter, A. Gromov, M. Hildebrandt, T. Panzner, and N. Schlumpf, “A 16-ch module for thermal neutron detection using zns:6lif scintillator with embedded wls fibers coupled to sipms and its dedicated readout electronics,” *Nuclear Instruments and Methods in Physics Research Section A: Accelerators, Spectrometers, Detectors and Associated Equipment*, vol. 845, pp. 494–498, 2017, proceedings of the Vienna Conference on Instrumentation 2016. [Online]. Available: <https://www.sciencedirect.com/science/article/pii/S0168900216303618>
- [23] M. Papadionysiou, “Monte Carlo simulation of a scintillation detector for spent fuel characterization in a hot cell,” Master thesis, Eidgenössische Technische Hochschule Zürich (ETHZ), 2017.
- [24] M. Papadionysiou, G. Perret, R. Zboray, R. Adams, and J.-B. Mosset, “Monte carlo simulation of a scintillation detector for spent fuel characterization in a hot cell,” *Nuclear Engineering and Design*, vol. 332, pp. 119–126, 2018. [Online]. Available: <https://www.sciencedirect.com/science/article/pii/S0029549318303339>
- [25] A. Wolfertz, G. Perret, and R. Adams, “Development of Compact Gamma Spectrometers and Gamma-Blind Fast Neutron Detectors,” in *Specialist Workshop on Advanced Measurement Method and Instrumentation for enhancing Severe Accident Management in*

Bibliography

- an NPP addressing Emergency, Stabilization and Long-term Recovery Phase*, no. 1026. Fukushima, Japan: OECD/NEA, 2020.
- [26] Kurt Müller, Fiber Optic P. + P. AG, Email to Alexander Wolfertz, 2021-08-04.
- [27] Wavelength shifting fibers. KURARAY CO., LTD. [Online]. Available: <http://kuraraypsf.jp/psf/ws.html>
- [28] *EPO-TEK 301*, EPOXY TECHNOLOGY, INC. [Online]. Available: <https://www.epotek.com/docs/en/Datasheet/301.pdf>
- [29] (2021) ZnS:Ag Phosphor Powder EJ-600. Eljen Technology. [Online]. Available: <https://eljentechnology.com/products/zinc-sulfide-coated/ej-600>
- [30] (2021) ASD-RGB3S-P, ASD-NUV3S-P. AdvanSiD. [Online]. Available: <https://advansid.com/products/product-detail/asd-rgb-nuv-3s-p>
- [31] (2021) MAX5026. Maxim Integrated. [Online]. Available: <https://www.maximintegrated.com/en/products/power/switching-regulators/MAX5026.html>
- [32] *Multilayer NTC Thermistors*, Panasonic Industry. [Online]. Available: <https://industrial.panasonic.com/cdbs/www-data/pdf/AUA0000/AUA0000C8.pdf>
- [33] (2017) MAR-6SM+. Mini-Circuits. [Online]. Available: <https://www.minicircuits.com/WebStore/dashboard.html?model=MAR-6SM%2B>
- [34] (2021) saleae. Saleae, Inc. [Online]. Available: <https://www.saleae.com/>
- [35] L. Becker-Sander, “Development of FPGA Signal Processing Electronics for NovelFast Neutron Detectors,” Master Thesis, Eidgenössische Technische Hochschule Zürich (ETHZ), 2020.
- [36] Logic 1.x Download - Saleae Support. Saleae, Inc. [Online]. Available: <https://support.saleae.com/logic-software/legacy-software/older-software-releases#logic-1-x-download-links>
- [37] X.-S. Yang, “Chapter 1 - introduction to algorithms,” in *Nature-Inspired Optimization Algorithms*, 2nd ed., X.-S. Yang, Ed. Academic Press, 2021, pp. 1–22. [Online]. Available: <https://www.sciencedirect.com/science/article/pii/B9780128219867000081>
- [38] U. S. G. Perret, *Measurement of Cf-252 Source # 1154 Intensity*, Paul Scherrer Institut, AN-41-18-09.
- [39] “Data extracted using the live chart of nuclides on-line data service from the ensdf database, accessed on 2022-05-04.” [Online]. Available: <https://www-nds.iaea.org/relnsd/vcharthtml/VChartHTML.html>

-
- [40] Berthold Technologies GmbH & Co.KG. (2021) LB 6411 Neutron Dose Rate Probe - Berthold Technologies. [Online]. Available: <https://www.berthold.com/en/radiation-protection/products/dose-and-dose-rate/neutron-dose-rate-probe-lb-6411/>
- [41] Freiburger Sensortechnik. SmartREM Neutron Monitor with MCA. [Online]. Available: <http://www.fst-sensortechnik.com/download/smartrem.pdf>
- [42] Rochman, Dimitri A., Vasiliev, Alexander, Dokhane, Abdelhamid, and Ferroukhi, Hakim, "Uncertainties for swiss lwr spent nuclear fuels due to nuclear data," *EPJ Nuclear Sci. Technol.*, vol. 4, p. 6, 2018. [Online]. Available: <https://doi.org/10.1051/epjn/2018005>
- [43] N. J. Roberts and L. N. Jones, "The content of 250Cf and 248Cm in 252Cf neutron sources and the effect on the neutron emission rate," *Radiation Protection Dosimetry*, vol. 126, no. 1-4, pp. 83–88, 05 2007. [Online]. Available: <https://doi.org/10.1093/rpd/ncm017>
- [44] K. G. plc. (2022) Gr1 | czt-based high performance gamma-ray spectrometer | kromek. Kromek Group plc. [Online]. Available: <https://www.kromek.com/product/gr1/>
- [45] "Isotope browser," International Atomic Energy Agency (IAEA). [Online]. Available: <https://play.google.com/store/apps/details?id=iaea.nds.nuclides>
- [46] Iwamoto, Osamu, Iwamoto, Nobuyuki, Shibata, Keiichi, Ichihara, Akira, Kunieda, Satoshi, Minato, Futoshi, and Nakayama, Shinsuke, "Status of jendl," *EPJ Web Conf.*, vol. 239, p. 09002, 2020. [Online]. Available: <https://doi.org/10.1051/epjconf/202023909002>
- [47] M. Chadwick, P. Obložinský, M. Herman, N. Greene, R. McKnight, D. Smith, P. Young, R. MacFarlane, G. Hale, S. Frankle, A. Kahler, T. Kawano, R. Little, D. Madland, P. Moller, R. Mosteller, P. Page, P. Talou, H. Trellue, M. White, W. Wilson, R. Arcilla, C. Dunford, S. Mughabghab, B. Pritychenko, D. Rochman, A. Sonzogni, C. Lubitz, T. Trumbull, J. Weinman, D. Brown, D. Cullen, D. Heinrichs, D. McNabb, H. Derrien, M. Dunn, N. Larson, L. Leal, A. Carlson, R. Block, J. Briggs, E. Cheng, H. Huria, M. Zerkle, K. Kozier, A. Courcelle, V. Pronyaev, and S. van der Marck, "ENDF/B-VII.0: Next Generation Evaluated Nuclear Data Library for Nuclear Science and Technology," *Nuclear Data Sheets*, vol. 107, no. 12, pp. 2931–3060, 2006, evaluated Nuclear Data File ENDF/B-VII.0. [Online]. Available: <https://www.sciencedirect.com/science/article/pii/S0090375206000871>
- [48] A. Theler, *Gamma irradiation in LOTUS with SILC*, École Polytechnique Fédérale de Lausanne (EPFL).
- [49] M. E. Anderson and R. A. Neff, "Neutron energy spectra of different size 239pube(α ,n) sources," *Nuclear Instruments and Methods*, vol. 99, pp. 231–235, 3 1972.
- [50] O. Klein and Y. Nishina, "Über die streuung von strahlung durch freie elektronen nach der neuen relativistischen quantendynamik von dirac," *Zeitschrift für Physik*, vol. 52, no. 11, pp. 853–868, Nov 1929. [Online]. Available: <https://doi.org/10.1007/BF01366453>

Bibliography

- [51] B. P. Soubelet, "Development of energy-selective fast neutron imaging for nondestructive elemental analysis," Doctoral thesis, Eidgenössische Technische Hochschule Zürich (ETHZ), 2020. [Online]. Available: <http://hdl.handle.net/20.500.11850/405611>
- [52] V. de Buys, "Characterization of a Neutron Detector Efficiency as a Function of Energy," Semester thesis, Eidgenössische Technische Hochschule Zürich (ETHZ), 2021.
- [53] H. Kromer, "Optimization of a compact D-D fast neutron generator for imaging applications," Doctoral thesis, Eidgenössische Technische Hochschule Zürich (ETHZ), 2020. [Online]. Available: <http://hdl.handle.net/20.500.11850/450395>
- [54] H. Kromer, R. Adams, and H.-M. Prasser, "Development, design, and testing of a microwave-driven compact rotating-target d-d fast neutron generator for imaging applications," *Applied Radiation and Isotopes*, vol. 174, p. 109715, 2021. [Online]. Available: <https://www.sciencedirect.com/science/article/pii/S0969804321001226>
- [55] E. D. Re, "Simulation and Optimization of Fast Neutron Detectors Based on Wavelength Shifting Fibers Embedded in a ZnS:Ag Scintillator," Master's thesis, Eidgenössische Technische Hochschule Zürich (ETHZ), 2020.
- [56] C. Seyffert, "Simulation of the Digital Signal Processing of a Novel Fast Neutron Detector Based on Wavelength Shifting Fibres Embedded in a ZnS(Ag)-Epoxy Mixture," Semester Thesis, Eidgenössische Technische Hochschule Zürich (ETHZ), 2020.
- [57] N. König, "Improved Modelling of Gamma-Blind Fast Neutron Detectors Using an ZnS:Ag Scintillator," Bachelor Thesis, Eidgenössische Technische Hochschule Zürich (ETHZ), 2021.
- [58] —, "Improved Simulation of Gamma-Blind Fast Neutron Detectors Using an ZnS:Ag Scintillator," Semester Thesis, Eidgenössische Technische Hochschule Zürich (ETHZ), 2022.
- [59] Kernkraftwerk Gösgen. Kernkraftwerk Gösgen-Däniken AG. [Online]. Available: <https://www.kkg.ch/>
- [60] LWR-PROTEUS Programme (1997 2005). [Online]. Available: <https://www.psi.ch/en/erp/lwr-experiments>
- [61] P. Grimm, *CASMO-4E Calculations of the Isotopic Inventories of the LWR-PROTEUS Phase II Irradiated Fuel Samples from KKG*, Paul Scherrer Institut, TM-41-07-07.
- [62] *Neutron Emission Measurements of PWR Spent Fuel Segments and Preliminary Validation of Depletion Calculations*. Paul Scherrer Institut (PSI), 2020. [Online]. Available: https://tendl.web.psi.ch/bib_rochman/physor2020-3.pdf
- [63] P. Grimm, *CASMO-5 Burnup Calculations for the LWR-PROTEUS Phase II Burnt Samples and Comparison with Measured Compositions*, Paul Scherrer Institut, TM-41-14-27.

- [64] P. Grimm, I. Günther-Leopold, and H. Berger, “Burnup Calculations and Chemical Analysis of Irradiated Fuel Samples Studied in LWR-PROTEUS Phase II,” *PHYSOR-2006, ANS Topical Meeting on Reactor Physics*, 2006.
- [65] I. Günther-Leopold, J. K. Waldis, B. Wernli, and Z. Kopajtic, “Measurement of plutonium isotope ratios in nuclear fuel samples by HPLC-MC-ICP-MS,” *International Journal of Mass Spectrometry*, vol. 242, no. 2, pp. 197–202, 2005, isotope Ratio Measurements SI. [Online]. Available: <https://www.sciencedirect.com/science/article/pii/S1387380604004646>
- [66] M. Murphy, F. Jatuff, P. Grimm, R. Seiler, R. Brogli, G. Meier, H.-D. Berger, and R. Chawla, “Reactivity and neutron emission measurements of highly burnt pwr fuel rod samples,” *Annals of Nuclear Energy*, vol. 33, no. 9, pp. 760–765, 2006. [Online]. Available: <https://www.sciencedirect.com/science/article/pii/S0306454906000661>
- [67] A. N. Tikhonov, A. V. Goncharsky, V. V. Stepanov, and A. G. Yagola, *Numerical Methods for the Solution of Ill-Posed Problems*, ser. Mathematics and Its Applications. Dordrecht: Springer Netherlands, 1995, vol. 328.
- [68] *Experts Meeting on Fast Neutron Imaging*. Technische Universität München (TUM), 2019. [Online]. Available: <https://indico.frm2.tum.de/event/193/>
- [69] Raspberry Pi Documentation - Camera. Raspberry Pi Ltd. [Online]. Available: <https://www.raspberrypi.com/documentation/accessories/camera.html>
- [70] *Parameter of Lens*. [Online]. Available: https://cdn-shop.adafruit.com/product-files/4562/4562_datasheet.pdf
- [71] S. Caruso, M. Murphy, F. Jatuff, and R. Chawla, “Determination of within-rod caesium and europium isotopic distributions in high burnup fuel rods through computerised gamma-ray emission tomography,” *Nuclear Engineering and Design*, vol. 239, no. 7, pp. 1220–1228, 2009. [Online]. Available: <https://www.sciencedirect.com/science/article/pii/S0029549309001344>
- [72] G. F. Knoll, *Radiation Detection and Measurement*, 4th ed. Don Fowley, 2010.
- [73] L. Galli, A. Baldini, F. Cei, M. Chiappini, M. Francesconi, M. Grassi, U. Hartmann, M. Meucci, F. Morsani, D. Nicolò, A. Papa, S. Ritt, E. Schmid, and G. Signorelli, “Wavedaq: An highly integrated trigger and data acquisition system,” *Nuclear Instruments and Methods in Physics Research Section A: Accelerators, Spectrometers, Detectors and Associated Equipment*, vol. 936, pp. 399–400, 2019, frontier Detectors for Frontier Physics: 14th Pisa Meeting on Advanced Detectors. [Online]. Available: <https://www.sciencedirect.com/science/article/pii/S0168900218309033>

Curriculum Vitae

Alexander Wolfertz

1 Personal Data

Name: Alexander Wolfertz
Address: Katzenbachstrasse 101
8052 Zürich
Date of Birth: 16.1.1995
Place of Birth: Göttingen D
Nationality: Germany

2 Education

Secondary School:	2007 – 2012	Kantonsschule Oerlikon
	2012 – 2013	Kantonsschule Zürich Nord
University:	2013 – 2014	Bachelor Mathematics ETHZ
	2014 – 2016	Bachelor Physics ETHZ
	2016 – 2018	Master Physics ETHZ
	2018 – 2022	PhD Energy EPFL

3 Work Experience

Teaching Assistant:	2016 – 2018	Linear Algebra, ETH Zürich
Research Assistant:	2018	Laboratory for Nuclear Energy Systems, ETH Zürich
PhD Student:	2018 – 2022	Paul Scherrer Institut (PSI)
Postdoc:	since 2022	Technische Universität München (TUM)

4 Other Activities

Auditor	2017 – 2019	Association Gladius et Codex
Treasurer	Since 2019	Association Gladius et Codex
Head of PR	2019 – 2021	PhD and Postdoc Association at PSI
Vice-President	2020 – 2021	PhD and Postdoc Association at PSI
President	2021	PhD and Postdoc Association at PSI
Member	2020 – 2022	PSI Employee Committee (PeKo)

5 Other Certificates and Honors

Special honors for outstanding work as part of the PSI Employee Committee.

Monitor certificate of the Swiss Historical European Martial Arts Association.

6 Publications

- Nicolí, Giorgio et al. (2018). “Cavity-Mediated Coherent Coupling between Distant Quantum Dots”. In: *Phys. Rev. Lett.* 120 (23), p. 236801. DOI: [10.1103/PhysRevLett.120.236801](https://doi.org/10.1103/PhysRevLett.120.236801). URL: <https://link.aps.org/doi/10.1103/PhysRevLett.120.236801>.
- Wolfertz, Alexander (May 8, 2018). “Development of a Gamma-Blind Fast Neutron Detector Based on ZnS and Wavelength-Shifting Fibers”. Master Thesis. Eidgenössische Technische Hochschule Zürich (ETHZ).
- Wolfertz, Alexander, Robert Adams, and Grégory Perret (2019). “First Tests of a Gamma-Blind Fast Neutron Detector Prototype Based on ZnS and Wavelength-Shifting Fibers”. English. In: ANS annual meeting 2019. The value of nuclear (June 9, 2019). Minneapolis, USA, pp. 426–428.
- (2020). “First tests of a gamma-blind fast neutron detector using a ZnS:Ag-epoxy mixture cast around wavelength-shifting fibers”. In: *Nuclear Instruments and Methods in Physics Research Section A: Accelerators, Spectrometers, Detectors and Associated Equipment* 971, p. 164003. ISSN: 0168-9002. DOI: <https://doi.org/10.1016/j.nima.2020.164003>. URL: <https://www.sciencedirect.com/science/article/pii/S0168900220304575>.

- Wolfertz, Alexander, Grégory Perret, and Robert Adams (2020). “Development of Compact Gamma Spectrometers and Gamma-Blind Fast Neutron Detectors”. English. In: *Specialist Workshop on Advanced Measurement Method and Instrumentation for enhancing Severe Accident Management in an NPP addressing Emergency, Stabilization and Long-term Recovery Phase*. 1026. OECD/NEA. Fukushima, Japan.
- Wolfertz, Alexander et al. (2020). “Overview over Fast Neutron Lab Activities”. In: *The 1st Workshop on Efficient Neutron Sources ENS2019*. Workshop on Efficient Neutron Sources (ENS2019) (Paul Scherrer Institut, Sept. 2, 2019). Villigen, CH, pp. 84–87.

7 Languages

German: Native tongue
 English: Fluent
 French: Basic Knowledge
 Latin: Basic Knowledge

8 Programming/Hardware Description/Typesetting Languages

Mathematica:	Good
Matlab:	Very Good
Java:	Very Good
C++:	Good
C:	Basic Knowledge
Brainfuck:	Good
PHP:	Basic Knowledge
Python:	Basic Knowledge
MCNP:	Basic Knowledge
VHDL:	Basic Knowledge
System Verilog:	Good
LaTeX:	Good
HTML:	Basic Knowledge